Improving predictions for collider observables by consistently combining fixed order calculations with resummed results in perturbation theory

Marek Schönherr

Institut für Kern- und Teilchenphysik

Fakultät Mathematik und Naturwissenschaften

Technische Universität Dresden

Improving predictions for collider observables by consistently combining fixed order calculations with resummed results in perturbation theory

vorgelegt von

Dipl.-Phys. Marek Schönherr

geboren am 29. März 1982 in Plauen.

Eingereicht am 15.09.2011

1. Gutachter: Prof. Dr. Dominik Stöckinger

2. Gutachter: Dr. Frank Krauss

Contents

Appendix 187

List of Figures

List of Tables

Chapter 1

Introduction

The LHC poses new challenges to both the experimental and the theoretical community. It operates at the highest centre-of-mass energies ever reached in a collider experiment and provides an enormous luminosity, leading to tremendously large event rates. On the experimental side, the huge phase space in conjunction with the exciting and intricate physics programme of the LHC, ranging from high-precision flavour physics at comparably low scales to the discovery of new particles in the TeV range necessitated the development and refinement of triggers and analysis techniques. In addition, from a more technological point of view, data acquisition, storage and processing therefore required the creation of a world-wide network satisfying the greatly increased computing needs.

On the theoretical side, on the other hand, demands for higher precision to correctly model signals of new physics and their backgrounds led to the reorientation of calculation and simulation paradigms facilitating the inclusion of the newest theoretical developments, thus, making them accessible to the experiments. These paradigm shifts manifest themselves in the modular structure of the modern general-purpose event generators, proving to be indispensable tools in both data analysis and particle level theory predictions. It is thus no surprise that these new tools have a sizable impact on the understanding of LHC physics.

1.1 Event generators

Figure 1.1 pictorially represents a hadron-collider event, where a $t\bar{t}h$ final state is produced and evolves by including effects of QCD bremsstrahlung in the initial and final state, the underlying event, hadronisation and, finally, the decays of unstable hadrons into stable ones. Event generators usually rely on the factorisation of such events into different well-defined phases, corresponding to different kinematic regimes. In the description of each of these phases different approximations are employed. In general the central piece of the event simulation is provided by the hard process (the dark red blob in the figure), which can be calculated in fixed order perturbation theory in the coupling constants owing to the correspondingly high scales. This part of the simulation is handled by computations based on matrix elements, which are either hard-coded or provided by special programs called parton-level or matrix-element (ME) generators. The QCD evolution described by parton showers then connects the hard scale of coloured parton creation with the hadronisation scale where the transition to the colourless hadrons occurs. The parton showers model multiple QCD bremsstrahlung in an approximation to exact perturbation theory, which is accurate to leading logarithmic order. At the hadronisation scale, which is of the order of a few Λ_{QCD}, QCD partons are transformed into primary hadrons (light green blobs) by applying purely phenomenological fragmentation models having typically around ten parameters to be fitted to data. The primary hadrons finally are decayed into particles that can be observed
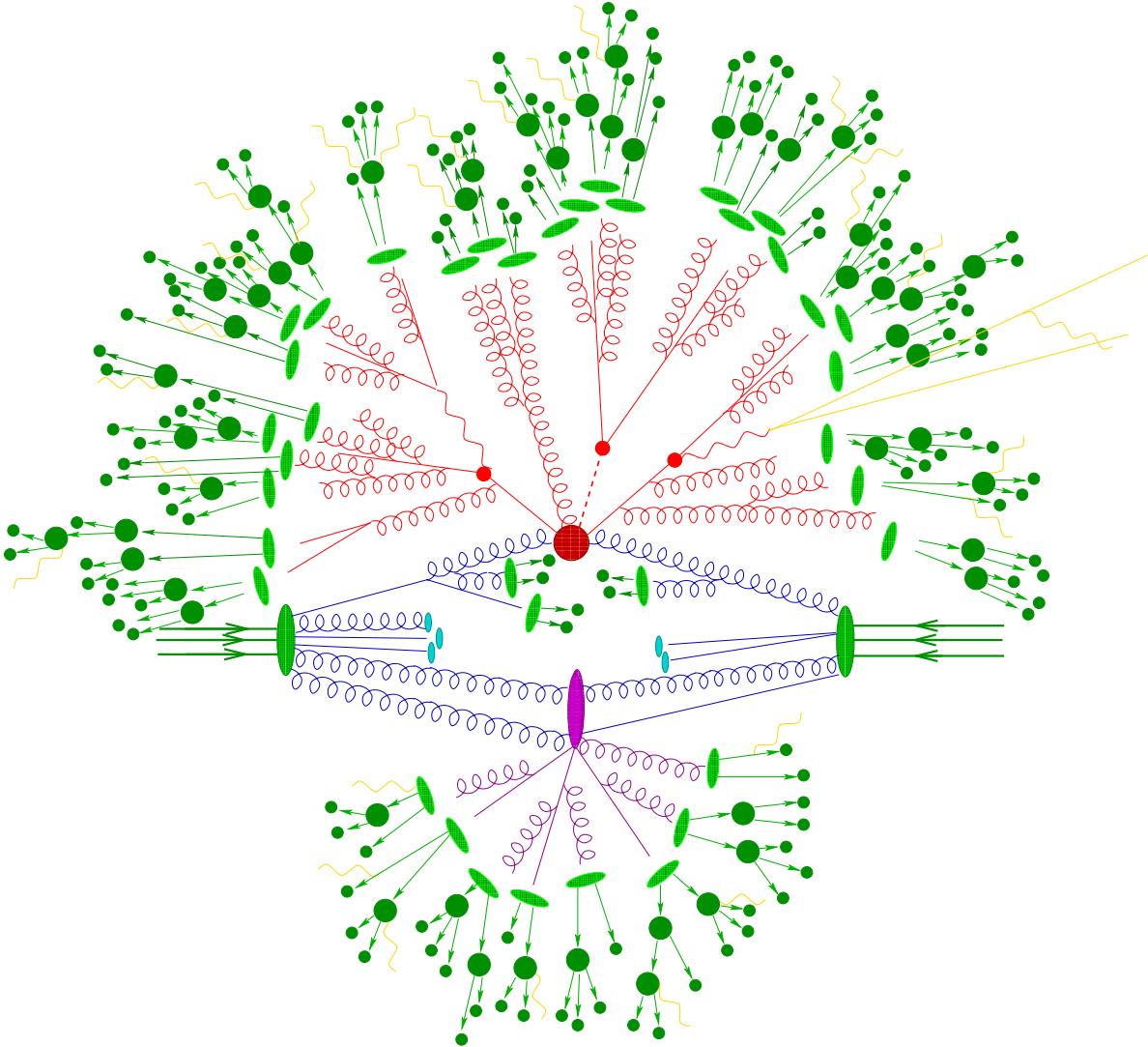
Figure 1.1: Pictorial representation of a $t\bar{t}h$ event as produced by an event generator according to the factorisation approach. The hard interaction (big red blob) is followed by the decay of both top quarks and the Higgs boson (small red blobs). Additional hard QCD radiation is produced (red) and a secondary interaction takes place (purple blob) before the final-state partons hadronise (light green blobs) and hadrons decay (dark green blobs). Photon radiation occurs at any stage (yellow).

in detectors. In most cases effective theories or simple symmetry arguments are invoked to describe these decays. Another important feature associated with the decays is QED bremsstrahlung, which is simulated by techniques that are accurate at leading logarithmic order and, eventually, supplemented with exact fixed-order results. A particularly difficult scenario arises in hadronic collisions, where remnants of the incoming hadrons may experience secondary hard or semi-hard interactions. This underlying event is pictorially represented by the purple blob in Figure 1.1. Such effects are beyond QCD factorisation theorems and therefore no complete first-principles theory is available. Instead, phenomenological models are employed again, with more parameters to be adjusted by using comparisons with data.

The most prominent examples of event generators [1] are the highly successful, well-established programs PYTHIA [2] and HERWIG [3, 4]. They have been constructed over the past decades alongside with experimental discoveries and most of the features visible in past and present experiments can be described by them. However, the need for higher precision to meet the decreasing size of the experimental uncertainties of increasingly complex experimentally accessible signatures of signal and background processes both at the Tevatron and the LHC necessitates a high level of modularity separating the physics at different scales in a clean and well defined way. This led to improved re-implementations in form of the programs PYTHIA8 [5] and HERWIG++ [6] – the successors of the of the programs mentioned above – and to the construction of the SHERPA event generator [7, 8]. All three programs, however, model the primary partonic interaction at leading order only.

In conjunction, in the past decade codes for next-to-leading order calculations have been made available to the public; prominent examples include MCFM [9] and NLOJET++ [10]. Furthermore, methods have been proposed for the consistent matching of next-to-leading order corrections with parton-shower algorithms [11, 12, 13]. Corresponding methods are implemented for example in the public programs MC@NLO [14], which was originally based on HERWIG but has been generalised to HERWIG++ and PYTHIA, in HERWIG++ and in some more specialised programs collected in the POWHEGBOX [15]. The automated NLO matching implemented in the SHERPA event generator will be subject of this thesis. However, the full next-to-leading order calculations underlying these new techniques are very complex and challenging. On the other hand, many important experimental signatures rely on final states with higher multiplicities. This has triggered substantial activity in perfecting techniques and tools at tree-level accuracy, such that by now several codes are available that can compute corresponding cross sections and generate events in a fully automated way. The most prominent examples include ALPGEN [16], CompHEP/CalcHEP [17, 18], HELAC-PHEGAS [19, 20, 21], MADGRAPH [22, 23], WHIZARD [24], AMEGIC++ [25] and COMIX [26]. Currently only AMEGIC++ and COMIX are part of, and integrated in, a full-fledged event generator, namely the SHERPA framework. In order to translate the multi-particle parton-level events, which are provided by these tools at leading order, into hadron-level events, several algorithms have been developed, all aiming at preserving the logarithmic accuracy of the parton shower and supplementing it with the exact perturbative leading order result for given jet multiplicities. In [27] an algorithm achieving this goal in e^+e^- annihilations into hadrons has been presented, it has been extended to hadronic collisions in [28] and improved in [29]. A similar algorithm for the dipole shower has been discussed in [30, 31], whereas more different ones have been published in [32, 33, 34, 35]. All these approaches have been compared in [36, 37] and a good agreement has been established.

1.2 The event generator SHERPA

SHERPA [7, 8], acronym for "Simulation of High Energy Reactions of PArticles", is a complete event generation framework that has been constructed from scratch and entirely written in the modern, object oriented programming language `C++`.

Construction paradigm

The construction of SHERPA has been pursued in a way largely defined by the following three paradigms:

- Modularity. Different physics aspects are implemented in almost independent modules, relying on a small number of framework and support modules, like, e.g., the event record etc.. Modularity allows, for example, to have more than one matrix-element generator or parton shower in parallel, with the user being in charge of making a choice. The central module, SHERPA, steers the interplay of all other parts and the actual generation procedure.

- Bottom-to-Top. Physics modules are typically developed in their own right, being tested and validated before they are incorporated into the full event generation framework. This in turn results in a quite flexible, minimal structure underlying the organisation of event generation.

- Separation of interface and implementation. In order to facilitate the two requirements above, SHERPA relies on a structure where the (nearly independent) physics modules are accessible only through physics-specific handlers. These handlers assist SHERPA in generating the event at different stages, each of which is steered through a specific implementation of `Event_Phase_Handler`, such as `Signal_Process` or `Jet_Evolution`. An example for such an interplay of event phase and physics handler is the `Matrix_-Element_Handler`, enabling the generation of parton-level events either by the built-in hard-coded matrix elements or by the matrix-element generators AMEGIC++ or COMIX. This is relevant for two event stages, the generation of the signal process and owing to the multijet merging procedure the evolution of the jets.

This overall structure fully reflects the paradigm of Monte Carlo event generation by factorising the simulation into well-defined, almost independent phases. Accordingly, each `Event_Phase_Handler` encapsulates in an abstract way a different aspect of event generation for high-energy particle reactions. This abstraction is then replaced by real physics using handlers, which ensure that the overall event generation framework can be blind to the finer details of the underlying physics and its implementation in form of a physics module.

Physics modules

In the following the main modules currently distributed with SHERPA[1] will be listed and briefly described.

- AMEGIC++ [25].
  This is one of SHERPA's matrix-element generators. It is based on Feynman diagrams, which are translated to helicity amplitudes using the methods of [38, 39]. AMEGIC++ has been thoroughly tested for multiparticle production in the Standard Model [40]. Its MSSM implementation has been validated in [41], as well as its ADD extension [42]. Further, AMEGIC++ natively supports various extensions of the Standard Model (a fourth generation, anomalous top quark couplings, anomalous weak gauge couplings, $U(1)$ phantom Higgs, a $U(1)_B$ Z' model, a hidden sector and an axigluon extension), the Two-Higgs-Doublet Model, and the inclusion of the effective $gg \to H$ and $\gamma\gamma \to H$ vertices in both the Standard Model and the MSSM. AMEGIC++ also allows for a model definition using FEYNRULES inputs [43, 44].
  AMEGIC++ employs the Monte Carlo phase-space integration library PHASIC. For the evaluation of initial-state (laser backscattering, initial-state radiation) and final-state integrals, the adaptive multi-channel method of [45, 46] is used by default together with a Vegas optimisation [47] of the single channels. In addition, final-state integration accomplished by RAMBO [48] and HAAG [49] is supported. Further, as detailed in [50], AMEGIC++ includes an automated implementation of the Catani-Seymour dipole subtraction terms [51, 52]. Together with interfaces to one-loop codes through the Binoth-Les Houches accord interface [53], dedicated interfaces to BLACKHAT [54] or MCFM [9] or internally hard-coded one-loop matrix elements it is a key ingredient in calculating next-to-leading order processes.

---

[1] The list below reflects the status of the package as of version 1.3.0.

- COMIX [26].

  SHERPA's second matrix element generator is based colour-dressed Behrends-Giele recursion relations [55], basing on [56, 57, 58, 59, 60]. It is therefore best suited for the calculation of high multiplicity final state [61]. The improved performance in the multileg regime owes to the usage of colour sampling and dedicated phase space integration and multi-threading routines.

- CSS [62].

  The CSS is a parton shower based on the Catani-Seymour dipole factorisation [51, 52]. The shower evolution is governed by the DGLAP equations and is ordered in the partons' relative transverse momentum. Coherence effects are accounted for by the incorporation of the soft limit into the splitting functions by construction [63]. All features needed for a consistent merging with matrix elements [27, 28, 29] are included. It has been extended to optionally include QED-evolution [64] or Hidden-Valley-evolution and its kinematics have been optimised.

- POWHEG [65].

  The POWHEG module is a variant of the CSS adapted to implementing the POWHEG and MENLOPS methods. To this end it is limited to a single emission and the possibility for matrix element reweighting is enabled. To this end it is able to calculate the fixed order parton shower approximation to a real emission matrix element and effect matrix element corrections.

- AMISIC++ [66].

  This module simulates multiple parton interactions according to [67]. In SHERPA the treatment of multiple interactions has been extended by allowing the simultaneous evolution of an independent parton shower in each of the subsequent collisions. This shower evolution is handled by the CSS.

- AHADIC++.

  AHADIC++ is SHERPA's hadronisation package for translating the partons (quarks and gluons) into primordial hadrons. The algorithm is based on the cluster-fragmentation ideas presented in [68, 69, 70, 71], which are also implemented in the HERWIG event generators. It should be noted that AHADIC++, essentially based on [72], indeed differs from the original versions.

- HADRONS++ [73].

  HADRONS++ is the module for simulating hadron and τ-lepton decays. The resulting decay products respect full spin correlations (if desired). Several matrix elements and form-factor models have been implemented, such as the Kühn-Santamaría model or form-factor parametrisations from Resonance Chiral Theory for the τ-leptons and form factors from heavy quark effective theory or light-cone sum rules for hadron decays.

- PHOTONS++ [74].

  The PHOTONS++ module holds routines to add QED radiation to hadron and τ-lepton decays based on the YFS algorithm [75]. The structure of PHOTONS++ is designed such that the formalism can be extended to scattering processes and to a systematic improvement to higher orders in perturbation theory, cf. [74]. The application of PHOTONS++ therefore fully accounts for corrections that are usually added by the application of PHOTOS [76].

SHERPA itself is the steering module that initialises, controls and evaluates the different phases during the process of event generation. Furthermore, all routines for the combination of parton showers and matrix elements, which are independent of the specific parton shower are found in this module.

In addition to the main modules of SHERPA, there is a set of tools providing basic routines for event generation, general methods for the evaluation of helicity amplitudes, some generic matrix elements, etc.. Interfaces to commonly used structures like the LHAPDF package [77], SLHA [78] or FEYNRULES [43, 44] inputs exist as well as interfaces to most frequently used output formats like HEPEVT and HEPMC. Similarly, beyond a native analysis package, SHERPA comprises a direct interface to the RIVET [79, 80] and HZTOOL [81] analysis packages.

1.3   Outline of this thesis

This thesis concerns itself with the consistent combination of fixed order matrix elements and resummed results and its implementation in the framework of the SHERPA event generator.

Part I details the combination of the Yennie-Frautschi-Suura (YFS) resummation, resumming soft photon logarithms in QED, with fixed-order higher-order matrix elements. First, the YFS formalism is reviewed in Chapter 2, detailing also the inclusion of fixed-order higher-order matrix elements. Then its implementation into the physics module PHOTONS++, part of the SHERPA event generator, is reported in Chapter 3. It, again, pays special attention on fixed-order hard-emission corrections, both through universal collinear approximations using the DGLAP formalism (see Part II) and through process-specific fixed-order matrix elements. Chapter 4 collects selected results of the implementation for selected processes with the Standard Model where all parts of the calculation can unambiguously be determined from first principles. Therein, the description of the Z boson lineshape and the radiative decay rates of μ and τ leptons are compared to descriptions using the DGLAP resummation and experimental data. Chapter 5, on the other hand, reports on an application of the YFS formalism to semileptonic B meson decays. Their decays currently cannot be described by first principles and low-energy effective models have to be employed. Nonetheless, by supplementing these effective models with QED gauge invariance the YFS formalism can still be employed and soft photon logarithms can be resummed. The theoretical framework to calculate the hard emission next-to-leading order corrections to these decays, together with a primitive matching to high-energy regimes beyond the validity of the low-energy effective models, as well as structure dependent corrections, stemming from the non-fundamentality of the involved mesons, are discussed. Subsequently results on both the inclusive decay widths and exclusive particle spectra are reported.

Part II is then devoted to the consistent combination of the Dokshitzer-Gribov-Lipatov-Altarelli-Parisi (DGLAP) resummation, resumming collinear parton radiation, with fixed-order higher-order matrix elements. Although being valid for, and actually being first shown to hold for, QED collinear radiation, this part of this thesis focuses on the application of the DGLAP resummation on QCD partons. The DGLAP resummation itself (in the QCD context) is introduced in Chapter 6. Chapter 7 then methodically introduces an abstract and universal parton shower formulation, focusing on its description of real emission corrections in the DGLAP-inspired[2] (soft-)collinear approximation in the DGLAP-inherent single-leg language. The obtained parton shower formulation can then straight forwardly be corrected to the exact expression using corrective weights on each such single leg. With these things at

---

[2] Parton showers essentially implement the DGLAP equation in a unitary algorithm. However, due to the presence of more terms than just the Altarelli-Parisi splitting kernels, be it due to terms arising because of momentum conservation for finite $k_\perp$ or explicitly incorporating them, the parton shower splitting kernels, and thus their effective approximation of the real emission matrix element, are referred to as DGLAP-inspired here.

hand, one of the known methods to combine the DGLAP resummation with fixed-order next-to-leading order matrix elements, is then reinterpreted as a simple matrix-element reweighted parton shower, supplied with a next-to-leading order weight. The consistency of this reinterpreted method is then shown explicitly, leading to the description of any infrared safe inclusive observable at both next-to-leading order and (next-to-)leading logarithmic accuracy. Its implementation in SHERPA is detailed and a wealth of results, examining both its consistency and its comparison with experimental data, is presented. Chapter 8 then details the combination of the reformulated POWHEG method with the well-known ME+PS method of merging tree-level matrix elements of increasing final state parton multiplicities[3] into one inclusive sample. The resulting algorithm, dubbed MENLOPS, then produces inclusive event samples describing any infrared safe inclusive observable at the same accuracy as the POWHEG method and observables, depending on additional jet activity, are described at leading order accuracy, as with the ME+PS method. The MENLOPS thus offers a simultaneous description of arbitrary observables surpassing both the POWHEG and ME+PS methods individually. Chapter 8 then closes with wealth of consistency checks and comparisons to experimental data.

A summary can be found in Chapter 8.4

---

[3] Although the ME+PS algorithm was extended to cover QED radiation, i.e. photons, as well, only its QCD application will be used in the context of Chapter 8.

Part I

Yennie-Frautschi-Suura resummation and fixed order calculations

Introduction

Higher-order QED corrections have important effects on experimentally accessible observables and need to be accounted for both at low- and high-energy colliders. Their impact has been studied in detail at SLC and LEP as well as the B-factories

The approach of Yennie, Frautschi and Suura (YFS), discussed in this part of this thesis, resides on the idea of constructing the infrared limits of both real and virtual corrections order by order and then resumming the universal expressions corresponding to the leading soft logarithms. These soft logarithms are independent of the inner process characteristics and can be calculated from the external particles and their four-momenta only. The big advantage of the YFS formalism is that in addition it allows for a systematic improvement of this soft eikonal approximation, order-by-order in the QED coupling constant. This explains why a good fraction of the most precise tools for the simulation of QED radiation root in this algorithm [82, 83, 84, 85].

The outline of this part of this thesis is as follows: After briefly reviewing the YFS formalism in Chapter 2 in the framework of particle decays, the Monte Carlo algorithm adopted here is detailed in Chapter 3. Special emphasis is put on how hard emission fixed-order corrections can be effected. Chapter 4 presents results obtained for the description of QED radiation in Drell-Yan production and compares the prediction for the radiative decay rates in the leptonic decay channels of muon and tau decays. Finally, in Chapter 5 the algorithm is used to compute higher order electroweak corrections to semileptonic B-meson decays and presents results both for the corrected integrated decay rates and exclusive kinematic distributions of observable leptons, mesons and photons.

Chapter 2

Yennie-Frautschi-Suura resummation

This part of this thesis is dedicated to a brief review of the Yennie-Frautschi-Suura (YFS) resummation [75] and its underlying ideas in the context of particle decays. Its derivation for scattering processes proceeds along the same lines and culminates in the equivalent final formulae. For a more in depth derivation see the original publication [75] or [86].

The YFS approach constructs an approximative description of real and virtual QED corrections to arbitrary scattering or decay processes, as depicted in Figure 2.1. The virtue of this formalism is that it can systematically be improved, order by order in the electromagnetic coupling constant α. The YFS approach bases on the observation that the soft limits for matrix elements with real and/or virtual photons exhibit a universal behaviour, and on the fact that the corresponding soft divergences can be factorised into universal factors multiplying leading order matrix elements.

When defining the final state as a configuration of primary decay products with momenta p_f and any number of additional soft photons with momenta k the fully inclusive decay rate reads

$$
\Gamma \;=\; \frac{1}{2M} \sum_{n_R=0}^{\infty} \frac{1}{n_R!} \int \mathrm{d}\Phi_p\,\mathrm{d}\Phi_k\,(2\pi)^4\,\delta\left(\sum p_i - \sum p_f - \sum k\right) \left| \sum_{n_V=0}^{\infty} \mathcal{M}_{n_R}^{n_V + \frac{1}{2}n_R} \right|^2 \quad (2.0.1)
$$

where p_i is the four-momentum of the decaying particle. Here and in the following n_V and n_R are the numbers of additional virtual and real photons, respectively, that show up in the higher-order matrix element but not in the uncorrected leading order matrix element (thus labeled by $\mathcal{M}_0^0$). Hence, the sub- and superscripts denote the number of additional final state photons and the relative order in α of the given matrix element. The starting point of the YFS algorithm is to approximate these dressed matrix elements through the leading order one times eikonal factors, which depend on the external particles only. This effectively catches the leading logarithmic QED corrections to the process. The correct result can then be restored order by order in perturbation theory by supplementing the non-leading, process-dependent pieces.

2.1 Resummation of virtual photon corrections

In the case of one virtual photon this can be formalised as

$$
\mathcal{M}_0^1 \;=\; \alpha B\,\mathcal{M}_0^0 + M_0^1\,, \quad (2.1.1)
$$
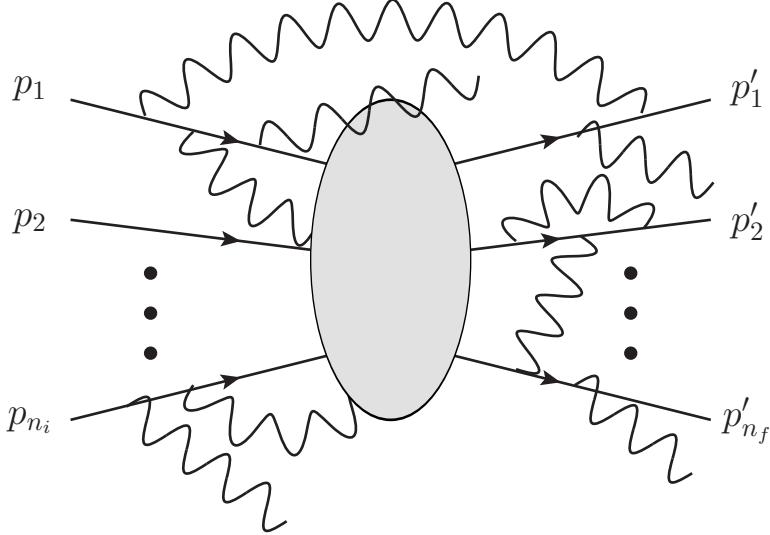
Figure 2.1: All order QED corrections to an arbitrary ampli-
tude with n_i initial state legs and n_f final state
legs.

where M_0^1 is the infrared-subtracted matrix element including one virtual photon (with M_0^1 finite when $k \to 0$ due to the subtraction). All soft divergences due to this virtual photon are contained in the process-independent, universal factor B, see [86] for a more thorough discussion. Here, and in the following, the sub- and superscripts denote the number of real photons and the order of α, respectively, both for the infrared-subtracted and for the original matrix elements.

Similar to the one-photon case, YFS showed that the subsequent insertion of further virtual photons in all possible ways leads to

$$
\begin{aligned}
\mathcal{M}_0^0 &= M_0^0 \\
\mathcal{M}_0^1 &= \alpha B \, M_0^0 + M_0^1 \\
\mathcal{M}_0^2 &= \frac{(\alpha B)^2}{2!} \, M_0^0 + \alpha B \, M_0^1 + M_0^2
\end{aligned}
\tag{2.1.2}
$$

and so on. Therefore, for a fixed order in α,

$$
\mathcal{M}_0^{n_V} = \sum_{r=0}^{n_V} M_0^{n_V - r} \frac{(\alpha B)^r}{r!}
\tag{2.1.3}
$$

and, summing over all numbers of virtual photons n_V,

$$
\sum_{n_V=0}^{\infty} \mathcal{M}_0^{n_V} = \exp(\alpha B) \sum_{n_V=0}^{\infty} M_0^{n_V} \, .
\tag{2.1.4}
$$

Since photons do not carry any charge and because virtual photons inserted in closed charged

loops do not produce any additional infrared singularity[1], this can be generalised to any number of real photons, such that

$$\left| \sum_{n_V=0}^{\infty} \mathcal{M}_{n_R}^{n_V+\frac{1}{2}n_R} \right|^2 = \exp(2\alpha B) \left| \sum_{n_V=0}^{\infty} M_{n_R}^{n_V+\frac{1}{2}n_R} \right|^2. \tag{2.1.5}$$

Hence, $M_{n_R}^{n_V+\frac{1}{2}n_R}$ is free of soft singularities due to virtual photons but it still may contain those due to real photons.

2.2 Resummation of real emission corrections

YFS showed in [75] that the factorisation for real photon emission proceeds on the level of the squared matrix elements rather than on the amplitude level. For a single photon emission therefore this yields

$$\frac{1}{2(2\pi)^3} \left| \sum_{n_V=0}^{\infty} M_1^{n_V+\frac{1}{2}} \right|^2 = \tilde{S}(k) \left| \sum_{n_V=0}^{\infty} M_0^{n_V} \right|^2 + \sum_{n_V=0}^{\infty} \tilde{\beta}_1^{n_V+1}(k). \tag{2.2.1}$$

Here, $\tilde{S}(k)$ is an eikonal factor containing the soft divergence related to the real photon emission, see Appendix [86]. Denoting with $\tilde{\beta}_{n_R}^{n_V+n_R}$ the complete IR-finite (subtracted) squared matrix element for the basic process plus the emission of n_R photons including n_V virtual photons and using the abbreviation

$$\tilde{\beta}_{n_R} = \sum_{n_V=0}^{\infty} \tilde{\beta}_{n_R}^{n_V+n_R}, \tag{2.2.2}$$

the squared matrix element for n_R real emissions, summed over all possible virtual photon corrections, can be written as

$$\left(\frac{1}{2(2\pi)^3} \right)^{n_R} \left| \sum_{n_V=0}^{\infty} M_{n_R}^{n_V+\frac{1}{2}n_R} \right|^2$$

$$= \tilde{\beta}_0 \prod_{i=1}^{n_R} \left[\tilde{S}(k_i) \right]$$

$$+ \sum_{i=1}^{n_R} \left[\frac{\tilde{\beta}_1(k_i)}{\tilde{S}(k_i)} \right] \prod_{j=1}^{n_R} \left[\tilde{S}(k_j) \right]$$

$$+ \sum_{\substack{i,j=1 \\ i \neq j}}^{n_R} \left[\frac{\tilde{\beta}_2(k_i,k_j)}{\tilde{S}(k_i)\tilde{S}(k_j)} \right] \prod_{l=1}^{n_R} \left[\tilde{S}(k_l) \right]$$

$$+ \dots$$

---

[1] A similar program cannot directly be translated to QCD, where the emitted gluons act as parts of antennae emitting further gluons, thus modifying the pattern of possible infrared poles and thus leading logarithms in each emission.

$$+ \sum_{i=1}^{n_R} \left[\tilde{\beta}_{n_R-1}(k_1, \ldots, k_{i-1}, k_{i+1}, \ldots, k_{n_R}) \, \tilde{S}(k_i) \right]$$

$$+ \ \tilde{\beta}_{n_R}(k_1, \ldots, k_{n_R}) \, . \tag{2.2.3}$$

Demanding agreement with the exact result up to $\mathcal{O}(\alpha)$, this expression thus contains only terms with $\tilde{\beta}_0^0$, $\tilde{\beta}_0^1$ and $\tilde{\beta}_1^1$. Then

$$\left(\frac{1}{2(2\pi)^3} \right)^{n_R} \left| \sum_{n_V=0}^{\infty} M_{n_R}^{n_V + \frac{1}{2} n_R} \right|^2$$

$$= \ \left[\tilde{\beta}_0^0 + \tilde{\beta}_0^1 \right] \prod_{i=1}^{n_R} \left[\tilde{S}(k_i) \right] + \sum_{i=1}^{n_R} \left[\frac{\tilde{\beta}_1^1(k_i)}{\tilde{S}(k_i)} \right] \prod_{j=1}^{n_R} \left[\tilde{S}(k_j) \right] + \mathcal{O}(\alpha^2) \, . \tag{2.2.4}$$

Inserting this into the expression for the decay rate and expressing the δ-functions ensuring four-momentum conservation as exponentials yields,

$$2M \cdot \Gamma = \quad \sum_{n_R} \frac{1}{n_R!} \int \mathrm{d}\Phi_{p_f} \left\{ \exp\left[2\alpha B \right] \int \mathrm{d}y \, \exp\left[iy \left(\sum p_i - \sum p_f \right) \right] \right.$$

$$\times \left. \left(\int \frac{\mathrm{d}^3 k}{k} \tilde{S}(k) e^{-iyk} \right)^{n_R} \left(\tilde{\beta}_0^0 + \tilde{\beta}_0^1 \right) \right\}$$

$$+ \sum_{n_R-1} \frac{1}{(n_R-1)!} \int \mathrm{d}\Phi_{p_f} \left\{ \exp\left[2\alpha B \right] \int \mathrm{d}y \, \frac{\mathrm{d}^3 K}{K} \, \exp\left[iy \left(\sum p_i - \sum p_f - K \right) \right] \right.$$

$$\times \left. \left(\int \frac{\mathrm{d}^3 k}{k} \tilde{S}(k) e^{-iyk} \right)^{n_R-1} \tilde{\beta}_1^1(K) \right\} \ + \ \mathcal{O}(\alpha^2)$$

$$= \int \mathrm{d}^4 y \int \mathrm{d}\Phi_{p_f} \left\{ \exp\left[2\alpha B \right] \exp\left[iy \left(\sum p_i - \sum p_f \right) + \int \frac{\mathrm{d}^3 k}{k} \tilde{S}(k) e^{-iyk} \right] \right.$$

$$\times \left. \left[\tilde{\beta}_0^0 + \tilde{\beta}_0^1 + \int \frac{\mathrm{d}^3 K}{K} \, e^{-iyK} \, \tilde{\beta}_1^1(K) \ + \ \mathcal{O}(\alpha^2) \right] \right\} \, . \tag{2.2.5}$$

As before, all singularities due to virtual photons are contained in B, while all singularities due to real emissions are incorporated in the integral over $\tilde{S}(k)$. To restore the momentum conserving δ-function the divergences have to be split off this integral. This can be done by simply subtracting the terms that are divergent for $k \to 0$. To this end, a small "soft" region Ω is defined together with an infrared-safe function $D(\Omega)$ such that

$$\int \frac{\mathrm{d}^3 k}{k} \, \tilde{S}(k) e^{-iyk}$$

$$= \int \frac{\mathrm{d}^3 k}{k} \left\{ \tilde{S}(k) \left[\left(1 - \Theta(k, \Omega) \right) + e^{-iyk} \Theta(k, \Omega) + \left(e^{-iyk} - 1 \right) \left(1 - \Theta(k, \Omega) \right) \right] \right\}$$

$$= 2\alpha\tilde{B}(\Omega) + D(\Omega) \tag{2.2.6}$$

where

$$
\begin{aligned}
D(\Omega) \;\; &= \;\; \int \frac{\mathrm{d}^3k}{k}\,\tilde{S}(k)\left[\left(e^{-iyk}-1\right)\left(1-\Theta(k,\Omega)\right)+e^{-iyk}\Theta(k,\Omega)\right] \\
&\xrightarrow{\Omega\to 0} \;\; \int \frac{\mathrm{d}^3k}{k}\,\tilde{S}(k)\,e^{-iyk}\,\Theta(k,\Omega)
\end{aligned}
\tag{2.2.7}
$$

and

$$2\alpha\tilde{B}(\Omega) \;\; = \;\; \int \frac{\mathrm{d}^3k}{k}\,\tilde{S}(k)\,(1-\Theta(k,\Omega)) = \int_{\Omega} \frac{\mathrm{d}^3k}{k}\,\tilde{S}(k)\,. \tag{2.2.8}$$

The Heaviside function $\Theta(k,\Omega)$ divides the phase space into two regions. While Ω comprises the region containing the infrared divergence, $(1-\Omega)$ is completely free of those divergences. Hence, $\Theta(k,\Omega) = 1$ if $k\notin\Omega$ and zero otherwise. Thus, $D(\Omega)$ is IR save and $\tilde{B}(\Omega)$ contains the divergence.

2.3 The Yennie-Frautschi-Suura form factor

Reinserting this into the cross section, executing the y-integration and reexpanding the exponentiated integral yields

$$
\begin{aligned}
2M\,\Gamma \;\; = \;\; &\sum_{n_R} \frac{1}{n_R!} \int \mathrm{d}\Phi_{p_f}\mathrm{d}\Phi'_k (2\pi)^4\delta^4\left(\sum p_i - \sum p_f - \sum k\right) e^{2\alpha(B+\tilde{B}(\Omega))} \\
&\times \prod_{i=1}^{n_R} \tilde{S}(k_i)\Theta(k_i,\Omega)\left(\tilde{\beta}_0^0 + \tilde{\beta}_0^1 + \sum_{i=1}^{n_R} \frac{\tilde{\beta}_1^1(k_i)}{\tilde{S}(k_i)} + \;\; \mathcal{O}(\alpha^2) \;\; \right).
\end{aligned}
\tag{2.3.1}
$$

Wherein the YFS form factor

$$Y(\Omega) \;\; = \;\; 2\alpha(B+\tilde{B}(\Omega)) \tag{2.3.2}$$

can be defined. It is infrared finite by construction through the inclusion of the leading logarithmic virtual corrections and, thus, constitutes the all-orders resummed contribution of the integrated unresolved photon region Ω to each cross-section summand.

The infrared subtracted squared matrix elements read, up to $\mathcal{O}(\alpha)$,

$$
\begin{aligned}
\tilde{\beta}_0^0 \;\; &= \;\; M_0^0 M_0^{0\,*} \\
\tilde{\beta}_0^1 \;\; &= \;\; M_0^0 M_0^{1\,*} + M_0^1 M_0^{0\,*} \\
\tilde{\beta}_1^1 \;\; &= \;\; \frac{1}{2(2\pi)^3}\, M_1^{\frac{1}{2}} M_1^{\frac{1}{2}\,*} - \tilde{S}(k)\, M_0^0 M_0^{0\,*}\,.
\end{aligned}
\tag{2.3.3}
$$

Chapter 3

A process independent implementation in SHERPA

In this part of this thesis the construction of the physics module PHOTONS++ for the SHERPA framework, as published in [86, 74], is reviewed as a prerequisite for Chapters 4 and 5. It aims at implementing higher order QED corrections using the framework of the Yennie-Frautschi-Suura (YFS) resummation [75] reviewed in the previous chapter in the context of particle decays. Up to the implementation of PHOTONS++, in Monte-Carlo event generators this has typically been left to the PHOTOS [87, 88] programme. However, there have been two reasons for replacing PHOTOS: First of all, PHOTOS builds on a parton-shower like collinear approximation for the simulation of photon emissions, which intrinsically has some shortcomings when the mass of the decaying particle is not much larger than the masses of its decay products. This has already been noted in [89, 90] and triggered the development of the module SOPHTY [89] in the framework of the HERWIG++ event generator. It also has been realised that the maintenance of interface structures to ancient, although well tested, additional codes such as PHOTOS becomes an overwhelming burden as modern event generators are improving.

The present implementation aims to address all decay topologies universally, in particular, in contrast to other YFS implementations like SOPHTY, no restrictions regarding the number of decay products are imposed. Further, a special focus is put upon systematic hard emission corrections. Here, the big advantage of the YFS formalism, allowing for a systematic improvement of the eikonal approximation, order-by-order in the QED coupling constant, is used. Therefor, either automatically generated universal collinear hard emission corrections or corrections effected through dedicated process-specific matrix elements are applied. This straightforward extension also explains why a good fraction of the most precise tools for the simulation of QED radiation root in this algorithm [82, 83, 84, 85].

3.1 The Algorithm

The following section presents an algorithm to *a posteriori* correct leading order processes for all-order resummed QED corrections in the Yennie-Frautschi-Suura (YFS) resummation scheme, reviewed in Chapter 2. It is therefore necessary to rearrange the all-orders expression, factorising the leading order process and accommodating a well defined momenta mapping from the leading order phase space to the respective multi-photon phase space after the corrections.
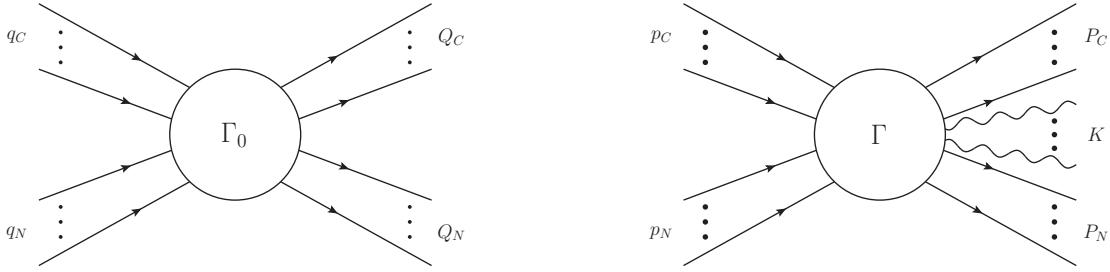
Figure 3.1: The definition of the momenta of an arbitrary scattering or decay process before (left) and after (right) QED corrections.

3.1.1 The master formula

The basic, undressed matrix element (no additional photons) reads

$$2M \cdot \Gamma_0 \;=\; \int \mathrm{d}\Phi_q \, (2\pi)^4 \delta^4(q_C + q_N - Q_C - Q_N) \, |\mathcal{M}|^2 \tag{3.1.1}$$

where the differential phase-space element for the outgoing momenta $q_i \in \{Q_C, Q_N\}$ is given by

$$\mathrm{d}\Phi_q = \prod_{i=1}^{n} \frac{\mathrm{d}^3 q_i}{(2\pi^3) 2 q_i^0} \,. \tag{3.1.2}$$

Here, and in the following, as depicted in Figure 3.1, the initial and final state momenta have been classified to whether the respective particles are charged or neutral: the sums of all initial state momenta are labeled by q_C and q_N for charged and neutral particles, respectively, while Q_C and Q_N denote the sums of all charged or neutral final state momenta. After QED corrections, the Q_C and Q_N will become P_C and P_N, while the q_C and q_N become p_C and p_N. K is the sum of all additional real, resolved Bremsstrahlungs-photons generated in the process, whereas photons already present in the core process are included in P_N and Q_N, respectively (an example for this seemingly unlikely case would be $Z \to \ell^+\ell^-\gamma$ involving a resolved photon, or the rare decay $B^+ \to K^{*+}\gamma$)[1].

In the previous section the factorisation of infrared divergent terms and the construction of infrared-finite expressions for cross sections with all possible numbers of resolved photons has been discussed. In these expressions the universal, process-independent parts of the QED corrections have been separated and exponentiated, the residual process dependence and the effect of particle spins etc. has been absorbed in infrared-finite, subtracted terms $\tilde{\beta}$, cf. eq. (2.3.1). With small changes in the notation this form of the cross section thus reads

$$2M \cdot \Gamma \;=\; \sum_{n_\gamma} \frac{1}{n_\gamma!} \int \mathrm{d}\Phi \, e^{Y(\Omega)} \prod_{i=1}^{n_\gamma} \tilde{S}(k_i) \Theta(k_i, \Omega) \, \tilde{\beta}_0^0 \, \mathcal{C} \,. \tag{3.1.3}$$

---

[1] Here lies a potential drawback of the YFS resummation: Photons already present in the basic process (multiplicity n_γ^{hard}) and photons added in the soft resummation (fixed order multiplicity n_γ^{soft}) to this process are regarded as being distinguishable. Hence, the symmetry factor associated to every higher order would read $1/(n_\gamma^{\mathrm{hard}}! \cdot n_\gamma^{\mathrm{soft}}!)$ instead of $1/(n_\gamma^{\mathrm{hard}} + n_\gamma^{\mathrm{soft}})!$. This, however, can be reconciled by the inclusion of a symmetry correction factor $(n_\gamma^{\mathrm{hard}}! \cdot n_\gamma^{\mathrm{soft}}!)/(n_\gamma^{\mathrm{hard}} + n_\gamma^{\mathrm{soft}})!$ in the exact higher order matrix elements $\tilde{\beta}_1^1$, etc.

Here, the phase space has been separated into a phase space element for the particles of the "core" process and one for the additional n_γ resolved real photons,

$$d\Phi = d\Phi_p \, d\Phi_k \, (2\pi)^4 \delta \left(p_C + p_N - P_C - P_N - K \right). \tag{3.1.4}$$

with

$$d\Phi_p = \prod_{i=1}^{n} \frac{d^3 p_i}{(2\pi)^3 2 p_i^0} \tag{3.1.5}$$

$$d\Phi_k = \prod_{i=1}^{n_\gamma} \frac{d^3 k}{k^0}. \tag{3.1.6}$$

Note that the factor $\frac{1}{2(2\pi)^3}$, missing in the photon phase space element, has already been incorporated in the eikonal factor $\tilde{S}(k)$, in accordance with the choice made in [75]. In the equation above, eq. (3.1.3), the leading order matrix element $\tilde{\beta}_0^0$ has been factored out and the remainder of the perturbative expansion in α has been combined in the factor $\mathcal{C}$,

$$\mathcal{C} = 1 + \frac{1}{\tilde{\beta}_0^0} \left(\tilde{\beta}_0^1 + \sum_{i=1}^{n_\gamma} \frac{\tilde{\beta}_1^1(k_i)}{\tilde{S}(k_i)} + \mathcal{O}(\alpha^2) \right). \tag{3.1.7}$$

Furthermore, the YFS-Form-Factor has been introduced

$$Y(\Omega) = \sum_{i<j} Y_{ij}(\Omega) = \sum_{i<j} 2\alpha \left(B_{ij} + \tilde{B}_{ij}(\Omega) \right) \tag{3.1.8}$$

where the sum $i < j$ runs over all pairs of charged particles, taking into account each pair only once. The infrared factors B_{ij} and $\tilde{B}_{ij}$ are defined as

$$B_{ij} = -\frac{i}{8\pi^3} Z_i Z_j \theta_i \theta_j \int d^4 k \frac{1}{k^2} \left(\frac{2p_i \theta_i - k}{k^2 - 2(k \cdot p_i)\theta_i} + \frac{2p_j \theta_j + k}{k^2 + 2(k \cdot p_j)\theta_j} \right)^2 \tag{3.1.9}$$

$$\tilde{B}_{ij}(\Omega) = \frac{1}{4\pi^2} Z_i Z_j \theta_i \theta_j \int d^4 k \, \delta(k^2) \left(1 - \Theta(k, \Omega) \right) \left(\frac{p_i}{p_i \cdot k} - \frac{p_j}{p_j \cdot k} \right)^2. \tag{3.1.10}$$

They are the generalisation of the quantities defined in the last section, cf. eqs. (2.1.1) and (2.2.8). Both contain the virtual and real infrared divergences, respectively. These divergences cancel according to the Kinoshita-Lee-Nauenberg theorem [91, 92]. Thus, each $Y_{ij}(\Omega)$ is guaranteed to be finite, which is explicitly shown in Appendix A.1. In the terms above, Z_i and Z_j are the charges of the particles i and j in terms of the positron charge e, and the signature factors $\theta = \pm 1$ for particles in the final or initial state, respectively. The symbol Θ, already defined at the end of Chapter 2, refers to a phase space constraint with Ω denoting the soft, unresolvable region of photon radiation. Hence, $\Theta(k, \Omega) = 1$ if $k \notin \Omega$ and zero otherwise. If this division is done by defining an energy cut-off, the definition of Ω is not Lorentz-invariant and the frame in which this cut-off forms a flat hypersurface also needs to be specified. The advantage of splitting the photon phase space in that manner lies in the alleviation of integrating $\tilde{S}(k)$ over k. If the cut-off is defined in the frame the photon generation and momentum reconstruction will be done in[2] then the integration over

---

[2] In the algorithm presented here, this will be the rest frame of the multipole, i.e. the combined rest frame of all charged particles $p_C + P_C$.

the photon energy separates from the angular integration (see Appendix A.2), leading to yet another simplification of the calculation.

The eikonal factor $\tilde{S}(k)$ has already been introduced in the last section. It is defined as

$$\tilde{S}(k) = \sum_{i<j} \tilde{S}_{ij}(k) = \frac{\alpha}{4\pi^2} \sum_{i<j} Z_i Z_j \theta_i \theta_j \left(\frac{p_i}{p_i \cdot k} - \frac{p_j}{p_j \cdot k} \right)^2 . \tag{3.1.11}$$

However, despite all terms being finite in eq. (3.1.3), it cannot be used straight away for the intended Monte Carlo implementation separating the generation of the leading order decay Γ_0 and applying higher order QED corrections afterwards. This roots in the fact that eq. (3.1.3) is written in terms of the already corrected final state momenta p_i and not the original undressed momenta q_i. The problem here is that the undressed momenta are defined in an n-body phase space whereas the dressed momenta are part of an $(n + n_\gamma)$-body phase space. This necessitates a bijective phase-space map of the n-body onto the $(n + n_\gamma)$-body phase space. In principle, the details of this phase-space map are irrelevant as long as it is infrared safe, i.e. the addition of an infinitely soft photon leads to the same kinematics as if this photon was not present. Thus, in this limit the momenta of the original particles in the $(n + n_\gamma)$-body phase space have to fall exactly onto those of the $(n + n_\gamma - 1)$-body phase space, and, if all photons are infinitely soft, onto those of the n-body phase space.

3.1.2 Phase space transformation

To solve this, consider the rest frame of all charged particles involved in the basic matrix element

$$P_M = p_C + P_C . \tag{3.1.12}$$

These particles form the multipole responsible for the Bremsstrahlung of the additional photons. In the rest frame of this multipole, a simple form of the phase space map can be formulated such that the additional photons are accommodated. Such a mapping definition is clearly not Lorentz-invariant, thus eq. (3.1.4) has to be rewritten explicitly in the rest frame of the multipole in question. The necessary transformations are detailed in [74, 86], here it suffices to give the result. It reads

$$
\begin{aligned}
d\Phi &= d\Phi_p \, d\Phi_k \, (2\pi)^4 \delta \left(p_C + p_N - P_C - P_N - K \right) \\
&= d\Phi_p \, d\Phi_k \, \frac{m_{M,p}^3}{M^2(P_C^0 + P_N^0 + K^0)} \, (2\pi)^3 \, \delta^3(\vec{P}_M) \, (2\pi) \, \delta \left(P_M^0 - P_C^0 - p_C^0 \right) .
\end{aligned}
\tag{3.1.13}
$$

In a similar fashion, the phase space related to the leading order uncorrected cross section can be transformed to

$$
\begin{aligned}
d\Phi_0 &= (2\pi)^4 d\Phi_q \, \delta^4 \left(q_C + q_N - Q_C - Q_N \right) \\
&= d\Phi_q \, \frac{m_{M,q}^3}{M^2(Q_C^0 + Q_N^0)} \, (2\pi)^3 \, \delta^3(\vec{Q}_M) \, (2\pi) \, \delta \left(Q_M^0 - Q_C^0 - q_C^0 \right) .
\end{aligned}
\tag{3.1.14}
$$

In both cases, $m_{M,p}$ ($m_{M,q}$) is the invariant mass of the corrected (uncorrected) multipole and the vector components P_C^0 and P_N^0 (Q_C^0 and Q_N^0) are taken in the P_M (Q_M) rest frame. The Jacobian emerging in both cases will ultimately find its way into a correction weight in the Monte Carlo realisation of the method.

3.1.3 Mapping of momenta

The mapping procedure still has to be defined in detail to reconstruct the particles' momenta. The main issue to be addressed is the distribution of the additional photons' momenta across the particles already present in the LO process. This mapping procedure thus has to fulfil all requirements of infrared safety, i.e. its projection to a lower dimensional phase space has to be continuous. Thus, as any photon's momentum $k_i \to 0$, the resulting procedure has to be identical *as if* this photon were not present. In particular, this leads to the requirement that for $K \to 0$ the leading order kinematics has to be recovered.

It is further chosen to reconstruct the multipole in its rest frame and distributing the additional photons' momenta as democratically as possible. This paradigm necessitates the differentiation of two situations: mixed multipoles with charged particles in both the initial and the final state and pure initial or final state multipoles. Both situations will be addressed in the following two paragraphs where, after introducing the general case, special emphasis is put on decay processes as they are relevant for the presented implementation. Formally, of course, both treatments will yield identical results, since only the soft limit of photon emission is defined from first principles and because both treatments respect this limit.

Mixed multipoles

Consider an $N \to M$ process which is to be corrected for higher order QED effects after the LO configuration has already been determined. All particle momenta can then be classified as follows

- $q_C = \sum\limits_{C_i} q_{C_i}$ is the sum of all charged initial states,

- $q_N = \sum\limits_{N_i} q_{N_i}$ is the sum of all neutral initial states,

- $Q_C = \sum\limits_{C_f} Q_{C_f}$ is the sum of all charged final states and

- $Q_N = \sum\limits_{N_f} Q_{N_f}$ is the sum of all neutral final states

of the LO configuration. Accordingly,

- $p_C = \sum\limits_{C_i} p_{C_i}$ is the sum of all charged initial states,

- $p_N = \sum\limits_{N_i} p_{N_i}$ is the sum of all neutral initial states,

- $P_C = \sum\limits_{C_f} P_{C_f}$ is the sum of all charged final states,

- $P_N = \sum\limits_{N_f} P_{N_f}$ is the sum of all neutral final states and

- $K = \sum\limits_{k} K_k$ is the sum of all radiated photons with energies above the threshold ω_{min}

in the QED-corrected configuration. Because of the presence of charged particles in both the initial and the final state they can be used to compensate for (part of) the photons' momentum. Hence, this method is then independent of the presence of neutral particles. Starting from the LO momentum configuration in the multipole rest frame

$$
\begin{aligned}
q_C &= \left(q_C^0, \vec{q}_C = -\vec{Q}_C \right) \\
q_N &= \left(q_N^0, \vec{q}_N = \vec{Q}_N + 2\vec{Q}_C \right) \\
Q_C &= \left(Q_C^0, \vec{Q}_C \right) \\
Q_N &= \left(Q_N^0, \vec{Q}_N \right) ,
\end{aligned}
\tag{3.1.15}
$$

this is mapped upon

$$
\begin{aligned}
p_C &= \left(p_C^0, \vec{p}_C = \sum_{C_i}(u\vec{q}_{C_i} + \tfrac{n_{C_f}}{n_{C_i}}\vec{\kappa}) \right) \\
p_N &= \left(p_N^0, \vec{p}_N = \sum_{N_i}(u\vec{q}_{N_i} + \vec{\kappa}) \right) \\
P_C &= \left(P_C^0, \vec{P}_C = \sum_{C_f}(u\vec{Q}_{C_f} - \vec{\kappa}) \right) \\
P_N &= \left(P_N^0, \vec{P}_N = \sum_{N_f}(u\vec{Q}_{N_f} - \vec{\kappa}) \right) \\
K &= \left(K^0, \vec{K} \right) ,
\end{aligned}
\tag{3.1.16}
$$

wherein $u \in (0, 1]$ is a scaling variable and $\vec{\kappa} = \frac{1}{2n_{C_f}+n_{N_i}+n_{N_f}}\vec{K}$. The scaling parameter u is determined by momentum conservation and all on-shell conditions as the solution of

$$
\begin{aligned}
0 = &\sum_{C_i}\sqrt{m_{C_i}^2 + (u\vec{q}_{C_i} + \tfrac{n_{C_f}}{n_{C_i}}\vec{\kappa})^2} + \sum_{N_i}\sqrt{m_{N_i}^2 + (u\vec{q}_{N_i} + \vec{\kappa})^2} \\
&- \sum_{C_f}\sqrt{m_{C_f}^2 + (u\vec{Q}_{C_f} - \vec{\kappa})^2} - \sum_{N_f}\sqrt{m_{N_f}^2 + (u\vec{Q}_{N_f} - \vec{\kappa})^2} - K^0 .
\end{aligned}
\tag{3.1.17}
$$

The indices $C_{i,f}$ and $N_{i,f}$ sum over the charged and neutral initial and final state particle momenta. Of course, for $K \to 0$ the scaling parameter $u \to 1$ and both momentum configurations coincide, as required. Due to the transformation being multiplicative in u and additive in κ with κ being independent of the LO momenta the results of [86] can easily be generalised. Thus the phase space element reads

$$
\begin{aligned}
\mathrm{d}\Phi = &(2\pi)^4 \, \mathrm{d}\Phi_q \, \mathrm{d}\Phi_k \, \delta^3\left(\vec{Q}_M\right) \delta\left(Q_M^0 - Q_C^0 - q_C^0\right) \frac{m_{M,p}^2}{M^2(P_C^0 + P_N^0 + K^0)} \, u^{3n-4} \\
&\times \frac{\displaystyle\sum_{C_i}\frac{\vec{q}_{C_i}^2}{q_{C_i}^0} + \sum_{N_i}\frac{\vec{q}_{N_i}^2}{q_{N_i}^0} - \sum_{C_f}\frac{\vec{Q}_{C_f}^2}{Q_{C_f}^0} - \sum_{N_f}\frac{\vec{Q}_{N_f}^2}{Q_{N_f}^0}}{\displaystyle\sum_{C_i}\frac{\vec{p}_{C_i}\vec{q}_{C_i}}{p_{C_i}^0} + \sum_{N_i}\frac{\vec{p}_{N_i}\vec{q}_{N_i}}{p_{N_i}^0} - \sum_{C_f}\frac{\vec{P}_{C_f}\vec{Q}_{C_f}}{P_{C_f}^0} - \sum_{N_f}\frac{\vec{P}_{N_f}\vec{Q}_{N_f}}{P_{N_f}^0}} \prod_{C_f}\left[\frac{Q_{C_f}^0}{P_{C_f}^0}\right] \prod_{N_f}\left[\frac{Q_{N_f}^0}{P_{N_f}^0}\right] .
\end{aligned}
\tag{3.1.18}
$$

Herein, Q_M and P_M are the momenta of the multipole rest frames before and after the addition of photon radiation, as defined in Section 3.1.2. Likewise m_M is its invariant mass. $M = \hat{s}$ is the invariant mass of the initial state.

In case of the decay processes this result reduces to the result obtained in [86] and M can again be identified with the decaying particle's mass. Then also the simplified version of eq. (3.1.18) is recovered

$$
\mathrm{d}\Phi = (2\pi)^4 \, \mathrm{d}\Phi_q \, \mathrm{d}\Phi_k \, \delta^3 \left(\vec{Q}_M \right) \delta \left(Q_M^0 - Q_C^0 - q_C^0 \right) \frac{m_{M,p}^3}{M^2 \left(P_C^0 + P_N^0 + K^0 \right)} u^{3n-4}
$$

$$
\times \frac{\frac{\vec{q}_C^2}{q_C^0} - \sum_{C,N} \frac{\vec{q}_i^2}{q_i^0}}{\frac{\vec{p}_C \vec{q}_C}{p_C^0} - \sum_{C,N} \frac{\vec{p}_i \vec{q}_i}{p_i^0}} \prod_{i=1}^n \left[\frac{q_i^0}{p_i^0} \right] .
$$

(3.1.19)

As above the product of the second line runs over all final state particles, and q_C and p_C is the initial state before and after QED corrections.

Pure initial or final state multipoles

In case there are no charged particles in either the initial or the final state the above algorithm fails since the multipole's restframe cannot be reproduced. Hence, in this case only the then necessarily present neutral particles can compensate for the additional photons' momenta. Defining the kinematics of the configuration before and after the addition of higher order corrections as in the previous case, the LO momentum configuration

$$
\begin{aligned}
q_C &= \left(q_C^0, \vec{q}_C = -\vec{Q}_C \right) \\
q_N &= \left(q_N^0, \vec{q}_N = \vec{Q}_N + 2\vec{Q}_C \right) \\
Q_C &= \left(Q_C^0, \vec{Q}_C \right) \\
Q_N &= \left(Q_N^0, \vec{Q}_N \right)
\end{aligned}
$$

(3.1.20)

is mapped upon

$$
\begin{aligned}
p_C &= \left(p_C^0, \vec{p}_C = \sum_{C_i} u\vec{q}_{C_i} \right) \\
p_N &= \left(p_N^0, \vec{p}_N = \sum_{N_i} (u\vec{q}_{N_i} + \vec{\kappa}) \right) \\
P_C &= \left(P_C^0, \vec{P}_C = \sum_{C_f} u\vec{Q}_{C_f} \right) \\
P_N &= \left(P_N^0, \vec{P}_N = \sum_{N_f} (u\vec{Q}_{N_f} - \vec{\kappa}) \right) \\
K &= \left(K^0, \vec{K} \right) ,
\end{aligned}
$$

(3.1.21)

wherein $u \in (0, 1]$ is a scaling variable and $\vec{\kappa} = \frac{1}{n_{N_i} + n_{N_f}} \vec{K}$. The scaling parameter u is again determined by momentum conservation and all on-shell conditions as the solution of

$$
\begin{aligned}
0 = & \sum_{C_i} \sqrt{m_{C_i}^2 + u^2 \vec{q}_{C_i}^2} + \sum_{N_i} \sqrt{m_{N_i}^2 + (u \vec{q}_{N_i} + \vec{\kappa})^2} \\
& - \sum_{C_f} \sqrt{m_{C_f}^2 + u^2 \vec{Q}_{C_f}^2} - \sum_{N_f} \sqrt{m_{N_f}^2 + (u \vec{Q}_{N_f} - \vec{\kappa})^2} - K^0 \,.
\end{aligned}
\tag{3.1.22}
$$

As above, the phase space element can be determined as

$$
\begin{aligned}
\mathrm{d}\Phi = & (2\pi)^4 \, \mathrm{d}\Phi_q \, \mathrm{d}\Phi_k \, \delta^3 \left(\vec{Q}_M \right) \delta \left(Q_M^0 - Q_C^0 - q_C^0 \right) \frac{m_{M,p}^2}{M^2 (P_C^0 + P_N^0 + K^0)} u^{3n-4} \\
& \times \frac{\sum_{C_i} \frac{\vec{q}_{C_i}^2}{q_{C_i}^0} + \sum_{N_i} \frac{\vec{q}_{N_i}^2}{q_{N_i}^0} - \sum_{C_f} \frac{\vec{Q}_{C_f}^2}{Q_{C_f}^0} - \sum_{N_f} \frac{\vec{Q}_{N_f}^2}{Q_{N_f}^0}}{\sum_{C_i} \frac{\vec{p}_{C_i} \vec{q}_{C_i}}{p_{C_i}^0} + \sum_{N_i} \frac{\vec{p}_{N_i} \vec{q}_{N_i}}{p_{N_i}^0} - \sum_{C_f} \frac{\vec{P}_{C_f} \vec{Q}_{C_f}}{P_{C_f}^0} - \sum_{N_f} \frac{\vec{P}_{N_f} \vec{Q}_{N_f}}{P_{N_f}^0}} \prod_{C_f} \left[\frac{Q_{C_f}^0}{P_{C_f}^0} \right] \prod_{N_f} \left[\frac{Q_{N_f}^0}{P_{N_f}^0} \right] \,.
\end{aligned}
\tag{3.1.23}
$$

Turning to the present case of particle decays, only one situation can occur: a decaying neutral particle of mass M where the multipole lies entirely in the final state. Here, again, the above result simplifies to

$$
\begin{aligned}
\mathrm{d}\Phi = & (2\pi)^4 \, \mathrm{d}\Phi_q \, \mathrm{d}\Phi_k \, \delta^3 \left(\vec{Q}_M \right) \delta \left(Q_M^0 - Q_C^0 \right) \frac{m_{M,p}^3}{M^2 \left(P_C^0 + P_N^0 + K^0 \right)} u^{3n-4} \\
& \times \frac{\frac{\vec{q}_N^2}{q_N^0} - \sum_{C,N} \frac{\vec{q}_i^2}{q_i^0}}{\frac{\vec{p}_N \vec{q}_N}{p_N^0} - \sum_{C,N} \frac{\vec{p}_i \vec{q}_i}{p_i^0}} \prod_{i=1}^{n} \left[\frac{q_i^0}{p_i^0} \right] \,.
\end{aligned}
\tag{3.1.24}
$$

wherein, again the simplified notation of [86] is adopted. Again, the product runs over the complete final state and q_N and p_N denote the single neutral initial state.

3.1.4 Event generation

Having transformed the phase space integrals allows to write the full decay rate including real and virtual QED radiation as

$$
\begin{aligned}
2M \cdot \Gamma = & \sum_{n_\gamma} \frac{1}{n_\gamma!} \int \mathrm{d}\Phi_q \, \mathrm{d}\Phi_k (2\pi)^4 \delta^3 \left(\vec{Q}_M \right) \delta \left(Q_M^0 - Q_C^0 - q_C^0 \right) e^{Y(\Omega)} \tilde{\beta}_0^0 \mathcal{C} \\
& \times \prod_{i=1}^{n_\gamma} \left[\tilde{S}(k_i) \Theta(k_i, \Omega) \right] \frac{m_{M,p}^3 \, u^{3n-4}}{M^2 \left(P_C^0 + P_N^0 + K^0 \right)} \frac{\frac{\vec{q}^2}{q^0} - \sum_{C,N} \frac{\vec{q}_i^2}{q_i^0}}{\frac{\vec{p} \vec{q}}{p^0} - \sum_{C,N} \frac{\vec{p}_i \vec{q}_i}{p_i^0}} \prod_{i=1}^{n} \left[\frac{q_i^0}{p_i^0} \right] \,,
\end{aligned}
\tag{3.1.25}
$$

where q and p now generally stand for the initial state particle. The leading order differential decay rate $\mathrm{d}\Gamma_0$, which will be generated beforehand and shall be corrected by the present algorithm *a posteriori*, can easily be extracted. Employing eq. (3.1.14) the full result then

reads

$$
\begin{aligned}
\Gamma \; = \; & \sum_{n_\gamma} \frac{1}{n_\gamma!} \int \mathrm{d}\Gamma_0 \, \mathrm{d}\Phi_k \, e^{Y(\Omega)} \prod_{i=1}^{n_\gamma} \left[\tilde{S}(k_i) \Theta(k_i, \Omega) \right] \\
& \times \frac{m_{M,p}^3}{m_{M,q}^3} \frac{Q_C^0 + Q_N^0}{P_C^0 + P_N^0 + K^0} \, u^{3n-4} \, \frac{\frac{\vec{q}^2}{q^0} - \sum_{C,N} \frac{\vec{q}_i^2}{q_i^0}}{\frac{\vec{p}\vec{q}}{p^0} - \sum_{C,N} \frac{\vec{p}_i \vec{q}_i}{p_i^0}} \prod_{i=1}^{n} \left[\frac{q_i^0}{p_i^0} \right] \mathcal{C} \,.
\end{aligned}
\tag{3.1.26}
$$

Up to here no approximations have been made at all. In order to generate the corresponding distribution with Monte Carlo techniques, however, this form still not fully factorises the leading order process from the higher order corrections. To simplify eq. (3.1.26) therefor, hit-or-miss and reweighting techniques are used, demanding upper bounds for the various pieces:

- All higher orders are neglected, thus setting $\mathcal{C}$ to one.

- The maximum of all Jacobians is given for $K = 0$, coinciding with the leading-order phase space.

- The dependences on the dressed momenta in the eikonal factors are removed by approximating these factors by those depending on the undressed variables from the generation.

The resulting crude distribution reads

$$
\Gamma_{\mathrm{cr}} = \sum_{n_\gamma=0}^{\infty} \frac{1}{n_\gamma!} \int \mathrm{d}\Gamma_0 \, \mathrm{d}\Phi_k \, e^{Y(\omega)} \prod_{i=1}^{n_\gamma} \tilde{S}_q(k_i) \Theta(k_i, \Omega).
\tag{3.1.27}
$$

After executing all k-integrations giving

$$
\int \prod_{i=1}^{n_\gamma} \frac{\mathrm{d}^3 k_i}{k_i^0} \tilde{S}_q(k_i) \Theta(k_i, \Omega) = \bar{n}^{n_\gamma}
\tag{3.1.28}
$$

the YFS-Form-Factor is estimated by

$$
Y(\Omega) \approx -\bar{n}
\tag{3.1.29}
$$

for suitable choices of Ω [3]. Reinserting this into the crude estimate, the leading order expression can be separated from the higher order QED corrections, and

$$
\Gamma_{\mathrm{cr}} = \Gamma_0 \sum_{n_\gamma=0}^{\infty} \left[\frac{1}{n_\gamma!} e^{-\bar{n}} \bar{n}^{n_\gamma} \right] \,.
\tag{3.1.30}
$$

The result is the undressed leading order process times a Poisson distribution with the average photon multiplicity $\bar{n}$. In this factorised state the photon distribution can be separated from the generation of the basic matrix element. Assuming the latter to be already generated it can *a posteriori* be corrected to the leading-logarithmic all-order QED correction by generating the photon distribution as follows (see Appendix A.2 for details):

---

[3] In this thesis (and in the code), this choice has been to limit the photon energies by setting an infrared energy cut-off of $1\,\mathrm{MeV}$, unless otherwise stated.

1. Generate the number of photons according to a Poisson distribution with mean $\bar{n}$.

2. Generate each photon's momentum according to $\tilde{S}_q(k)$. This implies

   - that its energy k^0 is distributed according to

   $$\rho(k^0) \sim \frac{1}{k^0} \tag{3.1.31}$$

   - and that the azimuthal and polar angles are distributed according to

   $$\rho(\theta, \phi) \sim \sum_{i<j} \left(\frac{q_i}{q_i \cdot e_k} - \frac{q_j}{q_j \cdot e_k} \right)^2, \tag{3.1.32}$$

   where e_k is a null vector of unit length,

   $$e_k^\mu = \frac{1}{k^0} k^\mu \quad \text{with} \quad e_k^2 = 0. \tag{3.1.33}$$

   It is possible that more than one hard photon is created such that the total energy of all photons exceeds the decaying system's energy. Obviously, this has to be avoided to guarantee energy conservation. A simple way of achieving this is a mere veto on such situations, accompanied with a repetition of photon generation, starting from step 1.

3. Reconstruct the momenta.

4. Calculate and apply all weights. This yields a total weight, namely

   $$W = W_{\text{dipole}} \times W_{\text{YFS}} \times W_{\text{J,L}} \times W_{\text{J,M}} \times W_{\mathcal{C}}, \tag{3.1.34}$$

   where the individual weights are given by

   $$W_{\text{dipole}} = \prod_{i=1}^{n_\gamma} \frac{\tilde{S}(p_C, P_C, k_i)}{\tilde{S}(p_C, Q_C, k_i)} \tag{3.1.35}$$

   $$W_{\text{YFS}} = \exp\left(Y(p_C, P_C, \Omega) + \bar{n} \right) \tag{3.1.36}$$

   $$W_{\text{J,L}} = \frac{m_{M,p}^3}{m_{M,q}^3} \frac{Q_C^0 + Q_N^0}{P_C^0 + P_N^0 + K^0} \tag{3.1.37}$$

   $$W_{\text{J,M}} = u^{3n-4} \frac{\frac{\vec{p}^2}{p^0} - \sum_{C,N} \frac{\vec{q}_i^2}{q_i^0}}{\frac{\vec{p}'\vec{p}}{p'^0} - \sum_{C,N} \frac{\vec{p}_i\vec{q}_i}{p_i^0}} \prod_{i=1}^{n} \left(\frac{q_i^0}{p_i^0} \right) \tag{3.1.38}$$

   $$W_{\mathcal{C}} = \mathcal{C}. \tag{3.1.39}$$

   Here, W_{dipole} corrects the emitting dipoles from the unmapped to the mapped momenta, W_{YFS} accounts for the exact YFS form factor, $W_{\text{J,L}}$ essentially denotes the Jacobian due to the Lorentz-transformation, $W_{\text{J,M}}$ is the weight due the momenta-mapping, and $W_{\mathcal{C}}$ incorporates higher-order corrections, where available.

   The maximum of the combined weight indeed is smaller than the maximal weight employed for generating the distribution, $W < W(K = 0)$. Hence application of the combined weight is just a realisation of a hit-or-miss method. The distribution obtained is now the exact distribution of (3.1.3) or (3.1.26).

3.2 Higher Order Corrections

In the last section, the procedure generating the QED corrections to cross sections, following eq. (2.3.1), has been outlined. By construction, the algorithm yields exact all-orders results, if all matrix elements are known. This, however, is never the case. On the other hand, the dominant universal soft photon contributions, real and virtual, are included to all orders in the YFS form factor, eq. (3.1.8). Thus, if the zeroth order undressed matrix element only is known, i.e. if $\mathcal{C} = 1$, the photons will be solely generated according to a product of eikonal factors $\tilde{S}(k_i)$. Consequently, their distribution will be correct in the soft limit only. Away from this limit, exact matrix elements at a given order may be mandatory to yield satisfactory and sufficient accuracy. For most applications on decay matrix elements it will be sufficient to implement the matrix element correction to the first order in α, i.e. for the emission of one additional real or virtual photon. Only for very specific processes, where the highest accuracy is mandatory, i.e. leptonic decays of W and Z bosons second order hard emission corrections need to be accounted for.

It should be noted here that hard photon emission predominantly occurs in situations where potential emitters are characterised by a large energy-to-mass ratio and that in any case hard photon emissions tend to populate regions in phase space that are collinear w.r.t. the emitters. In contrast, large angle radiation has the tendency to be predominantly soft.

3.2.1 Approximations for real emission matrix elements

As already explained, the vast majority of hard photon emissions deserving an improved description through corrections to the soft limit underlying the YFS approach occurs in the collinear region of emission phase space. In this region, the well-known collinear factorisation can be used to approximate $\tilde{\beta}_1^1$. This amounts to an inclusion of the leading collinear logarithms arising in this limit, which are incorporated for instance in the Altarelli-Parisi evolution equation [93] and corresponding splitting kernels.

Since masses are to be taken fully into account the quasi-collinear limit defined in [94, 95] replaces the more familiar collinear one. In this limit the matrix element factorises as

$$\sum_{\lambda_\gamma} \left| \mathcal{M}_1^{\frac{1}{2}}(p_i, k) \right|^2 \cong \begin{cases} e^2 Z_i^2 g^{(\text{out})}(p_i, k) \left| \mathcal{M}_0^0(p_i + k) \right|^2 & \text{if } i \in \text{F.S.} \\ e^2 Z_i^2 g^{(\text{in})}(p_i, k) \left| \mathcal{M}_0^0(x \cdot p_i) \right|^2 & \text{if } i \in \text{I.S.}. \end{cases} \tag{3.2.1}$$

Here the $g^{(\text{in,out})}(p_i, k)$ denote massive splitting functions. For instance, for the case of a fermion emitting a photon they are given by

$$g^{(\text{out})}(p_i, k) = \frac{1}{(p_i \cdot k)} \left(P_{ff}(z) - \frac{m_i^2}{(p_i \cdot k)} \right) \tag{3.2.2}$$

$$g^{(\text{in})}(p_i, k) = \frac{1}{x(p_i \cdot k)} \left(P_{ff}(x) - \frac{x \, m_i^2}{(p_i \cdot k)} \right), \tag{3.2.3}$$

where $x = \frac{p_i^0 - k^0}{p_i^0}$ and $z = \frac{p_i^0}{p_i^0 + k^0}$ are the fractions of the fermion energies kept after the emission of the photon, and where $P_{ff}(y)$ is the well-known Altarelli-Parisi splitting function

$$P_{ff}(y) = \frac{1 + y^2}{1 - y}. \tag{3.2.4}$$

The dipole splitting functions of [94] have been generalised further in [52] to incorporate also polarisation. Thus, in principle they could directly be used in the framework of the YFS formulation replacing the original eikonal factors. In the framework of this thesis, however, they are employed as universal correction factors, reweighting explicit photon emission such that the correct collinear limit is recovered. Since they interpolate smoothly between both limits they already include the soft limit. Therefore, in the correction weights, these soft terms have to be subtracted because they are already accounted for in the original YFS eikonals. In addition, since the dipole splitting kernels refer to an emitter and a spectator forming the dipole, for each dipole two such terms have to be applied, such that the squared matrix element with the dipole terms approximating the photon emission reads

$$
\left|\mathcal{M}_1^{\frac{1}{2}}\right|^2 \cong -e^2 \sum_{i \neq j} \left[Z_i Z_j \theta_i \theta_j g_{ij}(p_i, p_j, k) \left|\mathcal{M}_0^0\right|^2 \right] \tag{3.2.5}
$$

$$
\cong -e^2 \sum_{i < j} \left[Z_i Z_j \theta_i \theta_j \left(g_{ij}(p_i, p_j, k) + g_{ji}(p_j, p_i, k) \right) \left|\mathcal{M}_0^0\right|^2 \right] . \tag{3.2.6}
$$

Here, charge conservation in the form $\sum Z_i \theta_i = 0$ has been used. The second particle in each massive splitting function g_{ij} denotes the spectator of the emission process and accounts for the recoil, thus ensuring four-momentum conservation. It should also be noted that the sum in the equations above runs over charged particles only.

In order to subtract the soft terms, it is useful to consider the soft and quasi-collinear limits of the dipole splitting kernels $g_{ij}(p_i, p_j, k)$:

$$
g_{ij}(p_i, p_j, k) \overset{k \to 0}{\sim} \frac{1}{(p_i \cdot k)} \left(\frac{2(p_i \cdot p_j)}{(p_i \cdot k) + (p_j \cdot k)} - \frac{m_i^2}{(p_i \cdot k)} \right) \tag{3.2.7}
$$

$$
g_{ij}(p_i, p_j, k) \overset{p \cdot k \to 0}{\sim} g^{(\text{out/in})} . \tag{3.2.8}
$$

Because the soft limit is universal and spin-independent, it is a straightforward exercise to define soft-subtracted dipole splitting kernels

$$
\begin{aligned}
\bar{g}_{ij}(p_i, p_j, k) &= g_{ij}(p_i, p_j, k) - g_{ij}^{(\text{soft})}(p_i, p_j, k) \\
&= g_{ij}(p_i, p_j, k) - \frac{1}{(p_i \cdot k)} \left(\frac{2(p_i \cdot p_j)}{(p_i \cdot k) + (p_j \cdot k)} - \frac{m_i^2}{(p_i \cdot k)} \right) .
\end{aligned} \tag{3.2.9}
$$

The soft-subtracted dipole splitting kernels $\bar{g}_{ij}$ now have the correct (finite) soft limit while retaining the original quasi-collinear limit of g_{ij} (eq. (3.2.8)). Accordingly, the soft-subtracted matrix element can be approximated as

$$
\tilde{\beta}_1^1 \cong -\frac{\alpha}{4\pi^2} \sum_{i < j} Z_i Z_j \theta_i \theta_j \left(\bar{g}_{ij}(p_i, p_j, k) + \bar{g}_{ji}(p_j, p_i, k) \right) \tilde{\beta}_0^0 . \tag{3.2.10}
$$

The exact form of the $g_{ij}(p_i, p_j, k)$ for different emitter-spectator configurations will be given in Appendix A.3.

3.2.2 Real emission corrections

In order to achieve an even higher precision, the implementation of exact higher-order full matrix elements becomes mandatory. It should be clear, however, that large differences with the approximated matrix elements above will occur only in non-singular regions of comparably hard, wide-angle emissions. Since the module presented in this Chapter of this thesis, PHOTONS++, is embedded in the SHERPA framework it is easy to implement such infrared subtracted squared matrix elements, making use of tools and functions already provided within the framework. In particular, some basic building blocks for the calculation of helicity amplitudes already used in [25, 42] can be recycled to construct the necessary, infrared-subtracted one-photon real emission matrix elements, which are then evaluated at momentum configurations generated by the algorithm of Section 3.1. Exact first-order matrix elements have so been implemented for a number of relevant matrix elements, cf. Table 3.1. It is worthwhile to stress that second-order precision could be achieved by employing the same means, if necessary.

In general, the infrared-subtracted squared matrix element can be written as

$$\tilde{\beta}_1^1 \;\;=\;\; \frac{1}{2(2\pi)^3}\, \mathcal{M}_1^{\frac{1}{2}} \mathcal{M}_1^{\frac{1}{2}*} - \tilde{S}(k)\, \mathcal{M}_0^0 \mathcal{M}_0^{0\,*}\,, \qquad\qquad (3.2.11)$$

and it is only the amplitudes $\mathcal{M}$ that are process-specific and need to be listed for the different processes. It should be noted that within the SHERPA framework the real emission matrix elements are straightforward to implement. In contrast, the incorporation of loop matrix elements is somewhat more involved: in those cases the integral has to be calculated analytically and the divergences must be cancelled before implementation as a function of the outer momenta.

3.2.3 Virtual emission corrections

The only virtual corrections occurring to level $\mathcal{O}(\alpha)$ are

$$\begin{aligned}
\tilde{\beta}_0^1 \;\;&=\;\; M_0^1 M_0^{0\,*} + M_0^0 M_0^{1\,*} \\
&=\;\; \mathcal{M}_0^1 \mathcal{M}_0^{0\,*} + \mathcal{M}_0^0 \mathcal{M}_0^{1\,*} - 2\alpha B \tilde{\beta}_0^0\,.
\end{aligned} \qquad\qquad (3.2.12)$$

For the above case of decays of the type $V \to FF$ they read

$$\tilde{\beta}_0^1 \;\;=\;\; \frac{\alpha}{\pi} \left[\ln \frac{m_V^2}{m_F^2} - A \right] \tilde{\beta}_0^0 \qquad\qquad m_V^2 \gg m_F^2\,, \qquad\qquad (3.2.13)$$

with

$$A \;\;=\;\; \begin{cases} 1 \text{ in on-shell scheme} \\ \frac{7}{4} \text{ in } \overline{MS} \text{ scheme} \end{cases} \qquad\qquad (3.2.14)$$

which agrees with [96, 97]. Effects of potentially different left- and right-handed couplings c_L and c_R for different vector bosons only enter in terms suppressed by $\frac{m_F^2}{m_V^2}$ and are currently neglected in PHOTONS++.

For the process $W \to \ell\nu$, cf. [98], the first order virtual correction reads

$$\tilde{\beta}_0^1 \;=\; \frac{\alpha}{\pi}\left[\ln\frac{m_W}{m_\ell} + \tfrac{1}{2}\right]\tilde{\beta}_0^0 \qquad\qquad m_W^2 \gg m_\ell^2 \,. \tag{3.2.15}$$

process	real $\mathcal{O}(\alpha_{\mathrm{QED}})$	virtual $\mathcal{O}(\alpha_{\mathrm{QED}})$
$V^0 \to F^+ F^-$	✓	✓
$V^0 \to S^+ S^-$	✓	✓
$S^0 \to F^+ F^-$	✓	✓
$S^0 \to S^+ S^-$	✓	✓
$W^\pm \to \ell^\pm \nu_\ell$	✓	✓
$\tau^\pm \to \ell^\pm \nu_\ell \nu_\tau$	✓	✗
$S^0 \to S^\mp \ell^\pm \nu_\ell$	✓	✓
$S^0 \to V^\mp \ell^\pm \nu_\ell$	✓	✗

Table 3.1: List of available generic and specific infrared subtracted squared real-emission $(\tilde{\beta}_1^1)$ and virtual-correction $(\tilde{\beta}_0^1)$ matrix elements (V - vector, F - spin-$\frac{1}{2}$ fermion, S - scalar).

Chapter 4

The Z lineshape and radiative lepton decays

This section assesses the quality of the algorithm presented in Chapter 3 beyond what has been presented in [86, 74]. First, the impact of higher order QED corrections on the Z line shape at the LHC is investigated along with related observables. Then, in Section 4.2, the prediction of the radiative decay width of heavy leptons, muons and taus, is compared to experimental data.

4.1 The Z lineshape

The production of a massive weak gauge boson resonance, decaying into pairs of leptons, is a well known process with little background at hadron colliders, such as the LHC. It can, therefore, be used as a "standard candle" to calibrate detectors and luminosities. Further, such processes, occurring in association with multiple jets, are among the most prominent backgrounds in many new-physics searches with signals of the type multijets plus missing transverse energy plus leptons. Hence, an in depth understanding of especially the electroweak part of such events is paramount.

To this end, in the following the systematic uncertainties of various approaches to simulate such higher order QED corrections to the process $pp \rightarrow e^+e^- + X$ using different ansatzes are compared. Beyond the implementation of the YFS-resummation, detailed in the Section 3.1, the CSS parton shower algorithm, implementing a DGLAP-resummation (see Chapter 6) of higher order QED effects [99, 62, 64], is used. While the former rests on a resummation of large logarithms in the region where the emitted photon turns infinitely soft, the latter resums the large logarithms associated with collinear photon emission.

The implementation of the YFS-resummation of Section 3.1 for this process, calculating the higher order corrections to the leading order process $q\bar{q} \rightarrow e^+e^-$ in the full Standard Model, assumes the presence of an intermediated Z-boson. This assumption is necessitated by the restriction to particle decays of the YFS-resummation implementation. Thus, an effective narrow width approximation with a varying intermediate Z mass according to the invariant mass of the leading order lepton pair is employed. This approximation is expected to hold only if the region around the Z-peak is considered. Therefore, in all of the following examples the bare electrons of the leading order process are required to have $65\,\mathrm{GeV} < m_{ee} < 115\,\mathrm{GeV}$. Further, due to its restriction to particle decays, this implementation of the YFS-resummation neglects photon radiation off the initial state quarks. As described in Section 3.2, the YFS resummation can be trivially corrected for the effects of hard photon radiation using approximated real emission corrections, denoted YFS⊗CS in the following[1],

---

[1] The QED variants of the spin-averaged Catani-Seymour splitting functions are used to approximate the real emission matrix elements.
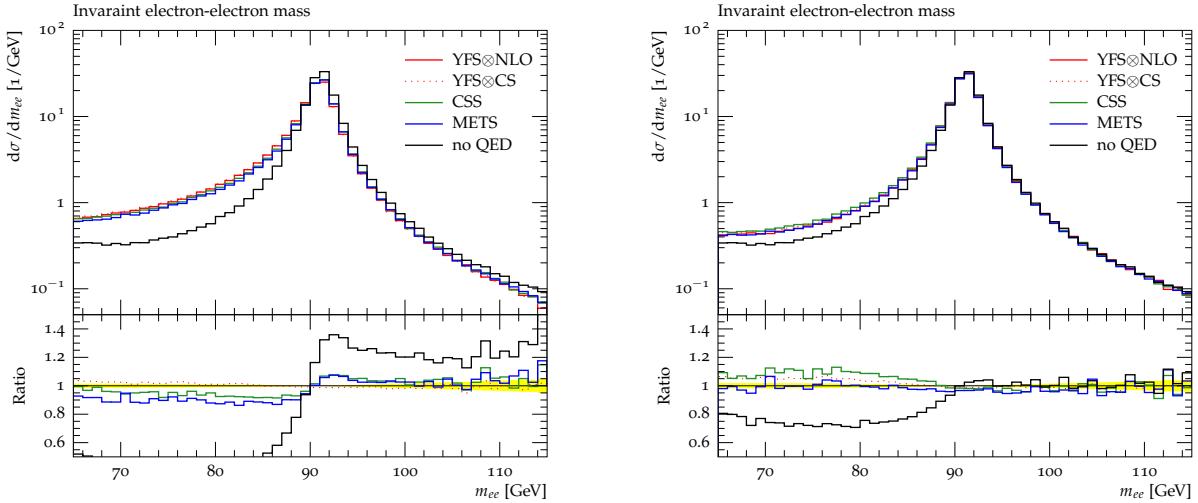
Figure 4.1: The reconstructed Z mass using the bare electrons (left) and the dressed electrons (right), recombined with all QED radiation in a $\Delta R = 0.2$ cone, for the various different approaches. The YFS⊗NLO prediction is taken as the reference.

or exact next-to-leading order matrix elements including virtual one-loop matrix elements, denoted YFS⊗NLO. The infrared cut-off, defined as minimum photon energy in the e^+e^- rest frame, is set to $E_{\text{gencut}} = 1\,\text{MeV}$. The collinear divergence is regulated by the electron mass.

The implementation of QED corrections within the CSS parton shower framework is detailed in [64]. To summarise, the QED versions of the spin-averaged Catani-Seymour dipole terms, reproducing the DGLAP collinear resummation behaviour, are used to define a Sudakov form factor for a $f \to f\gamma$ ($f = q, \ell$) branching. However, unlike in QCD where the limit $N_c \to \infty$ is taken to single out the leading positive definite contributions, a similar limit cannot be taken in QED. Thus, to arrive at a positive definite parton shower formulation an overestimate in the form of only considering oppositely charged dipoles is chosen instead. Nonetheless, this is only relevant if the number of charged particles is larger than two. The algorithm is run in three different settings: the pure QED parton shower approximation of the higher order corrections to the process $q\bar{q} \to e^+e^-$ without any assumption on intermediate particles, labeled CSS in the following; the QED parton shower approximation of the higher order corrections to the factorised decay $Z \to e^+e^-$ employing the same varying-mass narrow-width approximation as in the YFS case, labeled CSS-nw; and the matrix element merged results using the algorithm described in [64] and up to two additional photons in the matrix elements[2], labeled METS. The infrared cut-off, defined as minimum relative transverse momentum, is set to $p_\perp^{\text{gencut}} = 1\,\text{MeV}$.

4.1.1 Radiation pattern

Figure 4.1 now presents the invariant mass of the bare electrons (left) and the reconstructed electrons (right), recombining the bare leptons with all QED radiation in a $\Delta R =$

---

[2] The LO processes $q\bar{q} \to e^+e^-$, $q\bar{q} \to e^+e^-\gamma$ and $q\bar{q} \to e^+e^-\gamma\gamma$, without any assumption about intermediate particles, are merged with the parton shower result for the same process. Processes with initial state photons, occurring when an inclusive final state is considered, are expected to give only a very small contribution and are thus neglected. The merging scale $Q_{\text{cut}}^{\text{QED}}$ has been set to 1 GeV.
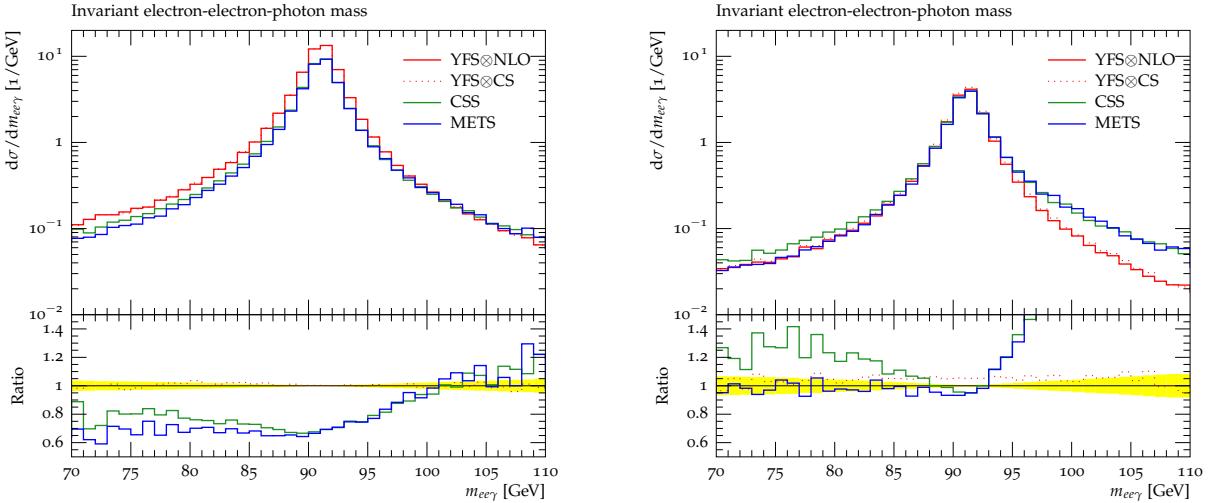
Figure 4.2: The invariant electron-electron-photon mass using the bare electrons (left) and the dressed electrons (right), recombined with all QED radiation in a $\Delta R = 0.2$ cone, for the various different approaches. The hardest photon not part of the reconstructed electron and a minimum energy of 1 GeV is selected. The YFS⊗NLO prediction is taken as the reference.

$\sqrt{(\Delta\phi)^2 + (\Delta\eta)^2} = 0.2$ cone, for the various different approaches. While the invariant mass of the bare leptons is sensitive to all types of energy loss, i.e. all photon radiation, the invariant mass of the recombined leptons, effectively integrating over the collinear part of the photon spectrum is sensitive only to wide-angle emission. Thus, examining both quantities provides details on the quality of the simulation in both the collinear regime, where the bulk of the radiation occurs, and the wide-angle regime.

In the predictions for the reconstructed Z mass using the bare electron definition the YFS⊗NLO (red solid line) and YFS⊗CS (red dotted line) predictions differ only slightly, indicating good agreement in the description of the largest part of the radiation spectrum. For the reconstructed Z mass using the dressed electron definition, however, both predictions differ by up to 10% in the low invariant mass region, highlighting the missing (destructive) interference terms in YFS⊗CS simulation. Equivalent results have been found in [86, 74].

Similarly, both methods using the DGLAP collinear resummation, the CSS (green solid line) and METS (blue solid line), show good agreement for the bare Z mass while differing for the dressed Z mass up to 10% in the low mass region. Again, this region reveals the different level of accuracy in the description of hard wide angle radiation, ascribed again to the missing destructive interference terms in the collinear approximation.

Finally, both resummation methods deviate from one another by about 10% in the peak region of the bare Z mass. This originates in the fact that hard collinear photon radiation is only accounted for up to $\mathcal{O}(\alpha)$ in both YFS⊗NLO and YFS⊗CS while it is resummed to all orders in both CSS and METS. The Z mass reconstructed from the dressed lepton momenta, however, shows very good agreement in the peak region. This indicates that, although differing in the description of the radiation in the collinear region, the inclusive picture is described similarly in both approaches. Most notably, both methods using exact $\mathcal{O}(\alpha)$ real emission matrix elements, YFS⊗NLO and METS, show very good agreement also in the low mass region, which is most sensitive to a correct description of hard wide angle radiation. The effects of additional photon radiation from the initial state quarks on these two observables is negligible.
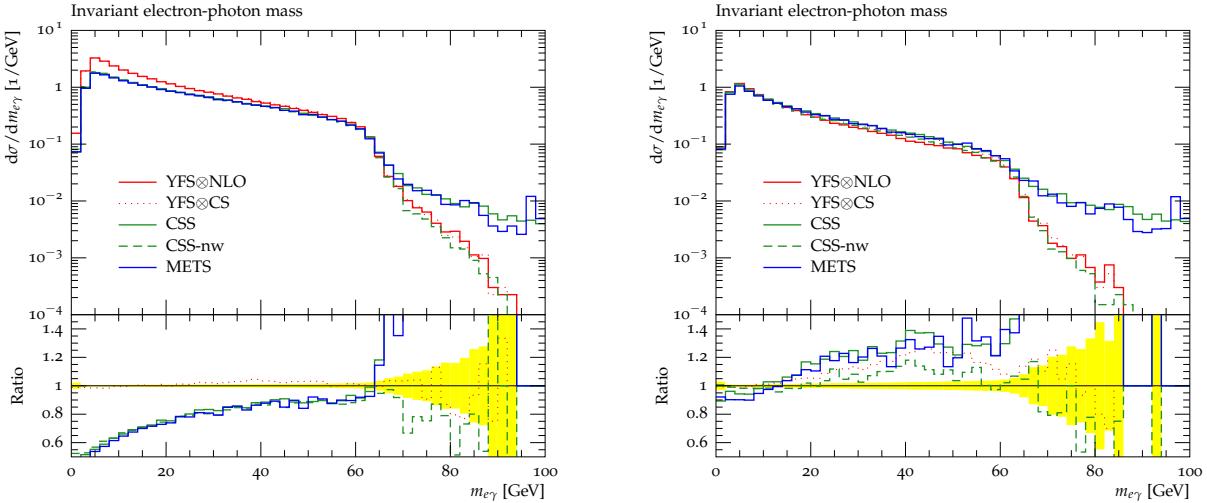
Figure 4.3: The invariant electron-photon mass, defined as the invariant mass of the
hardest photon and its nearest electron/positron, using the bare electron
(left) and the dressed electron (right), recombined with all QED radiation in
a $\Delta R = 0.2$ cone, for the various different approaches. The photon must not
be part of the reconstructed electron and must have a minimum energy of 1
GeV is selected. The YFS⊗NLO prediction is taken as the reference.

To exemplify the difference of the description of the real emission corrections further Figure
4.2 displays the invariant mass of both electrons and the hardest photon, using again the
bare leptons on the left plot and the dressed leptons on the right plot. The photon is required
to have an energy of at least 1 GeV and must not be part of the dressed electron. The first
thing to note is that the predicted number of such hard photons, equaling the integral of the
distributions using the bare leptons, differs by about 25% between the YFS resummation
implementations and the DGLAP resummation implementations. Then, after recombining
collinear photons with the electron, all distributions agree nicely in the peak region, and,
again, both methods using exact $\mathcal{O}(\alpha)$ real emission matrix elements also agree very well in
the low mass region. As in Figure 4.1, the pure CSS parton shower result overestimates the
amount of hard wide angle radiation. Similarly, this is also overestimated by the YFS⊗CS
simulation.

Another apparent feature is the disagreement of the simulations in the high mass region.
Here, the effect of hard photon radiation off the initial state quarks becomes apparent.
Not stemming from the decaying intermediate boson their invariant electron-electron-photon
mass does not peak at the nominal Z mass. These effects are accounted for in both the CSS
and METS DGLAP-type simulations, but not in the YFS-type simulations. Attributing it
to initial state radiation is confirmed by the CSS-nw prediction.

Likewise, Figure 4.3 displays the invariant mass of the hardest photon and the nearest
electron (in ΔR). Again, the photon is required to have an energy of at least 1 GeV and
must not be part of the electron definition. The electron is defined as the bare electron in
the left hand side plot and as the dressed electron, collecting all QED radiation within a
$\Delta R = 0.2$ cone, in the right hand side plot. This variable is most sensitive to the angular
correlations of the photon emission. The same pattern as before is found in the predictions.
The YFS-type resummations predict approximately 25% more radiation with $E_\gamma > 1\,\mathrm{GeV}$
which is predominantly close to the electron, leading to an excess of low invariant mass
electron-photon pairs. After recombining this collinear part of the photon spectrum with the
electron, the agreement is better. Partly, this deviation can be explained by using the spin-
averaged Catani-Seymour splitting functions for the approximated higher order corrections,

as can be seen from the relatively small difference between the YFS⊗CS and Css predictions. The rest can, again, be attributed to additional photon radiation off the initial state quarks. To make this explicit, a further prediction using the Css parton shower approximation but taking only radiation off the final state leptons into account, labeled Css-nw (green dashed line), is added to the plots. It deviates only slightly from its YFS-type counterpart YFS⊗CS. Similarly, lacking these quark irradiated photons Css-nw does not exhibit the high invariant mass tail of the Css and METS predictions, but follows YFS-type predictions also resting on the varying-mass narrow-width approximation.

4.1.2   Numerical stability

After exploring the impact of different ansatzes to resummed higher order corrections, this section puts the focus on the performance of the algorithms under variation of the unphysical infrared cutoff parameters E_{gencut} and $p_\perp^{\text{gencut}}$, respectively.

The YFS resummation implementations

To explore the dependence of the algorithm on the unphysical infrared cut-off parameter E_{gencut} it is varied over a large range and the impact upon the afore studied observables and pseudo-observables is examined. Therefor, Figures 4.4-4.6 show the variation of the reconstructed Z mass, the invariant electron-electron-photon mass and the invariant mass of the hardest photon and its nearest electron, using both the bare and dressed electron definitions defined in the previous section. The infrared cutoff is varied from 1 keV to 10 GeV therein and, avoiding redundance, the YFS⊗NLO implementation is used. The predictions for $E_{\text{gencut}} = 1$ keV are used as the reference in the ratio plots. The results for the infrared cutoff dependence of the YFS⊗CS are similar.

While the predictions for $E_{\text{gencut}} = 1\,\text{keV}$ and $E_{\text{gencut}} = 1\,\text{MeV}$ coincide for all six observables it is plainly visible that the other two choices, foremost $E_{\text{gencut}} = 10\,\text{GeV}$, do not fill important parts of the phase space. This can be seen in the total number of photons with $E_\gamma > 1\,\text{GeV}$, as well as in the dips in the distribution for the reconstructed Z mass and the empty regions in $m_{e\gamma}$. However, it is reassuring to note that outside these holes in the real radiation phase space, all four predictions coincide.

The DGLAP resummation implementations

Similarly to the last section, this section explores the dependence on the infrared cutoff $p_\perp^{\text{gencut}}$ of the Css implementation. Again, the same six observables and pseudo-observables are studied. Figures 4.7-4.9 show the predictions from the Css implementation for the reconstructed Z mass, the invariant electron-electron-photon mass and the invariant mass of the hardest photon and the nearest electron, again, using both the bare and dressed electron definitions. The infrared cutoff is varied from 1 keV to 10 GeV. The predictions for $p_\perp^{\text{gencut}} = 1$ keV are used as the reference in the ratio plots. The cutoff dependences of both the Css-NW and METS predictions are similar.

In case of the Css only the observables using dressed leptons stabilise when lowering the cutoff below 1 MeV. There, agreement on the level of 5% is found. The observables depending on the bare lepton definitions, however, still show a significant cutoff dependence. The reason for this behaviour lies in the definition of the cutoff. Although having the advantage of Lorentz invariance, a cutoff in the relative transverse momentum cuts away a significant part of the collinear radiation spectrum. In case of radiating off massive electrons in the considered process this peaks at $p_\perp \sim m_e$ [100, 86]. Thus, for a cutoff of $p_\perp^{\text{gencut}} = 1\,\text{MeV}$
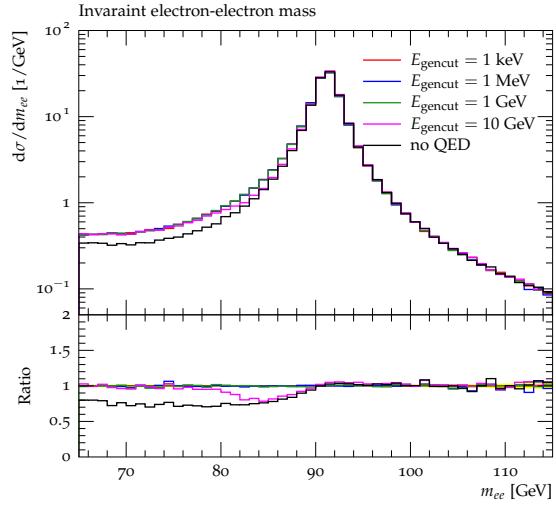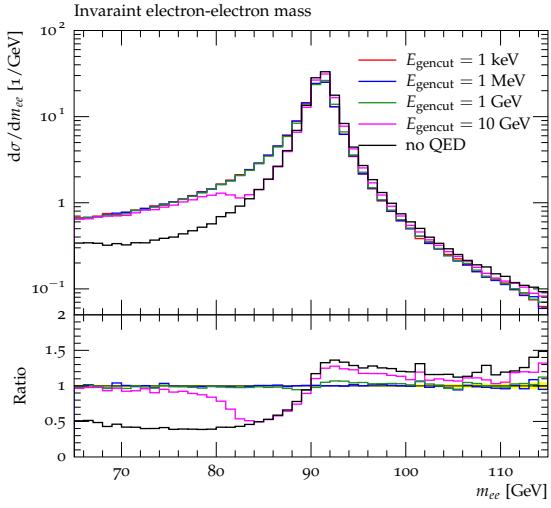
Figure 4.4: The dependence on the infrared cutoff E_{gencut} of the reconstructed Z mass using the bare electrons (left) and the dressed electrons (right).
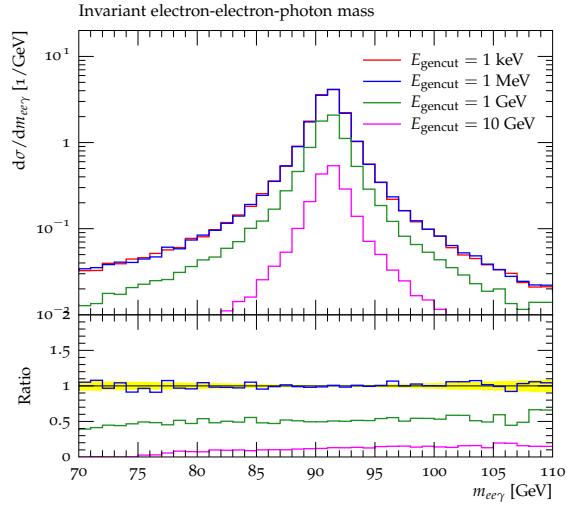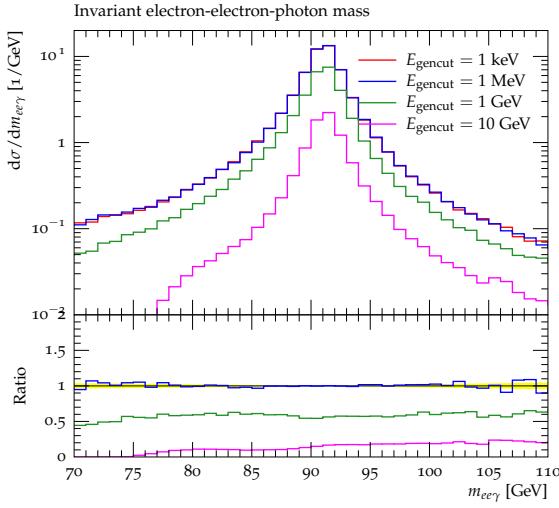

Figure 4.5: The dependence on the infrared cutoff E_{gencut} of the invariant electron-electron-photon mass using the bare electrons (left) and the dressed electrons (right).
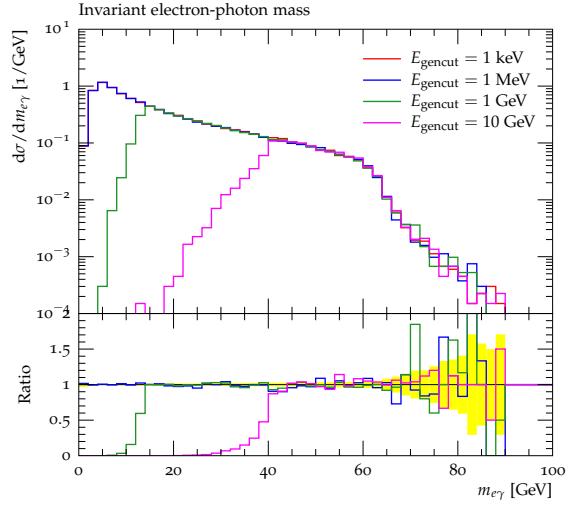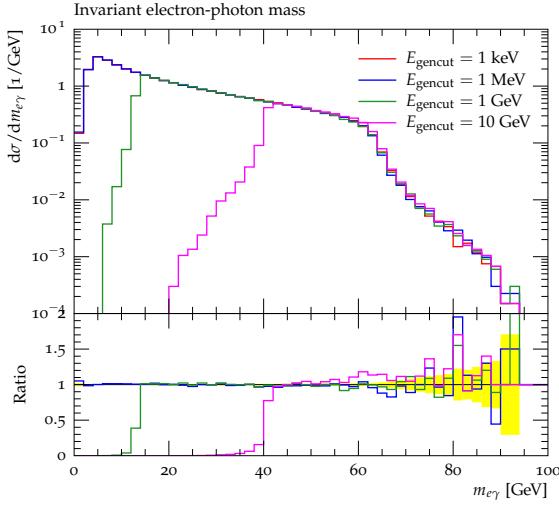
Figure 4.6: The dependence on the infrared cutoff E_{gencut} of the the invariant electron-photon mass using the bare electron (left) and the dressed electron (right).
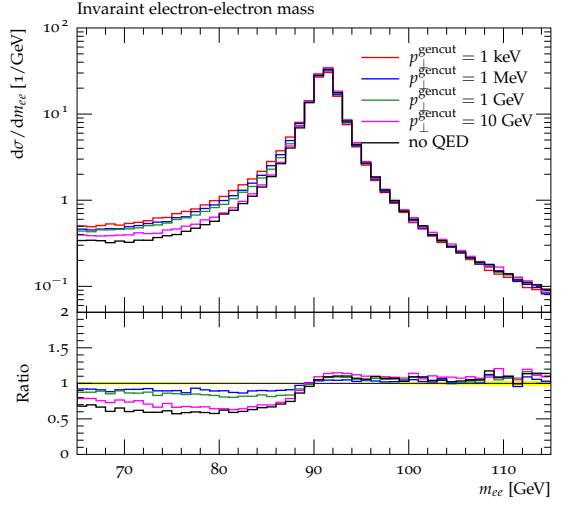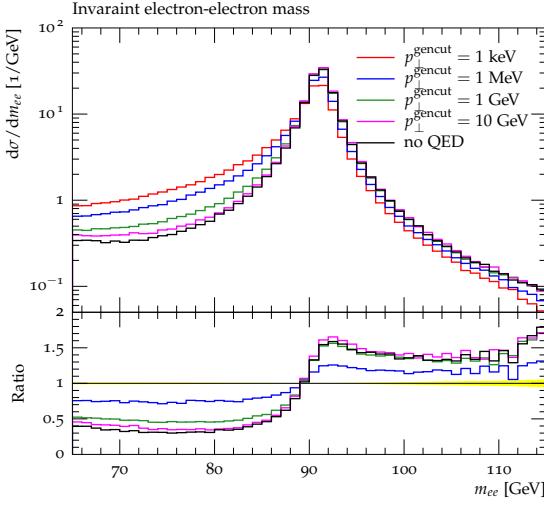
Figure 4.7: The dependence on the infrared cutoff $p_\perp^{\text{gencut}}$ of the reconstructed Z mass using the bare electrons (left) and the dressed electrons (right).
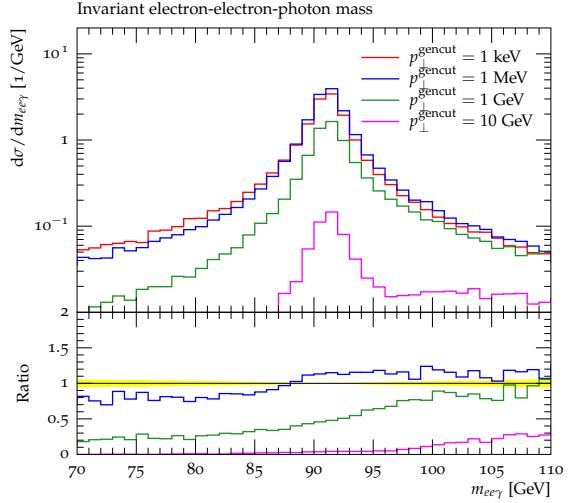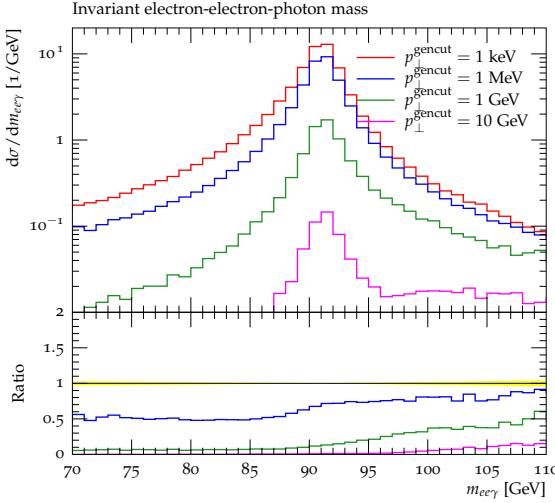
Figure 4.8: The dependence on the infrared cutoff $p_\perp^{\text{gencut}}$ of the invariant electron-electron-photon mass using the bare electrons (left) and the dressed electrons (right).
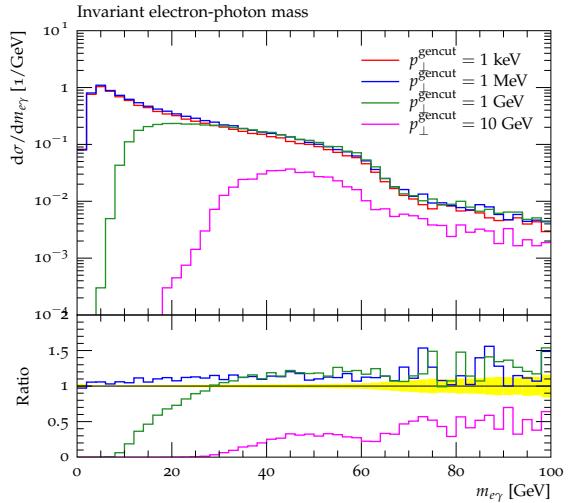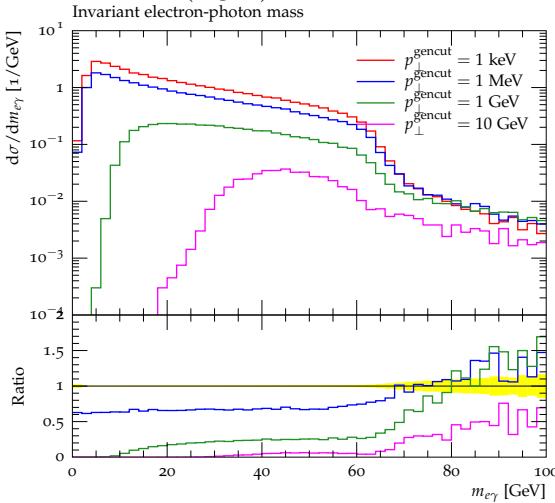
Figure 4.9: The dependence on the infrared cutoff $p_\perp^{\text{gencut}}$ of the the invariant electron-photon mass using the bare electron (left) and the dressed electron (right).

or higher missing hard collinear radiation is expected. Nonetheless, when this part of the spectrum is integrated out by "dressing" the electrons, the resulting spectra should agree. Similar effects occur for the radiation off the massless initial state quarks where no such deadcone effect, leading to a stabilisation in hard photon radiation as the cutoff is lowered, is present, thus flooding the bare observables with hard photons collinear to the incoming beams. Obviously, these effects are not present for the dressed observables. Along these lines, for too low cutoffs numerical inaccuracies might occur for the dynamic calculation of the quarks' Sudakov form factors. Of course, incorporating the quark masses in the calculation would cure this deficiency. This, however, would severely complicate the calculation of higher order QCD corrections not considered here.

Further, as in the case of the YFS resummation implementation, setting this cutoff too high leads to significant holes in the real radiation phase space influencing also regions beyond the $\Delta R = 0.2$ cone around the leptons. Differing amounts of radiation off the initial state quarks also play a role here.

4.2   Radiative lepton decays

The branching fraction of radiative leptonic decays in μ and τ decays (with at least one photon with $E_\gamma > 10\text{MeV}$) has been checked against PDG values [101]. Within the calculation, exact matrix element corrections for the real emission amplitude at $\mathcal{O}(\alpha)$ have been used, while the virtual contributions of $\mathcal{O}(\alpha)$ have been approximated in the limit $k \to 0$ within the Yennie-Frautschi-Suura resummation only. Thus, the ratio of the radiative decay width Γ_{rad} to the inclusive decay width Γ_{incl} is expected to be slightly overestimated as compared to full YFS$\otimes$NLO calculation, truncated at $\mathcal{O}(\alpha)$ for readabilities sake:

$$\frac{\Gamma_{\text{rad}}}{\Gamma_{\text{incl}}} = \frac{\Gamma_1^1(E_\gamma > 10\text{GeV})}{\Gamma_0^0 + \Gamma_0^1 + \Gamma_1^1} < \frac{\Gamma_1^1(E_\gamma > 10\text{GeV})}{\Gamma_0^0 + \Gamma_{0,\text{LL}}^1 + \Gamma_1^1} \ . \tag{4.2.1}$$

Herein the notations of the previous chapters have been adopted, i.e. $\Gamma_{n_R}^{n_V + n_R}$ denotes the decay rate including exactly n_R real and n_V virtual photons, such that the superscript signals the perturbative order in α at which it has been calculated relative to the inclusive decay. The "<"-relation holds as long as the non-logarithmic corrections $\Gamma_0^1 - \Gamma_{0,\text{LL}}^1$ are positive, a result found to hold for this process. Higher order corrections, effected through the YFS resummation, are added as the same terms to both sides of eq. (4.2.1). Hence, although they change the magnitude of the above ratio, they do not alter the inequality.

Tab. 4.1 then summarises the results and excellent agreement was found.

4.3   Summary and conclusions

In this part of this thesis the quality of the implementation of the YFS resummation and its supplementation by fixed order matrix elements was examined for processes that can be computed entirely on the basis of first principles and the gauge theories of the Standard Model. To this end the processes of Drell-Yan production at hadron colliders and the radiative leptonic decay modes of muons and taus have been chosen. For the case of Drell-Yan production it has been compared to the predictions of a pure and a matrix element corrected parton shower event sample, using the ME+PS method for QED evolution for the latter.

In the case of Drell-Yan production the focus rested upon observables related to the Z lineshape and additional hard photon radiation, examining all observables both for dressed and bare electron definitions to also assess the description of collinear hard photon radiation.

	$\dfrac{\Gamma(\mu \to e\,\nu_e\,\nu_\mu\,\gamma)}{\Gamma(\mu \to e\,\nu_e\,\nu_\mu, incl.)}$	$\dfrac{\Gamma(\tau \to e\,\nu_e\,\nu_\tau\,\gamma)}{\Gamma(\tau \to e\,\nu_e\,\nu_\tau, incl.)}$	$\dfrac{\Gamma(\tau \to \mu\,\nu_\mu\,\nu_\tau\,\gamma)}{\Gamma(\tau \to \mu\,\nu_\mu\,\nu_\tau, incl.)}$
PDG	0.014(4)	0.09(1)	0.021(3)
PHOTONS++	0.0147(1)	0.0999(3)	0.0233(2)

Table 4.1: A comparison of the branching ratios of the radiative leptonic μ and τ decay mode ($E_\gamma > 10$MeV) in relation to their inclusive leptonic mode calculated by PHOTONS++ and the PDG world average. The number in brackets reflects the absolute error on the last digit.

For all observables considered here good agreement was found using the dressed electron definition. The minor differences found could be fully attributed to the presence of radiation off the initial state quarks present only in the parton shower description. Larger deviations were found for observables using the bare electron definition. Thus being highly sensitive to hard collinear radiation, they emphasise the difference of the descriptions of such emissions. The findings are consistent with the fact that these hard collinear photons are described by a fixed-order next-to-leading oder matrix element correction only in the YFS resummation approach, they are described by the all-orders resummation of the parton shower in the DGLAP resummation approach. Therefore, considering also the results presented in [86, 74], the implementation in PHOTONS++ exhibits the desired accuracy.

Finally, the predicted ratios of the radiative leptonic decay widths to the total inclusive leptonic decay widths were calculated for all such decay modes of taus and muons. This ration was shown to be very well described by the implementation in PHOTONS++.

Chapter 5

Electroweak corrections to semileptonic B decays

In the Standard Model, the Cabibbo-Kobayashi-Maskawa (CKM) matrix [102, 103] governs the charged current weak interactions between the up- and down-type quarks of the three fermion generations. The precision determination of its matrix elements and its CP-violating complex phase in the B meson sector has been the focus of intense research over the past decade. The combination of various measurements to test the unitarity of the CKM matrix is considered a strong instrument in the search for physics beyond the Standard Model [104, 105].

In this chapter of this thesis, a calculation of the electroweak next-to-leading order corrections in exclusive semileptonic B meson decays into (pseudo)scalar mesons, $B \rightarrow D\,\ell\,\nu_\ell$, $B \rightarrow D_0^*\,\ell\,\nu_\ell$ and $B \rightarrow \pi\,\ell\,\nu_\ell$, ℓ denoting either an electron or a muon, is presented. Next-to-leading order corrections to such decays are an important aspect in the extraction of the CKM matrix elements $|V_{\rm cb}|$ and $|V_{\rm ub}|$ at B-factory experiments. Virtual electroweak bosons running in the loop as well as real photon emissions off all charged particles present in the decay alter the resulting decay dynamics and enhance the weak decay rate. To correct for the changed decay dynamics, experimentalists use approximative all-purpose next-to-leading order algorithms. These exploit universal factorisation theorems in the soft and/or collinear photon energy limit [106, 75, 93]. In addition, the total hadronic decay rate of semileptonic decays are corrected by the known leading logarithm of the virtual corrections of the partonic decay [107, 108].

Experience from exclusive semileptonic K meson decays illustrate the importance of having a good understanding of such radiative effects: until 2004 the global average of the extracted value of $|V_{\rm us}|$ from K_{l3}^+ and K_{l3}^0 decays implied the violation of CKM unitarity by two standard deviations [109]. Further measurements proved dissonant with these findings [110, 111, 112, 113], indicating that the achieved experimental precision needed an improved understanding of electroweak corrections. Since for many decays next-to-leading order calculations do not exist, experiments often use the approximative all-purpose algorithm PHOTOS [87, 76] to study the reconstruction efficiency and acceptance. The accuracy of this approach was tested by the KTeV collaboration, using the measured photon spectra from radiative K_{l3}^0 decays: the angular distribution of the simulated photons did not agree well with the predicted spectrum [114]. This lead to the development of the next-to-leading order Monte Carlo generator KLOR (see [114]), whose next-to-leading order calculation is based on a phenomenological model. Its predicted angular photon distribution agreed satisfactorily with the measured spectra. Although this approach is very precise, it is also the most complicated one to adopt for an experiment: electroweak next-to-leading order calculations only exist for a few decay modes, sometimes only valid in a limited region of phase-space. Most of these calculations are evaluated numerically and rely on customised Monte Carlo generators.

Over the last 10 years, an increasing amount of data and a better understanding of detector effects lead to a very accurate picture of physics at the B-factory experiments. This increased precision then lead to the demand of knowledge of next-to-leading order electroweak effects beyond the precision of approximative all-purpose algorithms. This chapter of this thesis aims at improving the status quo by providing a prediction for both total decay rates and differential distributions of a few representative kinematic variables. For the latter the predictions of a dedicated Monte-Carlo generator, BLOR [115], is compared to two all-purpose generators, SHERPA/PHOTONS++ [8, 74] and PHOTOS [87, 76]. While the latter is a -parton-shower Monte Carlo program intended to supplement generic leading logarithmic corrections to pure leading order decay generators, the former is a full-fledged hadron-level Monte Carlo generator for collider physics whose internal leading order (hadronic) decays are supplemented by a universal soft-photon-resummation systematically improved, where possible, by known exact next-to-leading order matrix elements. While the improved description of inclusive decay rates directly gives small corrections to the extracted values of $|V_{cb}|$ and $|V_{ub}|$ from semileptonic decays, the improved description of the decay kinematics influence extrapolation to corners of the phase space and, therefore, leads to both direct and indirect corrections.

The considerations of this chapter proceed as follows: Section 5.1 briefly reviews exclusive $B \to X \, \ell \, \nu_\ell$ decays at tree-level. Thereafter, Section 5.2 develops the next-to-leading order formalism, reviewing both the partonic short-distance results of [107, 108], the hadronic long-distance QED-improved effective decay and their matching to one-another, including also a detailed discussion on non-universal structure-dependent terms in Section 5.2.4. Contributions generically derivable through first principles are clearly distinguished from (at least partially unknown) model and decay channel dependent ones. The resulting expressions are then embedded into the resummation in the soft limit of Yennie, Frautschi and Suura [75] in Section 5.2.5. Section 5.3 then shortly reviews the basic principles of both BLOR and SHERPA/PHOTONS++ where the calculations of Section 5.1-5.2 have been implemented, and of PHOTOS. The total inclusive decay rates obtained are shown in Section 5.4.1 while differential distributions are shown in Section 5.4.2, also detailing the improvement over the current estimates. The influence of the structure-dependent terms, where known, on the results is presented in Section 5.4.3. Section 5.5 finally summarises the results.

Note that the charge-conjugated modes are implied throughout the following chapter.

5.1 Tree-level decay

The phenomenological interaction Lagrangian of the weak $B \to X \, \ell \, \nu$ decay to a (pseudo)scalar final state in Fermi's theory, with constant form factors of the hadronic current, $f_\pm$, is given by

$$\mathcal{L}_W = \frac{G_F}{\sqrt{2}} V_{xb} \left[\left(f_+ + f_- \right) \phi_X \, \partial^\mu \phi_B + \left(f_+ - f_- \right) \phi_B \, \partial^\mu \phi_X \right] \, \bar{\psi}_\nu P_R \gamma_\mu \psi_\ell \; + \; \text{h.c.}, \qquad (5.1.1)$$

where ψ_ℓ and ψ_ν are the Dirac fields of the lepton and the neutrino, ϕ_B and ϕ_X are the scalar fields of the initial and final state mesons, G_F the Fermi coupling, V_{xb} the CKM matrix element governing the strength of the $b \to x$ transition, and $P_R = 1 + \gamma_5$ is derived from the right-handed projection operator by absorbing the factor $\frac{1}{2}$ into the coupling definition. The Lagrangian of eq. (5.1.1) leads to the transition matrix element[1]

$$\mathcal{M}_0^0 = -i \frac{G_F}{\sqrt{2}} V_{xb} \, H_\mu(p_B, p_X; t) \; \bar{u}_\nu \, P_R \gamma^\mu v_\ell, \qquad (5.1.2)$$

---

[1]Throughout this part of this thesis $\mathcal{M}_m^n$ denote a matrix element at $\mathcal{O}(G_F \, \alpha^n)$ with m photons in the final state. The total decay rate at $\mathcal{O}(G_F \, \alpha^n)$ is denoted as Γ_m^n.
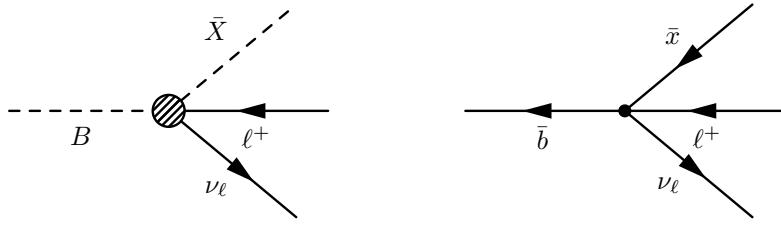
Figure 5.1: The tree-level weak $B \to \bar{X}\,\ell^+\,\nu_\ell$ decay is shown both in the phenomenological picture (left) and, at parton level, in Fermi's theory as low energy approximation of the Standard Model (right). The shaded circle represents the effective vertex parametrised by form factors $\mathrm{f}_\pm$, $x \in \{u, c\}$.

with the hadronic current, generalised to variable form factors,

$$
H_\mu(p_B, p_X; t) \;=\; \langle X | \bar{\psi}_x P_\mathrm{R} \gamma_\mu \psi_b | B \rangle \;=\; \big(p_B + p_X\big)_\mu \, \mathrm{f}_+(t) + \big(p_B - p_X\big)_\mu \, \mathrm{f}_-(t) \,. \tag{5.1.3}
$$

The four-momenta labels in eq. (5.1.2) are introduced in Fig. 5.1. The generalised form factors $\mathrm{f}_\pm = \mathrm{f}_\pm(t)$ now describe the phase-space dependent influence of the strong interaction on the weak decay dynamics and are functions of the squared momentum transfer from the hadronic to the leptonic system only, given at tree-level by

$$
t \;=\; \big(p_B - p_X\big)^2 \;=\; \big(p_\ell + p_\nu\big)^2 \,. \tag{5.1.4}
$$

The tree-level differential decay rate in the B-meson rest frame is then given by

$$
\mathrm{d}\Gamma_0^0 \;=\; \frac{1}{64\,\pi^3 m_B} \big|\mathcal{M}_0^0\big|^2 \, \mathrm{d}E_X \, \mathrm{d}E_\ell \,, \tag{5.1.5}
$$

with $E_X = p_X^0$ and $E_\ell = p_\ell^0$. The explicit expressions of the $\mathrm{f}_\pm(t)$ as function of the momentum transfer squared for the processes considered in this thesis, $B \to D\,\ell\,\nu$, $B \to D_0^*\,\ell\,\nu$ and $B \to \pi\,\ell\,\nu$, can be found in Appendix B.1.

5.2   Next-to-leading order corrections

The arising electroweak next-to-leading order corrections can be divided into two energy regimes: short-distance corrections at parton level, and long-distance corrections within the phenomenological model. First, Section 5.2.1 will discuss how both descriptions can be matched and renormalised. Section 5.2.2 then reviews the calculation of the virtual short-distance corrections of [107, 108]. The long-distance corrections, following from an extension of the phenomenological model, are then discussed in Section 5.2.3.

5.2.1 Matching of different energy regimes

The aim of this section is to develop a formalism to calculate the corrections at $\mathcal{O}(\alpha\, G_{\mathrm{F}})$. The standard approach involves calculating the one-loop graphs for the $B \to X\, \ell\, \nu_\ell$ decay in the effective theory with counterterms and compare it to the renormalised Standard Model result. Fixing the counterterms results in the desired matching of both results. The effective theory itself is non-renormalisable, but the Standard Model can be renormalised to measured quantities, e.g. the Fermi coupling constant of the muon decay, the electron mass, and the fine-structure constant, in order to produce finite predictions. Such a matching procedure was carried out in great detail by [116] for semileptonic Kaon decays where the leading order phenomenological decay is described by a chiral Lagrangian.

In the present case, however, an alternative route is pursued. Consider a general logarithmically divergent N-point tensor integral of rank p with a single massless photon propagator. It can be cast in the form

$$T^{\mu_1 \cdots \mu_p}(p_1, \ldots, p_{N-1}) \quad \propto \quad \int \mathrm{d}^4 k \; \frac{k^{\mu_1} \cdots k^{\mu_p}}{k^2 \, d_1 \ldots d_{N-1}} \,, \tag{5.2.1}$$

with denominators $d_i = (p_i - k)^2 - m_i^2$. The integral can then be split according to

$$\begin{aligned} T^{\mu_1 \cdots \mu_p}(p_1, \ldots, p_{N-1}) \quad \propto \quad & \int \mathrm{d}^4 k \left[\frac{k^{\mu_1} \cdots k^{\mu_p}}{k^2 \, d_1 \cdots d_{N-1}} - \frac{k^{\mu_1} \cdots k^{\mu_p}}{\left[k^2 - \Lambda^2\right] d_1 \cdots d_{N-1}} \right] \\ & + \int \mathrm{d}^4 k \, \frac{k^{\mu_1} \cdots k^{\mu_p}}{\left[k^2 - \Lambda^2\right] d_1 \cdots d_{N-1}} \,. \end{aligned} \tag{5.2.2}$$

This amounts to regulating the ultraviolet behaviour of the first term using an unphysical photon-like vector field of mass Λ and opposite norm, as proposed by Pauli and Villars in [117]. Its infrared behaviour is left unchanged, thus, relying on the Kinoshita-Lee-Nauenberg theorem [91, 92], these divergences are left to be canceled by the real corrections. The second term of eq. (5.2.2) is the equivalent of eq. (5.2.1), this time only with a massive photon. Hence, it is infrared finite and possesses the identical ultraviolet behaviour.

Transferring this observation to the present case of semileptonic B meson decays where, both in the effective theory and in the Standard Model, there is at most one massless photon propagator in any one-loop diagram, the virtual emission matrix element can be decomposed as

$$\mathcal{M}_0^1 \quad = \quad \mathcal{M}_{0,\mathrm{ld}}^1(\Lambda) + \mathcal{M}_{0,\mathrm{sd}}^1(\Lambda) \,. \tag{5.2.3}$$

The term $\mathcal{M}_{0,\mathrm{ld}}^1$ is now comprised of the Pauli-Villars regulated exchange of a massless photon, including its infrared divergence. The specific UV regulator effectively restricts the virtual photon's momentum to be smaller than Λ. Hence, it describes long-distance (ld) interactions only.

The term $\mathcal{M}_{0,\mathrm{sd}}^1$, on the other hand, carries the full ultraviolet behaviour of $\mathcal{M}_0^1$. It thus can be used for renormalising all parameters. Consequently, because eq. (5.2.2) is exact, all parameters in $\mathcal{M}_{0,\mathrm{ld}}^1$ are then renormalised automatically. Through the photon mass, its virtual propagator's momentum is effectively restricted to be larger than Λ. Hence, this term describes the short-distance (sd) interactions only.

The above is exact as long as the same Lagrangian input is used to calculate both the short-distance and the long-distance parts. In practice, however, due to the confining, non-perturbative nature of QCD this is not feasible for the processes at hand. For scales larger

than the hadron mass, where their partonic content can be resolved, electroweak corrections have to be calculated on the basis of (constituent) quarks. For scales smaller than the hadron mass, its parton content cannot be resolved, the bound-state hadrons themselves are the relevant degrees of freedom. Thence, supposing Λ is set such, that it effectively separates those two regimes, the long-distance QED corrections $\mathcal{M}_{0,\mathrm{ld}}^1$ can be calculated using the phenomenological model and for the short-distance corrections $\mathcal{M}_{0,\mathrm{sd}}^1$ the full Standard Model has to be invoked. This is justified, in principle, by the assumption, that the phenomenological model describes the Standard Model and its effective degrees of freedom at these low scales. This mere fact, however, directly leads to inconsistencies at the matching scale Λ, where both models should give the same answer. Thus, this matching is only approximate and the associated systematic uncertainties to this method can be estimated by varying the matching parameter, cf. Section 5.4.1.

The above reasoning leads to an optimal value for Λ: the smallest hadronic mass in the decay. Then, only low-energy virtual photons, not able to resolve either of both mesons, are described by the effective theory, while high-energy virtual photons are described by the short-distance picture of the full Standard Model, resolving the partonic content of both the charged and the neutral meson involved. Further, as long as $\Lambda > E_\gamma^{\mathrm{max}}$, the kinematic limit of the photon energy in single photon emission[2], the real emission of photons off these charged mesons are also correctly described by the phenomenological model (except for structure dependent terms discussed in Section 5.2.4).

Nonetheless, it has to be noted that there are conceptual problems if both hadronic scales differ significantly. Then, there is a large intermediate regime, where virtual photons are able to resolve one meson, but not the other. By the above choice of Λ it is expected to give the best approximate description in this region. Further, if the third scale E_γ^{max} exceeds Λ, real radiation, in the present ansatz always described using the phenomenological model, is able to resolve the final state meson, be it charged or neutral, as well. However, even if a considerable fraction is radiated at scales above Λ, this should have only negligible effects on the total decay rate as the bulk of the radiation is in the region $k \to 0$ and, therefore, adequately described.

5.2.2 Short-distance next-to-leading order corrections

The well-known Standard Model Lagrangian is used in this study to describe the partonic $b \to x\,\ell\,\nu$ decay in the short-distance regime. A representative collection of relevant next-to-leading order corrections to the tree-level decay, involving the exchange of virtual photons, W and Z bosons as well as Higgs scalars, is depicted in Fig. 5.2. Besides vertex corrections to the b-x-W and ℓ-ν-W vertices, wave function and propagator corrections, box diagrams involving the additional exchange of a neutral γ, Z or h bosons between the hadronic and leptonic systems are present. These next-to-leading order corrections read, calculated in [107] within the current algebra framework and concentrating on the renormalisation of the bare Fermi coupling $\hat{G}_\mathrm{F}$ for this process, to leading logarithmic accuracy

$$\hat{\mathcal{M}}_{0,\mathrm{sd}}^1(\Lambda) \;=\; \frac{\alpha\,\hat{G}_\mathrm{F}}{4\pi}\left[3\ln\frac{m_W}{\Lambda} + 6\bar{Q}\ln\frac{m_W}{\Lambda} - 3\bar{Q}\ln\frac{m_W^2}{m_Z^2} + \ldots\right]\tilde{\mathcal{M}}_0^0\,, \tag{5.2.4}$$

with $\hat{\mathcal{M}}_0^0 = \hat{G}_\mathrm{F}\tilde{\mathcal{M}}_0^0$, i.e. the leading order matrix element stripped of the Fermi coupling constant, and $\bar{Q}$ being the average charge of the quark line. The ellipsis stands for non-logarithmic terms. For the photonic contributions an infrared regulator has been introduced

---

[2] The maximum photon energy for single photon radiation in the rest frame of a decaying particle is half its mass, neglecting all other decay products' masses. Allowing for massive decay products further reduces this kinematic limit.
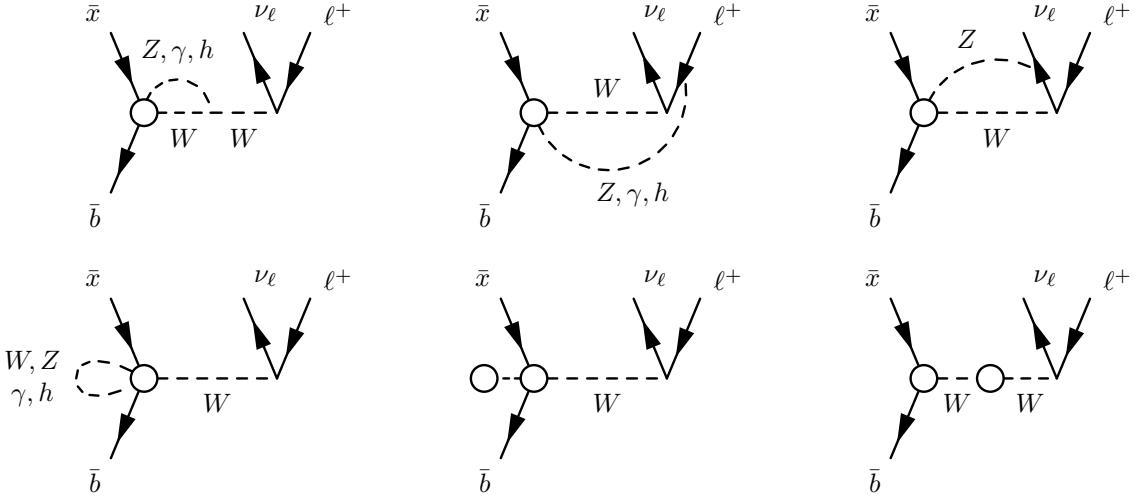
Figure 5.2: Representative Feynman diagrams of the Standard Model partonic decay $\bar{b} \to \bar{x}\,\ell^+\nu_\ell$ are shown. The white circles indicate hadronic contributions that are neglected in the short-distance expansion.

in the form of a photon mass $\Lambda \ll m_W$. Thus, the resulting matrix element has exactly the form required for the matching outlined in Section 5.2.1. The arising loop corrections are ultraviolet (UV) divergent and have been regularised in [107] by a UV cutoff set to m_W. Renormalisation of the parameters, again focusing on $\hat{G}_F$, is then achieved by comparison to the muon decay computed in the same computational framework, yielding the relation

$$G_F \;=\; \hat{G}_F \left[1 + \frac{3\alpha}{8\pi} \ln \frac{m_W^2}{m_Z^2} + \dots \right], \tag{5.2.5}$$

where G_F is now the renormalised Fermi decay constant as measured in the muon decay. This leads to the partonic short-distance virtual matrix element in the renormalised theory

$$
\begin{aligned}
\mathcal{M}^1_{0,\mathrm{sd}}(\Lambda) \;&=\; \frac{\alpha\,G_F}{4\pi} \left[3\ln \frac{m_W}{\Lambda} + 6\bar{Q}\ln \frac{m_W}{\Lambda} - \frac{3}{2}\left(1 + 2\bar{Q}\right)\ln \frac{m_W^2}{m_Z^2} + \dots \right] \tilde{\mathcal{M}}^0_0 \\
&=\; \frac{3\alpha}{4\pi}\left(1 + 2\bar{Q}\right)\ln \frac{m_Z}{\Lambda} \cdot \mathcal{M}^0_0\,,
\end{aligned}
\tag{5.2.6}
$$

where G_F has been reabsorbed into the leading order matrix element $\mathcal{M}^0_0$. In the case of semileptonic B decays $\bar{Q} = \frac{1}{2}|Q_{\bar{b}} + Q_{\bar{x}}| = \frac{1}{6}$, $x \in \{u,c\}$, this gives

$$\mathcal{M}^1_{0,\mathrm{sd}}(\Lambda) \;=\; \frac{\alpha}{\pi}\ln \frac{m_Z}{\Lambda} \cdot \mathcal{M}^0_0 \;+\; \dots. \tag{5.2.7}$$

The logarithm in eq. (5.2.7) then represents the leading logarithmic corrections to $\mathcal{O}(\alpha\,G_F)$ due to virtual particle exchange with (virtual) photon energies above Λ.
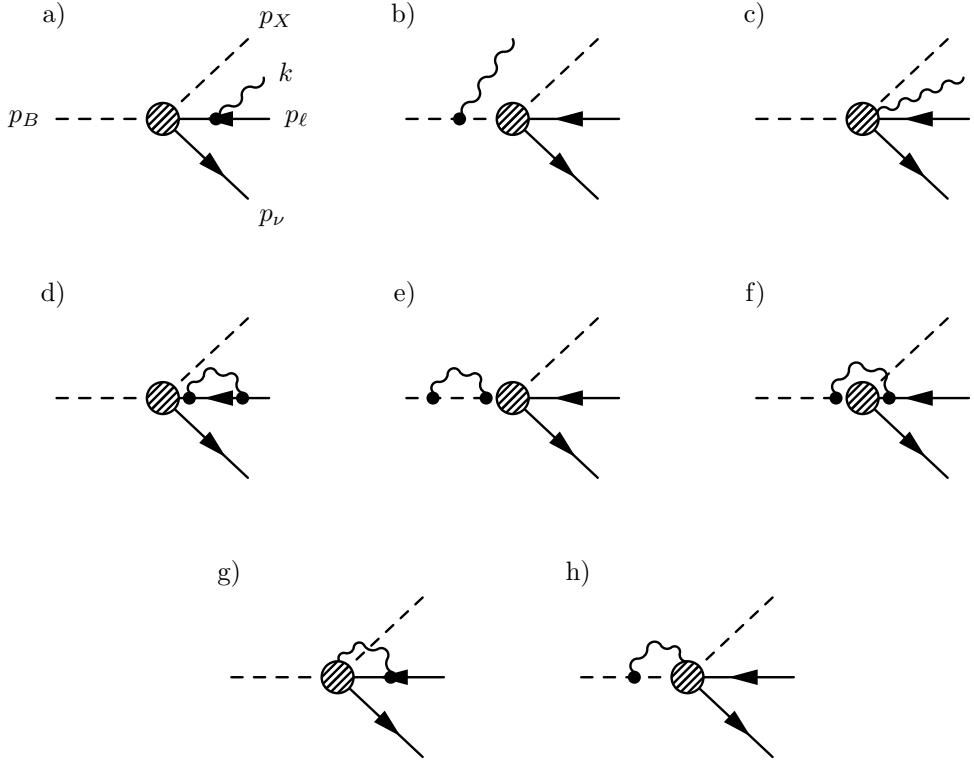
Figure 5.3: The Feynman diagrams for the next-to-leading order corrections
to $B^+ \to \bar{X}^0\,\ell^+\,\nu$ decays are shown.

5.2.3 Long-distance next-to-leading order corrections

The QED long-distance corrections to the phenomenological hadron decay can be calculated in an effective model that arises by requiring the phenomenological Lagrangian of the leading order decay to be invariant under local $U(1)_{\mathrm{em}}$ gauge transformations. Assigning the usual charges the following interaction terms in the Lagrangian arise in addition to eq. (5.1.1)

$$
\begin{aligned}
\mathcal{L}_{\mathrm{int,QED}} \;=\; & -eQ_\ell^-\bar{\psi}_\ell\gamma^\mu\psi_\ell A_\mu - ieQ_\phi A_\mu(\phi^+\partial^\mu\phi^- - \phi^-\partial^\mu\phi^+) + e^2 Q_\phi^2 A_\mu A^\mu\phi^+\phi^- \\
& + ie\sqrt{2}G_{\mathrm{F}}V_{xy}\mathrm{f}_\pm(Q_B \pm Q_X)\phi_B\phi_X A_\mu\,\bar{\psi}_\nu P_R\gamma^\mu\psi_\ell \;+\; \text{h.c.} \quad,
\end{aligned}
\tag{5.2.8}
$$

wherein the summation over $\phi \in \{\phi_B, \phi_X\}$ is implied. In addition to the point-like lepton-photon and meson-photon interactions, a vertex emission term arises. This term is connected to the bound-state nature of the meson. It is infrared finite and needed for gauge invariance. Further, in eq. (5.2.8) it is assumed that the meson-photon interaction is sufficiently described by scalar QED. Additional terms arise when moving away from this assumption, including intermediate lines of excited hadrons necessitating $X^* \to X\gamma$ vertices as well as contributions due to off-shell currents. These terms are discussed on general grounds in Section 5.2.4 and will be largely neglected in this study. This, in most cases, roots in their unavailability or, where known, in their smallness.

Figs. 5.3 and 5.4 depict the relevant real and virtual diagrams for $B^+ \to \bar{X}^0\,\ell^+\,\nu$ and $B^0 \to X^-\,\ell^+\,\nu$ decays at $\mathcal{O}(\alpha\,G_{\mathrm{F}})$. The real corrections diagrams a, b and c correspond to the emission of a real photon from either the charged legs of the decay, or the charged vertex itself. The virtual corrections group into three categories: diagrams d and e concern
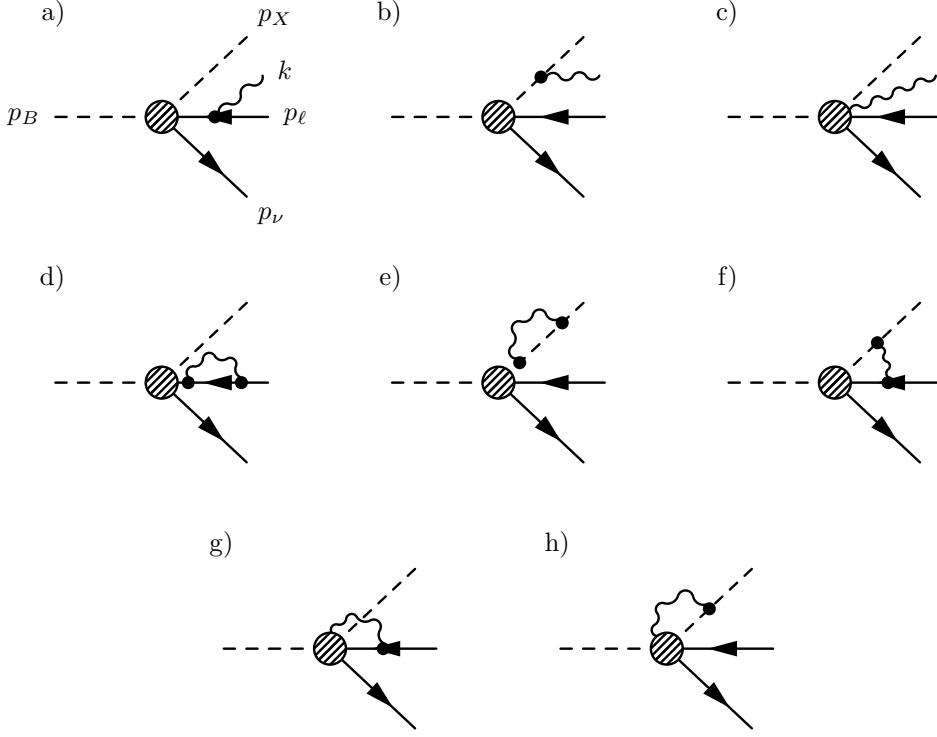
Figure 5.4: The Feynman diagrams for the next-to-leading order corrections to $B^0 \to X^- \ell^+ \nu$ decays are shown.

the wave-function renormalisation of the charged legs while diagram f is the dominant inter-particle photon exchange. Diagrams g and h are again due to emissions off the charged effective vertex and are, thus, infrared finite. The corresponding subtleties involving the vertex emissions are detailed in Appendix B.2.

In the virtual amplitude $\mathcal{M}^1_{0,\text{ld}}$ the arising ultraviolet divergences are regularised using the Pauli-Villars prescription [117] by introducing an unphysical heavy photon of mass Λ and opposite norm. Consequently, the virtual corrections have exactly the form required by the matching procedure outlined in Section 5.2.1 and all real emission processes are described in the long-distance picture.

Squaring the phenomenological real and virtual matrix elements results in the real and virtual next-to-leading order differential rates. In the B meson rest frame they read

$$\mathrm{d}\Gamma^1_1 = \frac{1}{(2\pi)^{12}} \frac{\mathrm{d}^3 p_X}{E_X} \frac{\mathrm{d}^3 p_\ell}{E_\ell} \frac{\mathrm{d}^3 p_\nu}{E_\nu} \frac{\mathrm{d}^3 k}{E_k} \, \delta^{(4)}\big(p_B - p_X - p_l - p_\nu - k\big) \left|\mathcal{M}^{\frac{1}{2}}_{1,\text{ld}}\right|^2 ,$$

$$\mathrm{d}\Gamma^0_0 + \mathrm{d}\Gamma^1_0 = \frac{1}{64\,\pi^3 m_B} \left(\left|\mathcal{M}^0_0\right|^2 + 2\mathcal{R}e\big[\mathcal{M}^0_0 \mathcal{M}^{1*}_{0,\text{ld}}(\Lambda)\big] + 2\left|\mathcal{M}^0_0\right|^2 \frac{\alpha}{\pi} \ln\frac{m_Z}{\Lambda} \right) \mathrm{d}E_X\,\mathrm{d}E_\ell .$$

$$(5.2.9)$$

Integrating eqs. (5.2.9) results in the next-to-leading order total decay rate. Comparing with the total tree-level decay rate, the integral over phase-space of eq. (5.1.5), yields the long-distance enhancement factor δ_{ld} due to next-to-leading order effects. It is

$$\Gamma = (1 + \delta_{\text{sd}} + \delta_{\text{ld}})\,\Gamma^0_0 = \Gamma^0_0 + \Gamma^1_0 + \Gamma^1_1 + \mathcal{O}(\alpha^2\, G_{\text{F}}) . \qquad (5.2.10)$$

with $\delta_{\rm sd} = \frac{2\alpha}{\pi} \ln \frac{m_Z}{\Lambda}$ from eq. (5.2.7). The exact form of the next-to-leading order matrix elements can be found in Appendix B.2.

5.2.4 Structure dependent terms

This section discusses the arising additional electromagnetic next-to-leading order corrections that cannot be grasped by simply replacing $\partial_\mu \to D_\mu$ to arrive at a $U(1)_{\rm em}$ gauge invariant phenomenological Lagrangian, as was described in the previous section. These include both deviations arising from the point-like meson-photon interaction assumed above and additional terms arising in the interaction of an off-shell hadronic current. Nonetheless, it is clear that in the relevant phase space region for the total inclusive decay rate, namely the region as $k \to 0$ near the infrared divergence, both the real and virtual next to leading order matrix elements are completely determined by the leading order decay, and the above procedure accurately reproduces the full theory in this region [106, 75, 118]. Hence, the real emission squared amplitude in this limit reads

$$\left|\mathcal{M}_1^{\frac{1}{2}}\right|^2 \overset{k \to 0}{=} -e^2 \left(\frac{p_M}{k \cdot p_M} - \frac{p_\ell}{k \cdot p_\ell} \right)^2 \left|\mathcal{M}_0^0\right|^2 \qquad \text{with } p_M \in \{p_B, p_X\}\,, \tag{5.2.11}$$

depending on whether B or X is charged. Physically this roots in the fact that the wavelength of an infinitely soft photon is much larger than the size of any strongly bound hadron. It, thus, cannot resolve its substructure and effectively interacts with its summed, then point-like charge. Further, such soft photons cannot push the hadronic current significantly off-shell, such that off-shell current interactions cannot become sizeable.

Introducing non-point-like meson-photon interactions does not only lead to corrections due to the hadron's size and its internal charge distribution, it also leads to additional vertices of the type $X \to X^*\gamma$, where X^* is a higher resonance of the X meson. This necessarily also introduces additional terms in the interaction of the hadronic and the leptonic current, especially if the resonance differs in its spin. B^* resonances in the initial state occur in the unphysical region. Hence, they are only relevant if their width is comparable to, or larger than, the mass separation $m_B^2 - m_{B^*}^2$ to the initial state B meson. In contrast, D^* resonances, for example, occurring in a final state line are allowed to be on-shell for a range of photon energies. Thus, a considerable correction may arise. [119] find the $D^{*+} \to D^+\gamma$ coupling to be compatible with zero while the $D^{*0} \to D^0\gamma$ coupling is small, but considerable. Both are considered and discussed in detail in Section 5.4.3.

Generally, following the argumentation of [120, 121] the electromagnetic current of the hadronic system can be split into two components: *inner-bremsstrahlung* (IB) contributions, which account for photon radiation from the external charged particles and are completely determined by the non-radiative process, and *structure-dependent* (SD) contributions, which describe intermediate hadronic states and represent new information with respect to the IB contributions.

The amplitude of a semileptonic B meson decay with full electromagnetic corrections reads

$$\mathcal{A}_\nu = i\,e\,\frac{G_{\rm F}}{\sqrt{2}} V_{\rm xb}\,\bar{u}_\nu\,P_{\rm R}\gamma^\mu \left(-\frac{H_\mu}{2p_\ell \cdot k} \left(\gamma_\nu \slashed{k} + 2p_{\ell,\nu}\right) + V_{\mu\nu} - A_{\mu\nu} \right) v_\ell\,, \tag{5.2.12}$$

with the hadronic current H_μ, as introduced in eq. (5.1.3). The hadronic vector and axial form factors of the photon-emitting hadronic current, incorporating among others the $X \to X^*\gamma$ coupling, are given by the unknown non-local operator

$$V_{\mu\nu} - A_{\mu\nu} = \int {\rm d}^4x\,e^{i\,k\cdot x}\,\langle X|T\,[\hat{h}_\mu(0)\,J_\nu^{\rm em}(x)]\,|B\rangle\,. \tag{5.2.13}$$

$J_\nu^{\rm em}$ denotes the electromagnetic current, $\hat{h}_\mu$ the quark-current in position-space and k is the photon momentum. The vector and axial-vector operators of eq. (5.2.13) obey the electromagnetic Ward-identities, obtained by contracting $k^\nu A_\nu$ of eq. (5.2.12),

$$
\begin{aligned}
k^\nu V_{\mu\nu} &= H_\mu\,, \\
k^\nu A_{\mu\nu} &= 0\,.
\end{aligned}
\tag{5.2.14}
$$

These properties of the individual pieces of the amplitude in conjunction with Low's theorem [106, 118] lead to the fact, that the leading terms of next-to-leading order amplitude in powers of the photon four-momentum k, i.e. the terms proportional to k^{-1} and k^0, are completely determined by the on-shell form factors of the tree-level decay.

Following [120], corrections beyond $\mathcal{O}(k^0)$ can be included by separating the non-local operator eq. (5.2.13) into SD and IB contributions. Since the IB and SD describe different physical mechanisms they are separately gauge invariant. Further, the SD amplitude must be of $\mathcal{O}(k)$ or higher. This, however, does not prevent the IB amplitude from containing terms of $\mathcal{O}(k)$ and higher as well.

Splitting the amplitude under these restrictions allows more terms to be collected in the IB part, still using only the knowledge of the non-radiative matrix element. This offers the advantage to obtain more precise predictions for the decay process, without formulating the (mostly unknown) SD contributions. The splitting of the transition matrix element requires a corresponding splitting of the non-local operator eq. (5.2.13) into SD and IB parts.

The axial contributions are strictly zero for photons emitted from the B- or X-meson, and therefore can be considered purely SD. They can be written in the form [122]

$$
\begin{aligned}
A_{\mu\nu} = A_{\mu\nu}^{\rm SD} = {}&- i\,\epsilon_{\mu\nu\rho\sigma}\Big[A_1\,p_X^\rho\,k^\sigma + A_2\,k^\rho\,(p_\ell + p_\nu)^\sigma\Big] \\
&- i\,\epsilon_{\nu\lambda\rho\sigma}\,p_X^\lambda\,k^\rho\,(p_\ell + p_\nu)^\sigma\Big[A_3\,(p_\ell + p_\nu)_\mu + A_4\,p_\mu\Big]\,.
\end{aligned}
\tag{5.2.15}
$$

Note that the Lorentz-invariant scalars A_i are non-singular in the limit $k \to 0$ by construction and are functions of the three independent scalar variables that can be built with p_B, p_X and k. The decomposition of the vector current reads

$$
V_{\mu\nu} = V_{\mu\nu}^{\rm IB} + V_{\mu\nu}^{\rm SD}\,,
\tag{5.2.16}
$$

where the IB piece is chosen in such a way, that

$$
\begin{aligned}
k^\nu V_{\mu\nu}^{\rm IB} &= H_\mu \\
k^\nu V_{\mu\nu}^{\rm SD} &= 0\,.
\end{aligned}
\tag{5.2.17}
$$

Herein, $V_{\mu\nu}^{\rm IB}$ can be constructed from leading order information only, cf. Appendix B.2. The SD vector contributions, on the other hand, contain additional information. They can be written as [123]

$$
\begin{aligned}
V_{\mu\nu}^{\rm SD} = {}&V_1\Big[k_\mu\,p_{X\nu} - (p\cdot k)\,g_{\mu\nu}\Big] + V_2\Big[k_\mu(p_\ell + p_\nu)_\nu - (k\cdot(p_\ell + p_\nu))g_{\mu\nu}\Big] \\
&+ V_3\Big[(k\cdot(p_\ell + p_\nu))(p_\ell + p_\nu)_\mu\,p_{X\nu} - (p_X\cdot k)(p_\ell + p_\nu)_\mu(p_\ell + p_\nu)_\nu\Big] \\
&+ V_4\Big[(k\cdot(p_\ell + p_\nu))(p_{X\mu}\,p_{X\nu} - (p_X\cdot k)\,p_{X\mu}(p_\ell + p_\nu)_\nu\Big]\,,
\end{aligned}
\tag{5.2.18}
$$

where the Lorentz-invariant scalars V_i are functions of the three independent scalar variables that can be built with p_B, p_X and k. All IB and SD contributions are finite as $k \to 0$. Consequently, as noted in [124, 125], terms of $\mathcal{O}(k)$ and higher can be shifted from the IB into the SD contributions.

The knowledge of the full SD contributions for semileptonic B meson decays is modest: [124] discusses the matter for $B \to \pi \ell \nu \gamma$ decays, using the soft-collinear effective theory to isolate the expressions for the SD contributions in the soft-pion and hard-photon part of phase-space. Section 5.4.3 compares their findings with the pure IB result from this study. The differences are non sizable. The recent work of [121] addresses the real SD corrections to $B \to D \ell \nu \gamma$ decays by using lattice results of the $D^* \to D \gamma$ coupling to estimate the dominant SD contributions when the D^* is on-shell. Section 5.4.3 also compares these SD contribution with the complete SD+IB picture. Again the differences turn out to be non sizable. The SD corrections to $B \to D_0^* \ell \nu \gamma$ are unknown, but given the large widths of the D_0^* and D_1^* states a non-negligible correction to the pure IB prediction can be expected.

Summarising, the decay amplitude can be separated as

$$
\begin{aligned}
\mathcal{A}_\nu &= i\, e\, \frac{G_F}{\sqrt{2}} V_{\rm xb}\, \bar{u}_\nu\, P_R \gamma^\mu \left(-\frac{H_\mu}{2 p_\ell \cdot k} \left(\gamma^\rho \slashed{k} + 2 p_\ell^\rho \right) + V_{\mu\nu}^{\rm IB} \right) v_\ell \\
&\quad + i\, e\, \frac{G_F}{\sqrt{2}} V_{\rm xb}\, \bar{u}_\nu\, P_R \gamma^\mu \left(V_{\mu\nu}^{\rm SD} - A_{\mu\nu}^{\rm SD} \right) v_\ell \,.
\end{aligned}
\tag{5.2.19}
$$

Therein, the first line collects all terms that can be derived from the leading order decay supplemented with local gauge invariance under the QED gauge group (assuming point-like hadrons). $V_{\mu\nu}^{\rm IB}$, as outlined in Appendix B.2, then contains the minimal terms to restore gauge invariance: besides the vertex emission terms of the constant form factor Lagrangian of eq. 5.2.8 additional terms arise from the generalisation to variable, momentum transfer-dependent form factors.

In contrast, the structure-dependent terms of the second line cannot be inferred from the leading order decay and QED gauge invariance. They have to be calculated separately for every decay mode and are mostly unknown. At the same time they vanish as the external photon's momentum $k \to 0$.

5.2.5 Soft-resummation and inclusive exponentiation

This section discusses a systematic improvement of the fixed order results discussed in the previous section. It briefly summarises the result of Chapter 2. Centring on the exponentiability of soft-radiative corrections and following the approach of Yennie, Frautschi and Suura [75], the fully inclusive decay rate

$$
\Gamma = \frac{1}{2M} \sum_{n_R=0}^{\infty} \frac{1}{n_R!} \int \mathrm{d}\Phi_{p_f} \mathrm{d}\Phi_k (2\pi)^4 \delta^4 \left(p_B - p_X - p_\ell - p_\nu - \sum k \right) \left| \sum_{n_V=0}^{\infty} \mathcal{M}_{n_R}^{n_V + \frac{1}{2} n_R} \right|^2
\tag{5.2.20}
$$

can be rewritten as

$$
\begin{aligned}
\Gamma = \frac{1}{2M} \sum_{n_R=0}^{\infty} \frac{1}{n_R!} &\int \mathrm{d}\Phi_{p_f} \mathrm{d}\Phi_k' (2\pi)^4 \delta^4 \left(p_B - p_X - p_\ell - p_\nu - \sum k \right) \\
&\times e^{Y(\Omega)} \prod_{i=1}^{n_R} \tilde{S}(k_i) \Theta(k_i, \Omega) \left(\tilde{\beta}_0^0 + \tilde{\beta}_0^1 + \sum_{i=1}^{n_R} \frac{\tilde{\beta}_1^1(k_i)}{\tilde{S}(k_i)} + \mathcal{O}(\alpha^2) \right)
\end{aligned}
\tag{5.2.21}
$$

by separating the universal spin-independent infrared divergent terms from the virtual and real emission amplitudes. $\mathrm{d}\Phi_{p_f}$ and $\mathrm{d}\Phi_k$ are the leading order and (multiple) extra emission phase space elements, while n_R and n_V count the additional real and virtual photons present in each amplitude. Therefore, using the same convention as before the sub- and superscripts of the (squared) matrix elements $\mathcal{M}$, M and $\tilde{\beta}$ denote their real emission photon multiplicity and their order of α in the perturbative expansion relative to the leading order.

The separation of infrared divergences proceeds by splitting

$$\mathcal{M}_0^1 = \alpha B \mathcal{M}_0^0 + M_0^1, \tag{5.2.22}$$

$$\frac{1}{2(2\pi)^3}\left|M_1^{\frac{1}{2}}\right|^2 = \tilde{S}(k)\left|M_0^0\right|^2 + \tilde{\beta}_1^1(k), \tag{5.2.23}$$

wherein M_0^1 and $\tilde{\beta}_1^1(k)$ are free of any infrared singularities due to virtual or real photon emissions. This separation can be continued iteratively, leading to

$$\left|\sum_{n_V=0}^{\infty}\mathcal{M}_{n_R}^{n_V+\frac{1}{2}n_R}\right|^2 = \exp(2\alpha B)\left|\sum_{n_V=0}^{\infty}M_{n_R}^{n_V+\frac{1}{2}n_R}\right|^2. \tag{5.2.24}$$

and

$$\left(\frac{1}{2(2\pi)^3}\right)^{n_R}\left|\sum_{n_V=0}^{\infty}M_{n_R}^{n_V+\frac{1}{2}n_R}\right|^2$$

$$= \tilde{\beta}_0\prod_{i=1}^{n_R}\left[\tilde{S}(k_i)\right] + \sum_{i=1}^{n_R}\left[\frac{\tilde{\beta}_1(k_i)}{\tilde{S}(k_i)}\right]\prod_{j=1}^{n_R}\left[\tilde{S}(k_j)\right] + \sum_{\substack{i,j=1\\i\neq j}}^{n_R}\left[\frac{\tilde{\beta}_2(k_i,k_j)}{\tilde{S}(k_i)\tilde{S}(k_j)}\right]\prod_{l=1}^{n_R}\left[\tilde{S}(k_l)\right] + \ldots$$

$$+ \sum_{i=1}^{n_R}\left[\tilde{\beta}_{n_R-1}(k_1,\ldots,k_{i-1},k_{i+1},\ldots,k_{n_R})\,\tilde{S}(k_i)\right] + \tilde{\beta}_{n_R}(k_1,\ldots,k_{n_R}), \tag{5.2.25}$$

with $\tilde{\beta}_{n_R} = \sum_{n_V=0}^{\infty}\tilde{\beta}_{n_R}^{n_V+n_R}$. Note that for a given phase space phase space configuration $\{p_1,\ldots,p_n,k_1,\ldots,k_{n_R}\}$ the infrared subtracted squared matrix elements $\tilde{\beta}_1(k_i)$ involve a projection onto the single emission subspace $\{\mathcal{P}p_1,\ldots,\mathcal{P}p_n,\mathcal{P}k_i\}$. Of course, momentum conservation holds for each projected subset. Thus, for every radiated photon the $\tilde{\beta}_1(k_i)$ are evaluated as if this photon was the only one in the event. Hence, truncating the perturbative series in the $\tilde{\beta}_{n_R}$ at the next-to-leading order leaves every single photon emission correct at $\mathcal{O}(\alpha)$.

Exponentiating the integral of the eikonal $\tilde{S}(k)$ upon insertion of the identity of eq. (5.2.25) over the unresolved phase space Ω, containing the infrared singularity gives rise to the Yennie-Frautschi-Suura form factor

$$Y(\Omega) = 2\alpha(B+\tilde{B}(\Omega)) \qquad \text{with} \qquad 2\alpha\tilde{B}(\Omega) = \int_\Omega\frac{\mathrm{d}^3k}{k}\,\tilde{S}(k) \tag{5.2.26}$$

and the residual perturbative series of the infrared-subtracted squared amplitudes $\tilde{\beta}_{n_R}^{n_V+n_R}$ in eq. (5.2.21). Hence, photon emissions contained in the unresolved soft region Ω are assumed to have a negligible effect on differential distributions, but are included in the overall normalisation. Furthermore, $Y(\Omega)$ is UV-finite and, thus, does not interfere with renormalisation of the $\tilde{\beta}_{n_R}^{n_V+n_R}$.

5.3   Methods

In this section a short overview over the generators used in this study and their underlying principles is given.

5.3.1   BLOR

BLOR [115] is a fixed order Monte Carlo Event generator specialised on QED corrections in semileptonic B meson decays. It separately generates decays for the born $(1 \to 3)$ and real emission $(1 \to 4)$ phase space events according to their individual cross sections

$$
\begin{aligned}
\mathrm{d}\Gamma_{1\to3} &= \mathrm{d}\Gamma_0^0 + \mathrm{d}\Gamma_0^1 \\
\mathrm{d}\Gamma_{1\to4} &= \mathrm{d}\Gamma_1^1 \,.
\end{aligned}
\tag{5.3.1}
$$

The infrared divergences present in $\mathrm{d}\Gamma_0^1$ and $\mathrm{d}\Gamma_1^1$ are regulated introducing a small but finite photon mass λ set to 10^{-7}GeV. The expressions of Section 5.2 are altered accordingly.

5.3.2   SHERPA/PHOTONS++

The SHERPA Monte Carlo [8], briefly described in Chapter 1, is a complete event generation frame work for high energy physics processes. Although its traditional strengths lie in the perturbative aspects of lepton and hadron colliders it also encompasses several modules for all non-perturbative aspects. In this work the hadron decay module HADRONS++ [73] and the universal higher order QED correction tool PHOTONS++ [86, 74] are used. The implementation of PHOTONS++ was described in detail in Section 3.1 and shall be briefly revisited here in the present context.

HADRONS++ generates the leading order decay events according to the respective form factor parametrisations of the involved hadronic and leptonic currents. PHOTONS++ then rewrites the differential all orders inclusive decay width of eq. (5.2.21) as

$$
\Gamma = \Gamma_0 \sum_{n_\gamma} \frac{1}{n_\gamma!} \int \mathrm{d}\Phi_k \, J_{\mathrm{P}}(k) \, e^{Y(\Omega)} \prod_{i=1}^{n_\gamma} \left[\tilde{S}(k_i)\Theta(k_i,\Omega) \right] \left(1 + \frac{\tilde{\beta}_0^1}{\tilde{\beta}_0^0} + \sum_{i=1}^{n_R} \frac{\tilde{\beta}_1^1(k_i)}{\tilde{\beta}_0^0 \cdot \tilde{S}(k_i)} + \mathcal{O}(\alpha^2) \right),
\tag{5.3.2}
$$

cf. [74]. Hence, the leading order input is corrected both for soft photon effects to all orders and hard photon emission to an arbitrary order. $J_{\mathrm{P}} \le 1$ represents the various Jacobians occurring when factoring out the leading order term. The perturbative series in the infrared-subtracted squared matrix elements includes only terms up to $\mathcal{O}(\alpha)$ for this study. The QED real emission squared amplitudes can alternatively be approximated using Catani-Seymour splitting function [51, 94, 52]

$$
\tilde{\beta}_{1,\mathrm{CS}}^1(k) = -\frac{\alpha}{4\pi^2} \sum_{i<j} Z_i Z_j \theta_i \theta_j \left(\bar{g}_{ij}(p_i,p_j,k) + \bar{g}_{ji}(p_j,p_i,k) \right) \tilde{\beta}_0^0 \,,
\tag{5.3.3}
$$

where in i and j run over all particles in the process. The exact form of the $\bar{g}_{ij}$ can be found in [74]. This approximation is also used if the exact real emission matrix element is not known.

The infrared cut-off was set to 10^{-6}GeV in the rest frame of the charged dipole, i.e. the $B^+ - \ell^+$ or the $X^- - \ell^+$ system, respectively.

5.3.3 PHOTOS

The PHOTOS Monte Carlo [87] is an "after-burner" algorithm, which adds approximate bremsstrahlung corrections to leading order events produced by an external code. In this study it is taken as a reference for the differential distributions since it is widely in use. PHOTOS bases on the factorisation of the real emission matrix element in the collinear limit

$$\left|\mathcal{M}_1^{\frac{1}{2}}\right|^2 \;=\; \sum_i \left|\mathcal{M}_0^0\right|^2 \cdot\; f(p_i, k)\,. \tag{5.3.4}$$

The radiation function $f(p_i, k)$ is given to leading logarithmic accuracy. It incorporates the Altarelli-Parisi emission kernel for radiation off the particular final state particle. Its exact form is spin dependent and can be found in [87, 76]. In its exponentiated mode the number of photons follows a Poisson distribution, while the individual photon's kinematics are determined by applying above equation iteratively. To also recover the soft limit of real photon emission matrix elements an additional weight was introduced [126]

$$W_{\text{soft}} \;=\; \frac{\displaystyle\sum_{i=1}^{n_\gamma}\left|\sum_{j=1}^{n_C} Q_j \frac{p_j\cdot\epsilon_i^*}{p_j\cdot k_i}\right|^2}{\displaystyle\sum_{i=1}^{n_\gamma}\sum_{j=1}^{n_C} Q_j^2 \left|\frac{p_j\cdot\epsilon_i^*}{p_j\cdot k_i}\right|^2}\,, \tag{5.3.5}$$

wherein n_γ and n_C are the photon and the final state charged multiplicity of the process. To regularise the emission function in the soft limit an energy cut-off is imposed in the rest frame of the decaying particle. The collinear divergence is regularised by the emitter's mass.

Initial state radiation is not accounted for as the mass of the decaying particle is the largest scale in the process and there are no associated collinear divergences or logarithmic enhancements. It could only be accounted for by supplementing PHOTOS with a matrix element correction. In case of heavy initial states eq. (5.3.5) still approximately recovers the soft limit.

In this analysis PHOTOS version 2.13 has been used in its exponentiated mode, including the soft interference terms. The infrared cut-off was set to $10^{-7}m_{B^{0,+}}$, respectively. BLOR supplemented the leading order decay events.

5.4 Results

In this section the results of the inclusion of the complete next-to-leading order corrections, both real and virtual short and long distance contributions, for various semileptonic B decay modes, focusing on the $B \to D$ decay channels, are reviewed and examined in detail. However, also results on the $B \to D_0^*$ and $B \to \pi$ are shown.

First, results for the next-to-leading order inclusive decay rates and their effects on the extraction of $|V_{\text{cb}}|$ from decay measurements will be shown in Section 5.4.1. Albeit not central to this thesis, the results for the $B \to D_0^*$ and $B \to \pi$ decay modes also contain implications on the extraction of $|V_{\text{cb}}|$ and $|V_{\text{ub}}|$. Then, in Section 5.4.2 the effects on differential distributions and spectra are investigated and compared against the standard tool used in many experimental analyses, PHOTOS. The parameters used are detailed in Table 5.1.

Parameter	Value		Parameter	Value
$m_{\Upsilon(4S)}$	10.5794 GeV		m_e	0.0005109989 GeV
$\Gamma_{\Upsilon(4S)}$	20.5 MeV		m_μ	0.10565837 GeV
m_{B^0}	5.27950 GeV		m_{ν_e}	0
m_{B^+}	5.27913 GeV		m_{ν_μ}	0
m_{D^0}	1.86950 GeV		m_W	80.419 GeV
m_{D^-}	1.86484 GeV		α	1/137.035999
			G_{F}	$1.16637 \cdot 10^{-5}$ GeV^{-2}

Table 5.1: Parameters used for all inclusive and differential decay rate calculations. All particle widths, except the $\Upsilon(4S)$ width, are considered negligible.

5.4.1 Next-to-leading order corrections to decay rates

One key prediction of this thesis is the process specific correction factor for higher order electroweak effects. These higher order corrections enter measurements of the CKMmixing angles V_{xb} via

$$\Gamma_{\mathrm{measured}} = \eta_{\mathrm{QCD}}^2 \, \eta_{\mathrm{EW}}^2 \, |V_{\mathrm{xb}}|^2 \, \tilde{\Gamma}_{\mathrm{LO}} \,, \tag{5.4.1}$$

and, thus,

$$|V_{\mathrm{xb}}| = \frac{1}{\eta_{\mathrm{EW}}} \cdot \sqrt{\frac{\Gamma_{\mathrm{measured}}}{\eta_{\mathrm{QCD}}^2 \tilde{\Gamma}_{\mathrm{LO}}}} \,. \tag{5.4.2}$$

$\tilde{\Gamma}_{\mathrm{LO}}$ is the leading order phenomenological decay rate stripped of the CKMmixing angle. η_{QCD} and η_{EW} incorporate the higher order QCD and electroweak corrections. Both contributions factorise at the NLO level. The electroweak correction factor is determined in this study at NLO accuracy in the QED-improved phenomenological long-distance description of the hadronic decay and at leading logarithmic accuracy in the underlying short-distance partonic decay in the Standard Model. While the leading logarithm of the short-distance correction depends only on the matching scale Λ of both descriptions and is, thus, independent of the actual decay properties, the long-distance corrections, in contrast, are sensitive to exactly these specifics.

The resulting correction factors,

$$\eta_{\mathrm{EW}}^2 = 1 + \delta_{\mathrm{sd}} + \delta_{\mathrm{ld}} = 1 + \frac{\Gamma_0^1 + \Gamma_1^1}{\Gamma_0^0} + \mathcal{O}(\alpha^2) \tag{5.4.3}$$

are a central outcome of this study. They are presented in Tab. 5.2 for the different semileptonic decay channels of charged and neutral B mesons into D mesons. As is evident, the long-distance QED corrections break the strong isospin symmetry. This originates in the different masses of the charged mesons in the strong isospin rotated decays. These masses both determine the amount of radiation from the meson line and enter the loop integrals. On the other hand, the difference in the size of the correction between the two leptonic channels of each decay mode is only very small since both masses are insignificant compared to the hadronic mass scales.

	η_{EW}^2	$1/\eta_{\text{EW}}$
$B^0 \to D^- \, e^+ \, \nu_e \, (\gamma)$	$1.0222(1 \pm 2 \pm 17 \pm 1)$	$0.9891(1 \pm 1 \pm 4 \pm 1)$
$B^0 \to D^- \, \mu^+ \, \nu_\mu \, (\gamma)$	$1.0222(1 \pm 2 \pm 17 \pm 1)$	$0.9891(1 \pm 1 \pm 4 \pm 1)$
$B^+ \to \bar{D}^0 \, e^+ \, \nu_e \, (\gamma)$	$1.0146(1 \pm 1 \pm 39 \pm 16)$	$0.9928(1 \pm 1 \pm 10 \pm 4)$
$B^+ \to \bar{D}^0 \, \mu^+ \, \nu_\mu \, (\gamma)$	$1.0147(1 \pm 1 \pm 39 \pm 16)$	$0.9927(1 \pm 1 \pm 10 \pm 4)$

Table 5.2: Predictions for $\eta_{\text{EW}} = \sqrt{1 + \delta_{\text{sd}} + \delta_{\text{ld}}}$ for the summed next-to-leading corrections are listed. The uncertainties in the parentheses are the sum of numerical, next-to-next-to-leading order, matching and missing structure dependent contributions.

	η_{EW}^2	$1/\eta_{\text{EW}}$
$B^0 \to D^- \, \ell \, \nu$	$1.0222(17)$	$0.9891(4)$
$B^+ \to D^0 \, \ell \, \nu$	$1.0146(43)$	$0.9928(10)$
$B \to D \, \ell \, \nu$	$1.0186(29)$	$0.9909(7)$

Table 5.3: Averaged integration results for $\eta_{\text{EW}}^2 = 1 + \delta_{\text{sd}} + \delta_{\text{ld}}$ and $1/\eta_{\text{EW}}$: The uncertainties in the parentheses are the sum of numerical, next-to-next-to-leading order, matching and missing structure dependent contributions.

The total uncertainty σ_{total} of the summed long- and short-distance correction is given by

$$\sigma_{\text{total}}^2 = \sigma_{\text{numerical}}^2 + \sigma_{\text{nnlo}}^2 + \sigma_\Lambda^2 + \sigma_{\text{SD}}^2 \,. \tag{5.4.4}$$

The leading uncertainty originates from the matching of the short- and long-distance results. Here, the mismatch of both theories, the Standard Model for the short-distance corrections and the QED-enhanced effective theory for the long-distance corrections, at the scale Λ, as discussed in Section 5.2.1, is the main source. These matching uncertainties are estimated choosing Λ of the scale of the final state meson's mass as a central value for Λ and then taking the difference to the result when using the scale 2Λ. Note that half the charged final state meson's mass is not a sensible choice for the matching scale since in this case a considerable fraction of the real radiation cross section would occur at scales greater than Λ and being described by the phenomenological model, thus ending up in the wrong picture.

Further, the effect of additional real short-distance contributions is studied by comparing the pure inner-bremsstrahlung calculation with the real emission results of [124] and [121]. And finally, the electroweak next-to-next-to-leading order effects are estimated as $\sigma_{\text{nnlo}} = \alpha \, (\delta_{\text{sd}} + \delta_{\text{ld}})$. It is clear that the complete model dependence from the phenomenological treatment of the long-distance contributions cannot be grasped with the above error estimation.

Tab. 5.3 presents the same results for $B \to D \, \ell \, \nu \, (\gamma)$ averaged over the different lepton species and the isospin rotated decays. The isospin averaged result is corrected for the difference in the production rate of B^0 and B^+ mesons, i.e.

$$\delta_{\text{sd}} + \delta_{\text{ld}} = \left(\delta_{\text{sd}} + \delta_{\text{ld}}^+\right) f_{+-} + \left(\delta_{\text{sd}} + \delta_{\text{ld}}^0\right) f_{00} \,, \tag{5.4.5}$$

with δ_{ld}^+ and δ_{ld}^0 the isospin breaking contributions for charged and uncharged charmed decays extracted from Tab. 5.2. The latter correction factor is the adequate choice to correct $|V_{\text{cb}}|$ from measurements demanding isospin.

Measurement	$\mathcal{G}(1)\,|V_{cb}| \times 10^{-3}$ with sd corrections only	$\mathcal{G}(1)\,|V_{cb}| \times 10^{-3}$ with sd and ld corrections
BaBar tagged [127]	42.30(2.36)	42.21(2.34)

Table 5.4: The impact of long-distance corrections on the correction factor η_{EW} is shown. The measurement estimates real next-to-leading order corrections via Photos and, thus, uses phase-space cuts and variables that provide a reduced sensitivity on the modeling of final state radiation. $\mathcal{G}(1)$ is the normalisation of the heavy quark form factor.

The impact of these correction factors on a selected measurement is listed in Tab. 5.4. Note that the measurement used Photos to estimate the effect on radiative corrections. Applying the stated factors only corrects the overall normalisation, differences due to changes in kinematic distributions, see Section 5.4.2, result in another correction for the extracted value of $|V_{cb}|$ that cannot be estimated here.

5.4.2 Next-to-leading order corrections to differential rates

In this section the results of both Blor and Sherpa/Photons++ are presented and compared against Photos. The focus lies on the absolute value of the spatial momentum of the produced meson and the lepton, i.e. $|\vec{p}_X|$ and $|\vec{p}_\ell|$. The chosen frame for these observables is the centre-of-momentum system of the electron and positron beam. Thus, the decaying B^0 and B^+ mesons already carry momentum corresponding to the $\Upsilon(4S) \to B^0\bar{B}^0$ and $\Upsilon(4S) \to B^+B^-$ decay kinematics. All quantities are shown as bare quantities, i.e. no recombination of photon and lepton/meson momenta was used. This is directly applicable if the charged particle momenta are extracted by measuring their curved tracks in a magnetic field or in photon-free calorimeters, as is the case in many BaBar and Belle analyses.

The prediction of each generator is normed to its inclusive decay width and the ratio plots show the relative difference

$$\Delta_O \;=\; \frac{\frac{1}{\Gamma_{\mathrm{tot},i}}\frac{\mathrm{d}\Gamma_i}{\mathrm{d}O} - \frac{1}{\Gamma_{\mathrm{tot,ref}}}\frac{\mathrm{d}\Gamma_{\mathrm{ref}}}{\mathrm{d}O}}{\frac{1}{\Gamma_{\mathrm{tot},i}}\frac{\mathrm{d}\Gamma_i}{\mathrm{d}O} + \frac{1}{\Gamma_{\mathrm{tot,ref}}}\frac{\mathrm{d}\Gamma_{\mathrm{ref}}}{\mathrm{d}O}} \tag{5.4.6}$$

to the Photos prediction for the given observable O in the given bin. Hence, the shortcomings of the approximations inherent in the standard tool currently used by most experiments are plainly visible. Further, due to the choice of normalisation, systematic errors, shown to be dominant in the previous section, are negligible here. Hence, the error bands shown are statistical errors only and are of comparable magnitude for all three generators predictions.

Decays $B \to D\,\ell\,\nu_\ell$

In Fig. 5.5 the predictions of all three generators for the decay $B^0 \to D^-\,e^+\,\nu_e$ using a form factor parametrisation from Heavy Quark Effective Theory, cf. Appendix B.1.1, are presented. For most of the phase space the agreement of the next-to-leading order shape is good. However, as can be seen in the absolute lepton momentum plot, Sherpa/Photons++
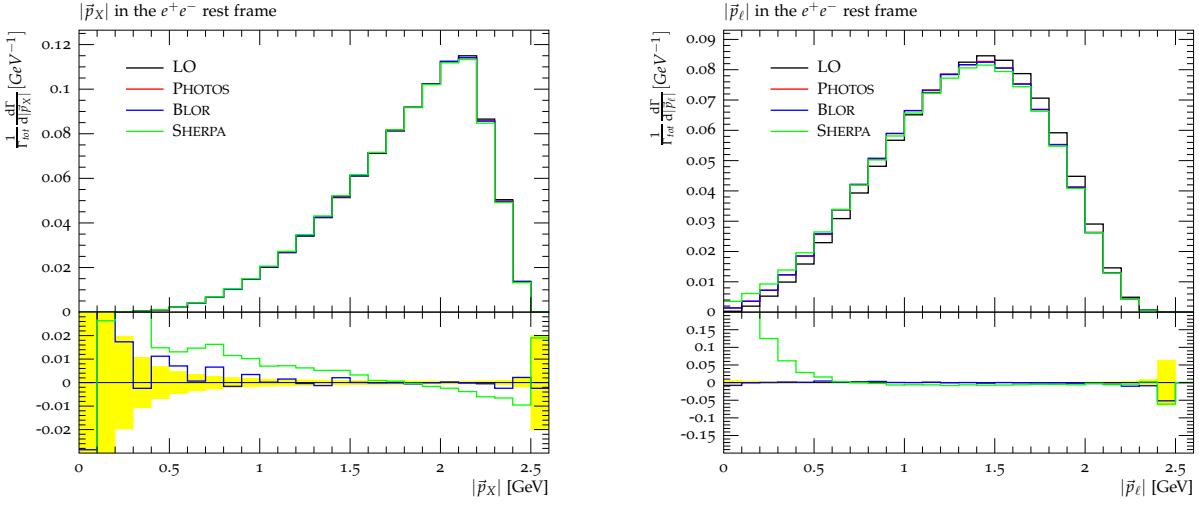
Figure 5.5: Lepton and meson momentum spectrum in the e^+e^- rest frame in the decay $B^0 \to D^- e^+ \nu_e$. All spectra are normed to the total inclusive decay width predicted by the respective generator. The ratio plot gives the relative deviation, bin by bin, of the predicted shapes with PHOTOS as reference. The shaded yellow area gives the statistical uncertainty of the reference distribution.
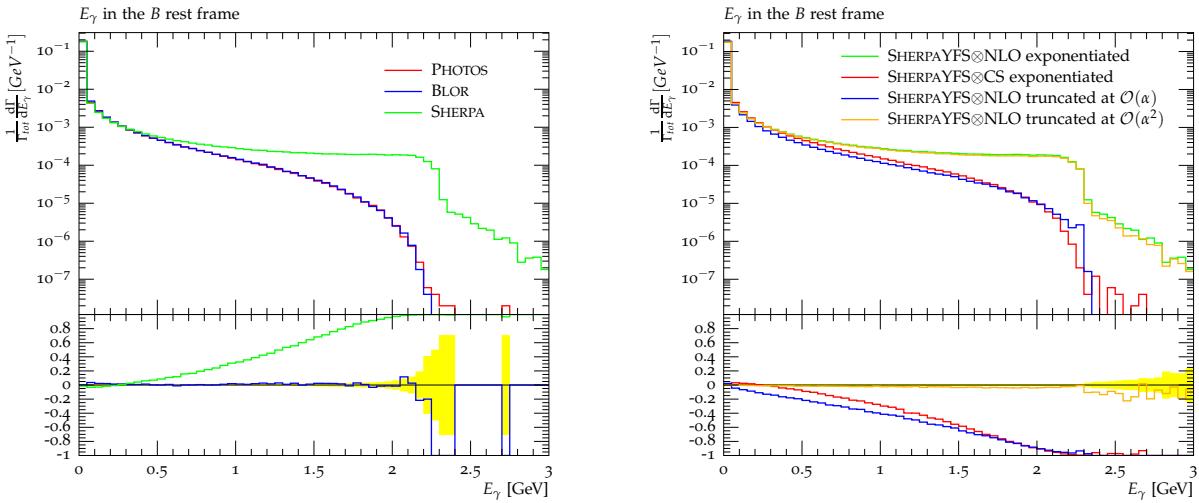
Figure 5.6: Total radiative energy loss, i.e. the sum of all photons radiated, in the decay $B^0 \to D^- e^+ \nu_e$ in the B rest frame. All spectra are normed to the total inclusive decay width predicted by the respective generator. The left panel shows the predictions of all three generators and the PHOTOS prediction is taken as the reference in the ratio plot. The right panel shows the predictions of SHERPA/PHOTONS++ in its full YFS⊗NLO exponentiated mode (green), a mode where the exact NLO matrix element of the perturbative expansion is replaced by universal Catani-Seymour dipole splitting kernels (red) and two modes where the exact real emission matrix elements are used, but the expansion in the resolved emission region is truncated at $\mathcal{O}(\alpha)$ (blue) and $\mathcal{O}(\alpha^2)$ (orange), thus allowing at most one and two photons, respectively. Here, the full exponentiated SHERPA/PHOTONS++ prediction is taken as reference in the ratio plot.
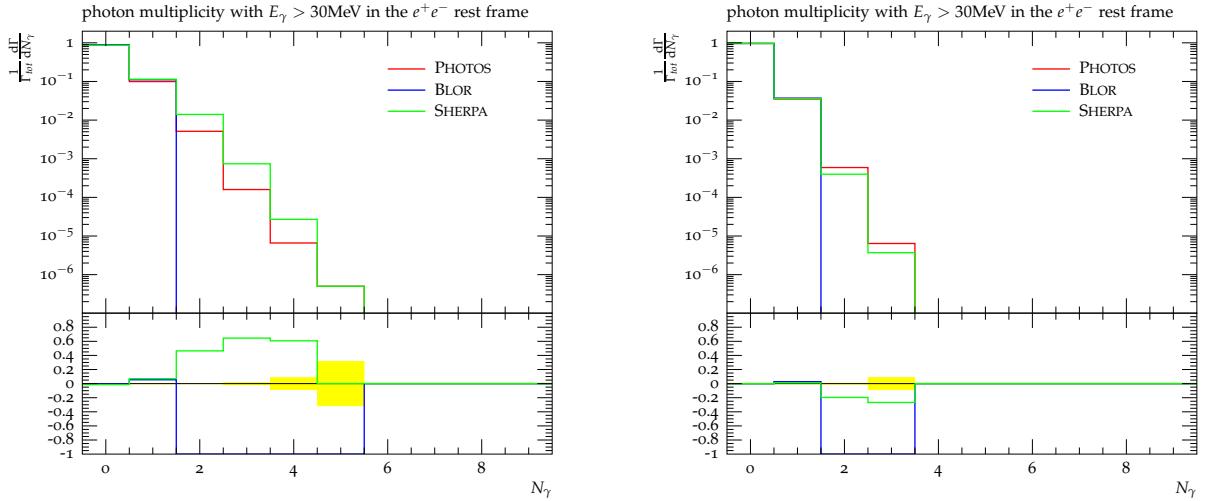
Figure 5.7: Multiplicities of photons with at least 30MeV in in the e^+e^- rest frame $B^0 \rightarrow D^- e^+ \nu_e$ on the right hand side and $B^0 \rightarrow D^- \mu^+ \nu_\mu$ on the left hand side. In the ratio plot PHOTOS was chosen as the reference.

predicts a slightly different shape close to $|\vec{p}_\ell|, |\vec{p}_X| = 0$. This limit cannot be measured directly in most experiments. Nonetheless, it influences the extrapolation to the full phase space, and thus determinations of total decay widths. In [128], for example, uncertainties related to such an extrapolation constituted up to 50% of the total experimental error. Further, the slight slope of the order of 1% exhibited in the prediction of SHERPA/PHOTONS++ for $|\vec{p}_X|$ is also present in the $|\vec{p}_\ell|$ spectrum. Both differences originate in the different modeling of radiative energy loss between the different programs, as shown in the following.

Fig. 5.6 displays the radiative energy loss, i.e. the sum of the energies of all photons radiated, in the rest frame of the decaying B^0. The predictions of the three different generators are shown in the left panel. For single photon emission in such a final state dipole there exists a kinematic limit on the photon's energy: $E_\gamma^{\max} = \frac{m_B}{2} \left(\frac{m_B}{m_X + m_\ell} - \frac{m_X + m_\ell}{m_B} \right)$ in the dipole's rest frame or $E_\gamma^{\max} = 2.3083 \text{GeV}$ in the B rest frame. This limit is clearly visible in Fig. 5.6. All events exceeding it, i.e. radiating more than $E_\gamma^{\max}$, must exhibit multi-photon radiation. Here (at least) two hard photons recoil against each other. Hence, this feature is present in both the SHERPA/PHOTONS++ and PHOTOS predictions, but not in the fixed order NLO prediction of BLOR. This tail is an $\mathcal{O}(\alpha^2)$ effect in the hard radiation and can only be described approximatively here. In PHOTOS it is described by an iteration of the emission kernels while SHERPA/PHOTONS++ describes this part of the spectrum by the next-to-leading order hard emission amplitude $\tilde{\beta}_1^1$ summed over all projections onto the single emission subspaces, cf. Section 5.2.5 and 5.3.2.

On the other hand, multi-photon radiation also enhances the amount of radiation in the region $E_\gamma < E_\gamma^{\max}$, if the probability of two relatively hard photons is sufficiently large. As exemplified in Fig. 5.7, in $B^0 \rightarrow D^- e^+ \nu_e$ double photon emission is relatively probable and, hence, leads to such an enhancement, whereas due to the much larger muon mass this feature is nearly absent in the decay to muons, Fig. 5.9. Of course, this enhancement of the radiative energy loss is an effect of $\mathcal{O}(\alpha^2)$ and can therefore only be described approximatively here.

Of equal importance as multi-photon radiation is the presence of the exact real emission matrix element, as is also shown in the right panel of Figs. 5.6 and 5.9. Approximating the real emission matrix elements with Catani-Seymour splitting functions, reproducing the

Altarelli-Parisi splitting functions used in PHOTOS in the (quasi-) collinear limit, leads to a mis-estimation of the radiative energy loss in the regime close to the kinematic boundary. It seems, however, that in the present cases collinearly approximated multi-photon emission mimics the exact fixed-order NLO behaviour reasonably well.

Close to the kinematic boundary on single photon emission, E_{max}, the vertex emission diagrams become important, as do the corrections for $t \neq t'$ (cf. Appendix B.2). These corrections have different sizes for the electron and muon channels due to their different masses and radiative properties. In principle, here also the structure-dependent corrections of Section 5.2.4 play a role. But, as is investigated in Section 5.4.3 they have negligible impact on the shape of the differential distributions. Thus, they can be safely neglected here.

Further, both SHERPA/PHOTONS++ and PHOTOS share a common soft limit, showing the compatibility of the inherent soft resummation of SHERPA/PHOTONS++ and the superimposed soft limit correction in PHOTOS. BLOR exhibits an (almost) constant off-set of a few percent owing to the lack of resummed contributions modeled in SHERPA/PHOTONS++ by virtue of the YFS form factor.

The lepton and meson spectra for $B^0 \to D^- \mu^+ \nu_\mu$ are shown in Fig. 5.8. Figs. 5.10 and 5.11 show strong isospin rotated processes $B^+ \to \bar{D}^0 e^+ \nu_e$ and $B^+ \to \bar{D}^0 \mu^+ \nu_\mu$, respectively. Thus, the radiating dipole is spanned between the initial state B^+ and the lepton. Radiation off the initial state meson is suppressed by its much larger mass, as compared to the D^-. Thus, multi-photon emission is also strongly suppressed. In these cases SHERPA/PHOTONS++ predict slightly smaller radiative corrections in the electron decay channel than either PHOTOS or BLOR. The differences are of the order of five percent; note that the scale was enlarged in the reference plot to better highlight the differences. These, to the largest extent, root in differences in the modeling of emission off the initial state charged meson.

Decays $B \to D_0^* \ell \nu_\ell$

The final state lepton and meson momentum spectra in the decays $B^{0,+} \to \bar{D}_0^{*-,0} \ell^+ \nu_\ell$, with $\ell = e, \mu$, are shown in Figs 5.12, 5.13, and 5.14, 5.15. The $B \to D_0^*$ transition current is modeled using Leibovich-Ligeti-Stewart-Wise-parametrised form factors, cf. Appendix B.1.3. Except for differences in the form factor parametrisations due to the D_0^* meson being a scalar instead of a pseudo-scalar and its higher mass, the effects of higher order corrections are comparable to the case of Section 5.4.2.

Decays $B \to \pi \ell \nu_\ell$

Figs. 5.16, 5.17 and 5.18, 5.19 show the decay channels into charged and neutral pions. The $B \to \pi$ transition current is modeled using the Ball-Zwicky form factor model described in Appendix B.1.2. Here, because of the comparably small mass of the charged pion effects due IB corrections for $t \neq t'$ become important. The structure-dependent contributions still have negligible impact on the differential distributions, as is shown in Section 5.4.3. Again, in the electron channel of the decay into a charged pion the correct treatment of hard multi-photon radiation, assuming they are sufficiently well described in the QED-enhanced phenomenological model, leads to comparably large deviations.

Nonetheless, it should be noted, as was also discussed earlier, that the matching procedure employed in this study runs into conceptual problems when applied to a $B \to \pi$ transition due to large difference between the hadronic mass scale $\Lambda = m_\pi$ and the maximal energy of an emitted photon, $E_\gamma^{\text{max}} = 2.6379\,\text{GeV}$ ($B^0 \to \pi^- e^+ \nu_e$). Consequently, a considerable fraction of the real emission phase space wherein the photon is able to resolve the pion is described by the effective theory only. Thus, the results obtained here should be considered with caution. However, they still are an improvement over the leading logarithmic corrections employed in standard analyses.
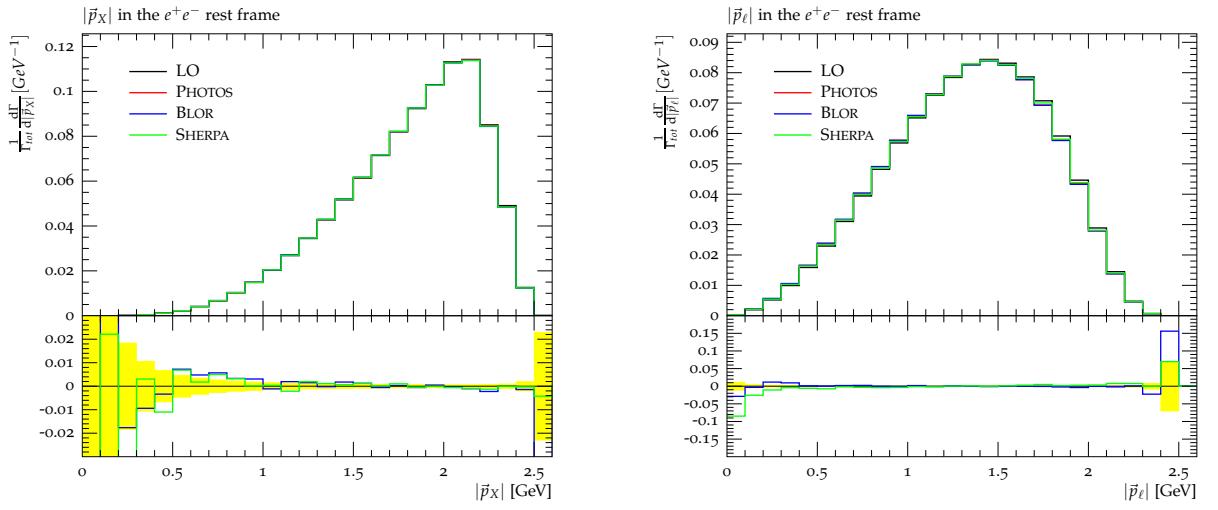
Figure 5.8: Lepton and meson momentum spectrum in the e^+e^- rest frame in the decay $B^0 \to D^- \mu^+ \nu_\mu$. The PHOTOS prediction is taken as the reference in the ratio plot.
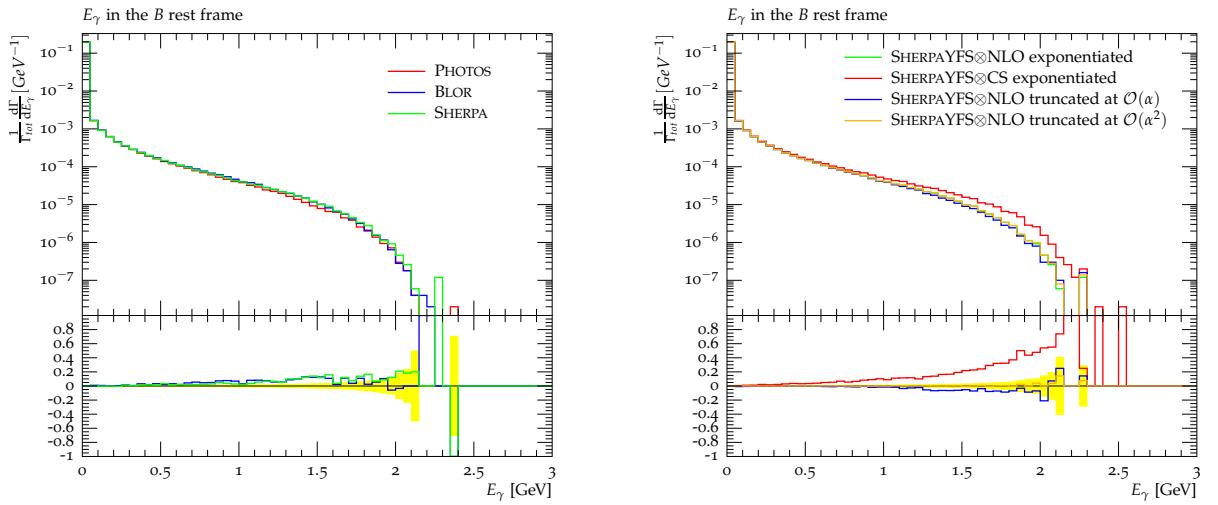

Figure 5.9: Total radiative energy loss, i.e. the sum of all photons radiated, in the decay $B^0 \to D^- \mu^+ \nu_\mu$ in the B rest frame. The labels are identical to those in Fig. 5.6.
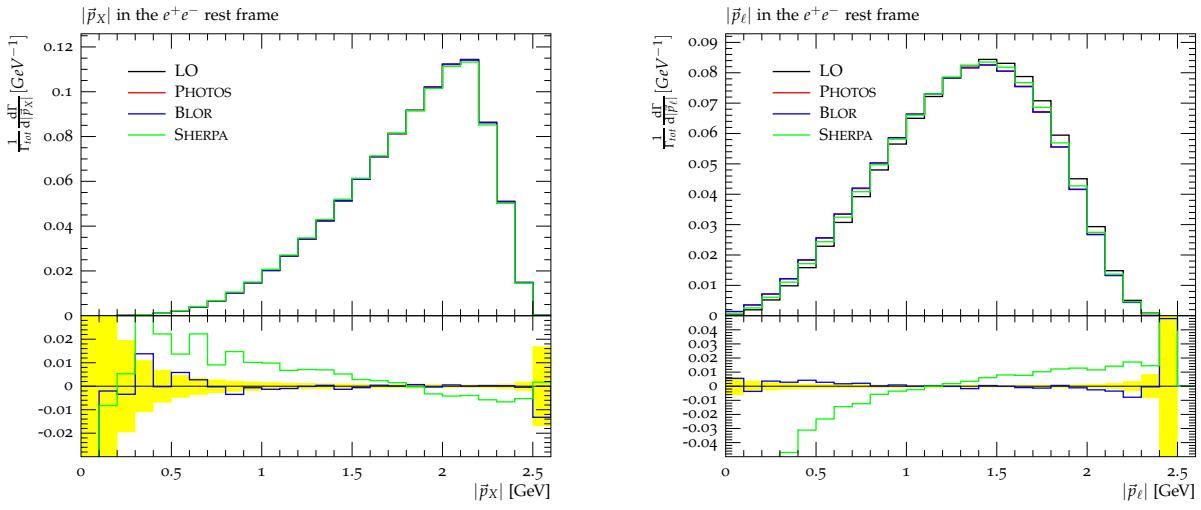
Figure 5.10: Lepton and meson momentum spectrum in the e^+e^- rest frame in the decay $B^+ \to \bar{D}^0 \, e^+ \, \nu_e$. The PHOTOS prediction is taken as the reference in the ratio plot.
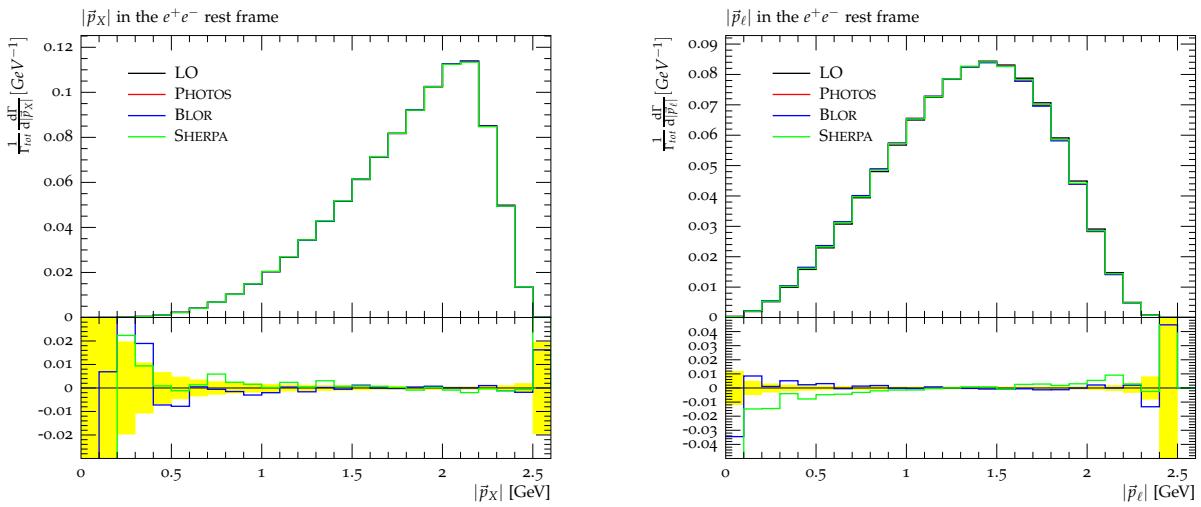
Figure 5.11: Lepton and Meson momentum spectrum in the e^+e^- rest frame in the decay $B^+ \to \bar{D}^0 \, \mu^+ \, \nu_\mu$. The PHOTOS prediction is taken as the reference in the ratio plot.
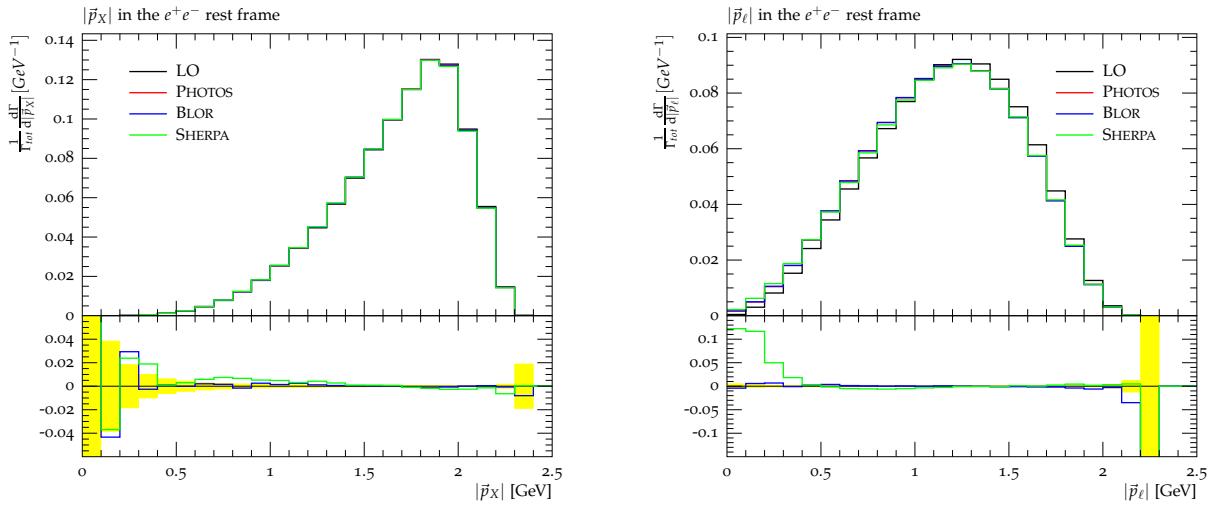
Figure 5.12: Lepton and Meson momentum spectrum in the e^+e^- rest frame in the decay $B^0 \to D_0^{*-} e^+ \nu_e$. The PHOTOS prediction is taken as the reference in the ratio plot.
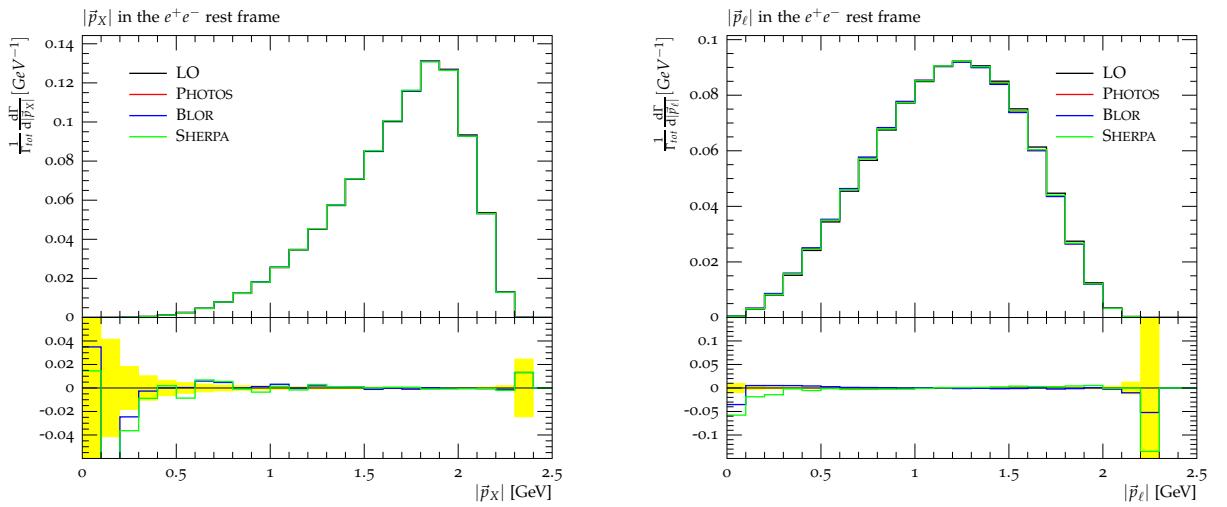
Figure 5.13: Lepton and Meson momentum spectrum in the e^+e^- rest frame in the decay $B^0 \to D_0^{*-} \mu^+ \nu_\mu$. The PHOTOS prediction is taken as the reference in the ratio plot.
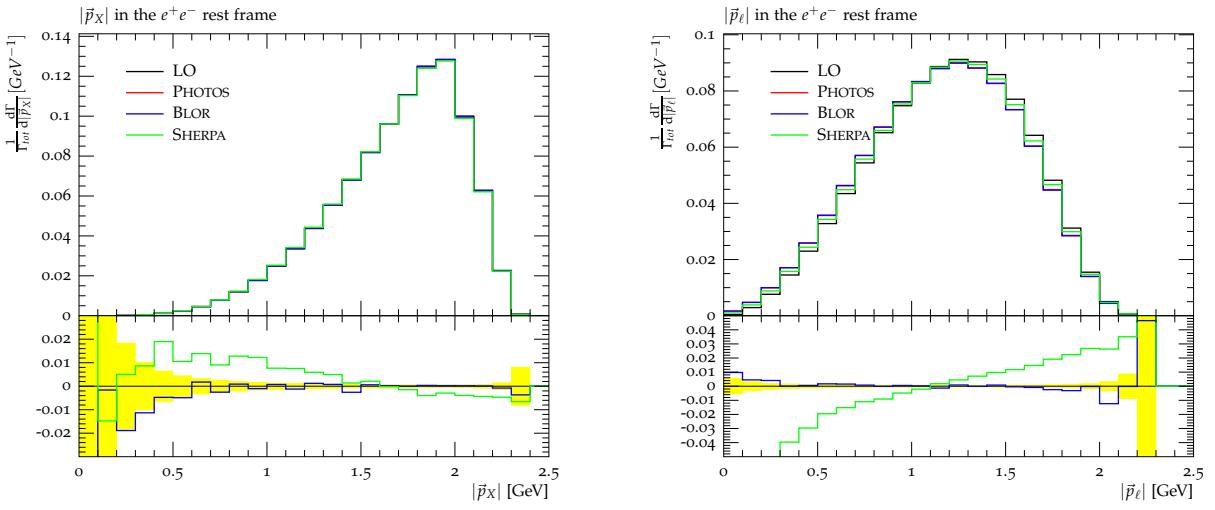
Figure 5.14: Lepton and Meson momentum spectrum in the e^+e^- rest frame in the decay $B^+ \rightarrow \bar{D}_0^{*0}\, e^+\, \nu_e$. The PHOTOS prediction is taken as the reference in the ratio plot.
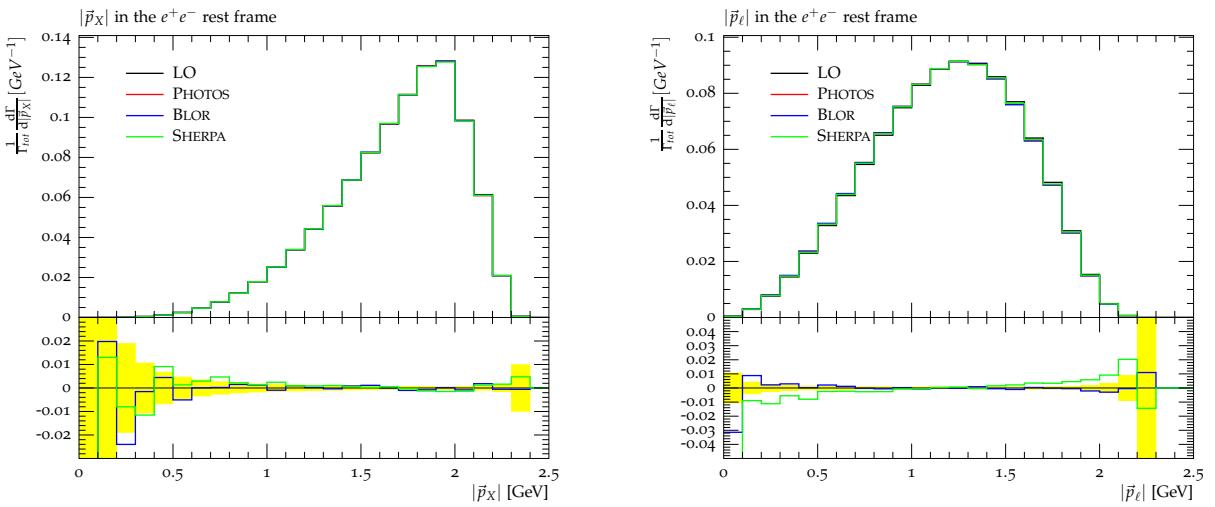
Figure 5.15: Lepton and Meson momentum spectrum in the e^+e^- rest frame in the decay $B^+ \rightarrow \bar{D}_0^{*0}\, \mu^+\, \nu_\mu$. The PHOTOS prediction is taken as the reference in the ratio plot.
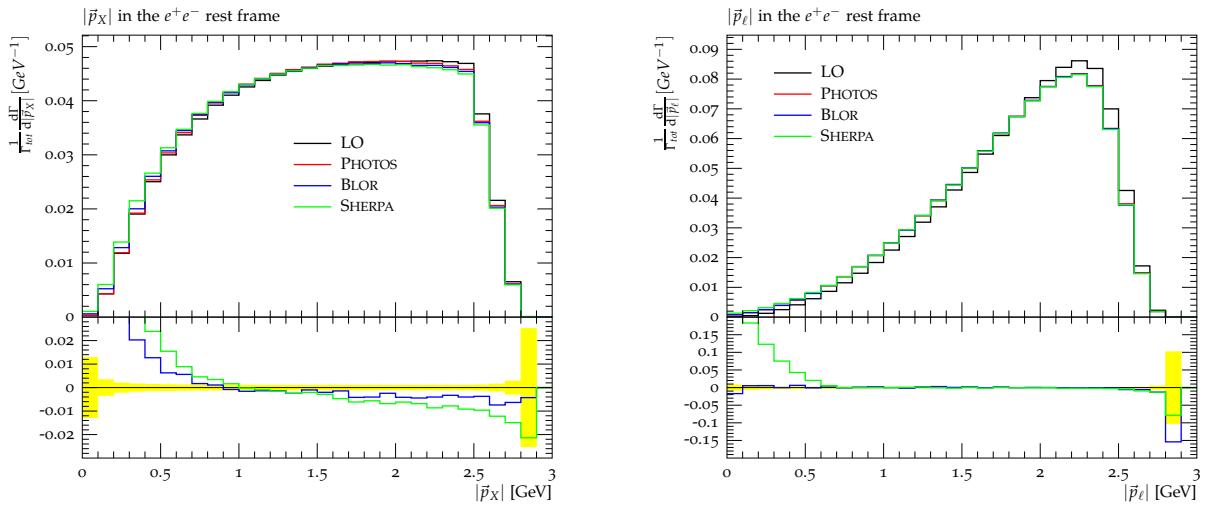
Figure 5.16: Lepton and Meson momentum spectrum in the e^+e^- rest frame in the decay $B^0 \rightarrow \pi^- \, e^+ \, \nu_e$. Both matrix-element-corrected multi-photon radiation and the IB terms for $t \neq t'$ exhibit a strong influence here. The PHOTOS prediction is taken as the reference in the ratio plot.
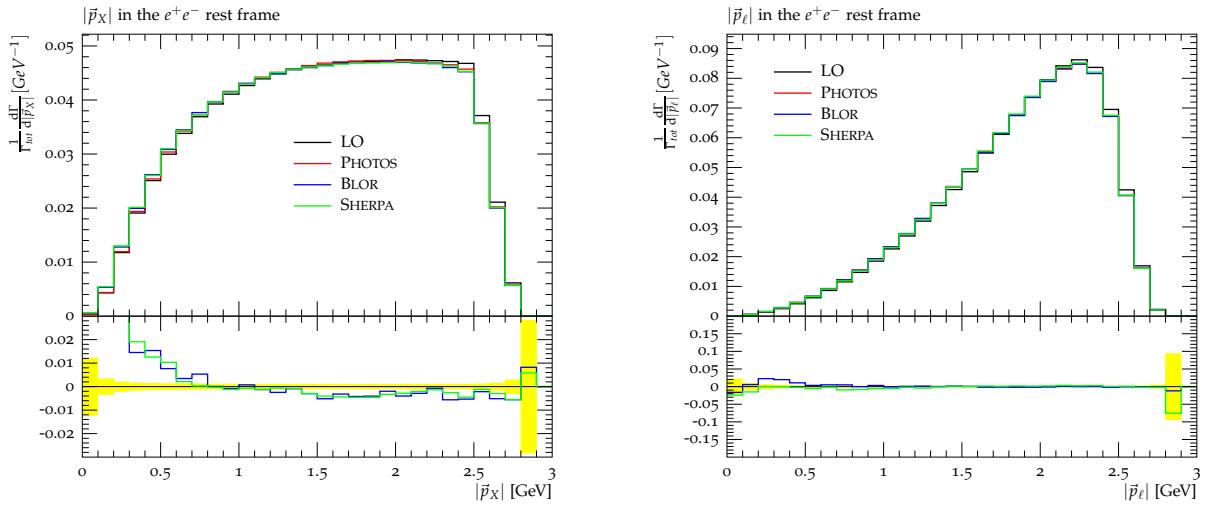
Figure 5.17: Lepton and Meson momentum spectrum in the e^+e^- rest frame in the decay $B^0 \rightarrow \pi^- \, \mu^+ \, \nu_\mu$. The IB terms for $t \neq t'$ exhibit a strong influence here. The PHOTOS prediction is taken as the reference in the ratio plot.
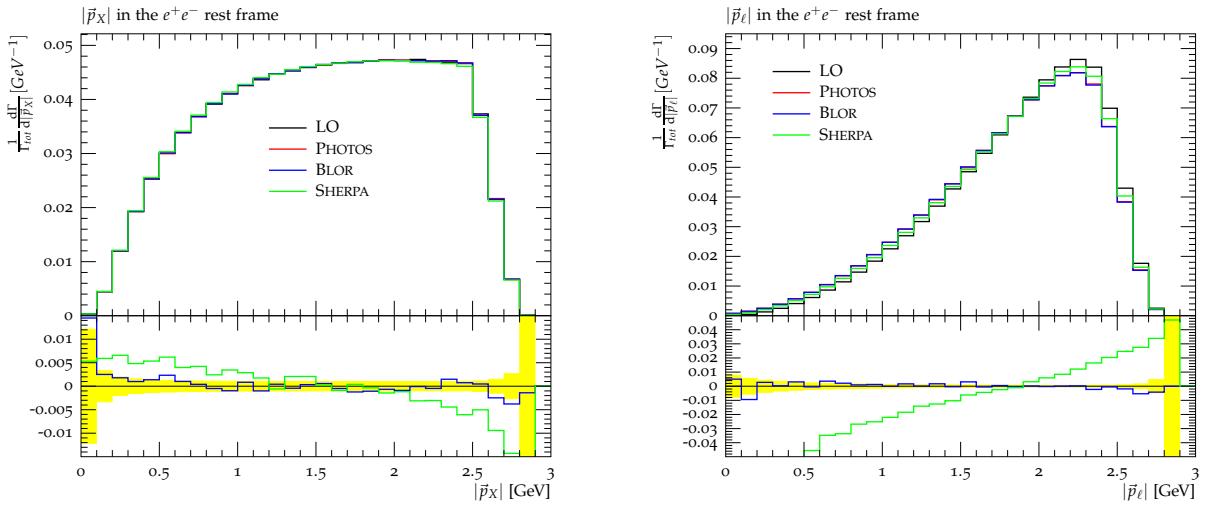
Figure 5.18: Lepton and Meson momentum spectrum in the e^+e^- rest frame in the decay $B^+ \to \pi^0\, e^+\, \nu_e$. The PHOTOS prediction is taken as the reference in the ratio plot.
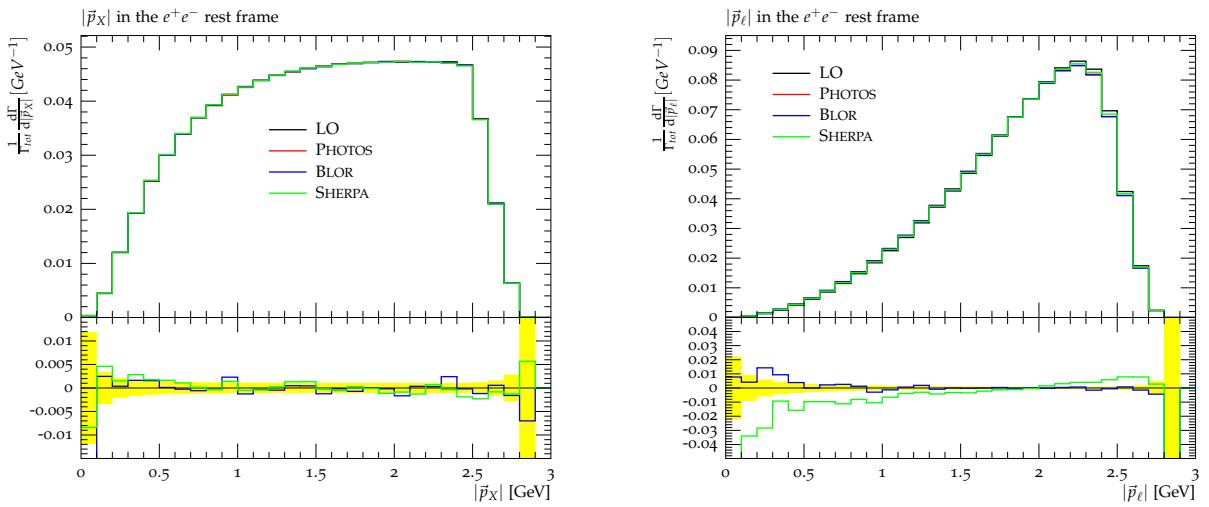
Figure 5.19: Lepton and Meson momentum spectrum in the e^+e^- rest frame in the decay $B^+ \to \pi^0\, \mu^+\, \nu_\mu$. The PHOTOS prediction is taken as the reference in the ratio plot.
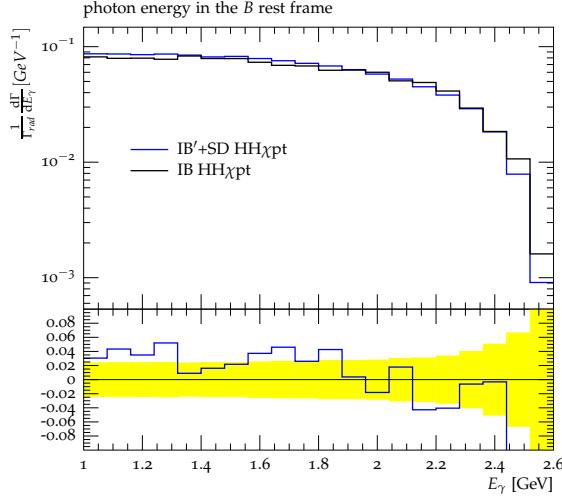
Figure 5.20: The photon energy spectrum in the decay $B^0 \to \pi^- e^+ \nu_e \gamma$ ($E_\gamma > 1\text{GeV}$) is shown. The complete IB+SD result of [124] (blue) is compared against the prediction of the IB terms only according to Section 5.2.4 (black) in the HHχpt form factor model. In the ratio plot the latter is taken as the reference.

5.4.3 Influence of explicit short-distance terms

In section the influence of explicitly calculated structure dependent terms, as introduced in Section 5.2.4, is investigated. The analysis is performed for the decay channel $B^0 \to \pi^- e^+ \nu_e$ with the results of [124] and the decay channels $B^{0,+} \to D^{-,0} e^+ \nu_e$ with the results of [121]. The same conclusions also apply to the muon channels.

For the charged pion channel, [124] employs a form factor model of the heavy-hadron chiral perturbation theory (HHχpt) [129, 130, 131, 132], valid in the region of $E_\gamma > 1\text{GeV}$. Despite the mismatch of the form factor model used in the present study the result depicted in Fig. 5.20 shows the structure-dependent contributions have little influence on the photon energy spectrum in this region. Due to their finiteness in the limit $k \to 0$, they are expected to behave similarly for $E_\gamma < 1\text{GeV}$. For the Ball-Zwicky form factor model used in this study, cf. Appendix B.1.2, the IB and SD correction are expected to behave similarly.

	$\delta_{\text{sd}} + \delta_{\text{ld(IB)}}$	$\delta_{\text{sd}} + \delta_{\text{ld(IB+part.SD)}}$	σ_{SD}
$B^0 \to D^- \ell^+ \nu_\ell(\gamma)$	0.02223(6)	0.02225(7)	0.00002
$B^+ \to D^0 \ell^+ \nu_\ell(\gamma)$	0.01463(5)	0.01627(6)	0.00158

Table 5.5: The effect of including the partial SD terms arising due to intermediate excited D^{*-} and D^{*0} mesons is shown. Because of the unknown size of the full SD contributions this single term, argued to be dominating, is used as an estimate on the systematic uncertainty σ_{SD} associated to the IB-only result of Section 5.4.1.
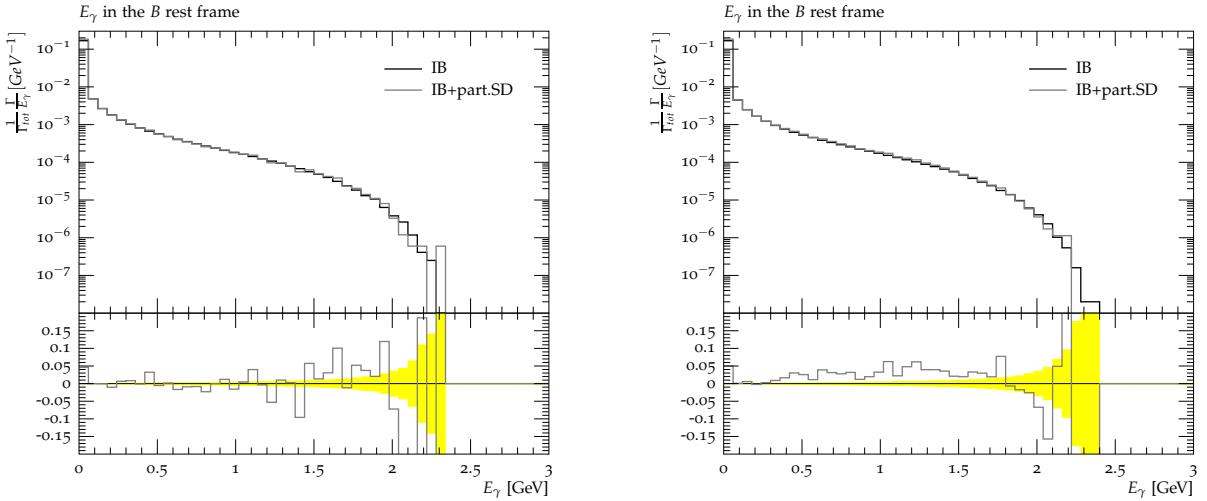
Figure 5.21: The photon energy spectra in the decays $B^0 \to D^- e^+ \nu_e \gamma$ on the left and $B^+ \to D^0 e^+ \nu_e \gamma$ on the right are shown. The result including partial SD terms arising due to intermediate excited mesons, D^{*-} and D^{*0} [121], and the associated coupling $X^* \to X\gamma$ (grey) is compared against the prediction of the IB terms only according to Section 5.2.4 (black) in the HQET form factor model. In the ratio plot the latter is taken as the reference.

In the D meson channels, [121] uses lattice results for the trilinear couplings of an exited D^* meson to a photon and its ground state: $g_{D^{*+}D^+\gamma} = -0.1(7)$ and $g_{D^{*0}D^0\gamma} = 2.7(1.2)$. The effects manifest themselves as corrections to the total decay widths and are summarized in Tab. 5.5: they prove minor in the case of D^-, and sizable in the case of D^0. The case is similar for the radiative spectra: a slight change in the shape of the radiative energy loss for the D^0 channel on the scale of less than 5%, while no such change occurs in the D^- channel. These particular SD corrections, however, only form a single term in one class of SD correction. Note that higher order charm resonances, i.e. through $D^{**}D\gamma$ processes, do not contribute to real corrections at NLO of the studied decay modes because of angular momentum and spin conservation. Therefore, the lowest order are believed to be one of the dominant terms, they are taken as an estimate for the error associated to neglecting all SD contributions.

Note, that the samples containing (partial) SD terms have larger statistical uncertainties.

5.5 Summary and conclusions

In this chapter of this thesis, electroweak corrections to semileptonic B decays were studied. A long-distance calculation in the QED improved effective Lagrangian was matched to the partonic short-distance result of [107] for (pseudo)scalar final state mesons. Structure dependent terms, e.g. due to non-local photon-charged meson interactions, intermediate resonant meson propagators or modifications to the effective weak meson decay due to off-shell currents, were not taken into account for the computed central values. This was done because they are only known for a very limited set of processes, and there usually only partially.

The results achieved with this method, detailed in Section 5.4, give more reliable predictions for total and differential decay rates, accompanied by quantifiable errors. The improved

predictions of the total decay rate were applied on two selected measurements of V_{cb} [127] and V_{ub} [133] resulting in small corrections to their respective central values. These exemplifications, however, are a mere reweighting of their stated results and correction factors. To fully assess the impact of the corrections to the leading order decay presented in this chapter of this thesis the form factors of the phenomenological models will have to be refitted with the results presented in Section 5.4.2. Here, special attention is again drawn to the large deviations near the endpoints of the kinematic distributions arising when both fixed-order next-to-leading order and resummed leading-logarithmic calculations are combined. Finally, the parts of the analyses relying on Monte Carlo estimates of the radiation pattern need to be corrected for the improved description presented in this thesis.

It should again be emphasised that the results presented for the decay of a B meson into a pion should be considered with care. The prescription of matching long- and short-distance corrections runs into conceptual problems for this particular process. This is due to the large hierarchy of the scales of the pion mass (the scale where a photon is able to resolve a pion) and the maximally allowed photon energy ($E_\gamma^{max} \sim 2.5\,\text{GeV}$, cf. Section 5.4.2). Consequently, the prediction for the total decay rate may receive significant corrections when a more elaborate matching scheme is used. Nonetheless, the differential distributions are unaffected.

Similarly, structure-dependent contributions, where known, have been shown to have negligible influence on the differential distributions while their impact on the total decay rates can be sizeable. Despite this fact, these structure-dependent contributions were not included in the predictions of the central values of the total decay rates, but only have been used to estimate their potential error. This treatment is justified since in all cases considered here they are only known partially.

Part II

Dokshitzer-Gribov-Lipatov-Altarelli-Parisi resummation and fixed order calculations

Introduction

Higher-order QCD corrections by now form an important ingredient to many phenomenological studies and experimental analyses at both the Tevatron and the LHC. Their impact has been similarly important for various studies of HERA and LEP data. Calculations invoking such corrections, typically at next-to leading order in the perturbative expansion in the strong coupling α_s, and in very few cases also at next-to-next-to leading order accuracy, have been used for a wide range of precision tests of our understanding of QCD and the Standard Model. They are also important for the subtraction of backgrounds in searches for new physics. When being compared to such calculations, experimental measurements are usually corrected for detector effects, while the perturbative result is corrected for hadronisation and multiparton interactions. Such non-perturbative corrections are typically determined by using models built in the multi-purpose Monte-Carlo event generators PYTHIA/PYTHIA8 [2, 5], HERWIG/HERWIG++ [3, 134], or SHERPA [7, 8]. Only after performing these corrections, theoretical predictions and experimental data are on the same footing. But, to describe perturbative QCD, these generators typically relied on leading-order matrix elements only, combined with parton showers implementing the Dokshitzer-Gribov-Lipatov-Altarelli-Parisi resummation, which in turn model QCD radiation effects in a leading logarithmic approximation.

Improvements to this approximation can be obtained through merging methods, called ME+PS methods, pioneered in [135, 27, 28], and further worked out in different varieties at different accuracies and for different parton showers, e.g. in [30, 32, 33, 34, 35]. In this merging approach, tree-level matrix elements for processes with different jet multiplicities are combined with parton showers, avoiding problems related to double counting of emissions. Lately, a new formulation has been proposed which can be proved to preserve the formal accuracy of the parton shower, independent of the process under consideration [29][3]. Despite varying degrees of formal accuracy amongst the various methods, their respective predictions tend to agree on a level expected from such improved leading order perturbation theory [36, 37]. In most cases the approach leads to a dramatic improvement in the description of hard QCD radiation, which makes it a state-of-the-art tool for many analyses, that depend on the *shape* of distributions related to hard QCD radiation.

However sophisticated at modeling multi-jet topologies, the above methods lack the precision of higher-order calculations regarding the overall normalisation, i.e. the cross section of the inclusive process under consideration. To accurately estimate uncertainties intrinsic to perturbative calculations, which manifest themselves for instance in uncertainties related to choices of renormalisation and factorisation scales, full next-to leading order corrections are a *sine qua non*.

So far, two different methods to achieve the systematic inclusion of complete NLO corrections for a fixed multiplicity have not only been described but also *implemented*, asserting their practicality. The first one has been dubbed MC@NLO [11]. By now it has been applied to a variety of processes using the framework of both the HERWIG [137, 138, 139, 140, 141] and the PYTHIA [142] event generators, proving its versatility. It effectively relies on using

---

[3]A similar procedure, although restricted to the case of e^+e^--annihilation into hadrons was also presented in [136].

the parton shower approximation in the calculation of the next-to-leading order expressions, thus avoiding double counting and related problems, and then correcting this approximation to the full result using a separate leading order event sample with real emission kinematics which is by construction finite. The MC@NLO method therefore effectively incorporates the parton shower in the NLO matrix element. The inherent second sample of correction events, however, is not restricted to be positive definite and may lead to a number of events with a negative weight. Although not problematic per se, such negatively weighted events were disfavoured by experimentalists for a long time. The second method includes the NLO corrections into the parton showers and is known as the POWHEG technique [12, 13]. In contrast to MC@NLO, it can ensure that only events with positive weights are generated. To achieve this, the simulation starts with a Born-level event, reweighted to include the full NLO correction, i.e. including virtual and real corrections, integrated over the real-emission subspace. The first emission is then produced using the exact real-emission matrix element, thus providing not only the correct differential cross section, but also the correct radiation pattern to first order in α_s. The big advantage of this technique is that it can be implemented in a shower-independent way, which has been used to some extent in [143, 144, 145, 146, 147, 148, 149, 150, 151], where different processes with trivial divergence structures have been implemented, leaving further parton evolution and non-perturbative corrections to PYTHIA and/or HERWIG. A few implementations for processes with non-trivial colour and divergence structures have been implemented in [152, 153, 154, 155]. In addition, there have been some implementations in the framework of HERWIG++ [156, 157, 158, 159, 160, 161, 162][4]. In fact, because the POWHEG method is very similar to traditional matrix-element corrections [163, 164, 165, 166, 167, 168], it is relatively simple to implement in a process-independent way and thus very well suited for the systematic inclusion of NLO QCD corrections to arbitrary processes. This is reflected by the fact that a corresponding toolbox has already been advertised in [15]. Although the code has not been published, an automated version of MC@NLO, dubbed aMC@NLO, has been used in [169, 170].

Obviously, the ultimate goal is to have a multi-jet merging prescription, accurate at NLO, and to simultaneously respect the logarithmic accuracy of the parton shower. A first step into this direction has been presented for the case of e^+e^- annihilation into hadrons in [171]. An alternative approach was suggested in [172], extending the method of [29] to NLO accuracy for the core interaction. This second method relies on the POWHEG technique to ensure the NLO cross section of the core process, keeping the multijet features of the ME+PS method.

The outline of Part II is thus as follows: Chapter 6 will review the DGLAP resummation of large logarithms arising in collinear parton emissions. Then, in Chapter 7 a formalism will be introduced, basing on the single leg/parton language of the DGLAP resummation, which allows for an abstract formulation of a parton shower and the subsequent reformulation of POWHEG method as an advanced matrix element corrected parton shower supplemented with a NLO weight [65]. This splitting kernel based formulation directly facilitates an automated implementation whose properties and capabilities to describe data are then assessed. Chapter 8 finally takes the reformulated POWHEG method as an input to combine it with the well known ME+PS method. The resulting MENLOPS method [173] thus features a simultaneous description of NLO-accurate inclusive observables, as in the POWHEG and MC@NLO methods, and LO-accurate multijet-dependent observables, as in the ME+PS method, of course not spoiling the DGLAP resummation in the collinear region.

---

[4] It is worth stressing, that in order to ensure formal accuracy a *truncated shower* must be used, as pointed out in the original publications proposing the method. This option is not available for all parton shower algorithms that have been used in the actual implementations.

Chapter 6

Dokshitzer-Gribov-Lipatov-Altarelli-Parisi resummation and approximate higher order corrections

This chapter reviews the Dokshitzer-Gribov-Lipatov-Altarelli-Parisi resummation, which will serve as a basis for discussing logarithmically enhanced higher order corrections in general and matrix element corrected parton showers in particular in the following chapters.

When studying scattering processes involving massless strongly charged partons[1] each order in the perturbative expansion of the QCD Lagrangian in α_s contains a term of the form

$$\alpha_s \log \frac{Q^2}{\kappa^2} \,, \tag{6.0.1}$$

relative to the previous order. Therein Q^2 is the scale of the hard interaction and κ^2 is a scale at which non-perturbative effects become important. Thus, the size of this interaction is enhanced by a potentially large logarithm as compared to a factor of just α_s times a constant. Thus, such higher order corrections can be of order one, and need to be resummed to all orders if quantitative predictions are to be made. To study how this factor arises QCD corrections to the naïve parton model have to examined, and a universal structure has to be found.

To this end, it is advantageous to follow the reasoning of [93, 177, 178] in the following review in Section 6.1. Section 6.2 then uses the collinear approximation inherent in the DGLAP resummation kernels to construct approximative real emission matrix elements. Their successive iteration leads to the definition of the Sudakov form factor [179], the probability for a parton to evolve between two scales without a further emission. It forms the basis in the construction of parton shower discussed in Chapter 7. Finally, Section 6.3 discusses the approximation of the real emission cross section in the limit of soft gluon emissions and how such corrections can be incorporated in the definition of the splitting kernels.
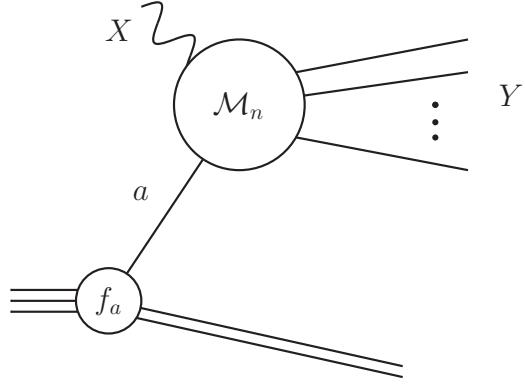
Figure 6.1: A representation of a generic scattering process in collisions involving initial state hadrons in the parton model. Parton a and a generic second initial state X scatter into a final state Y. f_a denotes the parton density of parton a inside the hadron.

6.1 Dokshitzer-Gribov-Lipatov-Altarelli-Parisi resummation

6.1.1 The naïve parton model

The description of a scattering process involving composite objects, or more specifically hadrons, in the naïve parton model [180] is depicted in Figure 6.1. The focus rests on one hard interaction probing the inner content of one hadron. The second initial state, denoted X in the above figure, remains unspecified. By virtue of the factorisation theorem [181, 182, 183] it cannot have an influence on the topic at hand, be it a virtual photon as in deep inelastic scattering or another hadron as in hadron-hadron collisions; it merely sets the scale Q^2. Similarly, the final state is collectively denoted Y.

The parton model itself rests on the assumption that interactions of hadrons at high energies are due to the interactions of their constituent partons. Therein, the internal structure of the hadrons is described by instantaneous parton distribution functions. Obviously, changes both in the number and the momenta of the constituent partons have to be negligible during the time of interaction. The probability $\mathrm{d}\mathcal{P}_a(x, Q^2)$ to find a parton with momentum fraction $x \in [\xi, \xi + \mathrm{d}\xi)$ of flavour a at some scale Q^2 is then given by

$$\mathrm{d}\mathcal{P}_a(x, Q^2) = f_a(\xi, Q^2)\delta(x - \xi)\,\mathrm{d}x\,\mathrm{d}\xi\,. \tag{6.1.1}$$

The so-called parton distribution function $f_a(x, Q^2)$ contains information about the bound state hadron and, thus, cannot be calculated perturbatively. It depends on soft processes that determine the hadron's internal structure containing quarks and gluons. For completeness, it needs to be noted that the parton distributions can be defined in terms of hadronic matrix elements of the quark and gluon number operators, cf. [183]. However, in the present context, this definition is not particularly useful, and is therefore omitted.

---

[1] The collinear factorisation and the following resummation was indeed first studied in the context of QED [174, 175, 176]. However, since this part of this thesis concerns itself with higher order QCD corrections, the following chapter focuses on the derivation and consequences of this resummation in the context of QCD.
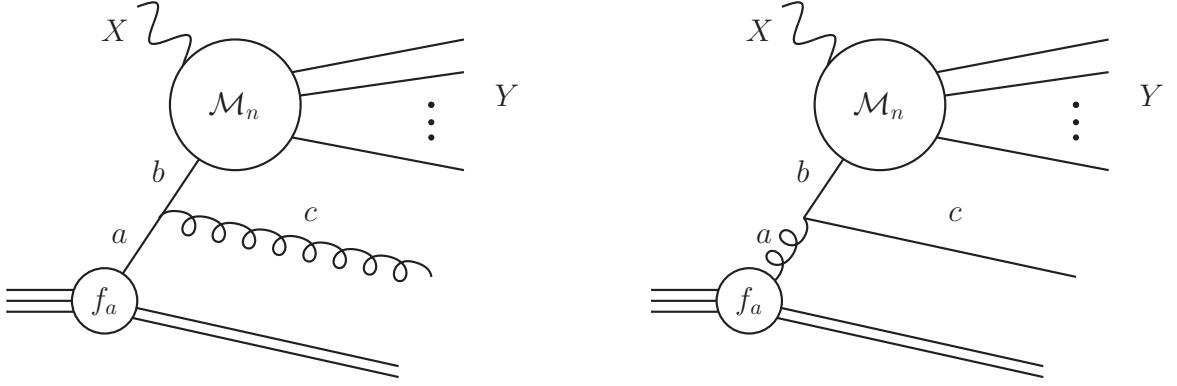
Figure 6.2: Next-to-leading order QCD corrections to the naive parton model of Figure 6.1. Parton a splits into partons b and c, before interacting with the second initial state X to produce the final state $Y + c$.

The cross section of the process of Figure 6.1 can then be computed as

$$\mathrm{d}\sigma(P + X \to Y + \ldots) \;\; = \;\; \sum_a \mathrm{d}\mathcal{P}_a(x, Q^2)\, \mathrm{d}\hat{\sigma}_a(a + X \to Y)\,, \tag{6.1.2}$$

wherein $\hat{\sigma}_a$ denotes the cross section with the partonic initial state a instead of the hadron P. The ellipsis again stands for the unspecified hadron remnant and the sum runs over all possible partons, i.e. quarks, anti-quarks, and gluons. The second initial state X may need to be treated similarly.

The parton distribution functions themselves, in the form $f_a(x, Q^2)$, are only rigorously defined in the infinite momentum frame. In this limit $|\vec{p}_h| \gg m_h$, i.e. the magnitude of the hadron's spatial momentum $\vec{p}_h$ is large compared to its mass m_h. The longitudinal size of the hadron is contracted by a factor $m_h/|\vec{p}_h|$ in this frame, such that all partons are restricted to move collinearly with the proton, making it possible to represent their momentum by a single ratio $x = |\vec{p}_a|/|\vec{p}_h| = E_a/E_h + \mathcal{O}(m_h^2/|\vec{p}_h|^2)$.

The naïve parton model, as defined above, predicts the behaviour of the parton distribution functions in the Bjørken limit, defined as $Q^2 \to \infty$ for fixed momentum fraction x,

$$f_a(x, Q^2) \;\; \xrightarrow{\;\; Q^2 \to \infty,\, x \text{ fixed} \;\;} \;\; f_a(x)\,. \tag{6.1.3}$$

This is known as Bjørken scaling [184, 180]. This scaling however, is violated by higher order QCD corrections supplying logarithms of Q^2.

6.1.2 QCD corrections to the parton model

Identifying the partons of the previous section with the quarks and gluons of QCD naturally leads to higher order corrections to the naïve parton model. Additional radiation off the partons allows them to acquire transverse momentum $k_\perp$ which is in fact not restricted to be small: it is only restricted by the kinematic limit Q^2. It is then a particular feature of renormalisable gauge theories with local fermion-vector interactions to introduce logarithms of this kinematic endpoint Q^2, explicitly breaking the Bjørken scaling.
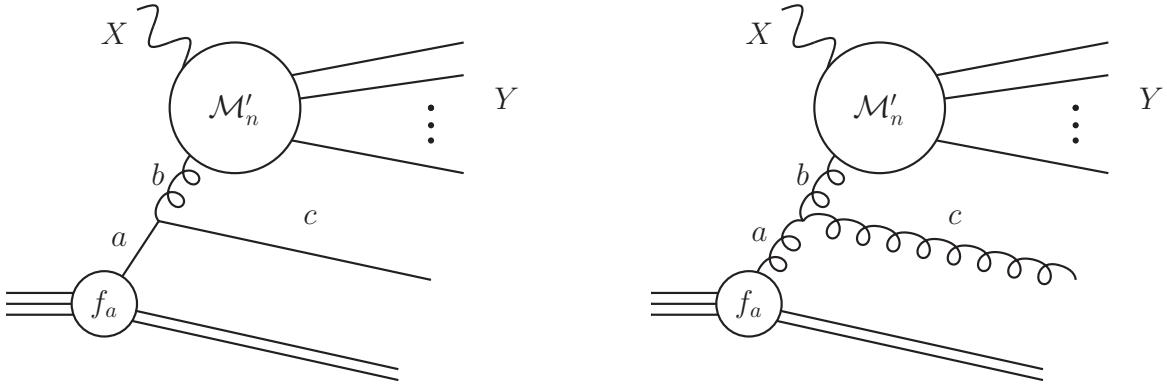
Figure 6.3: Next-to-leading order QCD corrections to the naive parton model of Figure 6.1 if matrix elements $\mathcal{M}'_n$ containing gluon initial states exist. Then again, as in Figure 6.2, parton a splits into partons b and c, before interacting with the second initial state X to produce the final state $Y + c$.

Consider the parton distribution function $\hat{f}_{ba}(x, Q^2)$ [2] to find parton b inside of parton a at momentum fraction x and scale Q^2. In the naïve parton model, corresponding to leading order QCD, this is given by

$$\hat{f}_{ba}(x, Q^2) = \delta_{ba}\,\delta(1-x)\,, \tag{6.1.4}$$

again exhibiting Bjørken scaling. The next-to-leading order real emission corrections can then be calculated directly, taking Figures 6.2 and 6.3 as a guideline. Because of calculating with massless particles infrared divergences are present. They can be regulated introducing an invariant cut-off κ^2 removing the singular region, resulting in

$$\frac{\alpha_s}{2\pi}\,P_{ba}(x)\log\frac{Q^2}{\kappa^2} + C_{ba}^{(\mathrm{R})}(x)\,. \tag{6.1.5}$$

The functions $P_{ba}(x)$ and $C_{ba}^{(\mathrm{R})}(x)$ are intimately related with the relevant QCD vertex, transforming parton a into parton b. $P_{ba}(x)$, known as the *splitting function*, is of special interest since it is defining the Q^2 dependence of the parton distribution function. Its explicit form depends of course on the involved parton flavours a and b and is given in Appendix C.

The form of the virtual corrections, computed at next-to-leading order, are dictated by momentum conservation and the Kinoshita-Lee-Nauenberg theorem [91, 92], i.e.

$$-\frac{\alpha_s}{2\pi}\left[K\log\frac{Q^2}{\kappa^2} - C^{(\mathrm{V})}\right]\delta_{ba}\,\delta(1-x)\,. \tag{6.1.6}$$

---

[2] Please note the occurrence of a second index for the parton distribution function $\hat{f}$. Contrary to hadronic parton distribution functions where the flavour of the "mother", i.e. the hadron, is always implicitly understood, partonic parton distribution functions always carry an index explicitly stating the mother partons flavour, within the confines of this work.

The x and Q^2 independent factor K can then be determined by requiring the conservation of the quark number, as is the case in QCD, i.e.

$$Q^2 \frac{\partial}{\partial Q^2} \int_0^1 \mathrm{d}x \; \hat{f}_{ba}(x, Q^2) \;\; = \;\; 0 \,. \tag{6.1.7}$$

Including K in the splitting function $P_{ba}(x)$ via the replacements

$$P_{ba}(x) \;\; \longrightarrow \;\; P_{ba}(x) + K \, \delta_{ba} \, \delta(1 - x) \,, \tag{6.1.8}$$

and defining $C_{ba}(x) = C_{ba}^{(\mathrm{R})}(x) + C^{(\mathrm{V})} \delta_{ba} \, \delta(1 - x)$, the parton distribution function of parton a including QCD corrections up to $\mathcal{O}(\alpha)$ then reads

$$\hat{f}_{ba}(x, Q^2) \;\; = \;\; \delta_{ba} \, \delta(1 - x) + \frac{\alpha_s}{2\pi} \left[P_{ba}(x) \log \frac{Q^2}{\kappa^2} + C_{ba}(x) \right] \,. \tag{6.1.9}$$

In this form the violation of Bjørken scaling is evident.

6.1.3 Factorisation and the collinear counterterm

Eq. (6.1.9) contains one left-over divergence, namely when parton b is created collinear to parton a with $k_\perp^2 \to 0$. This collinear divergence is not subject to the singularity cancellation with the virtual terms because, in practice, the hard process might be able to distinguish between the quark and the gluon. The limit $k_\perp^2 \to 0$ corresponds to a long-range part of the strong interaction that is not calculable in perturbative QCD. Hence, the invariant cut-off κ^2 takes on a physical meaning to effectively separate the perturbative from the non-perturbative regime[3].

Thus, to obtain a parton distribution function of a hadron $f_a(x, Q^2)$ its bare parton distribution function of the naïve parton model, $f_{a,0}(x)$, has to be convoluted with the partonic parton distribution function of the last section, eq. (6.1.9), giving

$$f_a(x, \mu_F^2) = f_{a,0}(x) + \frac{\alpha_s}{2\pi} \sum_b \int_x^1 \frac{\mathrm{d}\xi}{\xi} \, f_{b,0}(\xi) \left[P_{ab}\left(\frac{x}{\xi}\right) \log \frac{\mu_F^2}{\kappa^2} + C_{ab}\left(\frac{x}{\xi}\right) \right] \tag{6.1.10}$$

as the renormalised parton distribution. The sum runs over all parton flavours b present in the hadron the parton a could have originated from. The scale μ_F, introduced to define the renormalised parton distribution, is called the factorisation scale. It is to note that the

---

[3]Had the collinear divergence been regularised by the means of dimensional regularisation, a pole structure

$$\hat{f}_{ba}(x, Q^2)\Big|_{\mathrm{div}} \propto -\frac{1}{\epsilon} \, P_{ba}(x)$$

would have been recovered. The finite part would then have retained the same form as in eq. (6.1.9), only κ^2 would now have had the meaning of the dimensional renormalisation scale commonly denoted μ^2. Its physical interpretation, however, is less intuitive as the one of an invariant cut-off.

treatment of the finite constant C_{ab} is arbitrary and is defined by the factorisation scheme. Eq. (6.1.10) then leads to the parton distribution at any Q^2

$$f_a(x, Q^2) = \sum_b \int_x^1 \frac{d\xi}{\xi} \, f_b(\xi, \mu_F^2) \left\{ \delta_{ab} \delta \left(1 - \frac{x}{\xi}\right) + \frac{\alpha_s}{2\pi} \left[P_{ab}\left(\frac{x}{\xi}\right) \log \frac{Q^2}{\mu_F^2} + C_{ab}\left(\frac{x}{\xi}\right) \right] \right\}.$$

(6.1.11)

The ability to factorise short- and long-distance contributions to the parton distributions, and thus to any physical cross section according to eq. (6.1.2), is a fundamental property of the theory. This was proven to hold to all orders in perturbation theory in [181]. The factorisation scale μ_F itself is an arbitrary parameter, effectively separating the scales at which partons are considered part of the hadronic structure ($k_\perp < \mu_F$) and the scales where they are part of short-distance physics ($k_\perp > \mu_F$), which is calculable perturbatively. Hence, generalising eq. (6.1.2) to the QCD improved parton model and, as being the most relevant case in this part of this thesis, to two initial state protons, P_a and P_b, the factorised cross section reads

$$\sigma(P_a + P_b \to X + \ldots)$$
$$= \sum_{a,b} \int_0^1 dx_a \int_0^1 dx_b \, f_a(x_a, \mu_{Fa}) \, f_b(x_b, \mu_{Fb}) \, \hat{\sigma}_{ab}(a + b \to X, \mu_{Fa}, \mu_{Fb}, \mu_R).$$

(6.1.12)

Again, as in eq. (6.1.2), the ellipsis stands for the the proton remnants. In principle, for both proton's parton distribution functions the factorisation scales μ_{Fi} could be specified separately. However, in practice they are usually set to a common value $\mu_{Fa} = \mu_{Fb} = \mu_F$. Further, the dependence of the short distance cross section on the renormalisation scale μ_R is made explicit. In principle, introducing also higher order corrections to the parton distribution functions, they could also depend on μ_R. Further in many calculations, especially in all modern extractions of parton distribution functions from data [185, 186, 187, 188, 189], all arbitrary scales are set to a common value, $\mu_{Fa} = \mu_{Fb} = \mu_R = \mu$. Thus, the conventions here have to be carefully matched when carrying out a perturbative calculation based on the factorisation theorem and a set of parton distributions fitted to experimental data using another calculation, as not to introduce any inconsistencies.

6.1.4 The DGLAP equations

As already discussed earlier, the parton distribution functions of a hadron cannot be calculated perturbatively. Nonetheless, their dependence on the factorisation scale μ_F can be calculated. Thus, once measured at one scale they are known at any other scale in the perturbative regime. By demanding that $f_a(x, \mu_F^2)$ of eq. (6.1.11) is independent of μ_F the evolution equation is obtained. Differentiating with respect to μ_F^2 $\partial/\partial\mu_F^2$ gives a differential equation for the μ_F-dependence of $f_a(x, \mu_F^2)$

$$\mu_F^2 \frac{\partial}{\partial\mu_F^2} f_a(x, \mu_F^2) = \frac{\alpha_s}{2\pi} \sum_b \int_0^1 \frac{d\xi}{\xi} \, P_{ab}\left(\frac{x}{\xi}\right) f_b(\xi, \mu_F^2).$$

(6.1.13)

This equation is known as the DGLAP equation and represents the analogue of the β-function for parton density evolution. It was derived first for QED in [174, 175, 176], and for QCD in [93].

Introducing $t = \mu_F^2$ and replacing α_s by its running value $\alpha_S(t)$ gives

$$
t \frac{\partial}{\partial t}
\begin{pmatrix} f_{q_i}(x,t) \\ f_g(x,t) \end{pmatrix}
= \frac{\alpha_s(t)}{2\pi} \sum_{j=1}^{2N_f} \int_x^1 \frac{\mathrm{d}\xi}{\xi}
\begin{pmatrix} P_{q_i q_j}\left(\frac{x}{\xi}\right) & P_{q_i g}\left(\frac{x}{\xi}\right) \\ P_{g q_j}\left(\frac{x}{\xi}\right) & P_{gg}\left(\frac{x}{\xi}\right) \end{pmatrix}
\begin{pmatrix} f_{q_j}(\xi,t) \\ f_g(\xi,t) \end{pmatrix}
\tag{6.1.14}
$$

making the forms explicit for the QCD partons, quarks and gluons. The sum now runs over all quarks and anti-quarks. This form of the DGLAP equation does not only hold for QCD splittings at $\mathcal{O}(\alpha_s)$ but to any order in perturbative QCD, as shown in [190, 191]. Thus, eq. (6.1.14) generalises to

$$
t \frac{\partial}{\partial t}
\begin{pmatrix} f_{q_i}(x,t) \\ f_g(x,t) \end{pmatrix}
= \frac{\alpha_s(t)}{2\pi} \sum_{j=1}^{2N_f} \int_x^1 \frac{\mathrm{d}\xi}{\xi}
\begin{pmatrix} P_{q_i q_j}\left(\frac{x}{\xi}, \alpha_s(t)\right) & P_{q_i g}\left(\frac{x}{\xi}, \alpha_s(t)\right) \\ P_{g q_j}\left(\frac{x}{\xi}, \alpha_s(t)\right) & P_{gg}\left(\frac{x}{\xi}, \alpha_s(t)\right) \end{pmatrix}
\begin{pmatrix} f_{q_j}(\xi,t) \\ f_g(\xi,t) \end{pmatrix} .
$$

The regularised splitting kernels $P_{ab}(z, \alpha_s(t))$ now have a perturbative expansion in α_s

$$
\begin{aligned}
P_{q_i q_j}(z, \alpha_s) &= \delta_{ij} P_{qq}^{(0)}(z) + \tfrac{\alpha_s}{2\pi} P_{q_i q_j}^{(1)}(z) + \mathcal{O}(\alpha_s^2) \\
P_{q_i g}(z, \alpha_s) &= P_{q_i g}^{(0)}(z) + \tfrac{\alpha_s}{2\pi} P_{q_i g}^{(1)}(z) + \mathcal{O}(\alpha_s^2) \\
P_{g q_i}(z, \alpha_s) &= P_{g q_i}^{(0)}(z) + \tfrac{\alpha_s}{2\pi} P_{g q_i}^{(1)}(z) + \mathcal{O}(\alpha_s^2) \\
P_{gg}(z, \alpha_s) &= P_{gg}^{(0)}(z) + \tfrac{\alpha_s}{2\pi} P_{gg}^{(1)}(z) + \mathcal{O}(\alpha_s^2) .
\end{aligned}
\tag{6.1.15}
$$

Charge conjugation and flavour $SU(N_f)$ symmetries impose further relations

$$
\begin{aligned}
P_{q_i q_j} &= P_{\bar{q}_i \bar{q}_j} \\
P_{q_i \bar{q}_j} &= P_{\bar{q}_i q_j} \\
P_{q_i g} &= P_{\bar{q}_i g} \equiv P_{qg} \\
P_{g q_i} &= P_{g \bar{q}_i} \equiv P_{gq} ,
\end{aligned}
\tag{6.1.16}
$$

restricting their functional form. The leading order terms $P_{ab}^{(0)}$ are the familiar Altarelli-Parisi splitting kernels [93]. The next-to-leading order terms have been calculated in [192, 193, 194, 195, 196]. But, since they are not incorporated in standard Markovian parton-shower Monte-Carlo programs, they will not be discussed here[4]. The explicit form of the leading order splitting functions is discussed in Section C.

The leading order DGLAP splitting kernels $P_{ab}^{(0)}(z)$, representing the classical limit, can be interpreted for $z < 1$ as the probabilities of finding a parton a in a parton b with an energy fraction z and relative transverse momentum $k_\perp^2 < \mu^2$. However, due to the inclusion of virtual corrections, cf. eq. (6.1.8), this interpretation does not hold for $z = 1$.

The above consideration lead to the following sum rules

$$
0 = \int_0^1 \mathrm{d}z \, P_{qq}^{(0)}(z)
$$

$$
0 = \int_0^1 \mathrm{d}z \, z \left(P_{qq}^{(0)}(z) + P_{gq}^{(0)}(z) \right)
\tag{6.1.17}
$$

$$
0 = \int_0^1 \mathrm{d}z \, z \left(2N_f \, P_{qg}^{(0)}(z) + P_{gg}^{(0)}(z) \right)
$$

---

[4] Attempts have been made to incorporate the NLO splitting kernels in a Monte-Carlo simulation, cf. [197, 198]. Their inclusion in the Markovian simulations is however not straight forward due to their non-positive definiteness for $z < 1$.
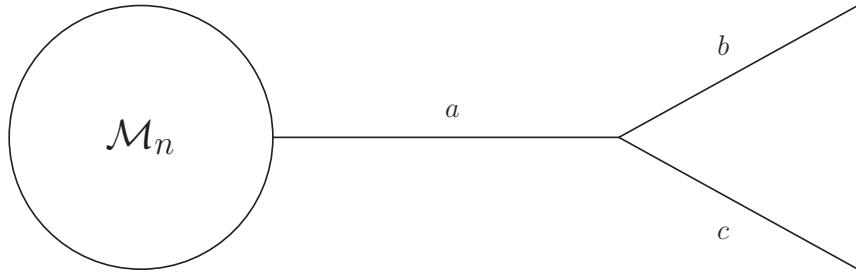
Figure 6.4: Kinematics of a generic timelike final state parton branching. While the splitting of one final state parton a into partons b and c is explicitly depicted, the rest of the matrix element is denoted by the gray blob.

corresponding to quark number and momentum conservation in both the splittings of quarks and gluons.

6.2 Parton evolution

6.2.1 Approximate real emission cross sections

This section discusses how real emission cross sections, approximated in the soft-collinear limit can be derived from the general considerations of the previous section. At first, final state timelike branchings are considered where one a final state parton a splits into two partons b and c, as depicted in Figure 6.4. The following relation is then assumed for the respective parton virtualities

$$p_b^2, p_c^2 \ll p_a^2 \equiv t \ . \tag{6.2.1}$$

This corresponds to a strict hierarchy in the variable t when moving away from the n-parton matrix element, taken as the baseline. Further, defining the energy fractions of partons b and c as

$$z = z_b = 1 - z_c = \frac{E_b}{E_a} = 1 - \frac{E_c}{E_a} \ , \tag{6.2.2}$$

the virtuality of parton a then reads in the collinear limit, where the opening angle θ between partons b and c tends to zero,

$$t = p_a^2 = q^2 = 2E_b E_c \left(1 - \cos\theta\right) \xrightarrow{\theta \to 0} z(1-z)\, \theta^2\, E_a^2 \ . \tag{6.2.3}$$

This is directly related to the relative transverse momentum of the splitting

$$k_\perp^2 = z(1-z)\, q^2 = z^2(1-z)^2\, \theta^2\, E_a^2 \ . \tag{6.2.4}$$

Thus, the the following differentials are equivalent

$$\frac{\mathrm{d}t}{t} = \frac{\mathrm{d}q^2}{q^2} = \frac{\mathrm{d}k_\perp^2}{k_\perp^2} = \frac{\mathrm{d}\theta^2}{\theta^2} \; . \tag{6.2.5}$$

To compute now the term in the real emission matrix element corresponding to a branching of one of its final state legs a into partons b and c the following factorisation is used

$$|\mathcal{M}_{n+1,ba}|^2 \;\; \propto \;\; |\mathcal{M}_n|^2 \otimes \frac{\alpha_s}{t} \, F_{ba}(z; \lambda_a, \lambda_b, \lambda_c) \; . \tag{6.2.6}$$

Herein, F_{ba} is the full vertex function in the collinear approximation, depending on the relative energies of partons a, b and c, and their respective spins (quarks) or polarisations (gluons) λ_a, λ_b and λ_c. Both the n- and $(n+1)$-parton matrix elements are well-defined in the collinear limit, where all particles are approximately on-shell. The collinear divergences of $\mathcal{M}_{n+1}$ are encoded in the $1/t$-propagator function while further singularities due to soft gluon emissions, $z_g \to 0$, might be present in vertex function. The convolution the n-parton matrix element with the vertex functions is necessary because of the latter's dependence on the spin/polarisation state of parton a. Integrating out these spin/polarisation degrees of freedom the vertex function reduces to

$$\langle F_{ba}(z; \lambda_a, \lambda_b, \lambda_c) \rangle = \int \frac{\mathrm{d}\phi}{2\pi} \, F_{ba}(z, \phi) = \hat{P}_{ba}(z) \; , \tag{6.2.7}$$

where $\hat{P}_{ba}(z)$ are the unregularised splitting functions[5]. Simultaneously the vertex function looses its spin dependence, and the above convolution reduces to a simple product of real functions.

Using this to compute cross sections from the collinearly approximated matrix elements, also initial state fluxes $\mathcal{F}$ and the final state phase space element $\mathrm{d}\Phi_n$ have to be considered. This leads to

$$\mathrm{d}\sigma_n = \mathcal{F} \, \mathrm{d}\Phi_n \, |\mathcal{M}_n|^2 \qquad \text{with} \qquad \mathrm{d}\Phi_n = \prod_{i \backslash a}^{n} \frac{\mathrm{d}^3 p_i}{2(2\pi)^3 E_i} \cdot \frac{\mathrm{d}^3 p_a}{2(2\pi)^3 E_a} \tag{6.2.8}$$

The product runs over all final state partons, except for a. Its phase space element is denoted separately. Initial state partons are assumed not to be present. Hence, all contributions to the real emission cross section come from branchings of final state partons. Thus, the flux factor remains unaltered for all contributions while the phase space element now reads

$$\begin{aligned} \mathrm{d}\Phi_{n+1} &= \prod_{i \backslash b,c}^{n+1} \frac{\mathrm{d}^3 p_i}{2(2\pi)^3 E_i} \cdot \frac{\mathrm{d}^3 p_b}{2(2\pi)^3 E_b} \cdot \frac{\mathrm{d}^3 p_c}{2(2\pi)^3 E_c} \\ &= \prod_{i \backslash a}^{n} \frac{\mathrm{d}^3 p_i}{2(2\pi)^3 E_i} \cdot \frac{\mathrm{d}^3 p_a}{2(2\pi)^3 E_a} \cdot \frac{1}{32\pi^3} \, \mathrm{d}t \, \mathrm{d}z \, \mathrm{d}\phi \\ &= \mathrm{d}\Phi_n \cdot \frac{1}{32\pi^3} \, \mathrm{d}t \, \mathrm{d}z \, \mathrm{d}\phi \; . \end{aligned} \tag{6.2.9}$$

---

[5]The unregularised Altarelli-Parisi splitting functions are related to the regularised Altarelli-Parisi splitting functions of eq. (6.1.15) through

$$P_{ab}(z) \quad = \quad \left[\hat{P}_{ab}(z) \right]_+$$

where $[\dots]_+$ is the so-called plus-distribution, introduced in Appendix C.
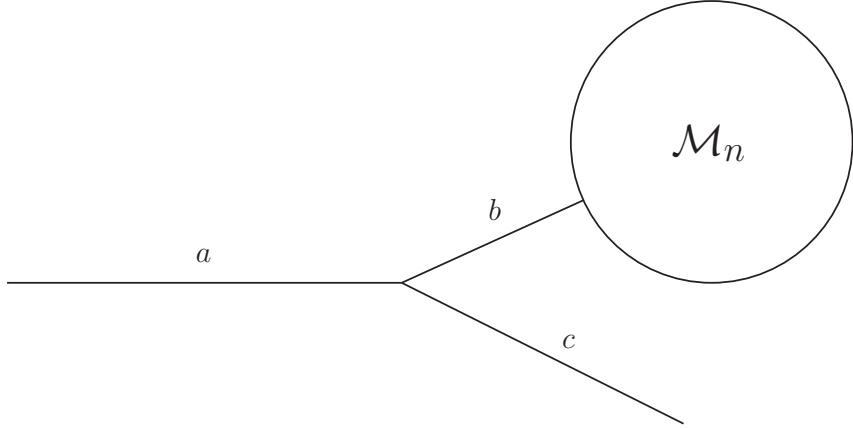
Figure 6.5: Kinematics of a generic spacelike initial state parton branching. While the splitting of one initial state parton a into partons b and c is explicitly depicted, the rest of the matrix element is denoted by the gray blob.

Herein, the linearity of the momentum conservation equation, $p_a = p_b + p_c$, and the Jacobians in the collinear approximation, derived from eq. (6.2.3) have been used. Thus, the $(n+1)$-parton matrix element in the collinear approximation, summed over all possible splitter partons a and all possible splitting products $b = g, q$, reads

$$d\sigma_{n+1} = d\sigma_n \otimes \sum_{a=1}^{n} \sum_{b=q,g} \frac{dt}{t} \, dz \, \frac{d\phi}{2\pi} \frac{\alpha_s}{2\pi} \, F_{ba}(z, \phi) \, . \tag{6.2.10}$$

Integrating out the spin dependence of $F_{ba}(z; \lambda_a, \lambda_b, \lambda_c)$, i.e. the dependence on the azimuthal angle ϕ, using eq. (6.2.7) leads to

$$d\sigma_{n+1} = d\sigma_n \cdot \sum_{a=1}^{n} \sum_{b=q,g} \frac{dt}{t} \, dz \, \frac{\alpha_s}{2\pi} \, \hat{P}_{ba}(z) \, . \tag{6.2.11}$$

Thus, the $(n+1)$-parton cross section in the collinear approximation can be expressed in terms of the n-parton cross section times a sum over unregularised Altarelli-Parisi splitting kernels describing all possible splittings, averaged over spins and polarisations of both the splitter and the splittees. The approximated $(n+1)$-parton cross section of eq. (6.2.10) possesses the same collinear divergence structure as the full $(n+1)$-parton cross-section, because it is derived in exactly these infrared divergent limits. For eq. (6.2.11), however, this is not necessarily the case due to the averaging over the intermediate parton a's spin/polarisation. Nonetheless, the approximation in the form of eq. (6.2.11) carries a great practical advantage: it only requires a spin-summed n-parton cross section as input and the convolution of eq. (6.2.10) reduces to a trivial product. Thus, no information about the n-parton matrix element is required beyond its parton flavours and momenta to calculate its dominant higher order corrections.

Turning now to processes with initial state partons and the associated spacelike parton branchings where one initial state parton a splits into two partons the kinematics are as follows: parton b, which is the previous n-parton process' initial state, and parton c which is

part of the new final state. Parton a is now the initial state of the $(n+1)$-parton process, as depicted in Figure 6.5. The kinematic invariants are assumed to have the following hierarchy

$$|p_a^2|, p_c^2 \ll |p_b^2| \equiv t \, . \tag{6.2.12}$$

The splitting variable z is defined as in eq. (6.2.2), i.e.

$$z = z_b = 1 - z_c = \frac{E_b}{E_a} = 1 - \frac{E_c}{E_a} \, . \tag{6.2.13}$$

Thus, the virtuality of parton b can be expressed as

$$t = |p_b^2| = |q^2| = 2 E_a E_c \left(1 - \cos \theta_c \right) = (1 - z) \, E_a^2 \, \theta_c^2 \, . \tag{6.2.14}$$

Again, this is directly related to the relative transverse momentum of the splitting

$$k_\perp^2 = z(1 - z) \, |q^2| = z(1 - z)^2 \, E_a^2 \, \theta_c^2 \, , \tag{6.2.15}$$

and, again, also eq. (6.2.5) holds for initial state splittings. The $(n+1)$-particle phase space can then be parametrised in this particular collinear branching as

$$\mathrm{d}\Phi_{n+1} = \mathrm{d}\Phi_n \cdot \frac{1}{32\pi^3} \, \mathrm{d}t \, \frac{\mathrm{d}z}{z} \, \mathrm{d}\phi \, , \tag{6.2.16}$$

following analogous steps to eq. (6.2.9). However now also the parton flux changes, obeying the relation

$$\mathcal{F}(E_b) = \mathcal{F}(z \, E_a) = z \, \mathcal{F}(E_a) \, , \tag{6.2.17}$$

and, thus, introducing again a factor z to eq. (6.2.16). Consequently, the $(n+1)$-parton collinearly approximated cross section factorises as in the case of final state branchings, eq. (6.2.10)

$$\mathrm{d}\sigma_{n+1} = \mathrm{d}\sigma_n \otimes \sum_{b=1}^{2} \sum_{a=q,g} \frac{\mathrm{d}t}{t} \, \mathrm{d}z \, \frac{\mathrm{d}\phi}{2\pi} \, \frac{\alpha_s}{2\pi} \, F_{ba}(z, \phi) \, , \tag{6.2.18}$$

or, averaging over spins and polarisations,

$$\mathrm{d}\sigma_{n+1} = \mathrm{d}\sigma_n \cdot \sum_{b=1}^{2} \sum_{a=q,g} \frac{\mathrm{d}t}{t} \, \mathrm{d}z \, \frac{\alpha_s}{2\pi} \, \hat{P}_{ba}(z) \, . \tag{6.2.19}$$

Thus, the same formula holds for initial and final state splittings, summing the splitting functions over all partons of the n-parton process for all possible splitting, i.e into/from quarks or gluons.
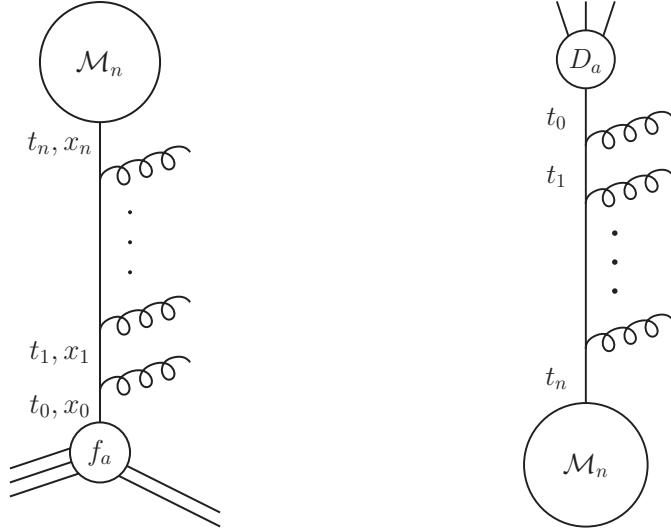
Figure 6.6: Graphical representation of (constrained) initial state and (unconstrained) final state evolution in the case of a quark line. Successive gluon emissions reduce the scale of the quark line from $t_n \sim Q^2$ at the hard process down to t_0, the infrared cut-off of the evolution signaling the onset of non-perturbative effects. The x_i in case of initial state evolution signify the momentum fraction of the parton at scale t_i of the proton it originates from. Both the t_i and the x_i obey the strict relations $t_0 < t_1 < \ldots < t_n$ and $x_0 > x_1 > \ldots > x_n$, respectively.

6.2.2 Parton evolution

As noted already at the very start of this chapter, for splittings in the soft-collinear limit factors of $\alpha_s \log(Q^2/\kappa^2)$ occur, where the logarithm is produced by integrating over $\hat{P}_{ba}(z)$ down to some resolution scale κ. If this resolution scale κ^2 is of the order of the hard interaction scale Q^2, the logarithm is of order one and the usual behaviour of the perturbative series in α_s is recovered. If now much softer objects are to be resolved $\kappa^2 \ll Q^2$ then the logarithm is large and higher orders in α_s do not decrease in size. Hence, these contributions have to be considered from every order in the perturbative series. The factorised cross section of both eq. (6.2.11) and eq. (6.2.19) now provides the means to analyse the dominant terms order-by-order iteratively.

Taking Figure 6.6 as a guideline, the parton evolution is again described by the DGLAP equation, eq. (6.1.13). In this context, the parton distribution function f_a may be the parton distribution of parton a inside the initial state hadron probed at scale t and momentum fraction x, or it is the momentum fraction distribution of the produced final state parton at scale t. Both follow the same evolution equation, although their direction of evolution differs, cf. Section 6.2.1. Being defined in terms of the regularised Altarelli-Parisi splitting kernels, the singularities present at $z \to 1$ corresponding to soft gluon emissions are regularised. While the above form is particularly useful for analytical analyses of the dominant higher order corrections in the collinear limit, they are not that well suited for studying particular properties of individual parton splittings or differential parton distributions. To this end, consider the probability of a parton a to emit any parton b at any scale t' inbetween the scales $t \sim Q^2$ and some infrared cut-off scale t_0. This is given by the considerations of the

last section by

$$
\mathcal{P}_a(t, t_0) \;=\; \sum_{b=q,g} \int_{t_0}^{t} \frac{\mathrm{d}t'}{t'} \int \mathrm{d}z \, \frac{\alpha_s(t')}{2\pi} \, \hat{P}_{ba}(z) \,, \tag{6.2.20}
$$

in collinear limit at leading order. Herein, the soft gluon singularites are still present in the unregularised kernels $\hat{P}_{ab}(z)$ and have to be regularised by tightening the integration boundaries to $z_{\min} > 0$ and $z_{\max} < 1$. The collinear singularity in $1/t$ is similarly regularised by introducing the scale t_0 as a lower limit on the t integration. Emissions outside the integration region, i.e. having either $z > z_{\max}$, $z < z_{\min}$ or $t' < t_0$, are considered unresolvable. Once parton a has radiated at scale t' and is thereby transformed into parton b, the probability it radiates again inbetween t' and t_0 is given by

$$
\mathcal{P}_b(t', t_0) \;=\; \sum_{c=q,g} \int_{t_0}^{t'} \frac{\mathrm{d}t''}{t''} \int \mathrm{d}z \, \frac{\alpha_s(t'')}{2\pi} \, \hat{P}_{cb}(z) \,. \tag{6.2.21}
$$

Consequently, the resulting distribution of the number of emissions between two scales t and t_0 follows Poisson statistics. Therefore, the probability of no emission inbetween both scales is given by

$$
\begin{aligned}
\Delta_a(t, t_0) &\equiv \left. \frac{\mathcal{P}_a(t, t_0)^n}{n!} \exp[-\mathcal{P}_a(t, t_0)] \right|_{n=0} \\
&= \exp\left[-\sum_{b=q,g} \int_{t_0}^{t} \frac{\mathrm{d}t'}{t'} \int \mathrm{d}z \, \frac{\alpha_s(t')}{2\pi} \, \hat{P}_{ab}(z) \right] \,.
\end{aligned} \tag{6.2.22}
$$

This is the so-called Sudakov form factor, representing probability of evolving from scale t to scale t_0 without any resolvable emission. It in fact sums all collinearly enhanced virtual contributions and non-resolvable real emissions to all orders. Therein, the virtual contributions are included via the unitarity of the splitting probability and the Kinoshita-Lee-Nauenberg theorem [91, 92], cf. eqs. (6.1.5)-(6.1.8). The phase space boundaries on the z integration can in principle be chosen arbitrarily. However, arguing on physical grounds, they should be chosen such, that the criterion of non-resolvability is fulfilled in a similar way both for the regions $z > z_{\max}$, $z < z_{\min}$ and the region $t' < t_0$. This leads to the relation

$$
z(1-z) > \frac{t_0}{t} \tag{6.2.23}
$$

for timelike final state partons. Thus,

$$
z_{\max} = 1 - z_{\min} \cong \frac{t_0}{t} \qquad \text{for } t_0 \ll t \,. \tag{6.2.24}
$$

With the help of the Sudakov form factor the DGLAP equation, eq. (6.1.13), can now be rewritten for resolved emissions in terms of the unregularised Altarelli-Parisi splitting functions as

$$
t \frac{\partial}{\partial t} f_a(x, t) = \sum_{b=q,g} \int \frac{\mathrm{d}z}{z} \frac{\alpha_s(t)}{2\pi} \, \hat{P}_{ab}(z) \, f_b\left(\frac{x}{z}, t\right) + \frac{f_a(x, t)}{\Delta_a(t, t_0)} t \frac{\partial}{\partial t} \Delta_a(t, t_0) \,. \tag{6.2.25}
$$

Of course, the same phase space restrictions to the z integral apply as in the Sudakov form factor itself. They again have been omitted for brevity. This then leads to an equation similar in form to the DGLAP equation, only now for f_a/Δ_a instead of f_a itself

$$t \frac{\partial}{\partial t} \frac{f_a(x,t)}{\Delta_a(t,t_0)} = \frac{1}{\Delta_a(t,t_0)} \sum_{b=q,g} \int \frac{\mathrm{d}z}{z} \frac{\alpha_s(t)}{2\pi} \hat{P}_{ab}(z) f_b\left(\frac{x}{z},t\right) . \tag{6.2.26}$$

In this form, this equation can be integrated, giving

$$f_a(x,t) = \Delta_a(t,t_0) f_a(x,t_0) + \sum_{b=q,g} \int_{t_0}^{t} \frac{\mathrm{d}t'}{t'} \frac{\Delta_b(t,t_0)}{\Delta_b(t',t_0)} \int \frac{\mathrm{d}z}{z} \frac{\alpha_s(t')}{2\pi} \hat{P}_{ab}(z) f_b\left(\frac{x}{z},t'\right) . \tag{6.2.27}$$

Using the property of the Sudakov form factorisation

$$\Delta_a(t_1,t_2) = \Delta_a(t_1,t') \cdot \Delta_a(t',t_2) , \tag{6.2.28}$$

which can directly be derived from eq. (6.2.22), corresponding to independent emissions, this simplifies to

$$f_a(x,t) = \Delta_a(t,t_0) f_a(x,t_0) + \sum_{b=q,g} \int_{t_0}^{t} \frac{\mathrm{d}t'}{t'} \int \frac{\mathrm{d}z'}{z'} \frac{\alpha_s(t')}{2\pi} \hat{P}_{ab}(z') \Delta_b(t,t') f_b\left(\frac{x}{z'},t'\right) . \tag{6.2.29}$$

This makes evolution of parton a evident: the first term gives the probability that parton a evolves from scale t to scale t_0 without any resolvable emission, while second term describes the probability of evolving from scale t down to scale of the first branching t' where it transforms into parton b. The evolution of parton b is then described by reinserting eq. (6.2.29) into itself, i.e.

$$f_b\left(\frac{x}{z'},t'\right) = \Delta_b(t',t_0) f_b\left(\frac{x}{z'},t_0\right) + \sum_{c=q,g} \int_{t_0}^{t'} \frac{\mathrm{d}t''}{t''} \int \frac{\mathrm{d}z''}{z''} \frac{\alpha_s(t'')}{2\pi} \hat{P}_{bc}(z'') \Delta_c(t',t'') f_c\left(\frac{x}{z'z''},t''\right) .$$

Thus, the differential branching pattern can be computed iteratively with the help of eq. (6.2.29).

6.2.3 Scale choices for the running coupling

In the previous section the coupling α_s was always taken to be running, i.e. varying with the scale of the respective branching. This running is defined via the QCD β-function as

$$\alpha_s(\mu) = \frac{\alpha_s(\mu_0)}{1 + \alpha_s(\mu_0)\beta_0 \log\frac{\mu}{\mu_0}} \tag{6.2.30}$$

However, the scale μ was always only indicated as being of the order of the branching scale t. Taking t simply as the virtuality $|q^2|$ of the branching parton then the Sudakov form factor of eq. (6.2.22) behaves in the limit $t \to \infty$ keeping t_0 fixed as

$$\Delta_a(t,t_0) \propto \left(\frac{t_0}{t}\right)^{c_1} \left(\frac{\alpha_s(t)}{\alpha_s(t_0)}\right)^{c_2} \propto \left(\frac{t_0}{t}\right)^{c_3} , \tag{6.2.31}$$

with the positive constants c_1, c_2 and c_3. Thus, at large t, the Sudakov form factor vanishes like a negative power of t. [199] show that instead $t = k_\perp^2 = z(1-z)|q^2|$ should be used as its argument. Expanding eq. (6.2.30) to next-to-leading order then gives

$$\alpha_s(k_\perp^2) = \alpha_s(|q^2|) + \beta_0 \log[z(1-z)] \frac{\alpha_s^2(|q^2|)}{4\pi} + \mathcal{O}(\alpha_s^3) \,. \tag{6.2.32}$$

Combining this with the $(1-z)^{-1}$ singularity found in all gluon emission unregularised Altarelli-Parisi splitting functions, $\hat{P}_{ab}(z)$, a next-to-leading order behaviour of the form

$$\alpha_s(k_\perp^2) \frac{1}{1-z} \xrightarrow{\ z \to 1\ } \frac{\log[1-z]}{1-z} \,. \tag{6.2.33}$$

This behaviour is indeed found in explicit calculations of higher-order corrections to the splitting functions $\hat{P}_{ab}(z)$. Thus, the Sudakov form factor vanishes more rapidly in the limit $t \to \infty$

$$\Delta_a(t, t_0) \ \propto \ \left(\frac{\alpha_s(t)}{\alpha_s(t_0)} \right)^{c_4 \log t} \,, \tag{6.2.34}$$

enhancing the radiation probability.

6.3   Soft emission corrections

In the previous sections a formalism has been reviewed that takes into account collinear enhancements of parton branchings to all orders in perturbation theory. However, there also exist enhancements of higher order corrections originating in the emission of soft massless gauge bosons: gluons in QCD and photons in QED. Evidences of the associated soft divergences have been present throughout the derivation of the DGLAP equation and the Sudakov form factor in the form of diverging unregularised Altarelli-Parisi splitting functions in the limit of $z \to 1$ and $z \to 0$. As shown in Appendix C, the soft divergence for $z \to 0$, present in $\hat{P}_{gg}(z)$ only, can be mapped by symmetry arguments onto the divergence $z \to 1$. However, these soft gluon divergences are not restricted to the collinear limit, but are are distributed all over the real emission phase space. This soft divergence is universal[6], and takes the same form as that derived in Part I of this thesis.

In the limit of soft gluon emissions the next-to-leading order amplitude factorises into eikonals, equivalently to eq. (2.2.1),

$$\begin{aligned}
\mathrm{d}\sigma_{n+1} &= \mathrm{d}\sigma_n \otimes \frac{\alpha_s}{2\pi} \omega \mathrm{d}\omega \frac{\mathrm{d}\Omega}{2\pi} \sum_{i,j} C_{ij} \frac{p_i \cdot p_j}{p_i \cdot q\, p_j \cdot q} \\
&= \mathrm{d}\sigma_n \otimes \frac{\alpha_s}{2\pi} \omega \mathrm{d}\omega \frac{\mathrm{d}\Omega}{2\pi} \sum_{i,j} \frac{-C_{ij}}{2} \left[\frac{p_i}{p_i \cdot q} - \frac{p_j}{p_j \cdot q} \right]^2 \,.
\end{aligned} \tag{6.3.1}$$

The n-parton cross section is convoluted with the colour factor C_{ij} in the spirit of [51]. Its explicit form is

$$C_{ij} = -\mathbf{T_i} \cdot \mathbf{T_j} = C_{ji} \,, \tag{6.3.2}$$

---

[6]Universal in this context means, that the soft limit is determined by the partons' charges and momenta only. Especially, it is independent of the partons' spin and flavour, contrary to the collinear limit.

where $\mathbf{T_i}$ and $\mathbf{T_j}$ are the (colour) charges of partons i and j. Thus, in QCD the C_{ij} are matrices in colour space. The sum in eq. (6.3.1) extends over all ordered pairs of charged particles, whose momenta are denoted p_i and p_j. q is the gluon momentum and ω is its energy. $d\Omega$ is the solid angle element. The second line of eq. (6.3.1) is the generalisation to massive partons emitting the soft massless gluon. The colour weighted some of the soft eikonals is also called the antenna pattern of the process.

In this form one sees that the simple single-parton evolution picture of the previous section, manifestly evident in the various forms of the DGLAP equation, is not suited to describe the soft divergence structure of a process. Thus, soft gluons are emitted coherently by the entire ensemble of charged particles. Further, since the soft limit is spin-independent, eq. (6.3.1) is the full equivalent of eq. (6.2.10). Ansatzes to incorporate both limits take the dipole factorisation as a basis and add DGLAP evolution on top of it, such that

$$d\sigma_{n+1} = d\sigma_n \otimes \sum_{i,j} dV_{ij} \tag{6.3.3}$$

with

$$dV_{ij} \rightarrow \begin{cases} \frac{dt}{t} dz \frac{d\phi}{2\pi} \frac{\alpha_s}{2\pi} F_{gi}(z,\phi) & \text{for } p_i \cdot k \rightarrow 0, \omega \text{ finite} \\[2mm] \frac{dt}{t} dz \frac{d\phi}{2\pi} \frac{\alpha_s}{2\pi} F_{gj}(z,\phi) & \text{for } p_j \cdot k \rightarrow 0, \omega \text{ finite} \\[2mm] \omega d\omega \frac{d\Omega}{2\pi} \frac{\alpha_s}{2\pi} C_{ij} \frac{p_i \cdot p_j}{p_i \cdot q \, p_j \cdot q} & \text{for } \omega \rightarrow 0 \, . \end{cases} \tag{6.3.4}$$

Examples of such an ansatz are the Catani-Seymour dipole subtraction [51, 95, 52] and the antenna factorisation [200, 201, 202, 203].

For QCD there are further methods to approximately incorporate both limits at the same time. In the limit of an infinite number of colours, $N_c \rightarrow \infty$, the colour correlation matrices read [62]

$$C_{ij} = -\mathbf{T_i} \cdot \mathbf{T_j} \rightarrow \begin{cases} \mathbf{T_i}^2 + \mathcal{O}(N_c^{-2}) & \text{for } i = q \\[2mm] \frac{1}{2} \mathbf{T}_i^2 + \mathcal{O}(N_c^{-2}) & \text{for } i = g \end{cases} \equiv C_i \, . \tag{6.3.5}$$

Thus, all $C_{ij} \equiv C_i$ depend only on the emitting parton. Further, all C_i are real valued numbers and the convolution of eq. (6.3.1) reduces to an ordinary product; the sum over ordered parton pairs i, j may be rewritten as a sum over single emitting partons of the n-body phase space. Similarly, the soft-collinear splitting functions V_{ij} reduce to V_i with the following properties

$$dV_{ij} \rightarrow dV_i = \begin{cases} \frac{dt}{t} dz \frac{d\phi}{2\pi} \frac{\alpha_s}{2\pi} F_{gi}(z,\phi) & \text{for } p_i \cdot k \rightarrow 0, \omega \text{ finite} \\[2mm] \omega d\omega \frac{d\Omega}{2\pi} \frac{\alpha_s}{2\pi} C_i \frac{p_i \cdot \varepsilon}{p_i \cdot q} & \text{for } \omega \rightarrow 0 \end{cases} \, . \tag{6.3.6}$$

ε is the polarisation of the external soft gluon. This enables to retain the simple single-parton evolution picture, however, coming at the cost of large-N_c accuracy in the soft limit only. These terms can also be approximately recovered by either using $t = \theta$ as the evolution variable, which is a valid choice according to eq. (6.2.5) and has been used in [204, 205], or by using a conventional evolution variable $t = |q^2|$ and imposing an additional veto, i.e. $\theta_0 < \theta_1 < ... < \theta_n$, cf. [206].

Chapter 7

Parton showers and fixed order corrections – The reinterpretation and automisation of the POWHEG method

The DGLAP resummation, as reviewed in the last chapter, allows for the constructing of parton showers, supplementing Born level processes with higher order real and virtual correction approximated in the collinear limit. Such parton showers are successful tools to describe intrajet evolution. However, by construction they grossly misestimate the amount and radiation pattern of hard wide angle emission. Further, employing parton showers only to estimate higher order effects lack, due to their unitarity, the overall normalisation of a true next-to-leading order calculation, i.e. the cross section of the inclusive process under consideration. This roots in the fact that the associated K-factor, the ratio of the leading and next-to-leading order cross section, is largely determined by non-logarithmic contributions. Further, to accurately estimate uncertainties intrinsic to perturbative calculations, which manifest themselves for instance in uncertainties related to choices of renormalisation and factorisation scales, full next-to leading order corrections are needed.

Two different methods to achieve the systematic inclusion of a complete NLO calculation in a parton shower Monte-Carlo: MC@NLO [11] and POWHEG [12, 13]. The latter one is adopted in this thesis and reformulated into a matrix element reweighted parton shower supplemented with a next-to-leading order weight. This reformulation facilitates an automated implementation, provided tree-level matrix element for the real emission correction are known. The framework of the SHERPA event generator provides both a parton shower, the CSS [62] based on Catani-Seymour splitting kernels [51, 52], and two tree-level matrix element generators, COMIX [26] and AMEGIC++ [25]. AMEGIC++ also contains an automated implementation of the Catani-Seymour subtraction terms [51, 52], rendering it well-suited for the present purpose.

This part of this thesis therefore reports on the methods and findings published in [65]. It outlines as follows: Section 7.1, after briefly introducing the notation facilitating the purpose of this chapter, reviews the decomposition real emission matrix elements into their singular limits employing a single-leg language. This single-leg formulation is well suited to discuss these matrix elements on the same footing as the DGLAP equation in the spirit of Section 6.2.1. This is then used to construct an abstract parton shower formalism in Section 7.2, implementing the DGLAP resummation in the form of Section 6.2.2. Section 7.3 then reviews a possibility to account for non-logarithmic higher-order corrections not present in the collinear approximation. Finally, Section 7.4 reformulates the POWHEG technique as an advanced method of effecting such fixed-order next-to-leading corrections upon an existing parton shower, supplementing it with a next-to-leading order weight. To guarantee full next-to-leading order accuracy for any observable, this reformulation of the POWHEG

method intimately links the decomposition of the real emission matrix elements by the parton shower and the subtraction terms. This will be discussed in great detail in Section 7.5. Section 7.6 then elaborates on the ambiguities of the POWHEG method and Section 7.7 uses these ambiguities to relate it to the MC@NLO method. Section 7.8 then briefly introduces the relevant parts of the SHERPA event generator necessary for its automation. The only missing bit of the NLO calculation driving the POWHEG method are the virtual contributions, which still need to be interfaced on a process-by-process basis. It is the first time that the POWHEG method has been automated using dipole subtraction rather than the Frixione-Kunszt-Signer method [207, 208]. The overall quality of the implementation will be exemplified in a number of characteristic processes containing only a single coloured line (i.e. two colour-charged particles) at the Born level in Section 7.9, including the hitherto unpublished case of W-pair production in hadronic collisions. Section 7.10 on the other hand presents results for non-trivial colour structures. Section 7.11 finally summarises the results.

7.1 Decomposition of the real-emission cross sections

This and the two following section will introduce the notation and the formalism necessary to discuss the formulation and implementation of the POWHEG method to incorporate next-to-leading order corrections into parton shower Monte Carlo generators in order to reach hadron level predictions with next-to-leading order accuracy in perturbative QCD and non-perturbative corrections calculated on an event-by-event basis. Therefore, the route of Section 6.2 is pursued, but with a notation adapted to the task at hand, precisely detailing all components entering a certain expression to explicitly keep track of all ratios of parton distributions, symmetry factors and the like. The starting point of the discussion is the factorisation theorem underlying the specific parton-shower model, like the DGLAP equation [174, 175, 176, 93], the colour-dipole model [209, 210, 211], Catani-Seymour factorisation [51, 52] or antenna factorisation [200, 201, 202, 203]. Except in collinear factorisation, the splitting functions of the parton shower depend on (at least) one additional parton, which is often referred to as the "spectator". In order to make this connection explicit, the notation of a dipole-like factorisation is adopted, which is sufficiently general to discuss all relevant features.

In the following, sets of n particles in a $2 \to (n-2)$ process will summarily be denoted by $\{\vec{a}\} = \{a_1, \ldots, a_n\}$, and the particles will be specified through their flavours $\{\vec{f}\} = \{f_1, \ldots, f_n\}$ and momenta $\{\vec{p}\} = \{p_1, \ldots, p_n\}$. The generic expression for a fully differential Born-level cross section in a scattering process with $(n-2)$ final-state particles can be written as a sum over all contributing flavour combinations as

$$\mathrm{d}\sigma_B(\{\vec{p}\}) = \sum_{\{\vec{f}\}} \mathrm{d}\sigma_B(\{\vec{a}\}) , \qquad \text{where} \qquad \mathrm{d}\sigma_B(\{\vec{a}\}) = \mathrm{d}\Phi_B(\{\vec{p}\}) \, \mathrm{B}(\{\vec{a}\}) . \qquad (7.1.1)$$

The individual terms in the sum are given by

$$\mathrm{B}(\{\vec{a}\}) = \mathcal{L}(\{\vec{a}\}) \, \mathcal{B}(\{\vec{a}\}) , \qquad \mathcal{B}(\{\vec{a}\}) = \frac{1}{F(\{\vec{p}\})} \frac{1}{S(\{\vec{f}\})} \, |\mathcal{M}_B|^2 (\{\vec{a}\}) ,$$

$$\mathrm{d}\Phi_B(\{\vec{p}\}) = \frac{\mathrm{d}x_1}{x_1} \frac{\mathrm{d}x_2}{x_2} \, \mathrm{d}\Phi_B(\{\vec{p}\}) , \quad \mathcal{L}(\{\vec{a}\}; \mu^2) = x_1 f_{f_1}(x_1, \mu^2) \, x_2 f_{f_2}(x_2, \mu^2) . \qquad (7.1.2)$$

Here, $|\mathcal{M}_B|^2 (\{\vec{a}\})$ denotes the partonic matrix element squared, with all factors due to averaging over initial state quantum numbers such as spin or colours absorbed into it, and $\mathrm{d}\Phi_B(\{\vec{p}\})$ is the corresponding differential n-particle partonic phase-space element; $S(\{\vec{f}\})$

is the symmetry factor due to identical flavours associated to the partonic subprocess, while $F(\{\vec{p}\})$ denotes the flux factor and $\mathcal{L}$ is the parton luminosity given by the corresponding parton distribution functions (PDFs). In the case of leptonic initial states, ignoring QED initial state radiation, the parton distribution functions $f(x, \mu^2)$ are replaced by $\delta(1-x)$.

In a similar fashion, the real-emission part of the QCD next-to-leading order cross section can be written as a sum, this time over parton configurations $\{a_1, \ldots, a_{n+1}\}$, i.e. including one additional parton. A corresponding subprocess cross section reads

$$\mathrm{d}\sigma_R(\{\vec{a}\}) = \mathrm{d}\Phi_R(\{\vec{p}\})\, \mathrm{R}(\{\vec{a}\})\,. \tag{7.1.3}$$

At this point, it is helpful to introduce a notation for mappings from real-emission parton configurations to Born parton configurations. Such mappings combine the partons a_i and a_j into a common "mother" parton $a_{\widetilde{ij}}$, in the presence of the spectator a_k by defining a new flavour $f_{\widetilde{ij}}$ and by redefining the particle momenta. To be specific,

$$b_{ij,k}(\{\vec{a}\}) = \left\{ \begin{array}{c} \{\vec{f}\} \setminus \{f_i, f_j\} \cup \{f_{\widetilde{ij}}\} \\ \{\vec{p}\} \to \{\vec{\tilde{p}}\} \end{array} \right.\,. \tag{7.1.4}$$

The flavour of the "mother" parton, $f_{\widetilde{ij}}$, is thereby fixed unambiguously by the QCD interactions, while the flavour of the spectator, f_k, remains unaltered, cf. also [51, 52]. The momentum map guarantees that all partons are kept on their mass shell.

Conversely, any Born parton configuration and a related branching process $\widetilde{ij}, \tilde{k} \to ij, k$ determine the parton configuration of a real-emission subprocess as

$$r_{\widetilde{ij},\tilde{k}}(f_i, \Phi_{R|B}\,; \{\vec{a}\}) = \left\{ \begin{array}{c} \{\vec{f}\} \setminus \{f_{\widetilde{ij}}\} \cup \{f_i, f_j\} \\ \{\vec{\tilde{p}}\} \to \{\vec{p}\} \end{array} \right.\,. \tag{7.1.5}$$

The radiative variables $\Phi_{R|B}$ are thereby employed to turn the n-parton momentum configuration into an n+1-parton momentum configuration using the inverse of the phase-space map defined by eq. (7.1.4). The flavour f_j is again determined unambiguously by the QCD interactions. Here, also two obvious generalisations of eq. (7.1.4) shall be defined, $b_{ij,k}(\{\vec{f}\})$ and $b_{ij,k}(\{\vec{p}\})$, which act on the parton flavours and on the parton momenta only. Correspondingly, such generalisations exist for eq. (7.1.5).

In the soft and collinear limits, the partonic matrix element squared, $\mathcal{R}(\{\vec{a}\})$, can be decomposed as a sum of terms $\mathcal{D}_{ij,k}(\{\vec{a}\})$,

$$\mathcal{R}(\{\vec{a}\}) \to \sum_{\{i,j\}} \sum_{k \neq i,j} \mathcal{D}_{ij,k}(\{\vec{a}\})\,. \tag{7.1.6}$$

This corresponds directly to eq. (6.3.3) incorporating both the collinear limit of eq. (6.2.6) and eq. (6.2.10), and the soft limit of eq. (6.3.1) in the spirit of [51, 52]. These terms $\mathcal{D}_{ij,k}(\{\vec{a}\})$ factorise into a Born-level term and a universal splitting kernel, encoding the transition of $a_{\widetilde{ij}}$ to a_i and a_j. The splitting is associated with a universal procedure for factorising the phase-space integral into a Born level part and a one-particle radiative phase space,

$$\mathrm{d}\Phi_R(\{\vec{p}\}) = \mathrm{d}\Phi_B(b_{ij,k}(\{\vec{p}\}))\, \mathrm{d}\Phi_{R|B}^{ij,k}(\{\vec{p}\})\,. \tag{7.1.7}$$

The existence of universal decompositions like in eq. (7.1.6) forms the basis of subtraction methods like the Catani-Seymour dipole subtraction [51, 52], antenna subtraction [200, 201, 202, 203], or the subtraction method of Frixione, Kunszt, and Signer [207, 208, 212]. It also serves as starting point for the construction of parton shower algorithms [62, 213, 214], which

aim at approximating parton emissions in the collinear and soft limits of the radiative phase space, to resum the associated large logarithms, cf. Section 6.2 and 7.2.

However, it is important to stress that, also away from the infrared limits, $\mathcal{R}(\{\vec{a}\})$ can be decomposed into a number of terms $\mathcal{R}_{ij,k}$ such each $\mathcal{R}_{ij,k}$ contains exactly one singular limit, analogous to the $\mathcal{D}_{ij,k}$,

$$\mathcal{R}_{ij,k}(\{\vec{a}\}) := \rho_{ij,k}(\{\vec{a}\}) \, \mathcal{R}(\{\vec{a}\}) \,. \tag{7.1.8}$$

The projector $\rho_{ij,k}(\{\vec{a}\})$ is discussed in great detail in Section 7.5. For the present purpose the precise form of the $\rho_{ij,k}(\{\vec{a}\})$ is of no interest. They only need to fulfil the following completeness relation

$$\sum_{\{i,j\}} \sum_{k \neq i,j} \rho_{ij,k}(\{\vec{a}\}) = 1 \qquad \forall \, \{\vec{a}\} \in \Phi_R \,, \tag{7.1.9}$$

and each $\rho_{ij,k}(\{\vec{a}\})$ must project on exactly one singular limit, i.e.

$$\mathcal{R}_{ij,k}(\{\vec{a}\}) \to \mathcal{D}_{ij,k}(\{\vec{a}\}) \,. \tag{7.1.10}$$

Thus, eq. (7.1.3) can now be rewritten as a sum of trivially factorised contributions

$$\mathrm{d}\sigma_R(\{\vec{a}\}) = \sum_{\{i,j\}} \sum_{k \neq i,j} \mathrm{d}\sigma_B(b_{ij,k}(\{\vec{a}\})) \, \mathrm{d}\sigma_{R|B}^{ij,k}(\{\vec{a}\}) \,, \tag{7.1.11}$$

where

$$\mathrm{d}\sigma_{R|B}^{ij,k}(\{\vec{a}\}) = \mathrm{d}\Phi_{R|B}^{ij,k}(\{\vec{p}\}) \, \frac{\mathrm{R}_{ij,k}(\{\vec{a}\})}{\mathrm{B}(b_{ij,k}(\{\vec{a}\}))} \,. \tag{7.1.12}$$

$\mathrm{d}\Phi_{R|B}^{ij,k}(\{\vec{p}\})$ are now exactly the radiation variables in the specific singular limit of $\mathcal{R}_{ij,k}$. Thus, according to Section 6.2.1, it can be written in terms of the collinear radiation variables $\mathrm{d}t$, $\mathrm{d}z$ and $\mathrm{d}\phi$. Further, $\mathrm{R}_{ij,k}(\{\vec{a}\}) = \mathcal{L}(\{\vec{a}\})\mathcal{R}_{ij,k}(\{\vec{a}\})$. These equations are key ingredients to understanding and implementing the POWHEG method.

7.2 Construction of a parton shower

This section aims at the abstract formulation of a generic parton shower algorithm, wherein the notation emphasises the single-leg evolution inherent to the DGLAP resummation. However, due to the requirement of local momentum conservation the presence of one or several spectators is strictly necessary. Through this notation the generalisation to dipole or even multipole based parton showers is trivial. Further, this notation also enables a straightforward correction of the parton shower approximation to the exact matrix elements discussed in the last section.

As was realised in Section 6.3, the non-Abelian nature of QCD prevents the terms $\mathcal{D}_{ij,k}$ in eq. (7.1.6) to factorise on the level of squared matrix elements, including all colour contributions. To arrive at a practical model for a parton shower, sub-leading colour configurations are therefore neglected, which leads to an *assumed* factorisation on the level of squared matrix elements. In the infrared limits one can then write

$$\mathcal{D}_{ij,k}(\{\vec{a}\}) \to \mathcal{B}(b_{ij,k}^{(\mathrm{PS})}(\{\vec{a}\})) \, \frac{S(b_{ij,k}^{(\mathrm{PS})}(\{\vec{f}\}))}{S(\{\vec{f}\})} \, \frac{1}{2 \, p_i p_j} \, 8\pi \, \alpha_s \, \mathcal{K}_{ij,k}(p_i, p_j, p_k) \equiv \mathcal{R}_{ij,k}^{(\mathrm{PS})}(\{\vec{a}\}) \,,$$

the parton shower's approximation to the real emission matrix element. Therein, the set of momenta $b_{ij,k}^{(PS)}(\{\vec{p}\})$ is determined by the phase-space map of the parton-shower model.[1] The parton map $b_{ij,k}^{(PS)}(\{\vec{a}\}))$ as well as its inverse $r_{\widetilde{ij},\tilde{k}}^{(PS)}(f_i, \Phi_{R|B}; \{\vec{a}\})$ are defined in full analogy to the subtraction terms' parton maps of eq. (7.1.4) and eq. (7.1.5). As noted, such an *assumed* factorisation, decoupling the colour degrees of freedom of the splitting from the ones of the leading order process, can only hold in the leading colour approximation ($N_c \to \infty$), as was shown in eq. (6.3.5). Thus, quantities $\mathcal{K}_{ij,k}$, known as the parton-shower evolution kernels which depend on the parton flavours f_i, f_j and f_k and on the radiative phase space, fulfil the limits of soft-collinear limits of eq. (6.3.6). Hence, their spin-averaged versions converge to the familiar unregularised Altarelli-Parisi splitting functions $\hat{P}_{i\,\widetilde{ij}}(z)$ in the collinear limit.

The denominator factor $2\,p_i p_j$ or any linearly dependent quantity is usually used to define the parton shower evolution variable, in the following denoted by t. Using the above model, the parton-shower approximation of eq. (7.1.12) can be derived as

$$d\sigma_{R|B}^{(PS)\,ij,k}(\{\vec{a}\}) = d\Phi_{R|B}^{ij,k}(\{\vec{p}\}) \frac{S(b_{ij,k}^{(PS)}(\{\vec{f}\}))}{S(\{\vec{f}\})} \frac{1}{2\,p_i p_j} 8\pi\,\alpha_s\,\mathcal{K}_{ij,k}(p_i, p_j, p_k) \frac{\mathcal{L}(\{\vec{a}\})}{\mathcal{L}(b_{ij,k}^{(PS)}(\{\vec{a}\}))}$$

$$= d\Phi_{R|B}^{ij,k}(\{\vec{p}\}) \frac{R_{ij,k}^{(PS)}(\{\vec{a}\})}{B(b_{ij,k}^{(PS)}(\{\vec{a}\}))} \ . \tag{7.2.2}$$

Partons produced in the parton shower are resolved at a certain evolution scale and can therefore be distinguished from partons at higher and lower scales. At most the final state two partons a_i and a_j, emerging from the same splitting process, can be seen as identical. Hence, the ratio of symmetry factors in eq. (7.1.12) changes to

$$\frac{S(b_{ij,k}^{(PS)}(\{\vec{f}\}))}{S(\{\vec{f}\})} \rightarrow \frac{1}{S_{ij}} = \begin{cases} 1/2 & \text{if } i,j > 2 \text{ and } a_i = a_j \\ 1 & \text{else} \end{cases} . \tag{7.2.3}$$

The integral over the radiative phase space can be written as

$$d\Phi_{R|B}^{ij,k}(\{\vec{p}\}) = \frac{1}{16\pi^2} dt\,dz\,\frac{d\phi}{2\pi}\,J_{ij,k}(t, z, \phi) \ , \tag{7.2.4}$$

with t the evolution variable, z the splitting variable, and ϕ an azimuthal angle. Here, J denotes the Jacobian factor, that potentially arises due to the transformation of variables. eq. (7.2.2) thus becomes

$$d\sigma_{R|B}^{(PS)\,ij,k}(\{\vec{a}\}) = \frac{dt}{t}\,dz\,\frac{d\phi}{2\pi}\,\frac{\alpha_s}{2\pi}\,\frac{1}{S_{ij}}\,J_{ij,k}(t, z, \phi)\,\mathcal{K}_{ij,k}(t, z, \phi) \frac{\mathcal{L}(\{\vec{a}\}; t)}{\mathcal{L}(b_{ij,k}^{(PS)}(\{\vec{a}\}); t)} \ , \tag{7.2.5}$$

which is the direct analogue of eq. (6.2.11). The assignment of the mother parton, the spectator and the underlying Born process can now be assumed to be fixed. Then, the sum runs over all possible real-emission configurations originating from this particular Born-level state instead. Furthermore, assuming independence of the individual emissions, i.e.

---

[1] Note that here only parton showers with local energy-momentum conservation are considered. Therefore, the phase-space maps $\{\vec{p}\}_R \to \{\vec{p}\}_B$ exist.

Poisson statistics, this leads to the constrained no-branching probability of the parton-shower model [215, 177] between the two scales t'' and t'

$$
\begin{aligned}
\Delta_{\widetilde{ij},\tilde{k}}^{(\mathrm{PS})}(t',t'';\{\vec{a}\}) &= \exp\left\{-\sum_{f_i=q,g}\int_{t'}^{t''}\frac{\mathrm{d}t}{t}\int_{z_{\min}}^{z_{\max}}\mathrm{d}z\int_0^{2\pi}\frac{\mathrm{d}\phi}{2\pi}\,J_{ij,k}(t,z,\phi)\right.\\
&\qquad\left.\times\frac{1}{S_{ij}}\frac{\alpha_s}{2\pi}\,\mathcal{K}_{ij,k}(t,z,\phi)\frac{\mathcal{L}(r_{\widetilde{ij},\tilde{k}}^{(\mathrm{PS})}(f_i,t,z,\phi;\{\vec{a}\});t)}{\mathcal{L}(\{\vec{a}\};t)}\right\}\qquad(7.2.6)\\
&= \exp\left\{-\sum_{f_i=q,g}\int_{t'}^{t''}\mathrm{d}\Phi_{R|B}^{ij,k}(\{\vec{p}\})\frac{\mathrm{R}_{ij,k}^{(\mathrm{PS})}(\{\vec{a}\})}{\mathrm{B}(b_{ij,k}^{(\mathrm{PS})}(\{\vec{a}\}))}\right\},
\end{aligned}
$$

which is the analogue of the Sudakov form factor of eq. (6.2.22) for constrained parton evolution. The integral boundaries as well as the values of t' and t'' of the second form are given implicitly according to eq. (7.2.4). It is worth noting that eq. (7.2.6) depends on the underlying Born process, since the flavour and momentum of the spectator enter as arguments of $J_{ij,k}$ and $\mathcal{K}_{ij,k}$, or $\mathrm{d}\Phi_{R|B}^{ij,k}$ and $\mathrm{R}_{ij,k}$. The ratio of $\mathcal{L}$ in eq. (7.2.6) accounts for a potential change of the parton luminosity when integrating over the initial-state phase space[2]. Note that the partons $\{\vec{a}\}$ in eq. (7.2.6) denote a Born-level set, while in (7.2.2) and (7.2.5) $\{\vec{a}\}$ denote a set of partons at real-emission level. Using the definition

$$
\Delta^{(\mathrm{PS})}(t_0,\mu^2;\{\vec{a}\}) = \prod_{\{\widetilde{ij},\tilde{k}\}}^{(\mathrm{PS})}\Delta_{\widetilde{ij},\tilde{k}}^{(\mathrm{PS})}(t_0,\mu^2;\{\vec{a}\})\qquad(7.2.7)
$$

the total cross section in the parton-shower approximation reads

$$
\begin{aligned}
\sigma_B &= \sum_{\{\vec{f}\}}\int\mathrm{d}\Phi_B(\{\vec{p}\})\,\mathrm{B}(\{\vec{a}\})\left[\Delta^{(\mathrm{PS})}(t_0,\mu^2;\{\vec{a}\})\right.\\
&\quad+\sum_{\{\widetilde{ij},\tilde{k}\}}^{(\mathrm{PS})}\sum_{f_i=q,g}\int_{t_0}^{\mu^2}\frac{\mathrm{d}t}{t}\int_{z_{\min}}^{z_{\max}}\mathrm{d}z\int_0^{2\pi}\frac{\mathrm{d}\phi}{2\pi}\,J_{ij,k}(t,z,\phi)\qquad(7.2.8)\\
&\quad\left.\times\frac{1}{S_{ij}}\frac{\alpha_s}{2\pi}\,\mathcal{K}_{ij,k}(t,z,\phi)\frac{\mathcal{L}(r_{\widetilde{ij},\tilde{k}}^{(\mathrm{PS})}(f_i,t,z,\phi;\{\vec{a}\});t)}{\mathcal{L}(\{\vec{a}\};t)}\Delta^{(\mathrm{PS})}(t,\mu^2;\{\vec{a}\})\right],
\end{aligned}
$$

or

$$
\begin{aligned}
\sigma_B &= \sum_{\{\vec{f}\}}\int\mathrm{d}\Phi_B(\{\vec{p}\})\,\mathrm{B}(\{\vec{a}\})\left[\Delta^{(\mathrm{PS})}(t_0,\mu^2;\{\vec{a}\})\right.\\
&\quad\left.+\sum_{\{\widetilde{ij},\tilde{k}\}}^{(\mathrm{PS})}\sum_{f_i=q,g}\int_{t_0}^{\mu^2}\mathrm{d}\Phi_{R|B}^{ij,k}(\{\vec{p}\})\frac{\mathrm{R}_{ij,k}^{(\mathrm{PS})}(\{\vec{a}\})}{\mathrm{B}(b_{ij,k}^{(\mathrm{PS})}(\{\vec{a}\}))}\Delta^{(\mathrm{PS})}(t,\mu^2;\{\vec{a}\})\right].
\end{aligned}\qquad(7.2.9)
$$

The superscript (PS) on the sum or product over emitter-spectator pairs denotes the fact, that only such pairings as present in the parton shower are considered. Thus, in conventional

---

[2] Note that, depending on the parton shower model, the x_i do not necessarily fulfil the relation $x_i = \tilde{x}_i/z$ [216, 64].

parton shower formulations emitter-spectator pairs whose colour correlator C_{ij}, cf. eq. (6.3.2) and eq. (6.3.5), vanishes in the large-N_c limit are discarded. The scale t_0 acts as the infrared cutoff of the parton shower. Simple inspection shows that the sum in the square bracket equals unity, since the second term can be written as

$$\int_{t_0}^{\mu^2} \mathrm{d}t \; \frac{\mathrm{d}\Delta^{(\mathrm{PS})}(t, \mu^2; \{\vec{a}\})}{\mathrm{d}t} \; . \tag{7.2.10}$$

This makes the probabilistic properties of the parton shower explicit. At the same time it also shows that this unitarity leads to the cross section in standard parton-shower Monte Carlos to be exactly the respective leading-order cross section. In order to evaluate the formal accuracy of the description of the radiation pattern, induced by the second term in the square bracket – the first term encodes the probability that there is no resolvable emission off the Born-level configuration – a corresponding observable must be introduced. This complicates the discussion somewhat and is therefore postponed to Secs. 7.4.1 and 7.4.2.

7.3   Matrix element corrections to parton showers

The aim of this section is to devise a simple method for reinstating $\mathcal{O}(\alpha_s)$ accuracy in the emission pattern of the parton shower, i.e. the hardest emission in the parton shower should follow the distribution given by the corresponding real-emission matrix element. Loosely speaking, the key idea is to replace the splitting kernels $\mathcal{K}$ with the ratio of real-emission and Born-level matrix elements. Thus, instead of the splitting kernels, this ratio is exponentiated in the Sudakov form factor and employed in simulating the splitting.

Comparing eqs. (7.1.12) and (7.2.2), a corresponding factor correcting the parton shower approximation $\mathcal{K}$ to resemble the exact ration R/B can be easily identified. Using eq. (7.2.3), this corrective weight can actually be defined per splitting function, i.e. per $\{ij, k\}$ pair. It reads

$$\begin{aligned}
w_{ij,k}(\{\vec{a}\}) &= \frac{\mathrm{d}\sigma_{R|B}^{ij,k}(\{\vec{a}\})}{\mathrm{d}\sigma_{R|B}^{(\mathrm{PS})\,ij,k}(\{\vec{a}\})} = \frac{\rho_{ij,k}^{(\mathrm{PS})}(\{\vec{a}\}) \, \mathcal{R}(\{\vec{a}\})}{\mathcal{R}_{ij,k}^{(\mathrm{PS})}(\{\vec{a}\})} \\
&= \frac{2\,p_i p_j}{8\pi\,\alpha_s} \frac{S(\{\vec{f}\})}{S(b_{ij,k}^{(\mathrm{PS})}(\{\vec{f}\}))} \frac{\rho_{ij,k}^{(\mathrm{PS})}(\{\vec{a}\}) \, \mathcal{R}(\{\vec{a}\})}{\mathcal{B}(b_{ij,k}^{(\mathrm{PS})}(\{\vec{a}\})) \, \mathcal{K}_{ij,k}(\{\vec{a}\})} \; .
\end{aligned} \tag{7.3.1}$$

$\rho_{ij,k}^{(\mathrm{PS})}$ is the parton shower's analogue of $\rho_{ij,k}$ introduced in eq. (7.1.8), it projects the real emission matrix element onto the singular regions of the parton shower. At this stage, because the parton shower only considers finite emission above some infrared cut-off t_0, both projectors are completely independent objects. Nonetheless, defining

$$\mathcal{R}^{(\mathrm{PS})}(\{\vec{a}\}) \equiv \sum_{\{i,j\}} \sum_{k \neq i,j}^{(\mathrm{PS})} \mathcal{R}_{ij,k}^{(\mathrm{PS})}(\{\vec{a}\}) \qquad \text{and} \qquad \mathcal{R}_{ij,k}^{(\mathrm{PS})}(\{\vec{a}\}) \equiv \rho_{ij,k}^{(\mathrm{PS})}(\{\vec{a}\})\mathcal{R}^{(\mathrm{PS})}(\{\vec{a}\}), \tag{7.3.2}$$

and employing the parton-shower approximation, eq. (7.2.1), gives

$$\begin{aligned}
w(\{\vec{a}\}) &= \left[\sum_{\{m,n\}} \sum_{l \neq m,n}^{(\mathrm{PS})} \frac{S(b_{mn,l}^{(\mathrm{PS})}(\{\vec{f}\}))}{S(\{\vec{f}\})} \frac{\mathcal{B}(b_{mn,l}^{(\mathrm{PS})}(\{\vec{a}\}))}{\mathcal{R}(\{\vec{a}\})} \frac{8\pi\,\alpha_s}{2\,p_m p_n} \mathcal{K}_{mn,l}(\{\vec{a}\}) \right]^{-1} \\
&= \left[\frac{\mathcal{R}^{(\mathrm{PS})}(\{\vec{a}\})}{\mathcal{R}(\{\vec{a}\})} \right]^{-1} \; .
\end{aligned} \tag{7.3.3}$$

Note that this global corrective weight is *splitter-spectator independent*. Correcting the parton shower to the full matrix element can thus be achieved through the following algorithm:

1. Determine an overestimate for eq. (7.3.3) for every possible splitting $\widetilde{ij} \to i\,j$, i.e. find a set of $W_{\widetilde{ij},f_i}$ for every Born flavour state $\{\vec{f}\}$ such that the global correction weight $w(r^{(\mathrm{PS})}_{\widetilde{ij},\tilde{k}}(f_i, \Phi_{R|B}; \{\vec{a}\})) \leq W_{\widetilde{ij},f_i}(\{\vec{f}\})$ for any real emission configuration $r^{(\mathrm{PS})}_{\widetilde{ij},\tilde{k}}(f_i, \Phi_{R|B}; \{\vec{a}\})$ that can be generated off the Born configuration $\{\vec{a}\}$ and splitting $\widetilde{ij} \to i\,j$ for all spectators $\tilde{k}$.

2. Replace the parton shower splitting kernels $\mathcal{K}_{ij,k}$ by the overestimate $W_{\widetilde{ij},f_i}(\{\vec{f}\})\,\mathcal{K}_{ij,k}$.

3. Accept parton-shower branchings with probability $w(r^{(\mathrm{PS})}_{\widetilde{ij},\tilde{k}}(f_i, \Phi_{R|B}; \{\vec{a}\}))/W_{\widetilde{ij},f_i}(\{\vec{f}\})$.

It can then be shown that the constrained no-branching probability of such a matrix-element corrected parton shower reads

$$
\Delta^{(\mathrm{ME})}_{\widetilde{ij},\tilde{k}}(t', t''; \{\vec{a}\}) = \exp\left\{ -\sum_{f_i=q,g} \frac{1}{16\pi^2} \int_{t'}^{t''} \mathrm{d}t \int_{z_{\min}}^{z_{\max}} \mathrm{d}z \int_0^{2\pi} \frac{\mathrm{d}\phi}{2\pi} J_{ij,k}(t,z,\phi) \right.
$$
$$
\left. \times \frac{1}{S_{ij}} \frac{S(r_{\widetilde{ij},\tilde{k}}(f_i; \{\vec{f}\}))}{S(\{\vec{f}\})} \frac{\rho^{(\mathrm{PS})}_{ij,k}\, \mathrm{R}(r^{(\mathrm{PS})}_{\widetilde{ij},\tilde{k}}(f_i, t, z, \phi; \{\vec{a}\}))}{\mathrm{B}(\{\vec{a}\})} \right\} ,
$$

(7.3.4)

wherein the obvious argument of the projector $\rho^{(\mathrm{PS})}_{ij,k}$ has been suppressed for brevity. The ratio R/B in eq. (7.3.4) coincides with the ratio in the original publications presenting the POWHEG method. In the relatively simple cases treated so far [12, 13, 143, 144, 145, 147, 148, 146, 152, 153, 150, 149], the various symmetry factors in the equation above cancel and can be neglected. For more complicated flavour structures this factor may differ from one and therefore must be retained.

Employing again the definition of eq. (7.2.7), but this time for the Sudakov form factor $\Delta^{(\mathrm{ME})}$ constructed from the ratio R/B yields the cross section in the matrix element improved parton shower approximation. It reads

$$
\sigma_B = \sum_{\{\vec{f}\}} \int \mathrm{d}\Phi_B(\{\vec{p}\})\, \mathrm{B}(\{\vec{a}\}) \left[\Delta^{(\mathrm{ME})}(t_0, \mu^2; \{\vec{a}\}) \right.
$$

(7.3.5)

$$
+ \sum_{\{\widetilde{ij},\tilde{k}\}}^{(\mathrm{PS})} \sum_{f_i=q,g} \frac{1}{16\pi^2} \int_{t_0}^{\mu^2} \mathrm{d}t \int_{z_{\min}}^{z_{\max}} \mathrm{d}z \int_0^{2\pi} \frac{\mathrm{d}\phi}{2\pi} J_{ij,k}(t,z,\phi)
$$
$$
\left. \times \frac{1}{S_{ij}} \frac{S(r_{\widetilde{ij},\tilde{k}}(f_i; \{\vec{f}\}))}{S(\{\vec{f}\})} \frac{\rho^{(\mathrm{PS})}_{ij,k}\, \mathrm{R}(r^{(\mathrm{PS})}_{\widetilde{ij},\tilde{k}}(f_i, t, z, \phi; \{\vec{a}\}))}{\mathrm{B}(\{\vec{a}\})} \Delta^{(\mathrm{ME})}(t, \mu^2; \{\vec{a}\}) \right] .
$$

Again, the term in the square bracket equals one and thus reflects the probabilistic nature of this approach. Consequently, in the matrix-element improved parton-shower approximation the total cross section is given by the Born cross section, although the radiation pattern has improved. For a detailed discussion of the real-emission term see Section 7.4.2.

7.4 The reformulation of the POWHEG method

In this thesis, the POWHEG method is reinterpreted as an advanced matrix-element correction technique for standard parton showers. Having introduced the necessary notation in the last three sections, this section outlines the parallels between the POWHEG method and traditional matrix-element corrections. It then assesses the fixed-order and resummation properties of the POWHEG method.

7.4.1 Approximate NLO cross sections

In the previous two sections it has become clear that the total cross section of events simulated in a parton-shower Monte-Carlo is determined by the "seed" cross section, typically computed at Born level. While matrix-element improvement of the naive parton-shower picture will lead to radiation patterns which are accurate to $\mathcal{O}(\alpha_s)$, the total cross section of the event sample and any observable that can be defined at Born level will still be given by the respective leading-order expression. To allow for a simulation with next-to-leading order accuracy, including the cross section of the event sample, a prescription to assign a corresponding weight and multiplicity of the seed event must be found.

The solution is to replace the original Born-level matrix element with a modified one [12, 13], denoted by $\bar{\mathrm{B}}$,

$$\mathrm{d}\sigma_B(\{\vec{a}\}) \;\to\; \mathrm{d}\sigma_{\bar{B}}(\{\vec{a}\}) \;:=\; \mathrm{d}\Phi_B(\{\vec{p}\})\,\bar{\mathrm{B}}(\{\vec{a}\})\,. \tag{7.4.1}$$

Such that the "seed" cross section, $\mathrm{d}\sigma_{\bar{B}}$, integrates to the full NLO result. When constructing such an *NLO-weighted differential cross section for the Born configuration*, certain approximations must be made, since NLO cross sections have two contributions, one with Born-like kinematics and one with real-emission like kinematics, both of which exhibit divergent structures. The value of a given infrared and collinear safe observable, O, computed at NLO, is given in terms of the Born term B, the real emission term R, and the virtual contribution (including the collinear counter-terms), denoted by $\tilde{\mathrm{V}}$, as

$$\begin{aligned}
\langle O \rangle^{(\mathrm{NLO})} = \sum_{\{\vec{f}\}} \int \mathrm{d}\Phi_B(\{\vec{p}\}) \left[\mathrm{B}(\{\vec{a}\}) + \tilde{\mathrm{V}}(\{\vec{a}\}) \right] O(\{\vec{p}\}) \\
+ \sum_{\{\vec{f}\}} \int \mathrm{d}\Phi_R(\{\vec{p}\})\,\mathrm{R}(\{\vec{a}\})\,O(\{\vec{p}\})\,.
\end{aligned} \tag{7.4.2}$$

It is obvious that the real-emission contribution cannot be simply combined with the Born and virtual terms, as it depends on different kinematics. In the following, the solution of this problem in the framework of the POWHEG method is outlined.

In order to compute eq. (7.4.2) in a Monte-Carlo approach, subtraction terms, rendering the real emission finite in $D = 4$ space-time dimensions are introduced. Corresponding integrated subtraction terms regularise the infrared divergences of the virtual terms. In the dipole subtraction method [51, 52], the equation above can then be written as

$$\begin{aligned}
\langle O \rangle^{(\mathrm{NLO})} = \sum_{\{\vec{f}\}} \int \mathrm{d}\Phi_B(\{\vec{p}\}) \left[\mathrm{B}(\{\vec{a}\}) + \tilde{\mathrm{V}}(\{\vec{a}\}) + \mathrm{I}(\{\vec{a}\}) \right] O(\{\vec{p}\}) \\
+ \sum_{\{\vec{f}\}} \int \mathrm{d}\Phi_R(\{\vec{p}\}) \left[\mathrm{R}(\{\vec{a}\})\,O(\{\vec{p}\}) - \sum_{\{i,j\}} \sum_{k \neq i,j} \mathrm{S}_{ij,k}(\{\vec{a}\})\,O(b_{ij,k}(\{\vec{p}\})) \right]\,.
\end{aligned}$$

Note that each $S_{ij,k}$ defines a separate phase-space map and that the observable O in the last term depends on the parton map $b_{ij,k}(\{\vec{p}\})$, rather than $\{\vec{p}\}$, which is a crucial feature of the subtraction procedure. The real and integrated subtraction terms $S_{ij,k}(\{\vec{a}\})$ and $I(\{\vec{a}\})$ fulfil the relation

$$I(\{\vec{a}\}) = \sum_{\{i,j\}} \sum_{k \neq i,j} \int d\Phi_{R|B}^{ij,k}(\{\vec{p}\}) \, S_{ij,k}(\{\vec{a}\}) \, . \tag{7.4.4}$$

Identifying $D_{ij,k}$ with $S_{ij,k}$, the term with real-emission kinematics in eq. (7.4.3) can then be decomposed according to eq. (7.1.8), resulting in

$$\sum_{\{\vec{f}\}} d\Phi_R(\{\vec{p}\}) \sum_{\{i,j\}} \sum_{k \neq i,j} \left[R_{ij,k}(\{\vec{a}\}) \, O(\{\vec{p}\}) - S_{ij,k}(\{\vec{a}\}) \, O(b_{ij,k}(\{\vec{p}\})) \right] \, . \tag{7.4.5}$$

Therein, the implicit projector $\rho_{ij,k}$ is defined in terms of $S_{ij,k}$ and its associated singular region, as in eq. (7.1.8). In the POWHEG method, this term is *approximated* as

$$\sum_{\{\vec{f}\}} d\Phi_R(\{\vec{p}\}) \sum_{\{i,j\}} \sum_{k \neq i,j} \left[R_{ij,k}(\{\vec{a}\}) - S_{ij,k}(\{\vec{a}\}) \right] O(b_{ij,k}(\{\vec{p}\})) \tag{7.4.6}$$

$$= \sum_{\{\vec{f}\}} d\Phi_B(\{\vec{p}\}) \sum_{\{\widetilde{ij},\tilde{k}\}} \sum_{f_i=q,g} d\Phi_{R|B}^{ij,k} \left[R_{ij,k}(r_{\widetilde{ij},\tilde{k}}(\{\vec{a}\})) - S_{ij,k}(r_{\widetilde{ij},\tilde{k}}(\{\vec{a}\})) \right] O(\{\vec{p}\}) \, .$$

Thus, in this form all contributions have the same dependence on the observable O. This allows the combination of all contributions into one function, the $\bar{B}$-function

$$\bar{B}(\{\vec{a}\}) = B(\{\vec{a}\}) + \tilde{V}(\{\vec{a}\}) + I(\{\vec{a}\})$$
$$+ \sum_{\{\widetilde{ij},\tilde{k}\}} \sum_{f_i=q,g} \int d\Phi_{R|B}^{ij,k} \left[R_{ij,k}(r_{\widetilde{ij},\tilde{k}}(\{\vec{a}\})) - S_{ij,k}(r_{\widetilde{ij},\tilde{k}}(\{\vec{a}\})) \right] \, . \tag{7.4.7}$$

Note that the difference with respect to an exact result lies in the phase-space dependence of the real-emission contribution to $\langle O \rangle$. To restore NLO accuracy, the following correction term must be added

$$\sum_{\{\vec{f}\}} d\Phi_B(\{\vec{p}\}) \sum_{\{\widetilde{ij},\tilde{k}\}} \sum_{f_i=q,g} \int d\Phi_{R|B}^{ij,k} \, R_{ij,k}(r_{\widetilde{ij},\tilde{k}}(\{\vec{a}\})) \left[O(r_{\widetilde{ij},\tilde{k}}(\{\vec{p}\})) - O(\{\vec{p}\}) \right] \, . \tag{7.4.8}$$

In the next section it will be shown that the combination of $\bar{B}$ with a matrix-element corrected parton shower can recover exactly this correction. It is also through this relation, that a relation between $\rho_{ij,k}$ and $\rho_{ij,k}^{(\mathrm{PS})}$ is established.

7.4.2 The POWHEG method and its accuracy

The key point of the POWHEG method is, to supplement Monte Carlo event samples from matrix-element corrected parton showers with a next-to-leading order weight to arrive at full NLO accuracy. This is achieved by combining the two methods discussed in Secs. 7.3 and 7.4.1. To obtain the $\mathcal{O}(\alpha_s)$ approximation to the cross section in the POWHEG method,

the parton-shower expression of the real-emission probability is combined with the approximated initial cross section, $\mathrm{d}\sigma_{\bar{B}}$. This yields the following master formula for the value of an infrared and collinear safe observable, O,

$$
\begin{aligned}
\langle O \rangle^{(\mathrm{POWHEG})} = \sum_{\{\vec{f}\}} \int \mathrm{d}\Phi_B(\{\vec{p}\})\,\bar{\mathrm{B}}(\{\vec{a}\}) &\Bigg[\Delta^{(\mathrm{ME})}(t_0, \mu^2; \{\vec{a}\})\, O(\{\vec{p}\}) \\
&+ \sum_{\{\widetilde{ij},\tilde{k}\}}^{(\mathrm{PS})} \sum_{f_i=q,g} \frac{1}{16\pi^2} \int_{t_0}^{\mu^2} \mathrm{d}t \int_{z_{\min}}^{z_{\max}} \mathrm{d}z \int_0^{2\pi} \frac{\mathrm{d}\phi}{2\pi}\, J_{ij,k}(t, z, \phi) \\
&\times \frac{1}{S_{ij}} \frac{S(r^{(\mathrm{PS})}_{\widetilde{ij},\tilde{k}}(\{\vec{f}\}))}{S(\{\vec{f}\})} \frac{\rho^{(\mathrm{PS})}_{ij,k}(r^{(\mathrm{PS})}_{\widetilde{ij},\tilde{k}}(\{\vec{a}\}))\,\mathrm{R}(r^{(\mathrm{PS})}_{\widetilde{ij},\tilde{k}}(\{\vec{a}\}))}{\mathrm{B}(\{\vec{a}\})} \\
&\times \Delta^{(\mathrm{ME})}(t, \mu^2; \{\vec{a}\})\, O(r^{(\mathrm{PS})}_{\widetilde{ij},\tilde{k}}(\{\vec{p}\})) \Bigg],
\end{aligned}
\tag{7.4.9}
$$

where obvious arguments of the parton shower parton map $r^{(\mathrm{PS})}_{\widetilde{ij},\tilde{k}}$ have been suppressed. Clearly, if the observable O on the right hand side of eq. (7.4.9) becomes one, the quantity computed is the total cross section, as for the cases discussed in Sections 7.2 and 7.3. This particular case, however, is insensitive to the details of the radiation pattern. eq. (7.4.9) can be rearranged as [12, 13]

$$
\begin{aligned}
\langle O \rangle^{(\mathrm{POWHEG})} = \sum_{\{\vec{f}\}} \int \mathrm{d}\Phi_B(\{\vec{p}\})\,\bar{\mathrm{B}}(\{\vec{a}\}) &\Bigg[O(\{\vec{p}\}) \\
&+ \sum_{\{\widetilde{ij},\tilde{k}\}}^{(\mathrm{PS})} \sum_{f_i=q,g} \frac{1}{16\pi^2} \int_{t_0}^{\mu^2} \mathrm{d}t \int_{z_{\min}}^{z_{\max}} \mathrm{d}z \int_0^{2\pi} \frac{\mathrm{d}\phi}{2\pi}\, J_{ij,k}(t, z, \phi) \\
&\times \frac{1}{S_{ij}} \frac{S(r^{(\mathrm{PS})}_{\widetilde{ij},\tilde{k}}(\{\vec{f}\}))}{S(\{\vec{f}\})} \frac{\rho^{(\mathrm{PS})}_{ij,k}(r^{(\mathrm{PS})}_{\widetilde{ij},\tilde{k}}(\{\vec{a}\}))\,\mathrm{R}(r^{(\mathrm{PS})}_{\widetilde{ij},\tilde{k}}(\{\vec{a}\}))}{\mathrm{B}(\{\vec{a}\})} \\
&\times \Delta^{(\mathrm{ME})}(t, \mu^2; \{\vec{a}\}) \left[O(r^{(\mathrm{PS})}_{\widetilde{ij},\tilde{k}}(\{\vec{p}\})) - O(\{\vec{p}\}) \right] \Bigg],
\end{aligned}
\tag{7.4.10}
$$

Two special cases should now be considered [12, 13]

- The infrared limit ($t \to 0$)
  In this case, only the first term in eq. (7.4.10) contributes, as any infrared safe observable maps the real-emission kinematics for collinear (soft) emissions to the kinematics of the (any) underlying Born configuration

$$
O(r^{(\mathrm{PS})}_{\widetilde{ij},\tilde{k}}(\{\vec{p}\})) \overset{t \to 0}{\Rightarrow} O(\{\vec{p}\})
$$

  The contribution to $\langle O \rangle^{(\mathrm{POWHEG})}$ from this phase-space region is therefore correct to $\mathcal{O}(\alpha_s)$. Further, close to this limit the dominant contributions to $\langle O \rangle$ come from the leading logarithmic terms in both the real emission matrix element and the matrix element corrected Sudakov form factor in the real emission term. Thus, also the accuracy of the DGLAP resummation is preserved.

- Hard emissions $(t \to \mu^2)$

  In this case $\Delta^{(\mathrm{ME})} \to 1$ and to $\mathcal{O}(\alpha_s)$ one can replace $\bar{\mathrm{B}} \to \mathrm{B}$. Thus, the second term in eq. (7.4.10) becomes

$$
\sum_{\{\vec{f}\}} \int \mathrm{d}\Phi_B(\{\vec{p}\}) \sum_{\{\widetilde{ij},\tilde{k}\}}^{(\mathrm{PS})} \sum_{f_i=q,g} \frac{1}{16\pi^2} \int^{\mu^2} \mathrm{d}t \int \mathrm{d}z \int \frac{\mathrm{d}\phi}{2\pi} \, J_{ij,k}(t,z,\phi)
$$

$$
\times \, \frac{S(r^{(\mathrm{PS})}_{\widetilde{ij},\tilde{k}}(\{\vec{f}\}))}{S(\{\vec{f}\})\, S_{ij}} \, \rho^{(\mathrm{PS})}_{ij,k}(r^{(\mathrm{PS})}_{\widetilde{ij},\tilde{k}}(\{\vec{a}\}))\, \mathrm{R}(r^{(\mathrm{PS})}_{\widetilde{ij},\tilde{k}}(\{\vec{a}\})) \left[O(r^{(\mathrm{PS})}_{\widetilde{ij},\tilde{k}}(\{\vec{p}\})) - O(\{\vec{p}\}) \right] .
$$

  Comparing this result with the correction term, eq. (7.4.8), reveals that both expressions differ by the factor $S(\{\vec{f}\})\, S_{ij}/S(r_{\widetilde{ij},\tilde{k}}(\{\vec{f}\}))$, which arises solely due to the way the real-emission phase space is populated by the parton shower (cf. Section 7.2). Therefore, the contribution to $\langle O \rangle^{(\mathrm{POWHEG})}$ from this phase-space region is correct to $\mathcal{O}(\alpha_s)$ as long as both parton maps are complete.

In the phase-space regions "between" these limits, the POWHEG method interpolates smoothly between the two above results. However, as will be derived in the following section, the $\mathcal{O}(\alpha_s)$ expansion of the POWHEG master formula, eq. (7.4.9), can be shown to coincide with fixed-order next-to-leading order result if specific relations between the two parton maps $\rho_{ij,k}$ and $\rho^{(\mathrm{PS})}_{ij,k}$ are established. o

7.5 The single-singularity projectors $\rho_{ij,k}$ and $\rho^{(\mathrm{PS})}_{ij,k}$

The functions $\rho_{ij,k}$ and $\rho^{(\mathrm{PS})}_{ij,k}$ are not projectors in the strict mathematical sense, i.e. neither $\rho_{ij,k} \cdot \rho_{ij,k} \neq \rho_{ij,k}$ nor $\rho^{(\mathrm{PS})}_{ij,k} \cdot \rho^{(\mathrm{PS})}_{ij,k} \neq \rho^{(\mathrm{PS})}_{ij,k}$. Nonetheless, both have to fulfil the following relations, cf. eq. (7.1.8) and eq. (7.3.2)

$$
\sum_{\{i,j\}} \sum_{k \neq i,j} \rho_{ij,k}(\{\vec{a}\}) = 1 \qquad \forall \, \{\vec{a}\} \in \Phi_R \tag{7.5.1}
$$

and

$$
\sum_{\{i,j\}} \sum_{k \neq i,j}^{(\mathrm{PS})} \rho^{(\mathrm{PS})}_{ij,k}(\{\vec{a}\}) = 1 \qquad \forall \, \{\vec{a}\} \in \Phi_R \mid t(\Phi_R) > t_0 \, . \tag{7.5.2}
$$

Further, eq. (7.4.7) demands that $\rho_{ij,k}(\{\vec{a}\})$ also fulfils the relation

$$
\rho_{ij,k}(\{\vec{a}\})\, \mathcal{R}(\{\vec{a}\}) \to \mathcal{D}_{ij,k}(\{\vec{a}\}) = \mathcal{S}_{ij,k}(\{\vec{a}\}) \tag{7.5.3}
$$

in the soft-collinear limits. While the completeness relation ensures

$$
\sum_{\{i,j\}} \sum_{k \neq i,j} \mathcal{R}_{ij,k}(\{\vec{a}\}) = \mathcal{R}(\{\vec{a}\}) \qquad \forall \, \{\vec{a}\} \in \Phi_R \tag{7.5.4}
$$

the second relation guarantees the presence of exactly one singular structure in each $\mathcal{R}_{ij,k}$, namely that of the corresponding subtraction term. The latter is a vital prerequisite in Section 7.4, where the subtracted real emission contribution to the total cross section is broken down into a sum of dipole contribution. Each of them has to be finite, thus the divergence structures of $\mathcal{R}_{ij,k}(\{\vec{a}\})$ and $\mathcal{S}_{ij,k}(\{\vec{a}\})$ have to match exactly. Because the parton shower only considers resolved emission above some infrared cut-off t_0 this condition does not have to be satisfied by the $\rho_{ij,k}^{(\mathrm{PS})}$. In fact, it is explicitly violated by the fact that the parton shower neglects terms which are subleading in colour, and thus neglects their singularity structure.

Without any further specifications of the relations between $\rho_{ij,k}$ and $\rho_{ij,k}^{(\mathrm{PS})}$, it could only be shown in the last section that the POWHEG master formula, eq. (7.4.9), correctly reproduces the fixed-order next-to-leading order results in the limit $t \to 0$ and $t \to \mu^2$. To achieve next-to-leading order accuracy over the full phase space for an arbitrary observable eq. (7.4.9) has to be expanded in α_s giving

$$
\begin{aligned}
\langle O \rangle^{(\mathrm{POWHEG})} = & \sum_{\{\vec{f}\}} \int \mathrm{d}\Phi_B(\{\vec{p}\}) \left(\mathrm{B} + \tilde{\mathrm{V}} + \mathrm{I} \right)(\{\vec{a}\}) \, O(\{\vec{a}\}) \\
& + \sum_{\{\vec{f}\}} \sum_{\{\widetilde{ij},\tilde{k}\}} \sum_{f_i = q,g} \int \mathrm{d}\Phi_B(\{\vec{p}\}) \, \mathrm{d}\Phi_{R|B}^{ij,k} \left(\rho_{ij,k}(r_{\widetilde{ij},\tilde{k}}(\{\vec{a}\})) \, \mathrm{R}(r_{\widetilde{ij},\tilde{k}}(\{\vec{a}\})) \, \Theta(t_0 - t_{ij,k}) \right. \\
& \qquad\qquad\qquad\qquad\qquad\qquad \left. - \mathrm{S}_{ij,k}(r_{\widetilde{ij},\tilde{k}}(\{\vec{a}\})) \right) O(\{\vec{a}\}) \\
& + \sum_{\{\vec{f}\}} \int \mathrm{d}\Phi_B(\{\vec{p}\}) \left[\sum_{\{\widetilde{ij},\tilde{k}\}} \sum_{f_i = q,g} \int_{t_0}^{\mu^2} \mathrm{d}\Phi_{R|B}^{ij,k} \, \rho_{ij,k}(r_{\widetilde{ij},\tilde{k}}(\{\vec{a}\})) \, \mathrm{R}(r_{\widetilde{ij},\tilde{k}}(\{\vec{a}\})) \right. \\
& \qquad\qquad \left. - \sum_{\{\widetilde{ij},\tilde{k}\}}^{(\mathrm{PS})} \sum_{f_i = q,g} \int_{t_0}^{\mu^2} \mathrm{d}\Phi_{R|B}^{ij,k} \, \rho_{ij,k}^{(\mathrm{PS})}(r_{\widetilde{ij},\tilde{k}}^{(\mathrm{PS})}(\{\vec{a}\})) \, \mathrm{R}(r_{\widetilde{ij},\tilde{k}}^{(\mathrm{PS})}(\{\vec{a}\})) \right] O(\{\vec{a}\}) \\
& + \sum_{\{\vec{f}\}} \sum_{\{\widetilde{ij},\tilde{k}\}}^{(\mathrm{PS})} \sum_{f_i = q,g} \int_{t_0}^{\mu^2} \mathrm{d}\Phi_B(\{\vec{p}\}) \, \mathrm{d}\Phi_{R|B}^{ij,k} \, \rho_{ij,k}^{(\mathrm{PS})}(r_{\widetilde{ij},\tilde{k}}^{(\mathrm{PS})}(\{\vec{a}\})) \, \mathrm{R}(r_{\widetilde{ij},\tilde{k}}^{(\mathrm{PS})}(\{\vec{a}\})) \, O(r_{\widetilde{ij},\tilde{k}}^{(\mathrm{PS})}(\{\vec{a}\})) \\
& + \mathcal{O}(\alpha_s^2) \, .
\end{aligned}
$$

$$(7.5.5)$$

From this expansion it is immediately clear that observables that vanish on the Born phase space, i.e. $O(\{\vec{\alpha}\}) = 0$ for every Born configuration $\{\vec{a}\}$, are determined at the same accuracy as in a fixed-order NLO calculation. This is guaranteed by the completeness relation eq. (7.5.2). However, due to the term in the third line which arises because of the potential mismatch of the parton maps and projectors between the parton shower and the subtraction algorithms, the observable's dependence on the Born phase space is distorted. Its dependence is already given to NLO accuracy by the terms of the first two lines. Thus, it remains

to be shown that

$$
\begin{aligned}
\Bigg[\sum_{\{\widetilde{ij},\tilde{k}\}} \sum_{f_i=q,g} \int_{t_0}^{\mu^2} & \mathrm{d}\Phi_{R|B}^{ij,k} \, \rho_{ij,k}(r_{\widetilde{ij},\tilde{k}}(\{\vec{a}\})) \, \mathrm{R}(r_{\widetilde{ij},\tilde{k}}(\{\vec{a}\})) \\
- \sum_{\{\widetilde{ij},\tilde{k}\}}^{\mathrm{(PS)}} \sum_{f_i=q,g} \int_{t_0}^{\mu^2} & \mathrm{d}\Phi_{R|B}^{ij,k\,\mathrm{(PS)}} \, \rho_{ij,k}^{\mathrm{(PS)}}(r_{\widetilde{ij},\tilde{k}}^{\mathrm{(PS)}}(\{\vec{a}\})) \, \mathrm{R}(r_{\widetilde{ij},\tilde{k}}^{\mathrm{(PS)}}(\{\vec{a}\})) \Bigg] = \mathcal{O}(\alpha_s^2)
\end{aligned}
\tag{7.5.6}
$$

for every Born phase configuration $\{\vec{a}\}$. Obviously, the above statement holds true if both parton maps coincide. Introducing $\bar{\rho}_{ij,k}$ as a common projector for both the subtraction terms and the parton shower, then necessarily also defining identical parton maps, $\bar{b}_{ij,k}(\{\vec{a}\})$ and $\bar{r}_{\widetilde{ij},\tilde{k}}(\{\vec{a}\})$, the $\mathcal{O}(\alpha_s)$ expansion of the POWHEG master formula then reads

$$
\begin{aligned}
\langle O \rangle^{\mathrm{(POWHEG)}} = & \sum_{\{\vec{f}\}} \int \mathrm{d}\Phi_B(\{\vec{p}\}) \left(\mathrm{B} + \tilde{\mathrm{V}} + \mathrm{I} \right)(\{\vec{a}\}) \, O(\{\vec{a}\}) \\
& + \sum_{\{\vec{f}\}} \sum_{\{\widetilde{ij},\tilde{k}\}} \sum_{f_i=q,g} \int \mathrm{d}\Phi_B(\{\vec{p}\}) \, \mathrm{d}\Phi_{R|B}^{ij,k} \left(\bar{\rho}_{ij,k}(\bar{r}_{\widetilde{ij},\tilde{k}}(\{\vec{a}\})) \, \mathrm{R}(\bar{r}_{\widetilde{ij},\tilde{k}}(\{\vec{a}\})) \, \Theta(t_0 - t_{ij,k}) \right. \\
& \hspace{6cm} \left. - \mathrm{S}_{ij,k}(\bar{r}_{\widetilde{ij},\tilde{k}}(\{\vec{a}\})) \right) O(\{\vec{a}\}) \\
& + \sum_{\{\vec{f}\}} \sum_{\{\widetilde{ij},\tilde{k}\}} \sum_{f_i=q,g} \int_{t_0}^{\mu^2} \mathrm{d}\Phi_B(\{\vec{p}\}) \, \mathrm{d}\Phi_{R|B}^{ij,k} \, \bar{\rho}_{ij,k}(\bar{r}_{\widetilde{ij},\tilde{k}}(\{\vec{a}\})) \, \mathrm{R}(\bar{r}_{\widetilde{ij},\tilde{k}}(\{\vec{a}\})) \, O(\bar{r}_{\widetilde{ij},\tilde{k}}(\{\vec{a}\})) \\
& + \mathcal{O}(\alpha_s^2) \, ,
\end{aligned}
\tag{7.5.7}
$$

coinciding, up to $\mathcal{O}(\alpha_s^2)$ terms, with the fixed-order next-to-leading expression for any infrared safe observable O. Further, the equality of both parton maps consequently enforces the usage of a shower algorithms which matches the subtraction formalism. Thus, when employing the Catani-Seymour subtraction scheme [51, 52], as is done in this thesis, this enforces the usage of a parton shower based on the same phase space maps, e.g. [62, 213], cf. Section 7.8.

In general, however, since most parton showers operate in the $N_c \to \infty$ limit, the parton maps cannot coincide for every emitter-spectator pair $\{\widetilde{ij}, \tilde{k}\}$ for processes with non-trivial colour structures at the Born level, i.e. where the Born amplitude contains more than just a δ-function in colour space. This is because pairs $\{\widetilde{ij}, \tilde{k}\}$ corresponding to a subleading colour dipoles in an $1/N_c$ expansion of the amplitude are not present in the parton shower maps. These missing dipoles, however, contribute to the soft limit, as was shown in Section 6.3. For $t > t_0$ their respective contributions are finite and can be effected collectively through the remaining correction weights $w_{ij,k}$ of eq. (7.3.1) of the leading terms in the large N_c expansion, resulting in a correct description of the real emission amplitude in $N_c = 3$ through the corrected parton shower[3].

---

[3] In practice, it turns out that most of these subleading colour contributions are opposite in sign to the leading colour contributions, thus effectively lowering the correction weights $w_{ij,k}$ and improving the numerical behaviour of the ME-correction algorithm.

Thus, by the above arguments, the form of the common projector $\bar{\rho}_{ij,k}$ is fixed to resemble $\rho_{ij,k}^{(PS)}$ for $t > t_0$. Nonetheless, in the singular limit still the condition eq. (7.5.3) has to hold, thus enforcing

$$
\bar{\rho}_{ij,k}(\{\vec{a}\}) = \begin{cases} \rho_{ij,k}(\{\vec{a}\}) & \text{for } t(\{\vec{a}\}) < t_0 \\ \\ \rho_{ij,k}^{(PS)}(\{\vec{a}\}) & \text{for } t(\{\vec{a}\}) > t_0 \end{cases} \quad . \tag{7.5.8}
$$

In particular, for subleading colour dipoles the projector needs to vanish above t_0 in order to fulfil eqs. (7.5.1)-(7.5.3).

To derive an explicit functional form for the projectors $\bar{\rho}_{ij,k}$ suitable for a Monte Carlo implementation it is advantageous to separate the Monte Carlo phase space definitions, usually implemented through phase space cuts $\Theta(\{\vec{a}\})$ to regularise Born processes which are already divergent by themselves, from the observable definition. In this notation the subtracted real emission contribution to a fixed-order next-to-leading order calculation would read

$$
\sum_{\{\vec{f}\}} \int d\Phi_R(\{\vec{a}\}) \left[\mathcal{R}(\{\vec{a}\}) \, \Theta(\{\vec{a}\}) \, O(\{\vec{a}\}) \right.
$$
$$
\left. - \sum_{\{i,j\}} \sum_{k \neq i,j} \mathcal{S}_{ij,k}(\{\vec{a}\}) \, \Theta(b_{ij,k}(\{\vec{a}\})) \, O(b_{ij,k}(\{\vec{a}\})) \right] \quad . \tag{7.5.9}
$$

In general, for $t(\{\vec{a}\}) < t_0$ the $\rho_{ij,k}$ can now be defined as

$$
\rho_{ij,k}(\{\vec{a}\}) = \frac{\mathcal{S}_{ij,k}(\{\vec{a}\}) \, H(b_{ij,k}(\{\vec{a}\}))}{\sum_{\{m,n\}} \sum_{l \neq m,n} \mathcal{S}_{mn,l}(\{\vec{a}\}) \, H(b_{mn,l}(\{\vec{a}\}))} \quad . \tag{7.5.10}
$$

Such a form was already suggested in [13]. Herein the function $H(b_{ij,k}(\{\vec{a}\}))$ is defined on the Born phase space. Its precise functional form is arbitrary, as long as it fulfils the following constraints:

- When $b_{ij,k}(\{\vec{a}\})$ approaches the Born singularity, $H(b_{ij,k}(\{\vec{a}\}))$ needs to vanish sufficiently fast such that

$$
\sum_{\{\vec{f}\}} \int d\Phi_R(\{\vec{a}\}) \left[\mathcal{R}_{ij,k}(\{\vec{a}\}) \, \Theta(\{\vec{a}\}) - \mathcal{S}_{ij,k}(\{\vec{a}\}) \, \Theta(b_{ij,k}(\{\vec{a}\})) \right]
$$

  is still integrable.

- $H(b_{ij,k}(\{\vec{a}\}))$ needs to be well behaved, such that numerical integration is feasible. Most importantly it should be positive definite and free of integrable divergences.

- For all $b_{ij,k}(\{\vec{a}\})$ where $\Theta(b_{ij,k}(\{\vec{a}\})) \neq 0$ $H(b_{ij,k}(\{\vec{a}\}))$ should be equal to unity. This is not a strict requirement, but otherwise event weights of the other parts of the next-to-leading order calculation would have to be modified accordingly.

To illustrate this further, first consider the process of the production of a W boson at a hadronic collider. Since there are no divergences present in this process at the Born level the trivial choice $H(b_{ij,k}(\{\vec{a}\})) = \Theta(b_{ij,k}(\{\vec{a}\})) = 1$ throughout the phase space is sufficient, because $\Theta(\{\vec{a}\}) = 1$ then implies $\Theta(b_{ij,k}(\{\vec{a}\})) = 1$ for all parton maps. Thus, the decomposition of $\mathcal{R}$ into singular regions is complete because if $\mathcal{R}(\{\vec{a}\})\,\Theta(\{\vec{a}\}) \neq 0$ then all $\mathcal{S}_{ij,k}(\{\vec{a}\})\,H(b_{ij,k}(\{\vec{a}\})) = \mathcal{S}_{ij,k}(\{\vec{a}\})\,\Theta(b_{ij,k}(\{\vec{a}\})) \neq 0$.

Next consider the case of the production of a Drell-Yan pair at a hadron collider. Here the Born phase space has to be cut to shield against the virtual photon singularity. However since, when working within the Catani-Seymour subtraction scheme, all parton maps leave Lorentz-invariant quantities of the Drell-Yan pair unchanged the choice $H(b_{ij,k}(\{\vec{a}\})) = \Theta(b_{ij,k}(\{\vec{a}\})) = 1$ is again sufficient, provided the Born amplitude's phase space cuts are defined invariantly. Again, the reason for this to hold is that $\Theta(\{\vec{a}\}) = 1$ implies $\Theta(b_{ij,k}(\{\vec{a}\})) = 1$ for all parton maps.

For a less trivial example consider now the production of vector boson in association with a jet. In order to define the process at Born level, a phase space cut has to be introduced shielding against the divergence when the transverse momentum of the jet goes to zero. Requiring a minimum transverse momentum of the jet of $p_{\perp\mathrm{cut}}$ would be sufficient to achieve this. However, with this choice $\Theta(\{\vec{a}\}) = 1$ does no longer imply $\Theta(b_{ij,k}(\{\vec{a}\})) = 1$ to hold for all parton maps. Thus, choosing $H(b_{ij,k}(\{\vec{a}\})) = \Theta(b_{ij,k}(\{\vec{a}\}))$ as in the above cases will lead to some $\mathcal{R}_{ij,k}$ being zero. Its singularity region will then be redistributed to all other $\mathcal{R}_{ij,k}$. Naïvely one might argue that in the strict limit, where this specific $\mathcal{R}_{ij,k}$ is singular $\mathcal{S}_{ij,k}(\{\vec{a}\})\,\Theta(b_{ij,k}(\{\vec{a}\}))$ will not vanish due to the infrared safety of the definition of the parton maps in any subtraction algorithm. However, close to the singular limit this situation does indeed occur and then lead to an incomplete subtraction of $\mathcal{R}_{ij,k}$ and $\mathcal{S}_{ij,k}$ leaving a very large weight[4]. Thus, functional forms of $H(b_{ij,k}(\{\vec{a}\}))$ have to be found that reduce the effect of such incomplete subtractions to a minimum, dampen the Born singularity, a potentially doubly singular region for $\mathcal{R}$ and the $\mathcal{S}_{ij,k}$, enough and, therefore, leave the subtracted real emission integral well defined. In Section 7.10, where processes of this structure are under investigation, this becomes relevant.

In contrast, for $t(\{\vec{t}\}) > t_0$ the $\rho_{ij,k}^{(\mathrm{PS})}$ are defined on a completely finite phase space region. Thus, the definition

$$
\rho_{ij,k}^{(\mathrm{PS})}(\{\vec{a}\}) \;=\; \frac{\mathcal{R}_{ij,k}^{(\mathrm{PS})}(\{\vec{a}\})}{\displaystyle\sum_{\{m,n\}}\sum_{l \neq m,n}\mathcal{R}_{mn,l}^{(\mathrm{PS})}(\{\vec{a}\})}
\tag{7.5.11}
$$

with the definitions of eq. (7.2.1) is completely sufficient.

7.6 Theoretical ambiguities

The Powheg method possesses an ambiguity regarding which parts of the real emission matrix elements are and which are not to be exponentiated. This was first noted in [146]

---

[4] This feature of incomplete subtraction is also present in a fixed-order next-to-leading order calculation using any subtraction scheme. There, however, events fall in only two categories, the observable defined on the Born phase space or the observable defined on the real emission phase space, making an accidental cancellation of such incomplete subtractions with the opposite configuration, $\Theta(\{\vec{a}\}) = 0$ and $\Theta(b_{ij,k}(\{\vec{a}\})) = 1$, very likely. But as soon as such incompletely subtracted events are showered they are distributed to many different observable categories, depending on the exact shower evolution of such an event. It is needless to say, that the likelihood for such accidental cancellations of incomplete subtractions is then very much reduced.

and heavily used in [149]. To this end, the real emission matrix element is split into a singular and a regular contribution,

$$\mathcal{R}(\{\vec{a}\}) = \mathcal{R}^{(\mathrm{s})}(\{\vec{a}\}) + \mathcal{R}^{(\mathrm{r})}(\{\vec{a}\}) \, . \tag{7.6.1}$$

$\mathcal{R} \to \mathcal{R}^{(\mathrm{s})}$ has to hold in the singular limits, i.e. $\mathcal{R}^{(\mathrm{s})}$ has to contain all the singular logarithms. $\mathcal{R}^{(\mathrm{r})}$, thus, in turn is free of any singularities or associated large logarithms which need to be resummed. Consequently, the POWHEG master formula, eq. (7.4.9), can be altered in the following way

$$
\begin{aligned}
\langle O \rangle^{(\mathrm{POWHEG})} &= \sum_{\{\vec{f}\}} \int \mathrm{d}\Phi_B(\{\vec{p}\}) \, \widetilde{\mathrm{B}}(\{\vec{a}\}) \Bigg[\, \widetilde{\Delta}^{(\mathrm{ME})}(t_0, \mu^2; \{\vec{a}\}) \, O(\{\vec{p}\}) \\
&\quad + \sum_{\{\widetilde{ij},\tilde{k}\}}^{(\mathrm{PS})} \sum_{f_i=q,g} \frac{1}{16\pi^2} \int_{t_0}^{\mu^2} \mathrm{d}t \int_{z_{\min}}^{z_{\max}} \mathrm{d}z \int_0^{2\pi} \frac{\mathrm{d}\phi}{2\pi} \, J_{ij,k}(t,z,\phi) \\
&\quad \times \frac{1}{S_{ij}} \frac{S(r^{(\mathrm{PS})}_{\widetilde{ij},\tilde{k}}(\{\vec{f}\}))}{S(\{\vec{f}\})} \frac{\rho^{(\mathrm{PS})}_{ij,k}(r^{(\mathrm{PS})}_{\widetilde{ij},\tilde{k}}(\{\vec{a}\})) \, \mathrm{R}^{(\mathrm{s})}(r^{(\mathrm{PS})}_{\widetilde{ij},\tilde{k}}(\{\vec{a}\}))}{\mathrm{B}(\{\vec{a}\})} \\
&\quad \times \widetilde{\Delta}^{(\mathrm{ME})}(t, \mu^2; \{\vec{a}\}) \, O(r^{(\mathrm{PS})}_{\widetilde{ij},\tilde{k}}(\{\vec{p}\})) \Bigg] \\
&\quad + \sum_{\{\vec{f}\}} \int \mathrm{d}\Phi_R(\{\vec{p}\}) \, \mathrm{R}^{(\mathrm{r})}(\{\vec{a}\}) \, O(\{\vec{p}\}) \, ,
\end{aligned}
\tag{7.6.2}
$$

i.e. the non-singular part is removed from the exponentiation and then added as an explicit separate leading order sample. Therein are defined, in full analogy to eq. (7.4.7) and eq. (7.3.4),

$$
\begin{aligned}
\widetilde{\mathrm{B}}(\{\vec{a}\}) &= \mathrm{B}(\{\vec{a}\}) + \widetilde{\mathrm{V}}(\{\vec{a}\}) + \mathrm{I}(\{\vec{a}\}) \\
&\quad + \sum_{\{\widetilde{ij},\tilde{k}\}} \sum_{f_i=q,g} \int \mathrm{d}\Phi_{R|B}^{ij,k} \left[\mathrm{R}^{(\mathrm{s})}_{ij,k}(r_{\widetilde{ij},\tilde{k}}(\{\vec{a}\})) - \mathrm{S}_{ij,k}(r_{\widetilde{ij},\tilde{k}}(\{\vec{a}\})) \right] \, ,
\end{aligned}
\tag{7.6.3}
$$

and

$$
\begin{aligned}
\widetilde{\Delta}^{(\mathrm{ME})}_{\widetilde{ij},\tilde{k}}(t', t''; \{\vec{a}\}) &= \exp \Bigg\{ - \sum_{f_i=q,g} \frac{1}{16\pi^2} \int_{t'}^{t''} \mathrm{d}t \int_{z_{\min}}^{z_{\max}} \mathrm{d}z \int_0^{2\pi} \frac{\mathrm{d}\phi}{2\pi} \, J_{ij,k}(t,z,\phi) \\
&\quad \times \frac{1}{S_{ij}} \frac{S(r_{\widetilde{ij},\tilde{k}}(f_i; \{\vec{f}\}))}{S(\{\vec{f}\})} \frac{\rho^{(\mathrm{PS})}_{ij,k} \, \mathrm{R}^{(\mathrm{s})}(r^{(\mathrm{PS})}_{\widetilde{ij},\tilde{k}}(f_i, t, z, \phi; \{\vec{a}\}))}{\mathrm{B}(\{\vec{a}\})} \Bigg\} \, .
\end{aligned}
\tag{7.6.4}
$$

To show the NLO order accuracy the consideration of Section 7.5 still apply to the exponentiated part of eq. (7.6.2). This ambiguity has two important consequences. Firstly, the resummation properties, encoded in the Sudakov form factor of eq. (7.6.4), depend on the specific choice of the separation between $\mathcal{R}^{(\mathrm{s})}$ and $\mathcal{R}^{(\mathrm{r})}$. Of course, in the region of large logarithms where resummation effects are important this dependence is minimised by construction. Secondly, the exponentiated part of the real emission cross section, $\mathcal{R}^{(\mathrm{s})}$, always comes with a prefactor of $\widetilde{B}/B = 1 + \mathcal{O}(\alpha_s)$, thus introducing arbitrary $\mathcal{O}(\alpha_s^2)$ terms to

$\langle O \rangle$. In contrary, the explicitly added non-exponentiated regular parts $\mathcal{R}^{(\mathrm{r})}$ do not have such a prefactor. Hence, the precise numerical magnitude of the $\mathcal{O}(\alpha_s^2)$ terms introduced through the exponentiation, according to eq. (7.6.3), depends again on the splitting definition between $\mathcal{R}^{(\mathrm{s})}$ and $\mathcal{R}^{(\mathrm{r})}$. This is especially important for processes with large NLO/LO K-factors, locally corresponding exactly to $\widetilde{B}/B$, such as Higgs boson production in gluon fusion or the associated production of a $b\bar{b}$ pair and a W boson [149].

This freedom thus presents an intrinsic uncertainty when matching next-to-leading order matrix elements and parton showers.

7.7 MC@NLO

This section introduces the alternative method for matching fixed-order next-to-leading order calculations to parton showers, called MC@NLO [11], using the same single-leg notation of the previous sections. This allows to straight forwardly establish the equality of both methods at next-to-leading order and leading logarithmic accuracy and, further, to assess their relation to one another. MC@NLO employs a pseudo-subtraction using the parton shower approximation $\mathcal{R}^{(\mathrm{PS})}$ to a given real emission correction $\mathcal{R}$. Thus, again starting from the fixed order expression, cf. eq. (7.4.3),

$$
\begin{aligned}
\langle O \rangle^{(\mathrm{NLO})} = & \sum_{\{\vec{f}\}} \int \mathrm{d}\Phi_B(\{\vec{p}\}) \left[\mathrm{B}(\{\vec{a}\}) + \tilde{\mathrm{V}}(\{\vec{a}\}) + \mathrm{I}(\{\vec{a}\}) \right] O(\{\vec{p}\}) \\
& + \sum_{\{\vec{f}\}} \int \mathrm{d}\Phi_R(\{\vec{p}\}) \left[\mathrm{R}^{(\mathrm{PS})}(\{\vec{a}\})\,O(\{\vec{p}\}) - \sum_{\{i,j\}} \sum_{k \neq i,j} \mathrm{S}_{ij,k}(\{\vec{a}\})\,O(b_{ij,k}(\{\vec{p}\})) \right] \\
& + \sum_{\{\vec{f}\}} \int \mathrm{d}\Phi_R(\{\vec{p}\}) \left[\mathrm{R}(\{\vec{a}\})\,O(\{\vec{p}\}) - \mathrm{R}^{(\mathrm{PS})}(\{\vec{a}\})\,O(\{\vec{p}\}) \right] .
\end{aligned}
\tag{7.7.1}
$$

This form uses the parton shower approximation $\mathcal{R}^{(\mathrm{PS})}$ defined in eq. (7.3.2) as an intermediate subtraction term. However, in order for every term in eq. (7.7.1) to be separately finite, $\mathcal{R}^{(\mathrm{PS})}$ would have to exhibit the same singularity structure as the exact real emission matrix element $\mathcal{R}$, i.e.

$$
\mathcal{R} \to \mathcal{R}^{(\mathrm{PS})} = \sum_{\{i,j\}} \sum_{k \neq i,j}^{(\mathrm{PS})} \mathcal{R}_{ij,k}^{(\mathrm{PS})}(\{\vec{a}\}) ,
\tag{7.7.2}
$$

in full analogy to eq. (7.1.6). This relation, however, does not hold in a general case. The reason lies both in the usual employment of the $N_c \to \infty$ approximation and the usage of spin-averaged splitting kernels in the parton shower. Nonetheless, *supposing*[5] the parton shower approximation to the real emission matrix element fulfils the above property this

---

[5] In the original formulation of the MC@NLO method [11, 137] the leading colour parton shower approximation was modified to smoothly transform into the real emission matrix element in the soft gluon emission limit to circumvent the impossibility to map its general soft singularity structure onto the Altarelli-Parisi splitting functions, see Section 6.3. This was justified by the assumption that infrared-safe observables are insensitive to the angular distribution of soft gluon emissions.

implies that every $\mathcal{R}_{ij,k}^{(\mathrm{PS})}$ corresponds directly to a subtraction term $\mathcal{S}_{ij,k}$ if every $\mathcal{R}_{ij,k}^{(\mathrm{PS})}$ covers exactly one singular region only. Hence, $\mathcal{S}_{ij,k}$ and $\mathcal{R}_{ij,k}^{(\mathrm{PS})}$ coincide in the singular limits, but may differ in the finite regions. Similarly, all sums necessarily run over the same set of indices. Consequently, without the need of a further projector a modified $\bar{B}$-function, $\widetilde{B}$, can be defined

$$
\begin{aligned}
\widetilde{\mathrm{B}}(\{\vec{a}\}) ={} & \mathrm{B}(\{\vec{a}\}) + \tilde{\mathrm{V}}(\{\vec{a}\}) + \mathrm{I}(\{\vec{a}\}) \\
& + \sum_{\{\widetilde{\imath\jmath},\tilde{k}\}} \sum_{f_i=q,g} \int \mathrm{d}\Phi_{R|B}^{ij,k} \left[\mathrm{R}_{ij,k}^{(\mathrm{PS})}(r_{\widetilde{\imath\jmath},\tilde{k}}(\{\vec{a}\})) - \mathrm{S}_{ij,k}(r_{\widetilde{\imath\jmath},\tilde{k}}(\{\vec{a}\})) \right] .
\end{aligned}
\tag{7.7.3}
$$

This leads to the Mc@Nlo master formula for the expectation value of any arbitrary infrared safe observable O

$$
\begin{aligned}
\langle O \rangle^{(\mathrm{MC@NLO})} ={} & \sum_{\{\vec{f}\}} \int \mathrm{d}\Phi_B(\{\vec{p}\}) \, \widetilde{\mathrm{B}}(\{\vec{a}\}) \left[\Delta^{(\mathrm{PS})}(t_0,\mu^2;\{\vec{a}\}) \, O(\{\vec{p}\}) \right. \\
& + \sum_{\{\widetilde{\imath\jmath},\tilde{k}\}} \sum_{f_i=q,g} \frac{1}{16\pi^2} \int_{t_0}^{\mu^2} \mathrm{d}t \int_{z_{\min}}^{z_{\max}} \mathrm{d}z \int_0^{2\pi} \frac{\mathrm{d}\phi}{2\pi} \, J_{ij,k}(t,z,\phi) \\
& \qquad \times \frac{1}{S_{ij}} \frac{S(r_{\widetilde{\imath\jmath},\tilde{k}}^{(\mathrm{PS})}(\{\vec{f}\}))}{S(\{\vec{f}\})} \frac{\mathrm{R}_{ij,k}^{(\mathrm{PS})}(r_{\widetilde{\imath\jmath},\tilde{k}}^{(\mathrm{PS})}(\{\vec{a}\}))}{\mathrm{B}(\{\vec{a}\})} \\
& \qquad \left. \times \Delta^{(\mathrm{PS})}(t,\mu^2;\{\vec{a}\}) \, O(r_{\widetilde{\imath\jmath},\tilde{k}}^{(\mathrm{PS})}(\{\vec{p}\})) \right] \\
& + \sum_{\{\vec{f}\}} \int \mathrm{d}\Phi_R(\{\vec{p}\}) \left[\mathrm{R}(\{\vec{a}\}) - \mathrm{R}^{(\mathrm{PS})}(\{\vec{a}\}) \right] O(\{\vec{p}\}) .
\end{aligned}
\tag{7.7.4}
$$

Note the absence of any single-singularity projectors from the above definition. Nonetheless, still the parton maps of the parton shower and the subtraction terms may differ, leading to a term

$$
\sum_{\{\widetilde{\imath\jmath},\tilde{k}\}} \sum_{f_i=q,g} \int_{t_0}^{\mu^2} \mathrm{d}\Phi_{R|B}^{ij,k} \left[\mathrm{R}_{ij,k}^{(\mathrm{PS})}(r_{\widetilde{\imath\jmath},\tilde{k}}(\{\vec{a}\})) - \mathrm{R}_{ij,k}^{(\mathrm{PS})}(r_{\widetilde{\imath\jmath},\tilde{k}}^{(\mathrm{PS})}(\{\vec{a}\})) \right] O(\{\vec{a}\})
\tag{7.7.5}
$$

which potentially still spoils NLO accuracy. Nonetheless, *supposing* both parton maps are identical, a requirement also shown to be mandatory for the Powheg method in the Section 7.5, NLO accuracy is preserved. Further, contrary to the Powheg method, no additional terms not present in parton shower are exponentiated in the Mc@Nlo formalism. The approximation made in these exponentiated so-called $\mathbb{S}$-events is then corrected to fixed order by the so-called $\mathbb{H}$-events, a finite leading order sub-sample.

Finally, eq. (7.7.4) exposes the relation of Mc@Nlo and the Powheg method. Exploiting the ambiguity of the Powheg method, elaborated upon in Section 7.6, and making the explicit choice of

$$
\mathcal{R}^{(\mathrm{s})}(\{\vec{a}\}) = \mathcal{R}^{(\mathrm{PS})}(\{\vec{a}\}) \qquad \text{and} \qquad \mathcal{R}^{(\mathrm{r})}(\{\vec{a}\}) = \mathcal{R}(\{\vec{a}\}) - \mathcal{R}^{(\mathrm{PS})}(\{\vec{a}\})
\tag{7.7.6}
$$

sets both methods on equal footing. Mc@Nlo thus chooses explicitly to exponentiate only those terms the parton shower does exponentiate, leaving the rest to be added in as a leading order sample. Consequently, Mc@Nlo retains *all* resummation properties of the parton shower.

7.8 Realisation of the POWHEG method in the SHERPA Monte Carlo

This section concerns itself on the details of the implementation of the POWHEG method describer in the last section within the framework of the SHERPA Monte Carlo event generator. It introduces its components necessary for this study.

The SHERPA event generator framework [7, 8], was briefly introduced in Section 1.2. SHERPA's strong point is the consistent simulation of high multiplicity processes. To this end, SHERPA contains two internal tree-level matrix element generators AMEGIC++ [25] and COMIX [26] for the simulation of high-multiplicity final states of well separated partons. Soft and collinear parton radiation is generated in SHERPA by means of a parton shower based on Catani–Seymour dipole factorisation [62]. The program also allows to steer external modules for the computation of virtual corrections using a standardised interface [53]. The corresponding real corrections and subtraction terms in the Catani-Seymour formalism [51, 52] are then provided automatically by AMEGIC++ [50].

SHERPA is therefore perfectly suited to implement the POWHEG method as all prerequisites outlined in Section 7.4 are found within a single, coherent framework.

7.8.1 Matrix elements and subtraction terms

For this study, the matrix-element generator AMEGIC++ [25] is employed. It is based on the construction of Feynman diagrams, which are evaluated using the helicity methods introduced in [38, 217]. For the computation of NLO cross sections in QCD-associated processes, AMEGIC++ provides the fully automated generation of dipole subtraction terms [50], implementing the Catani-Seymour formalism [51, 52]. As outlined in Section 7.4.1, such a subtraction procedure is a necessary ingredient to be able and compute NLO QCD cross sections with Monte-Carlo methods.

In the Catani-Seymour method, the soft and collinear singularities of the real-emission amplitude squared, $\mathcal{R}(\{\vec{a}\})$, are removed by a local subtraction term (cf. eq. (7.4.3))

$$
\begin{aligned}
\mathcal{S}(\{\vec{a}\}) &= \sum_{\{i,j\}} \sum_{k \neq i,j} \mathcal{S}_{ij,k}(\{\vec{a}\}) \\
&= \sum_{i,j} \sum_{k \neq i,j} \tilde{\mathcal{D}}_{ij,k}(\{\vec{a}\}) + \sum_{i,j} \sum_{a} \tilde{\mathcal{D}}_{ij}^{a}(\{\vec{a}\}) + \sum_{a,j} \sum_{k \neq j} \tilde{\mathcal{D}}_{k}^{aj}(\{\vec{a}\}) + \sum_{a,j} \sum_{b \neq a} \tilde{\mathcal{D}}^{aj,b}(\{\vec{a}\}) \, .
\end{aligned}
\tag{7.8.1}
$$

On the first line, the notation of Section 7.4.1 is adopted, while on the second line the definitions of [51, 52] are restored by defining $i, j, k > 2$, $a, b = 1, 2$ and requiring all indices to be mutually distinct. Along those lines, $\tilde{\mathcal{D}}_{ij,k}$, $\tilde{\mathcal{D}}_{ij}^{a}$, $\tilde{\mathcal{D}}_{k}^{aj}$ and $\tilde{\mathcal{D}}^{aj,b}$ are the four types of Catani-Seymour dipole terms, as depicted in Fig. 7.1, for final-state splittings with final-state spectators, final-state splittings with initial-state spectators, initial-state splittings with final-state spectators and initial-state splittings with initial-state spectators, respectively. This implies that for final-state splittings, i.e. $i, j > 2$,

$$
\mathcal{S}_{ij,k} = \mathcal{S}_{ji,k} = \frac{1}{2} \tilde{\mathcal{D}}_{ij,k} \qquad \text{and} \qquad \mathcal{S}_{ij,a} = \mathcal{S}_{ji,a} = \frac{1}{2} \tilde{\mathcal{D}}_{ij}^{a} \, ,
\tag{7.8.2}
$$

while for initial-state splittings

$$
\mathcal{S}_{aj,k} = \tilde{\mathcal{D}}_{k}^{aj} \qquad \text{and} \qquad \mathcal{S}_{aj,b} = \tilde{\mathcal{D}}^{aj,b} \, .
\tag{7.8.3}
$$

(1) FF

(2) FI

(3) IF

(4) II
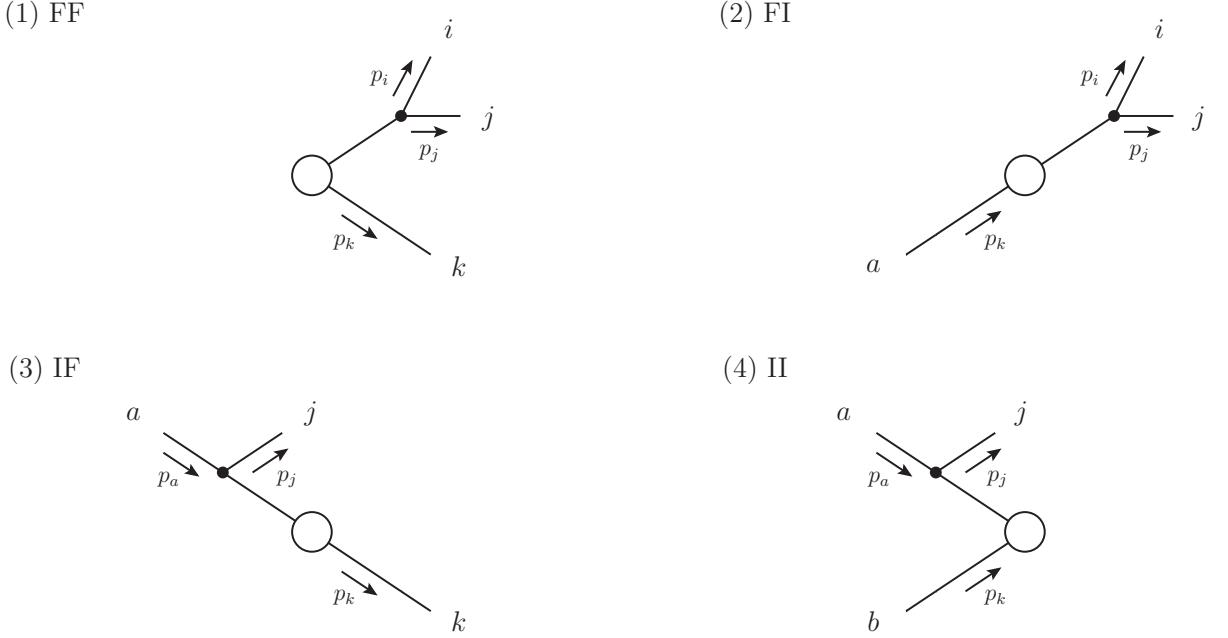
Figure 7.1: Effective diagram for the splitting of (1) a final-state parton connected to a final-state spectator, (2) a final-state parton connected to an initial-state spectator, (3) an initial-state parton connected to a final-state spectator and (4) an initial-state parton connected to an initial-state spectator in the standard Catani-Seymour notation. The blob denotes the colour correlated leading order matrix element, and the incoming and outgoing lines label the initial-state and final-state partons participating in the splitting.

Due to its analytic integrability over the extra emission phase space $\mathrm{d}\Phi_{R|B}^{ij,k}$ in $D = 4 - 2\epsilon$ dimensions, the subtraction term $\mathcal{S}$, in its integrated form $\mathcal{I}$ of eq. (7.4.4), as well as the collinear counter-terms can be added back to the virtual contributions to cancel their poles in ϵ,

$$\left\{\epsilon\left[\tilde{\mathcal{V}}(\{\vec{a}\}) + \mathcal{I}(\{\vec{a}\})\right]\right\}_{\epsilon=0} = \left\{\epsilon\left[\mathcal{V}(\{\vec{a}\}) + \mathcal{I}(\{\vec{a}\}) + \mathcal{C}(\{\vec{a}\})\right]\right\}_{\epsilon=0} = 0 \,, \qquad (7.8.4)$$

wherein $\mathcal{V}$ is the one-loop matrix element convoluted with the Born amplitude and $\mathcal{C}$ is the collinear counter-term.

The implementation in SHERPA's matrix element generator AMEGIC++, expanding upon its tree-level capabilities to generate $\mathcal{B}$ and $\mathcal{R}$, is able to generate both the subtraction terms $\mathcal{S}$ and their integrated counterparts $\mathcal{I}$ as well as the collinear counter-term $\mathcal{C}$ in an automated fashion. The virtual contributions $\mathcal{V}$, however, are obtained from dedicated external codes interfaced using the Binoth-Les Houches Accord [53]. Having all this at hand, the assembly of the $\bar{\mathrm{B}}$-function of eq. (7.4.7), integrable in $D = 4$ dimensions, is feasible in an automated way. This involves integrating over the real-emission subspace of the phase space of the NLO real correction to the Born process, cf. eq. (7.4.7), and adding the result to the terms with Born-level kinematics.

The only remaining issue is to construct an integration method, which, starting from a given Born configuration, is able to fill the real-emission phase space in an efficient manner. Having an implementation of the Catani-Seymour subtraction method at hand, the

Type	α	z		Type	α	z
FF	$y_{ij,k}$	$\tilde{z}_i$		IF	u_j	$x_{jk,a}$
FI	$1 - x_{ij,k}$	$\tilde{z}_i$		II	$\tilde{v}_j$	$x_{j,ab}$

Table 7.1: Definition of integration variables in eq. (7.8.5) for the various dipole configurations of Fig. 7.1.

Type	$z_{i,jk}$	$\tilde{y}_{ij,k}$		Type	$z_{j,ak}$	$\tilde{y}_{ja,k}$
FF	$\tilde{z}_i$	$y_{ij,k}$		IF	$x_{jk,a}$	$\dfrac{u_j}{x_{jk,a}}$
FI	$\tilde{z}_i$	$\dfrac{1-x_{ij,a}}{x_{ij,a}}$		II	$x_{j,ab}$	$\dfrac{\tilde{v}_j}{x_{j,ab}}$

Table 7.2: Mapping of variables for eqs. (7.8.6) and (7.8.7). Note that the definitions for massless partons in [51, 52] are employed.

construction of an integrator for the real-emission subspace based on CS-subtraction terms is rendered a straightforward exercise. The actual integration can be decomposed into three one-dimensional integrals (cf. eq. (7.2.4)) [51, 52]

$$\mathrm{d}\Phi_{R|B}^{ij,k} = \frac{2\,p_{\widetilde{ij}}p_{\tilde{k}}}{16\pi^2}\,\mathrm{d}\alpha\,\mathrm{d}z\,\frac{\mathrm{d}\phi}{2\pi}\,\tilde{J}_{ij,k}(\alpha, z, \phi)\,, \tag{7.8.5}$$

with the two integration variables α and z given in Tab. 7.1, cf. [50]. The azimuthal angle, ϕ, is common to all configurations.

Several different integration channels, each based on a separate CS dipole, can be combined to yield a multi-channel integrator [45] for the real-emission phase space. The a-priori weights in the multi-channel can be employed to better adapt to the emission pattern of the process under consideration. Additionally, every one-dimensional integrator can be individually improved using the VEGAS algorithm [218, 47].

7.8.2 The parton shower

SHERPA implements a parton shower based on Catani-Seymour (CS) dipole factorisation, named CSS [62]. The model was originally proposed in [219, 220] and worked out and implemented in parallel in [62, 213]. It relies on the factorisation of real-emission matrix elements in the CS subtraction framework [51, 52]. While the original algorithm has been improved in several ways [29, 64], the following section describes its version specially adapted to fill the needs of the POWHEG implementation.

Consider the process depicted in Fig. 7.1, where a parton $\widetilde{ij}$, accompanied by a spectator parton $\tilde{k}$, splits into partons i and j, with the recoil absorbed by the spectator k. Conveniently the combined momenta are identified as $p_{ij} = p_i + p_j$ and $Q = p_{ij} + p_k$. A Lorentz–invariant transverse momentum, $\tilde{\mathrm{k}}_T^2$, which acts as ordering parameter in the parton shower algorithm, can now be defined as

$$\tilde{\mathrm{k}}_T^{(\mathrm{FS})\,2} = \left|Q^2 - m_i^2 - m_j^2 - m_k^2\right|\,\tilde{y}_{ij,k}\,z_{i,jk}(1 - z_{i,jk}) - (1 - z_{i,jk})^2\,m_i^2 - z_{i,jk}^2\,m_j^2\,, \tag{7.8.6}$$

where m_i, m_j and m_k are the parton masses. The above relation holds, independent of whether the spectator parton is a final- or initial-state particle for all final-state splittings, while for initial-state splittings $a \to \widetilde{aj}\, j$, again independent of the type of spectator, the ordering parameter is given by

$$\tilde{k}_T^{(\mathrm{IS})\, 2} = \left| Q^2 - m_j^2 - m_a^2 - m_k^2 \right| \tilde{y}_{ja,k} \left(1 - z_{j,ak} \right) - m_j^2 - \left(1 - z_{j,ak} \right)^2 m_a^2 \,. \tag{7.8.7}$$

The precise definition of $\tilde{y}$ and the splitting variables z for the various dipole types are listed in Tab. 7.2.

Sudakov form factors for all branching types, taking into account finite masses of final-state partons and strictly relying on the Lorentz-invariant variables z and $\tilde{k}_T^2$, have been derived. The corresponding evolution kernels, as defined in eq. (7.2.1), read

$$\mathcal{K}_{ij,k}(\tilde{k}_T^2, z) = \frac{1}{\bar{S}_{ij}} \frac{1}{\mathcal{N}_{\mathrm{spec}}} \left\langle V_{ij,k}(\tilde{k}_T^2, z) \right\rangle \,, \tag{7.8.8}$$

where $\mathcal{N}_{\mathrm{spec}}$ is the number of spectator partons of the off-shell particle $a_{\widetilde{ij}}$ in the large N_C limit. The spin-averaged dipole functions $\langle V \rangle$, taken in four dimensions, depend on the type of emitter and spectator parton and are listed in [62]. Their infrared singularities are regularised through the parton shower cutoff, t_0, typically of the order of 1 GeV^2. The denominator factor $\bar{S}_{ij}$ avoids double-counting identical final states in final-state evolution and is given by

$$\frac{1}{\bar{S}_{ij}} = \begin{cases} 1/2 & \text{if } i, j > 2 \\ 1 & \text{else} \end{cases} \,. \tag{7.8.9}$$

A potential shortcoming of the original approach in [62] is that certain dipole functions connecting the initial and final state may acquire negative values in some non-singular regions of the phase space. This prohibits their naive interpretation in terms of splitting probabilities and leaves the corresponding parts of the phase space unpopulated. The problem was solved recently by altering the finite parts of the affected splitting functions such that they reproduce corresponding full matrix elements [221]. The splitting kinematics are defined through the Catani-Seymour phase space maps.

To generate an emission using the matrix-element correction technique presented in Section 7.3, it is important to be able and access matrix-element information during the parton-shower evolution, such that eq. (7.3.3) can be implemented in a process-independent manner. SHERPA provides an interface between its tree-level matrix-element generators and its parton shower, which allows for all the necessary interactions. Together with an implementation of the phase-space maps $b_{ij,k}(\{\vec{a}\})$, that correspond to the inverse of the Catani-Seymour splitting kinematics, eq. (7.3.3) can then be realised easily.

7.8.3 Implementation & techniques

This section details the implementation of the POWHEG method within the SHERPA framework described in detail in the previous sections. Simulating events according to eq. (7.4.9) proceeds in two steps:

1. Computing $\bar{B}(\{\vec{a}\})$, cf. eq. (7.4.7).
   AMEGIC++ [25] is used to generate Born and real-emission matrix elements. Subtraction terms are evaluated in the Catani-Seymour scheme [51, 52] according to [50], as described in Section 7.8.1. Virtual contributions are computed by external programs, which can be interfaced using the Binoth-Les Houches accord [53] or through dedicated interfaces. The sum over integrated subtracted real-emission contributions in eq. (7.4.7) is sampled using a variable number of points. Each integral in turn is evaluated in a Monte-Carlo fashion by using a single point in the respective radiative phase space, $\Phi_{R|B}^{ij,k}$.

2. Generating the hardest emission.
   A matrix-element corrected version of SHERPA's parton shower CSS [62, 64], described in Section 7.8.2, is employed to generate the hardest emission. For each trial emission, AMEGIC++ is invoked to obtain the matrix elements needed to compute the corrective weight according to eq. (7.3.1)

$$
w_{ij,k}(\{\vec{a}\}) = \frac{\rho_{ij,k}^{(\mathrm{PS})}(\{\vec{a}\})\,\mathcal{R}(\{\vec{a}\})}{\mathcal{R}_{ij,k}^{(\mathrm{PS})}(\{\vec{a}\})} \ . \tag{7.8.10}
$$

   The emissions are then ordered as in the CSS, i.e. in the relative transverse momentum $k_\perp$, cf. eqs. (7.8.6) and (7.8.7).

A special situation can arise in some next-to-leading calculations, where certain real-correction parton configurations cannot be mapped onto any of the underlying Born contributions using $b_{ij,k}^{(\mathrm{PS})}(\{\vec{a}\})$. Then two cases can distinguished: mappings that are forbidden because of kinematic restrictions of the phase space mapped onto and mappings that are forbidden because of a mismatch in parton flavours.

An example for the former case would be a situation where two high-p_T quarks emerge from a gluon that is collinear to the beam direction in the process $u\bar{u} \to e^+e^- d\bar{d}$. The collinear singularity of the underlying Born process $u\bar{u} \to e^+e^- g$ is then screened by the large gluon virtuality. However, a subtraction algorithm would put the gluon on-shell and thus identify a singular configuration, below the cut on the Born phase space.

An example for the latter case would be the parton-level subprocess $u\bar{u} \to e^-\bar{\nu}_e c\bar{s}$, contributing at NLO to the production of a W^- accompanied by a jet. At $\mathcal{O}(\alpha_s^2)$ the W can only be produced by emitting it from a final state $c\bar{c}$ or $s\bar{s}$ quark line. In the framework of a parton-shower, this would be counted as an electroweak correction to dijet production. In other words, such configurations cannot be connected to any meaningful ratio R/B.

Both of the above examples have in common that they do not lead to singularities, as the collinear pole is screened by large parton virtualities. Such contributions to the real-emission cross section do not exponentiate. They can therefore be dealt with in a uniform way. A solution to the problem was introduced in [146] in order to treat radiation zeros in W production, see Section 7.6. Its automation is discussed in Section 7.8.4. Therein, real-radiation corrections R are split into a potentially singular part $\mathcal{R}^{(\mathrm{s})}$, that can be mapped onto an underlying Born contribution, and into a regular part $\mathcal{R}^{(\mathrm{r})}$, where this is not possible or not desired. In this case, no phase-space maps need to be defined. Such a splitting into singular and non-singular parts can also be employed to implement a different scheme for matching logarithmic contributions from the parton shower and hard matrix elements, see Sections 7.4 and 7.7.

Details on how the splitting between singular and non-singular pieces is achieved for processes with existing underlying Born configurations can be found in Section 7.8.4. Nonetheless, the event generation then proceeds as above, replacing R → R$^{(\mathrm{s})}$, and adding R$^{(\mathrm{r})}$ explicitly as a leading order sub-sample.

7.8.4   Automatic identification of Born zeros

It was noted in [146] that eq. (7.3.3) can develop spurious singularities as the matrix element of the underlying Born process may be zero, while the real-emission matrix element is not. Such configurations do not exponentiate, as $\mathcal{R}$ is not singular when $\mathcal{B} \to 0$. This fact can

be employed to formulate a general solution to the problem [146]. One can split $\mathcal{R}$ into two parts, a singular one, $\mathcal{R}^{(\mathrm{s})}$, and a regular one, $\mathcal{R}^{(\mathrm{r})}$.

$$\mathcal{R}^{(\mathrm{s})} = \mathcal{R} \, \frac{Z}{Z + H} \, , \qquad \text{and} \qquad \mathcal{R}^{(\mathrm{r})} = \mathcal{R} \, \frac{H}{Z + H} \, , \qquad (7.8.11)$$

where

$$Z = \frac{\mathcal{B}}{\mathcal{B}_{\mathrm{max}}} \, , \qquad \text{and} \qquad H = \kappa_{\mathrm{res}}^2 \, \frac{t}{t_{\mathrm{max}}} \, . \qquad (7.8.12)$$

Note that $\mathcal{B}_{\mathrm{max}}$ can be determined during the integration of the seed cross section, while t_{max} is given as a universal function of the hadronic centre-of-mass energy, depending only on the definition of t in the parton shower model. The resolution factor κ_{res} then determines the relative splitting between $\mathcal{R}^{(\mathrm{s})}$ and $\mathcal{R}^{(\mathrm{r})}$: the larger κ_{res}, the larger the fraction $\mathcal{R}^{(\mathrm{r})}$ of $\mathcal{R}$.

The necessity of such a splitting of the real emission matrix element can be determined on an event-by-event basis by comparing the correction factor of eq. (7.3.1), $w_{ij,k}$, to a predefined threshold $w_{ij,k}^{\mathrm{th}}$. Thus, regular non-exponentiated $\mathcal{R}^{(\mathrm{r})}$ events are only produced if $w_{ij,k} > w_{ij,k}^{\mathrm{th}}$. Such a treatment ensures that both the exponentiation of the real-emission matrix element is as inclusive as possible and the parton-shower correction factor does not get too large, rendering event generation too inefficient.

7.9 Results for processes with trivial colour structures

This following sections collect results obtained with the implementation of the POWHEG algorithm in the SHERPA event generator. The focus of this section rests on processes exhibiting a trivial colour structure, i.e. containing only a single coloured line, to assess the performance of the algorithm. This is exemplified in a variety of processes, listed in detail in Section 7.9.1 with their respective cuts and relevant settings. Rooting in the identity of the $N_c \to \infty$ limit with the exact $N_c = 3$ expression, as discussed in Section 7.5, for such processes the necessary equality of both projectors, $\rho_{ij,k}$ and $\rho_{ij,k}^{(\mathrm{PS})}$, is trivially fulfilled when using the Catani-Seymour subtraction method in combination with the CSS, see Section 7.8. The function $H(\{\vec{a}\})$ in eq. (7.5.10) can then be chosen to coincide with the phase space constraint $\Theta(\{\vec{a}\})$ for every configuration of the Born phase space. The resulting distributions are thus correct at next-to-leading order accuracy for any observable throughout the phase space.

Where applicable, the CTEQ6.6 [222] parton distribution functions (and, correspondingly, the $\overline{\mathrm{MS}}$ renormalisation scheme) have been employed and the strong coupling has been defined accordingly as $\alpha_s(m_Z) = 0.118$ with NLO running for both the matrix elements and the parton shower. In Section 7.9.2 the internal consistency of the implementation is checked by performing scale variations, cross section comparisons with ordinary NLO calculations, and variations of internal parameters of POWHEG. Comparisons of results from the new implementation with predictions from tree-level matrix-element parton-shower merging (ME+PS) are presented in Section 7.9.3. Finally, comparisons with experimental data are made in Section 7.9.4. For DIS analyses the HZTOOL framework [81] is used while all other analyses have been performed using RIVET and are documented in the corresponding manual [80].

7.9.1 Process listing

Jet production in e^+e^- collisions

The annihilation of e^+e^- into hadrons is studied at LEP Run 1 energies, $E_{CMS} = 91.25$ GeV. This setup allows to validate the algorithms of Section 7.4 in pure final-state QCD evolution, which is the simplest testing ground. The parton shower cut-off scale has been set to $k_{T,\min}^2 = 1.6$ GeV^2. Even though the improvements discussed in this thesis are purely related to perturbative physics, the results are presented after hadronisation with the Lund model [223, 224, 2] to make comparison to experimental results more meaningful. The ME+PS samples have been generated with up to one additional jet in the matrix elements and the phase space slicing parameter was set to $\log(y_{cut}) = -2.25$. For the virtual matrix elements, the code provided by the BLACKHAT collaboration [54, 225, 226, 227, 228, 229] was used.

Deep-inelastic lepton-nucleon scattering

Hadronic final states in deep-inelastic lepton-nucleon scattering (DIS) are studied at HERA Run 1 energies, $E_{CMS} = 300$ GeV. Just like e^+e^--annihilation into hadrons, this process boasts a wealth of precise experimental data. From the theoretical perspective, it is invaluable, as it allows to test QCD factorisation in an extremely clean environment. The associated scale, given by the virtuality of the exchanged γ^*/Z-boson is not fixed, but potentially varies by orders of magnitude, which allows to test perturbative QCD predictions in various kinematic limits. The results are presented at the parton level only, as hadronisation corrections have little effect on the observables selected and the focus lies on the potential improvements in the perturbative part of the simulation. The Monte-Carlo settings correspond to those in [221]. ME+PS samples have been generated with up to one additional jet in the matrix element and the phase space slicing parameters were set to $\bar{Q}_{cut} = 5$ and $S_{DIS} = 0.6$ (cf. [221]). Virtual matrix elements were provided by BLACKHAT [54, 225, 226, 227, 228, 229].

Drell-Yan lepton pair production

Drell-Yan lepton pair production at Tevatron Run 2 energies is investigated, simulating $p\bar{p}$ collisions at $E_{CMS} = 1.96$ TeV. A cut on the invariant mass of the lepton pair of $66 < m_{\ell\ell}/\text{GeV} < 116$ is applied at the matrix-element level. For the ME+PS samples matrix elements with up to one additional jet were generated and a phase-space slicing cut of $Q_{cut} = 20$ GeV was applied. Virtual matrix elements were provided by BLACKHAT [54, 225, 226, 227, 228, 229]. The factorisation and renormalisation scales for the NLO matrix element were chosen as $\mu_R^2 = \mu_F^2 = m_{\perp,\ell\ell}^2$. In all tree-level matrix elements SHERPA's default scale choice was employed: The matrix element is clustered onto a core $2 \to 2$ configuration using a k_T-type algorithm with recombination into on-shell particles. Scales are defined as the lowest invariant mass or negative virtuality in the core process. Hadronisation and multiple parton interactions have been disabled to allow for a study at the parton-shower level. The $Z \to \ell\ell$ decay is corrected for QED next-to-leading order and soft-resummation effects in the Yennie-Frautschi-Suura (YFS) approach [74].

The three reactions listed in Sections 7.9.1-7.9.1 essentially amount to one and the same process at the parton level, as they only differ by crossing of initial- and final-state legs. Their combination allows to validate the implementation of the matrix-element corrections in Section 7.3 for all possible dipole configurations with quark splitters.

W boson production

Production of W bosons is presented in $p\bar{p}$ collisions at $E_{\mathrm{CMS}} = 1.8$ TeV. Although in principle similar to the Drell-Yan case, this process is of special interest to validate the automatic decomposition of the real-emission term into singular and non-singular pieces, as outlined in Section 7.8.4. If not stated otherwise, the parameters for this decomposition are set to $\kappa_{\mathrm{res}} = 4$ and $w_{ij,k}^{\mathrm{th}} = 100$. A cut on the invariant mass of the lepton-neutrino pair of $m_{\ell\nu} > 10$ GeV was applied at the matrix-element level. For the ME+PS samples matrix elements with up to one additional jet were used and a phase space slicing cut of $Q_{\mathrm{cut}} = 20$ GeV was applied. Virtual matrix elements were provided by BLACKHAT [54, 225, 226, 227, 228, 229]. The factorisation and renormalisation scales for the NLO matrix element were chosen as $\mu_R^2 = \mu_F^2 = m_{\perp,\ell\nu}^2$. In all tree-level matrix elements SHERPA's default scale choice was employed, cf. Section 7.9.1. Hadronisation and multiple parton interactions have been disabled. The $W \rightarrow \ell\nu$ decay is corrected for QED next-to-leading order and soft-resummation effects in the YFS approach [74].

Higgs boson production through gluon-gluon fusion

The production of Higgs bosons through gluon-gluon fusion is simulated for proton-proton collisions at $E_{\mathrm{CMS}} = 14$ TeV. The coupling to gluons is mediated by a top-quark loop and modeled through an effective Lagrangian [230, 231]. Again, this process is technically very similar to the Drell-Yan case, but it also allows to validate matrix-element corrections to the remaining initial-state splitting functions. Next-to-leading order corrections are rather large at nominal LHC energies, with a ratio of $K \approx 2$ between the NLO and the LO result for the total cross section. This fact has spurred tremendous efforts to perform fully differential calculations at NNLO [232, 233, 234] and several predictions have been presented which merged such fixed-order results with resummation at next-to-next-to-leading logarithmic accuracy [235, 236], as the process is expected to have high phenomenological relevance at LHC energies. However, this Chapter of this thesis centres on the behaviour of the theory at NLO only, as a prediction beyond this level of accuracy is clearly not within the capabilities of the POWHEG method.

Considering a decay of the Higgs boson into the $\tau^+\tau^-$ final state, a cut for the invariant mass of the τ pair of $115 < m_{\tau\tau}/\mathrm{GeV} < 125$ was applied at the matrix-element level. For the ME+PS merged samples matrix elements with up to one additional jet were used and a phase-space slicing cut of $Q_{\mathrm{cut}} = 20$ GeV was applied. The virtual matrix elements have been implemented according to [160]. The factorisation and renormalisation scales for the NLO matrix element were chosen as $\mu_R^2 = \mu_F^2 = m_{\perp,\tau\tau}^2$. In all tree-level matrix elements SHERPA's default scale choice was employed, cf. Section 7.9.1. Hadronisation and multiple parton interactions have been disabled. The $h \rightarrow \tau\tau$ decay is corrected for QED soft-resummation and approximate next-to-leading order effects in the YFS approach [74].

Z–pair production

The production of pairs of Z bosons is studied for proton-proton collisions at $E_{\mathrm{CMS}} = 14$ TeV. This is an important background for the golden-plated Higgs-boson discovery mode at the LHC. Detailed studies of the decay properties of the Z bosons and their correlations are known to allow for a determination of some properties of the Higgs boson, when found. Among these correlations are, e.g. the relative orientation of the decay planes of the bosons.

A cut on the invariant mass of each lepton pair of $66 < m_{\ell\ell}/\mathrm{GeV} < 116$ was applied at the matrix-element level. For the ME+PS samples matrix elements with up to one additional jet were used and a phase-space slicing cut of $Q_{\mathrm{cut}} = 20$ GeV was applied. Virtual matrix

elements were provided by MCFM [9, 237, 238]. The factorisation and renormalisation scales were chosen as $\mu_R^2 = \mu_F^2 = m_{ZZ}^2$. Hadronisation and multiple parton interactions have been disabled to allow for a study at the parton shower level. Each $Z \to \ell\ell$ decay is corrected for QED next-to-leading order and soft-resummation effects in the YFS approach [74].

W^+W^-–production

W^+W^-–production is also studied for proton-proton collisions at $E_{\mathrm{CMS}} = 14$ TeV. It is worth noting that this process hitherto has not been treated in the POWHEG approach. Similar to the Z–pair production, it is an important background to the search channel for the Standard-Model Higgs boson, at masses around and above 130 GeV. Again, in order to suppress this background, distributions which depend on correlations of decay products of the W's in phase space are heavily used.

A cut on the invariant mass of each lepton-neutrino pair of $m_{\ell\nu} > 10$ GeV was applied at the matrix-element level. For the ME+PS samples matrix elements with up to one additional jet were used and a phase-space slicing cut of $Q_{\mathrm{cut}} = 20$ GeV was applied. Virtual matrix elements were provided by MCFM [9, 237, 238]. The factorisation and renormalisation scales were chosen as $\mu_R^2 = \mu_F^2 = m_{WW}^2$. Hadronisation and multiple parton interactions have been disabled to allow for a study at the parton-shower level. Each $W \to \ell\nu$ decay is corrected for QED next-to-leading order and soft-resummation effects in the YFS approach [74].

7.9.2   Tests of internal consistency

The aim of this section is to provide consistency checks on the different aspects of the POWHEG implementation in SHERPA. At first, total cross sections as obtained from POWHEG are compared with the corresponding results from a standard NLO calculation. In this case, the public release SHERPA-1.2.2 [6] serves as the reference, which includes an implementation of [50]. Results for e^+e^- annihilation into hadrons and deep-inelastic positron-proton scattering are presented in Tab. 7.3. Numbers for inclusive Z-boson production with decay to an electron-positron pair, for inclusive W-boson production with decay to an electron-neutrino pair, and for Higgs-boson production via a top-quark loop with decay into τ are listed in Tables 7.4 and 7.5. The agreement between the POWHEG results and those of the standard integration method typically is within a 1σ range as given by the respective Monte-Carlo errors.

To examine differences between POWHEG and a parton-shower Monte Carlo regarding the exponentiation of the real-emission matrix elements in POWHEG, $\mathcal{R}$ can be approximated by its parton-shower equivalent in eq. (7.3.3), thus leading to a corrective weight of $w(\{\vec{a}\}) = 1$. Performing this (seemingly trivial) replacement does not only constitute a mandatory cross-check, whether the parton-shower approximation is retained, but it also estimates the size of corrections that can be expected at all when switching to NLO accuracy in the event simulation. Apart from the overall normalisation, in processes with no additional phase space dependence introduced by the loop matrix element, the emission pattern in POWHEG should be identical to the parton-shower result. This is verified in inclusive Z-boson production at Tevatron energies as displayed in Figure 7.2. For low transverse momentum (low jet resolution) $p_\perp \ll \mu_F$ both distributions coincide within statistical errors, which are indicated by the yellow band in Figure 7.2. For large values the emission phase space is severely restricted in the parton-shower approach, as $t < \mu_F^2 \approx m_Z^2$ and $p_\perp \lesssim t$. Any contribution to this phase-space region must therefore originate from configurations where more than one hard parton recoils against the lepton pair. Such configurations are suppressed by higher orders of α_s, and therefore the emission rate is gravely underestimated by the parton shower. As a direct consequence, all deviations are then manifestations of the exponentiation of non-logarithmic terms, which can be sizeable in the hard wide-angle emission region.

		$e^+e^- \to$ hadrons		$e^+p \to e^+ + j + X$	
		$E_{\mathrm{cms}} = 91.2$ GeV		$E_{\mathrm{cms}} = 300$ GeV $Q^2 > 150$ GeV^2	
$\mu = \mu_R = \mu_F$	Factor	POWHEG	NLO	POWHEG	NLO
$\sqrt{Q^2}$	1/2	30179(18)	30195(20)	3906(9)	3908(10)
	1	29411(17)	29416(18)	4047(10)	4050(11)
	2	28680(16)	28697(18)	4180(10)	4188(11)

Table 7.3: Cross sections in pb for e^+-e^- annihilation into hadrons at LEP and deep-inelastic positron-proton scattering at HERA as calculated in the POWHEG framework and in a conventional fixed order NLO calculation [50].

		$p\bar{p} \to W^+ + X$		$p\bar{p} \to Z + X$	
		$E_{\mathrm{cms}} = 1.8$ TeV $m_{\ell\nu} > 10$ GeV		$E_{\mathrm{cms}} = 1.96$ TeV $66 < m_{\ell\ell} < 116$ GeV	
$\mu = \mu_R = \mu_F$	Factor	POWHEG	NLO	POWHEG	NLO
$m_{\ell\nu}/m_{\ell\ell}$	1/2	1235.4(5)	1235.1(1.0)	243.96(14)	243.84(16)
	1	1215.0(5)	1214.9(9)	239.70(13)	239.59(16)
	2	1201.4(5)	1202.0(9)	236.72(13)	236.77(15)
$m_\perp$	1/2	1231.0(5)	1230.3(1.0)	243.00(14)	243.06(16)
	1	1211.8(5)	1211.7(9)	239.01(13)	238.96(15)
	2	1198.8(5)	1199.3(9)	236.23(13)	236.13(14)

Table 7.4: Cross sections in pb for inclusive $W^+[\to e^+\nu_e]$ and $Z[\to e^+e^-]$ production at the Tevatron as calculated in the POWHEG framework and in a conventional fixed order NLO calculation [50].

		$pp \to h + X$	
		$E_{\mathrm{cms}} = 14$ TeV $115 < m_{\tau\tau} < 125$ GeV	
$\mu = \mu_R = \mu_F$	Factor	POWHEG	NLO
$m_{\ell\nu}/m_{\ell\ell}$	1/2	2.3153(13)	2.3130(13)
	1	2.4487(12)	2.4474(13)
	2	2.5811(13)	2.5786(13)
$m_\perp$	1/2	2.2873(13)	2.2869(14)
	1	2.4255(12)	2.4231(19)
	2	2.5623(13)	2.5620(14)

Table 7.5: Cross sections in pb for inclusive $h[\to \tau^+\tau^-]$ production via a top-quark loop at the LHC as calculated in the POWHEG framework and in a conventional fixed order NLO calculation [50].
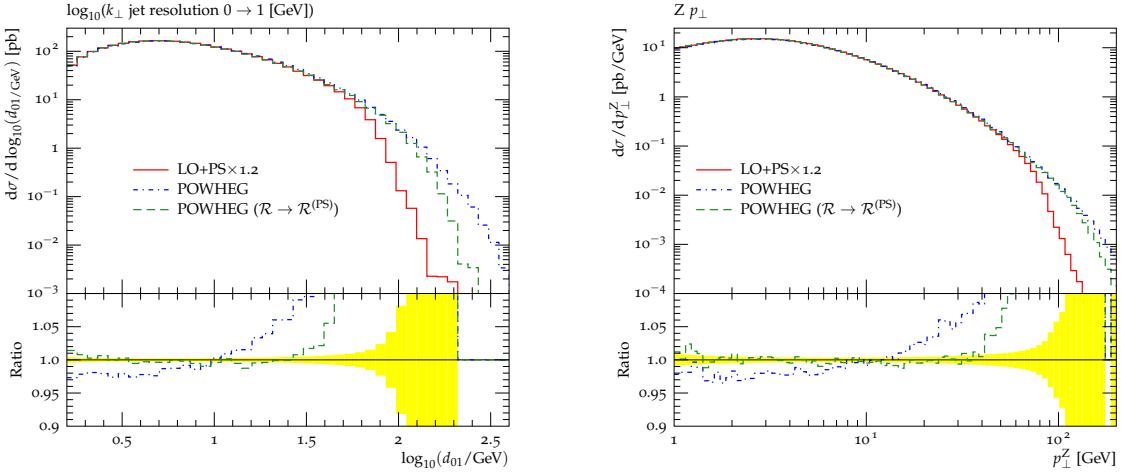
Figure 7.2: $0 \to 1$ jet resolution in k_T clustered jets and transverse momentum of the reconstructed Z-boson in Drell-Yan lepton-pair production at the Tevatron. The standard parton shower effected on the leading order matrix elements (solid, red) is compared to the POWHEG formulation (dotted, blue) and to POWHEG with the real emission matrix element $\mathcal{R}$ replaced by its parton-shower approximation $\mathcal{R}^{(\mathrm{PS})}$ (dashed, green).

The automatic splitting of the real-emission matrix element into singular and regular contributions as presented in Section 7.8.4 contains two unphysical parameters: κ_{res}, which governs the relative sizes of the exponentiated, singular part $\mathcal{R}^{(\mathrm{s})}$ and the non-exponentiated, regular part $\mathcal{R}^{(\mathrm{r})}$, and $w_{ij,k}^{\mathrm{th}}$, which determines when the above separation is actually employed. The effect of κ_{res} on the central parton shower correction factor $w_{ij,k}$ is detailed in Figure 7.3. There, it can be seen that for values of κ_{res} chosen neither too low, such that the maximum of the correction factor rises beyond reasonable bounds rendering the reweighting of the parton shower inoperable, nor too high, such that parts of leading logarithmic structure of $\mathcal{R}$ are not exponentiated, event generation with the accuracy aimed at by the POWHEG algorithm is feasible. Hence, the results of the Monte-Carlo simulation should be fairly independent of κ_{res} and $w_{ij,k}^{\mathrm{th}}$, if varied within a reasonable range. Figure 7.4 displays predictions for transverse momentum spectra in W-boson production for several values of κ_{res}. As expected, no significant variations of the emission pattern can be observed. The small differences that can be seen when changing the resolution scale κ_{res} are entirely within the logarithmic accuracy of the parton-shower approach and therefore also within the logarithmic accuracy of the real-emission contribution in POWHEG. Variations in $w_{ij,k}^{\mathrm{th}}$ only have very little influence on physical distributions.

7.9.3 Comparison with tree-level matrix-element parton-shower merging

By comparing POWHEG results to a standard parton shower combined with LO matrix elements (LO+PS), it can be established whether observables are produced correctly in regions where the soft/collinear approximations in the parton shower are equivalent to the R/B ratios in POWHEG. An example is the distribution of the jet resolution scale d_{01}, using the longitudinally invariant k_T-algorithm in W/Z + jets production. This observable amounts to the k_T-scale where a 1-jet event is clustered into a 0-jet event. Figure 7.5

---

[6] See http://www.sherpa-mc.de.
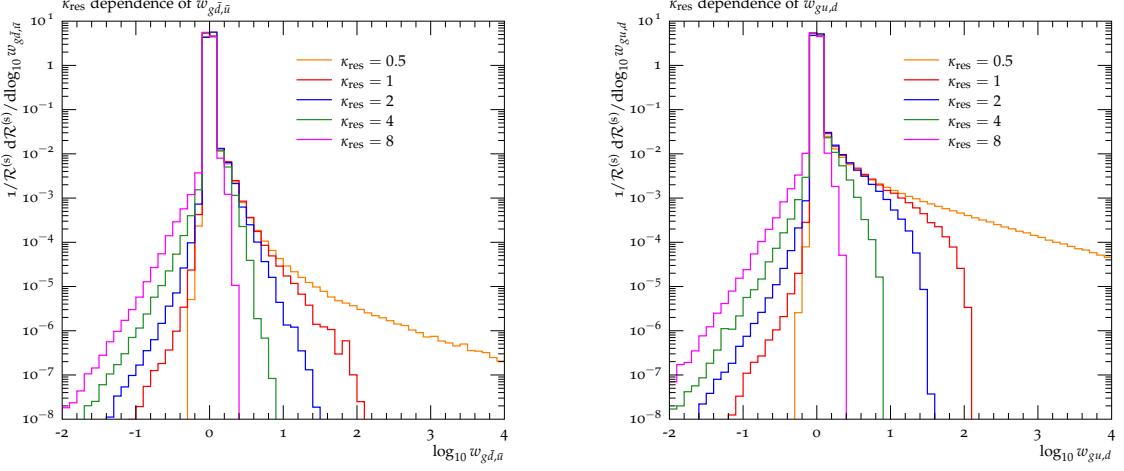
Figure 7.3: Dependence of the parton shower correction factor $w_{ij,k}$ on the Z-H-splitting parameter κ_{res} for W^- production at the Tevatron. $w_{ij,k}^{\text{th}} = 100$ was kept fixed.
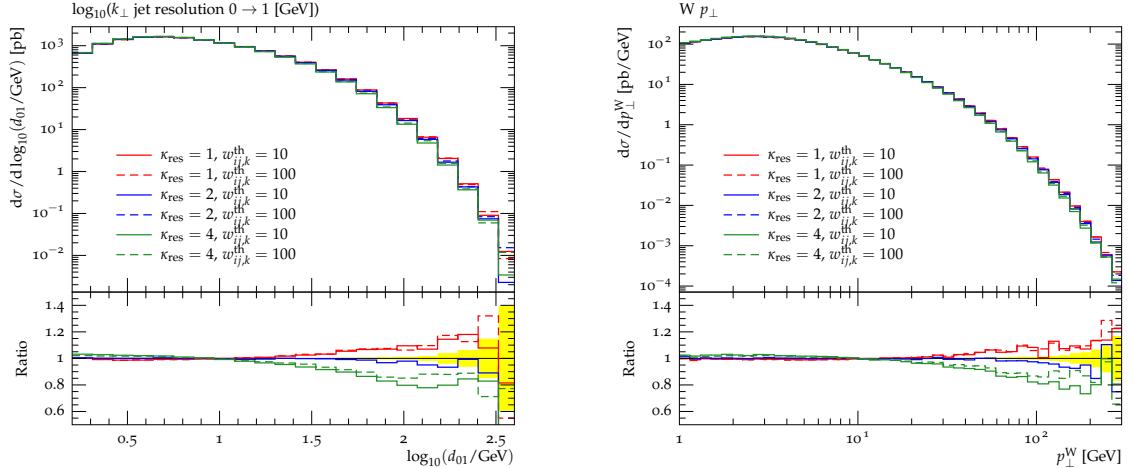

Figure 7.4: Predictions for $0 \to 1$ jet resolution in k_T clustered jets and transverse momentum of the reconstructed W boson in W-boson production at the Tevatron for different settings of the Z-H-splitting parameters κ_{res} and $w_{ij,k}^{\text{th}}$.

shows that there is good agreement between the LO+PS and POWHEG results for $d_{01} < 50$ GeV.[7] For harder emissions the LO+PS approach fails due to the restricted phase space, as explained in the previous section.

In this thesis, the POWHEG method is regarded as an advanced matrix-element correction technique for the parton-shower algorithm, in which the correction is supplemented with *local* K-factors to implement full NLO corrections. It is therefore useful to compare the respective results with matrix-element parton-shower merged samples (ME+PS), which are rescaled by a suitably chosen *global* K-factor. Such samples are known to yield approximate NLO radiation patterns by effectively implementing higher-order matrix-element corrections

---

[7]Here and in the following, the yellow band indicates the size of statistical errors on the POWHEG event sample.
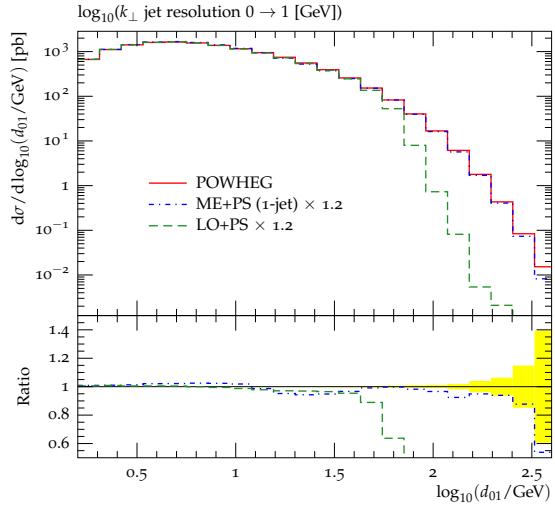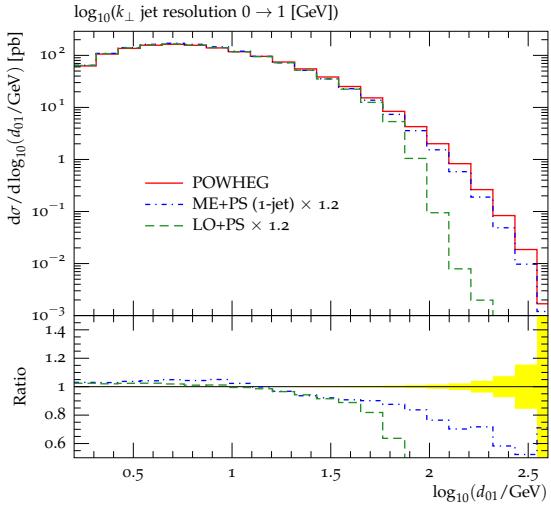
Figure 7.5: Predictions for the $0 \to 1$ jet resolution in k_T clustered jets in Z/γ^* (left) and W (right) boson production at the Tevatron.
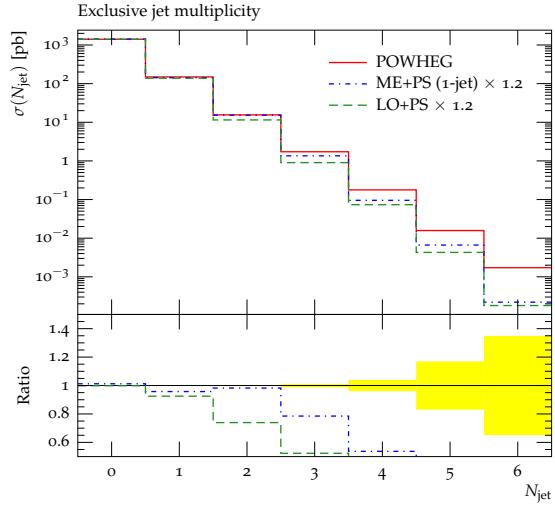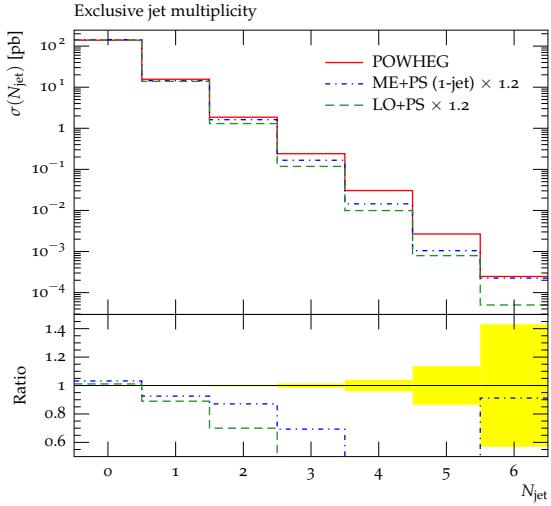

Figure 7.6: Exclusive jet multiplicity for jets with $p_\perp > 20$ GeV in the k_T algorithm in Z/γ^* (left) and W (right) boson production at the Tevatron.
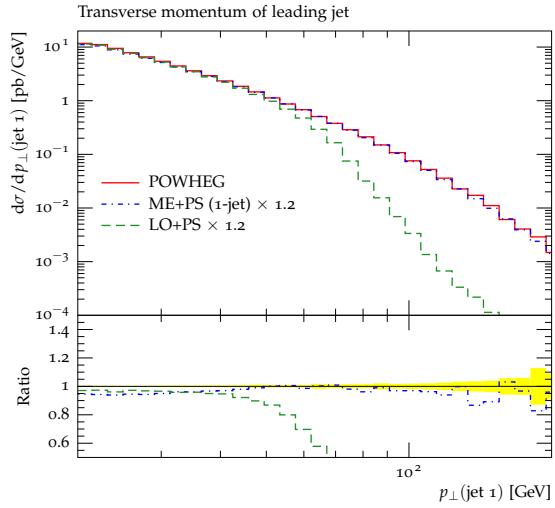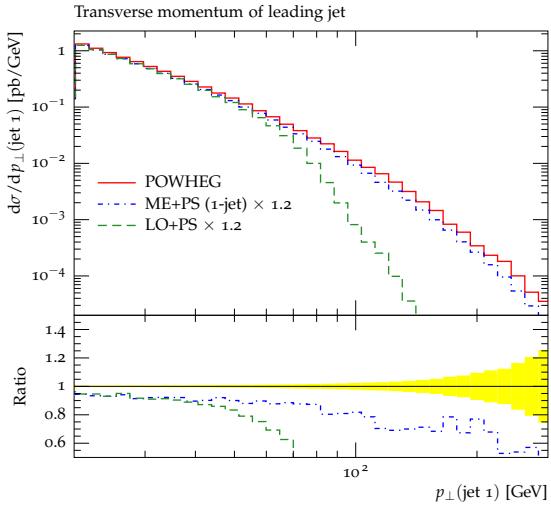

**Figure 7.7:** Transverse momentum of the leading jet in Z/γ^* (left) and W (right) boson production at the Tevatron.
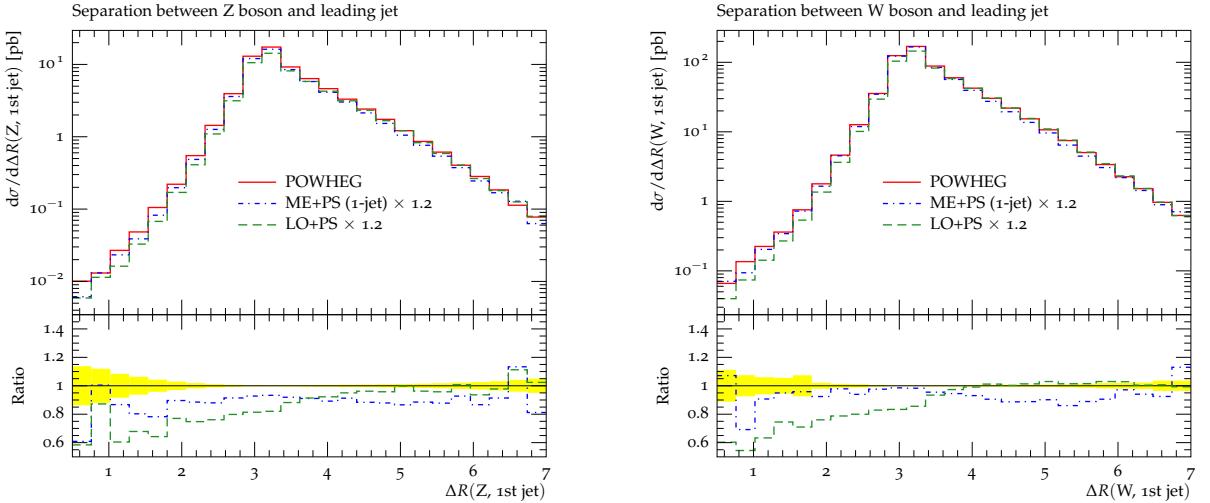
Figure 7.8: Separation between vector boson and leading jet in Z/γ^* (left) and W (right) boson production at the Tevatron.

into the parton shower. An implementation of one of the most advanced ME+PS algorithms to date is available within the SHERPA framework [29] such that a direct comparison with POWHEG is a straightforward exercise. However, because of the lack of virtual contributions in the LO+PS and ME+PS samples, an agreement of the total rate cannot be expected. Thus, in the comparisons below the following *global K*-factors were employed:

- $K = 1.038$ for $e^+e^- \to$ hadrons at LEP energies,

- $K = 1.2$ for Z/γ^* and W production at Tevatron energies,

- $K = 1.2$ for ZZ production at the LHC (14 TeV),

- $K = 1.34$ for W^+W^- production at the LHC (14 TeV), and

- $K = 2.1$ for Higgs production through gluon fusion at the same LHC energies.

When comparing POWHEG results to ME+PS results including matrix elements up to the 1-jet final state one should obtain a very similar radiation pattern. The observed agreement indeed is very good, as expected. Figure 7.5 shows that, for example, the differential one-jet rates in W/Z-boson production agrees on the 20% level, even for relatively large scales ($d_{01} >$ 50 GeV). The remaining differences can be attributed to the differences in the Sudakov form factors: While POWHEG exponentiates R/B, the ME+PS method uses standard Sudakov form factors at the logarithmic accuracy of the parton shower.

Such differences become visible also in the multiplicity distribution of k_T jets with $p_\perp > 20$ GeV in Drell-Yan and W production, cf. Figure 7.6. The 0-jet and 1-jet rates agree within 10% between POWHEG and ME+PS, but for higher multiplicity final states the POWHEG method predicts significantly more jets. Here a ME+PS simulation with more jets in the matrix element would lead to better agreement.

Now focusing on the properties of the leading jet produced in association with a W or Z boson, the transverse momentum of the leading jet is shown in Figure 7.7. Here the LO+PS approach fails to describe the hard tail of the distribution, again due to lacking phase space, while the POWHEG and ME+PS approaches agree within 20%. The separation in η-ϕ space between this jet and the W/Z boson is displayed in Figure 7.8. Clear differences are observed
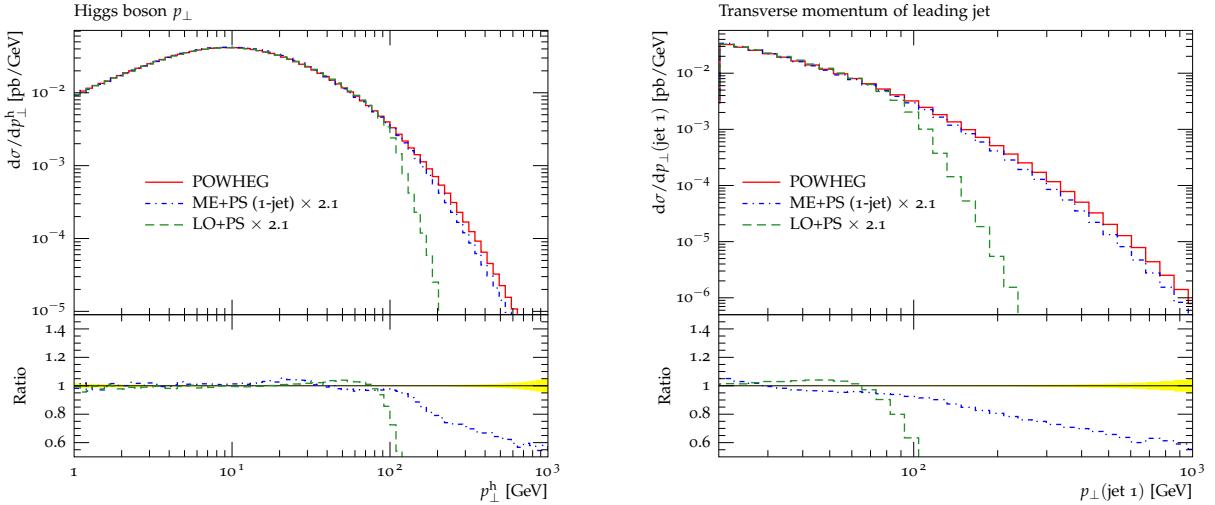
Figure 7.9: Transverse momentum of the Higgs boson (left) and leading jet (right) in $gg \to h$ fusion at nominal LHC energies.
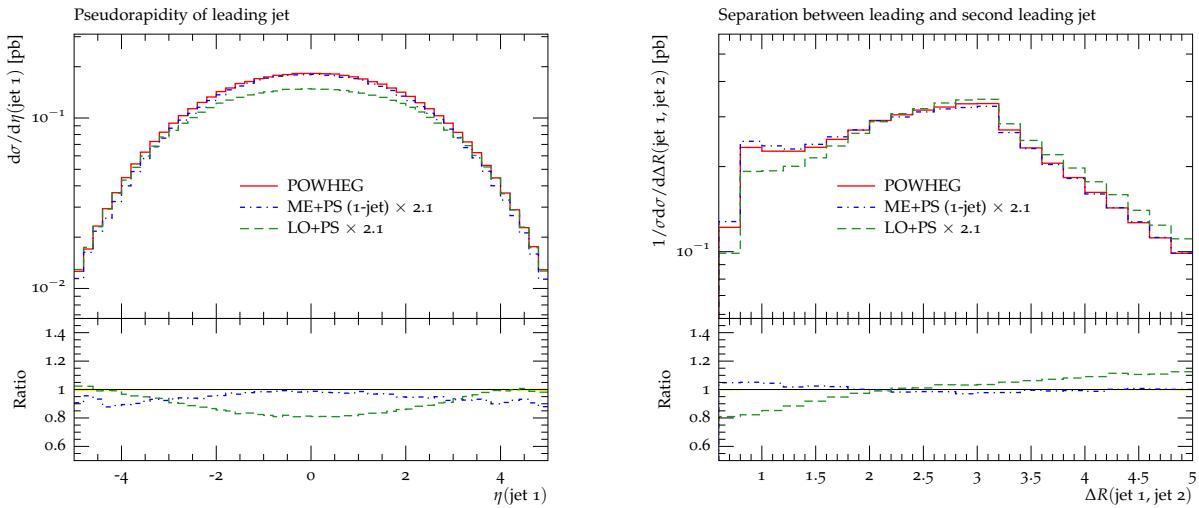

Figure 7.10: Rapidity of the leading jet (left) and separation of the leading and second-leading jet (right) in $gg \to h$ fusion at nominal LHC energies.

in the shape of the distribution when comparing the LO+PS approach with both POWHEG and ME+PS. This is expected, since parton showers cover only a restricted area of the phase space, and, in addition, they do not encode the full final-state correlations described by the matrix elements. On the other hand, results from the POWHEG and ME+PS methods agree very well, with differences below 10% only.

The transverse momentum of the Higgs boson and the transverse momentum of the leading jet displayed in Figure 7.9 give a similar picture as in vector boson production: All three methods agree very well for low transverse momenta. In the high $p_\perp$ region the POWHEG and ME+PS approaches show differences up to 40%.

Figure 7.10 shows that minor differences arise between the LO+PS and the POWHEG and ME+PS approaches in the pseudorapidity spectrum of the leading jet. This can be understood as a direct consequence of the different transverse momentum distributions in the LO+PS method, as harder jets tend to be more central than softer ones. The POWHEG and
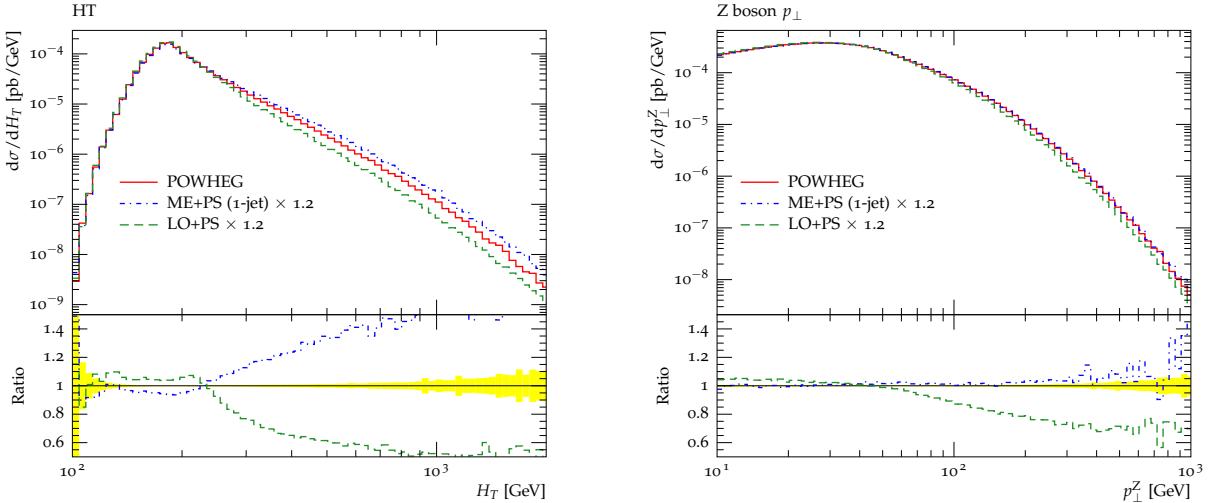
Figure 7.11: H_T (left) and transverse momentum of the individual Z bosons (right) in ZZ production at nominal LHC energies.
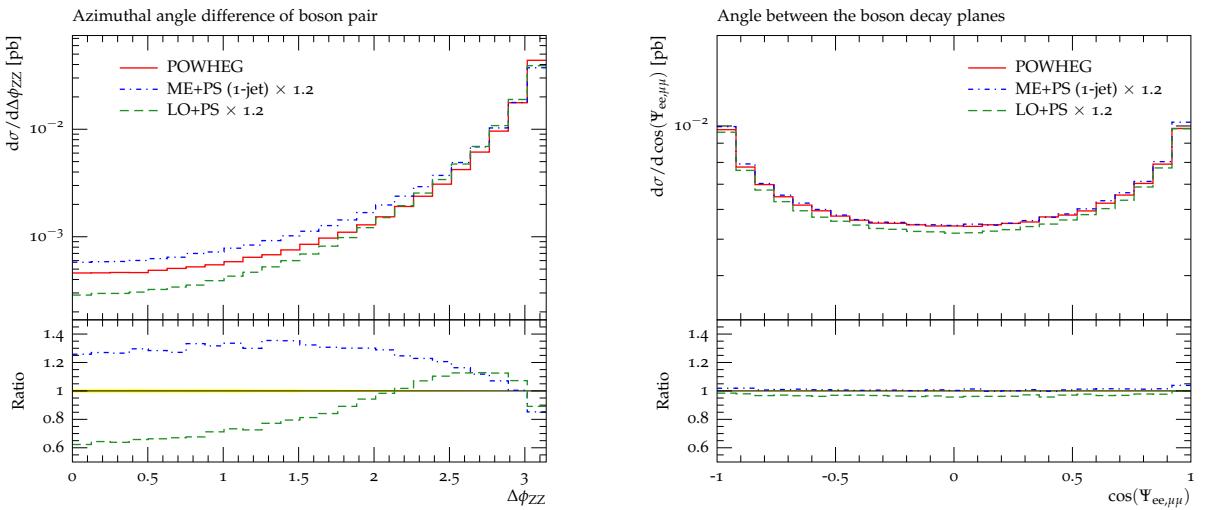

Figure 7.12: Azimuthal angle between the two Z bosons (left) and angle between the two Z decay planes (right) in ZZ production at nominal LHC energies.

ME+PS approaches agree well in the central rapidity region and show up to 10% difference only in the forward region. The distribution of η-ϕ separation between the two leading jets proves again that the POWHEG and ME+PS predictions are very similar, with deviations below the 5% level. Again, the LO+PS prediction shows a slightly different behaviour, because of the reasons stated above.

Looking at diboson production at nominal LHC energies of 14 TeV, Figure 7.11 (left) shows a comparison of the scalar sum H_T of the transverse momenta of jets and leptons in Z-pair production. Deviations of up to 50% become visible between the three compared approaches. This is especially true in the high-H_T region. It is well understood that the predictions of the LO+PS approach are softer than either of the two other approaches, due to the restricted emission phase space. The relatively large differences between the ME+PS approach and POWHEG are naively not expected, but might stem from using consistent but somewhat oversimplified scale schemes. This surely should be analysed in more detail in further studies
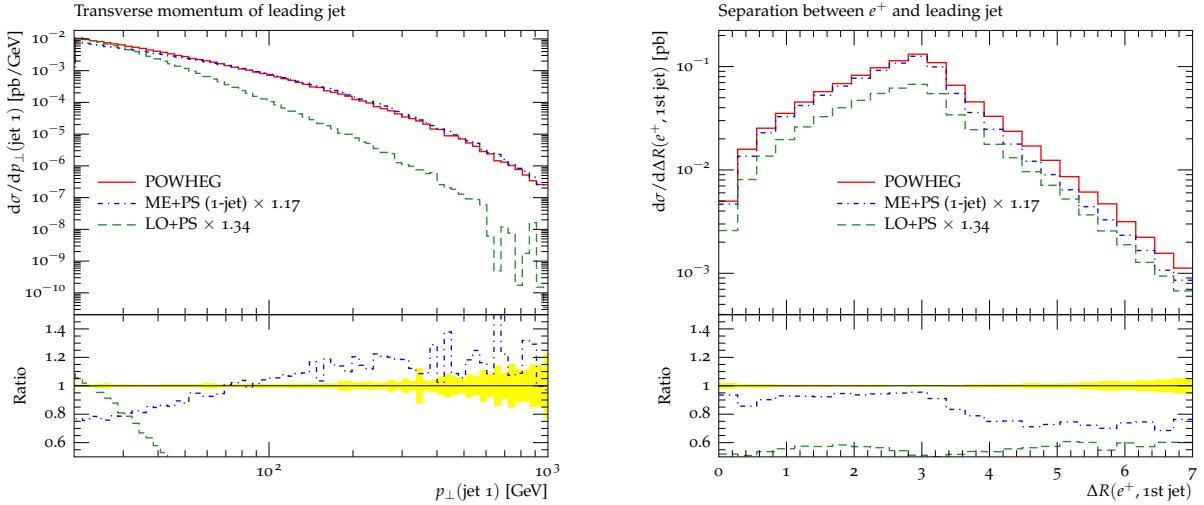
Figure 7.13: Transverse momentum of the leading jet (left) and separation of the lepton and leading jet (right) in W^+W^- production at nominal LHC energies.
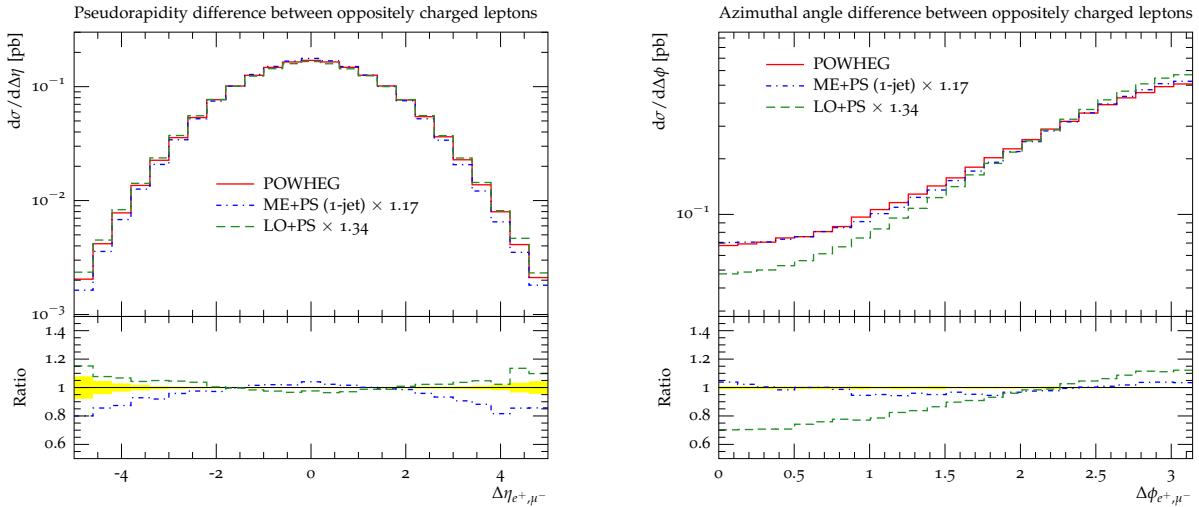

Figure 7.14: Pseudorapidity difference (left) and azimuthal angle (right) between the two oppositely charged leptons in W^+W^- production at nominal LHC energies.

where pair production processes, including WH and ZH would be studied. The transverse momentum distributions of the individual Z bosons (Figure 7.11 right) on the other hand agree very well in both approaches, while it is again obvious that the LO+PS sample cannot describe the hard region of this spectrum.

In the azimuthal separation of the two Z bosons, see Figure 7.12, a similar feature as in H_T can be found: The events are harder in ME+PS than in POWHEG, leading to increased decorrelation of the boson pair. In Figure 7.12 (right) it can be seen that the angle between the boson decay planes is predicted very consistently in all three approaches.

Properties of the leading jet in W^+W^- pair production at LHC energies are displayed in Figure 7.13. On the left hand side one can see the transverse momentum of the leading jet and on the right hand side the separation between lepton and leading jet. For both the
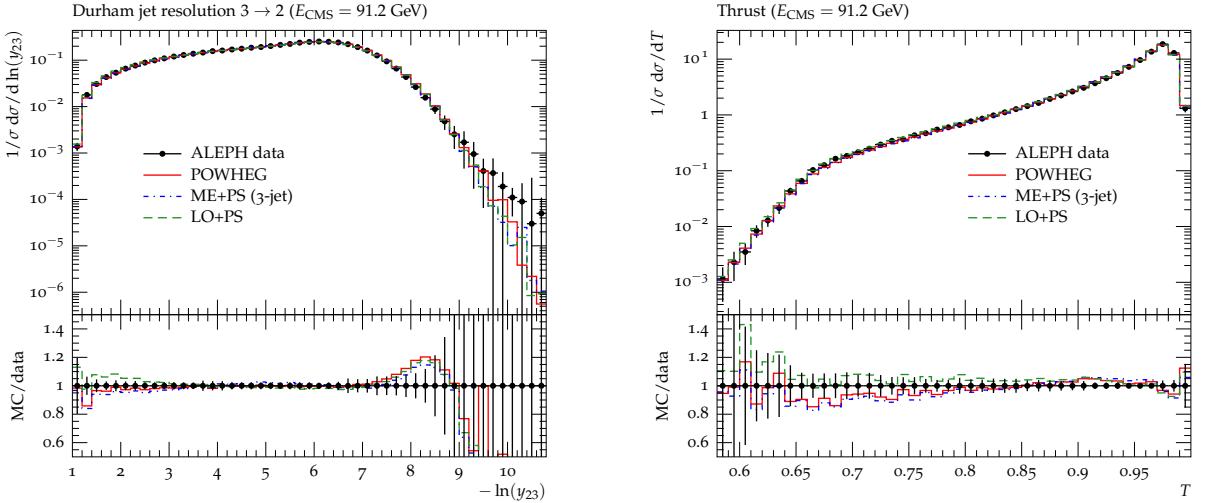
Figure 7.15: Durham $2 \to 3$ jet resolution (left) and thrust distribution (right) compared to data from the ALEPH experiment[239].
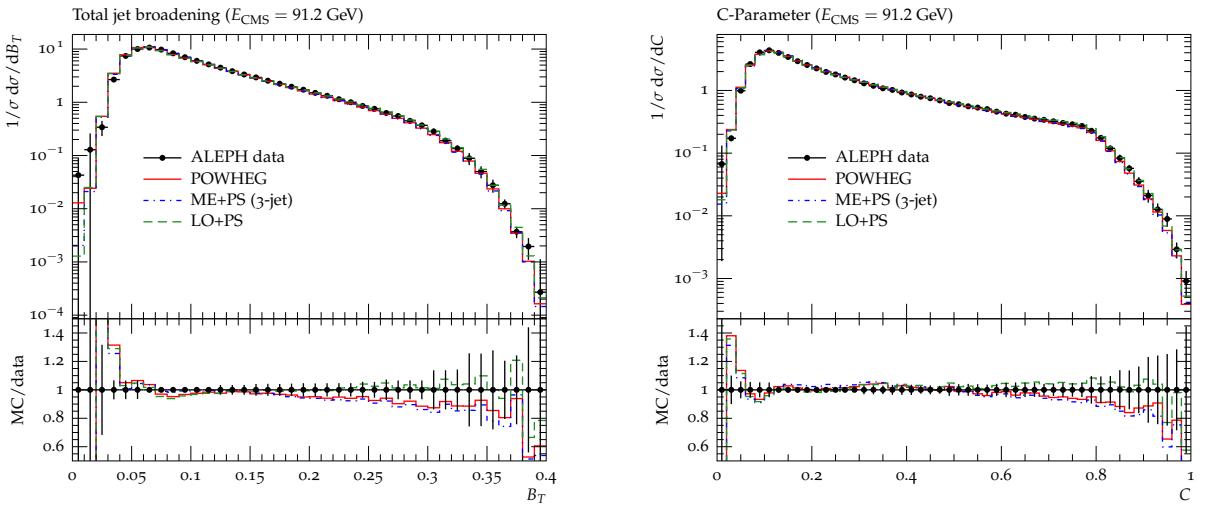

Figure 7.16: Total jet broadening (left) and C-Parameter (right) compared to data from the ALEPH experiment[239].

ME+PS and POWHEG approaches agree well within 20% and the LO+PS sample severely underestimates the hardness of the first jet due to its phase-space restrictions.

Figure 7.14 displays observables related to the two oppositely charged leptons from the two decays. The pseudorapidity difference (left) agrees within 20% for all three approaches, while their azimuthal decorrelation is significantly lower in the LO+PS sample than in the ME+PS and POWHEG approaches, which agree very well.

7.9.4 Comparison with experimental data

The remainder of this section is dedicated to a comparison of results from the POWHEG approach with experimental data to assert the improved description of data, provided by this method.

For the reaction $e^+e^- \to$ hadrons at LEP1 energies the LO+PS and ME+PS predictions do not show significant differences except in extreme regions of phase space. The POWHEG prediction confirms that picture. This is largely due to the fact that the parton-shower algorithm, which is employed in SHERPA is based on Catani-Seymour subtraction terms and those terms constitute a rather good approximation to the real-emission matrix element in the process $e^+e^- \to q\bar{q}g$.

In the distribution of the Durham jet resolution at which 3-jet events are clustered into 2-jet events (Figure 7.15 left) all three approaches agree very well with the measurement over large parts of the phase space. Only in the hard emission region $y_{23} > 0.05$ deviations from the LO+PS result can be seen. It is encouraging, although not surprising to note that both POWHEG and ME+PS describe the data better. Good agreement of all three approaches with each other and with the measurement is also observed e.g. for the thrust distribution (Figure 7.15 right), the total jet broadening (Figure 7.16 left) and the C-Parameter (Figure 7.16 right).

As was discussed in [221], deep-inelastic scattering processes offer the opportunity to test perturbative QCD in a region where the factorisation scale of the inclusive process, Q^2, is smaller than the scale of the actual event, which might be set e.g. by the transverse momentum of a hard jet. As measurements can be performed down to very low values of Q^2, many hard jets must usually be included in the simulation to achieve a good description of data throughout the phase space. This method cannot be used in the context of this work, as the POWHEG implementation in SHERPA can so far only be employed for the core process $e^{\pm}q \to e^{\pm}q$. Therefore, results are presented for the high-Q^2 region only and the discussion of the low-Q^2 domain is postponed to Chapter 8, cf. also [173], where the merging of POWHEG samples with higher-multiplicity matrix elements will be discussed. Figure 7.17 shows reasonable agreement between the POWHEG results and experimental data in a measurement of the di-jet cross section performed at the H1 experiment [240, 241]. Deviations from the LO+PS result are apparent, especially at lower values of Q^2, as the phase space of the parton shower is severely restricted by the low factorisation scale. Similar findings apply to the rapidity spectra shown in Figure 7.18.

The probably most discussed observable probing the influence of QCD radiation in hadron-hadron collisions is the transverse momentum of the lepton pair in Drell-Yan production, which is displayed in Figure 7.19. Very good agreement, compared to a recent measurement, is found for both the POWHEG and ME+PS approaches, while the LO+PS method is not able to describe large parts of the spectrum because of the restricted real-emission phase space. The rapidity of the Z boson in Figure 7.19 is described very well by all three approaches.

The situation is very similar in W-boson production. A comparison of POWHEG predictions with Tevatron data from the DØ experiment [244] is shown in Figure 7.20, where very good agreement between the Monte-Carlo result and the data can be observed. In addition to the direct comparison the uncertainties related to a variation of the renormalisation and factorisation scales are also shown. Thereby, two different strategies are pursued: While the inner (dark) band shows the uncertainty related to a variation of the scale in the hard matrix elements only, the outer (light) band shows the influence of varying the scales also in the parton-shower evolution. It is rather obvious that the latter approach yields the larger variations, as it is associated with an uncertainty in the choice of the strong coupling for the real-emission subprocess. While this process essentially determines the shape of the transverse momentum distribution in Figure 7.20, it enters at tree-level accuracy only, thus leading to a rather large scale dependence.
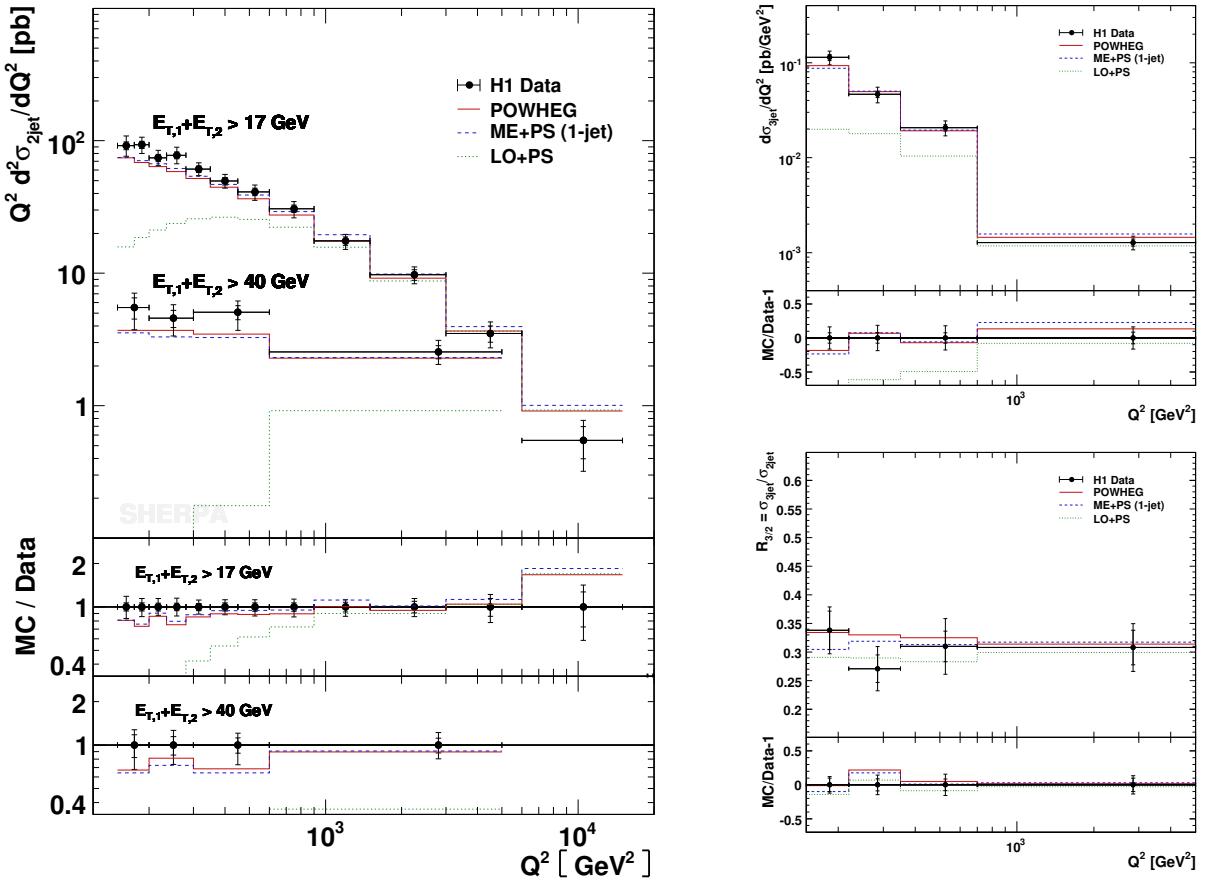
Figure 7.17: The di-jet cross section as a function of Q^2 in bins of $E_{T,1} + E_{T,2}$ (left), the three-jet cross section as a function of Q^2 (right top) and the ratio of the three- over the two-jet rate as a function of Q^2 (right bottom) compared to data from the H1 experiment [240, 241].
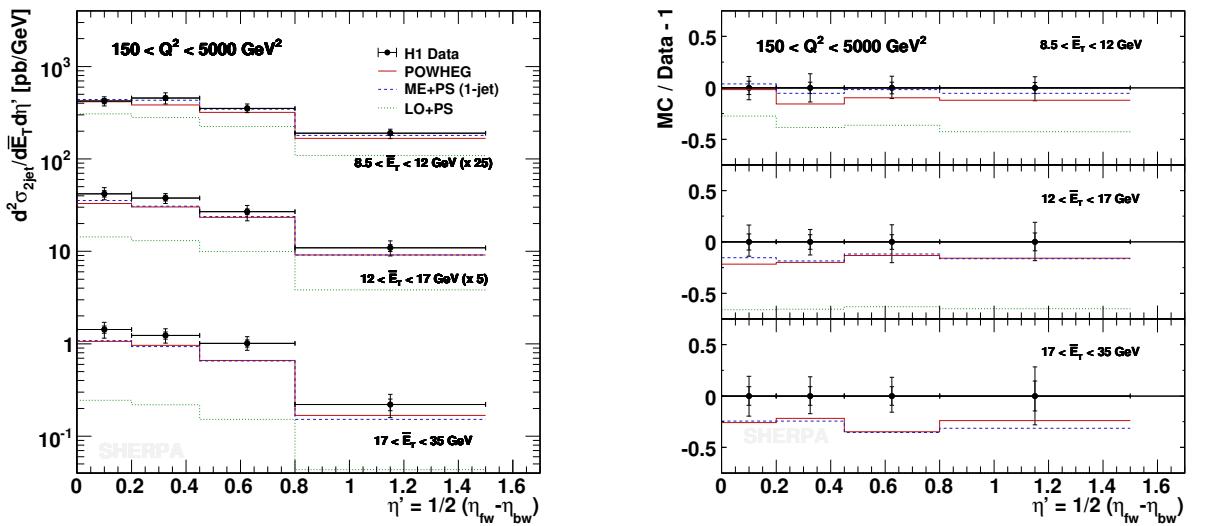
**Figure 7.18:** The di-jet cross section as a function of η', compared to data from the H1 experiment [240]. η' denotes half the rapidity difference of the two leading jets in the Breit frame.
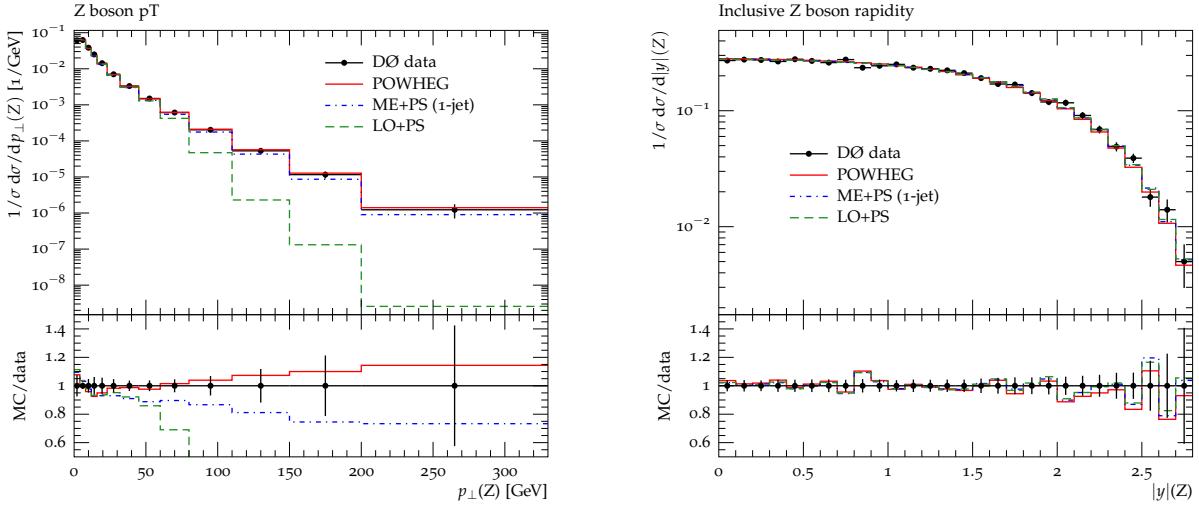
Figure 7.19: Transverse momentum and rapidity of the Z boson in Drell-Yan lepton-pair production at the Tevatron compared to data from the DØ experiment[242, 243].
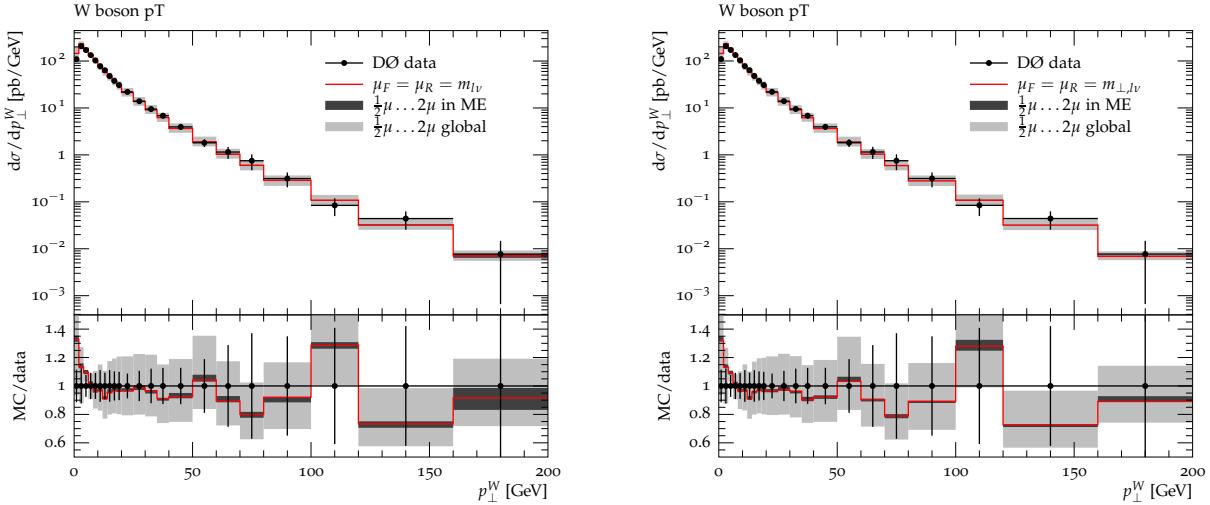

Figure 7.20: Transverse momentum of the W boson in $W+$jets production at the Tevatron compared to data from the DØ experiment [244]. Scale variations of the POWHEG prediction by factors of $1/2$ and 2 are displayed for two different scale schemes, $\mu_F = \mu_R = m_{l\nu}$ (left) and $\mu_F = \mu_R = m_{\perp,l\nu}$ (right). The inner (dark) band displays the variations associated with redefining the scales for matrix elements alone, while the outer (light) band also takes variations in the running coupling of the parton shower evolution into account.

7.9.5 Comparison with existing POWHEG results

In this section the predictions of the automated implementation are compared to results from the dedicated codes in the HERWIG++ 2.4.2 event generator [3, 134] [8]. Drell-Yan lepton pair

---

[8]Thanks are extended to David Grellscheid, Keith Hamilton and Peter Richardson for their help with settings in the HERWIG++ generator run card.
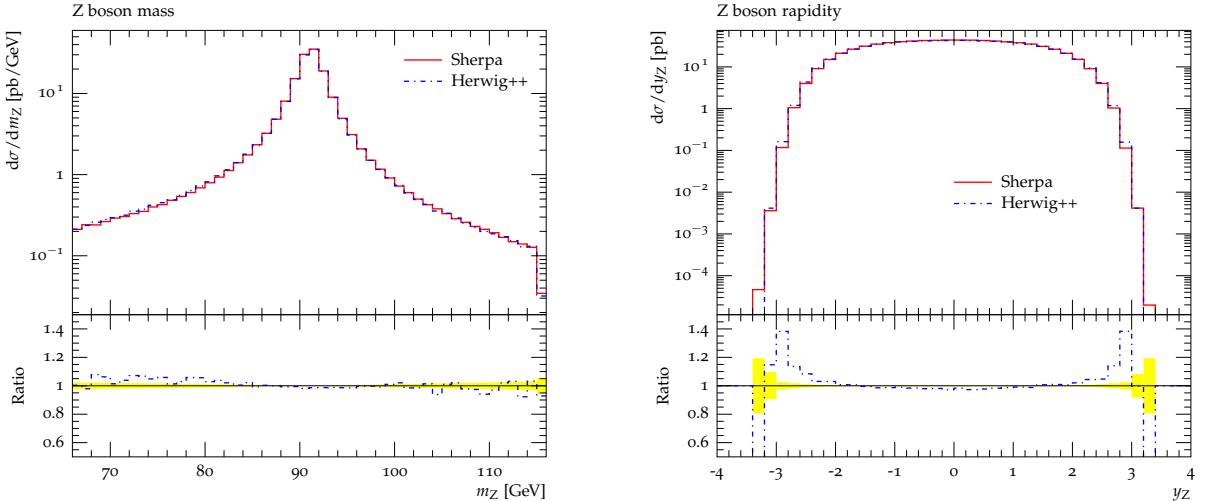
Figure 7.21: Invariant mass (left) and rapidity (right) of the lepton pair in Z/γ^* production at the Tevatron compared to HERWIG++.
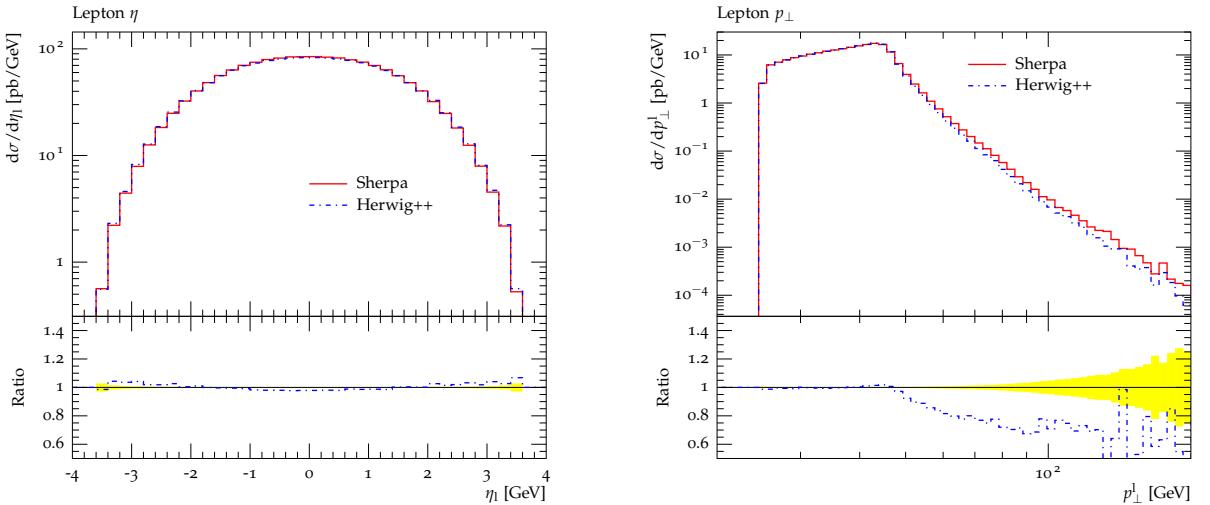

Figure 7.22: Pseudorapidity (left) and transverse momentum (right) of the lepton in Z/γ^* production at the Tevatron compared to HERWIG++.

production and Higgs boson production through gluon-gluon fusion are analysed. HERWIG++ was set up to use the CTEQ6.6 [222] PDF and matrix element cuts have been chosen identical to the ones employed in SHERPA. The same analyses as for SHERPA have been performed on the HERWIG++ events and serve as a basis for the following discussion. Corresponding details can be found in Sections 7.9.3 and 7.9.4.

For Drell-Yan lepton pair production predictions of inclusive observables related to the lepton pair are compared in Figures 7.21-7.23. Excellent agreement is found for the mass and rapidity of the lepton pair as well as the pseudorapidity of the individual leptons. Looking at the transverse momentum of both, individual leptons and the lepton pair, one finds the SHERPA predictions to be slightly harder, which also seems to be favoured by the DØ data shown on the right hand side plot of Figure 7.23.

Further distributions sensitive to the hard radiation pattern are displayed in Figures 7.23–7.25. The transverse momentum spectrum for the leading jet is consistent for both implementations over large regions of phase space. The pseudorapidity of the leading jet shows
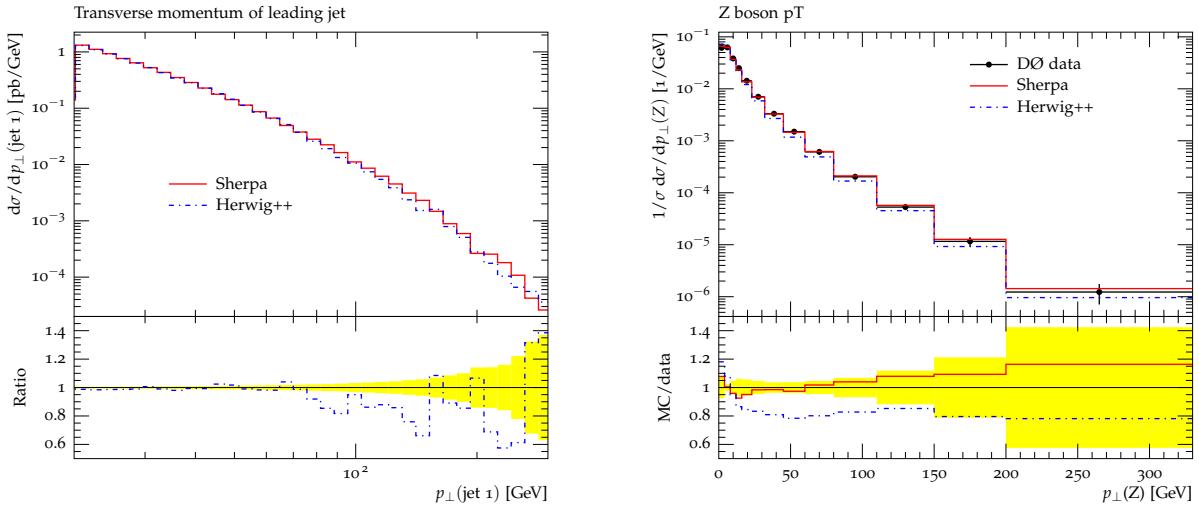
Figure 7.23: Transverse momentum of the leading jet (left) and of the lepton pair (right) in Z/γ^* production at the Tevatron compared to HERWIG++ and against data from the DØ collaboration [245].
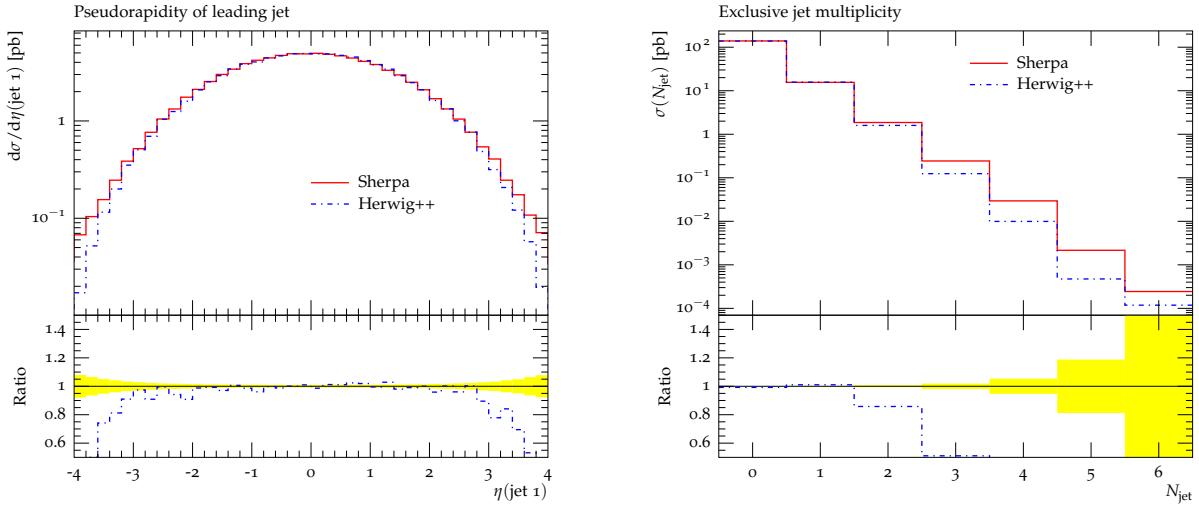
Figure 7.24: Predictions for the pseudorapidity of the hardest jet (left) and the exclusive jet multiplicity (right) in Z/γ^* production at the Tevatron compared to HERWIG++.
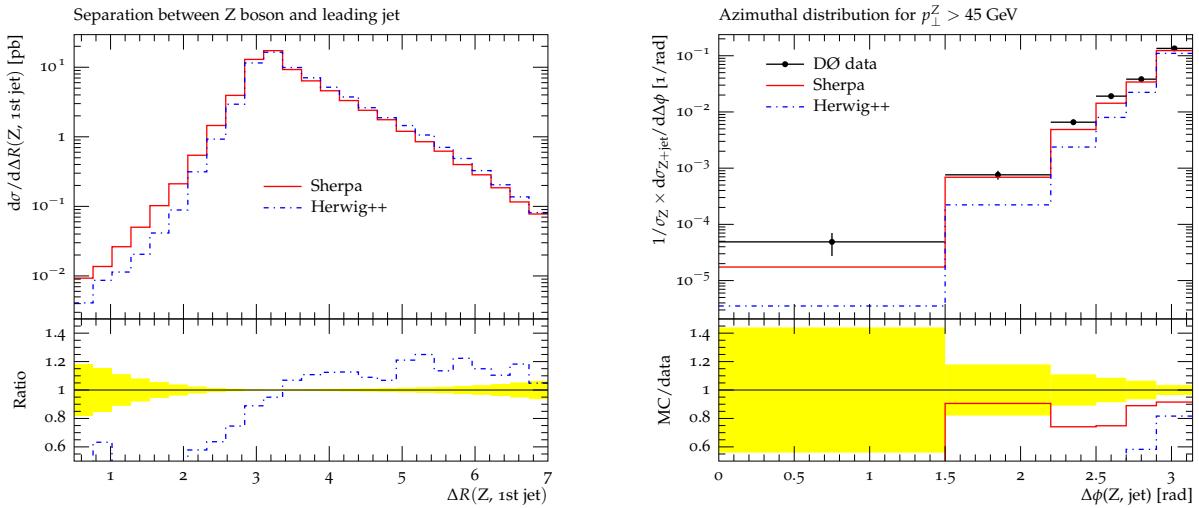
Figure 7.25: Separation of the leading jet and the lepton pair in ΔR (left) and $\Delta \phi$ (right) in Z/γ^* production at the Tevatron compared to HERWIG++ and DØ [245].
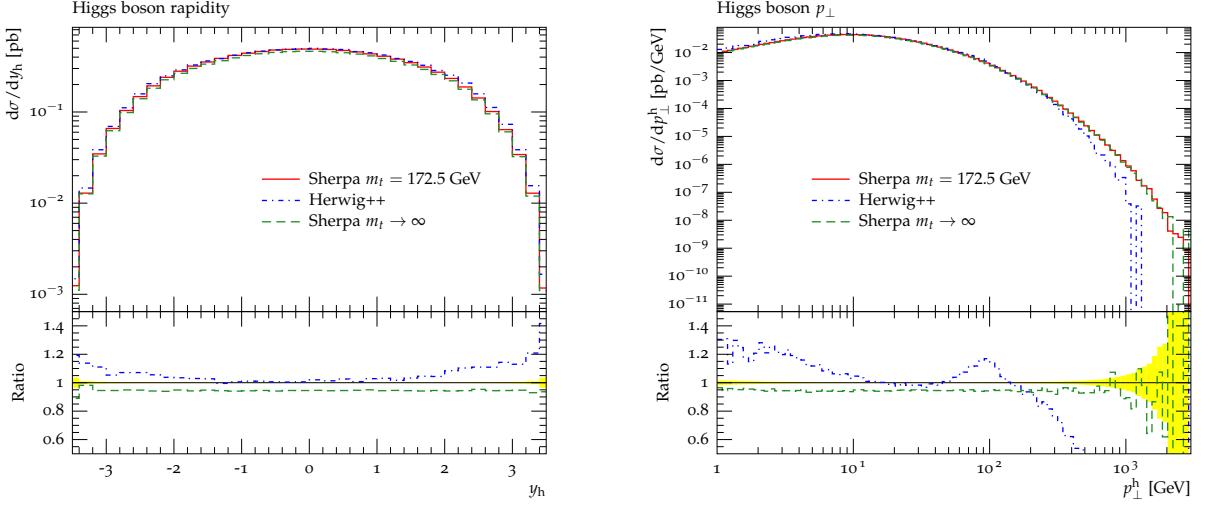
Figure 7.26: Rapidity (left) and transverse momentum (right) of the reconstructed Higgs boson in $gg \to h$ fusion at nominal LHC energies compared to HERWIG++.
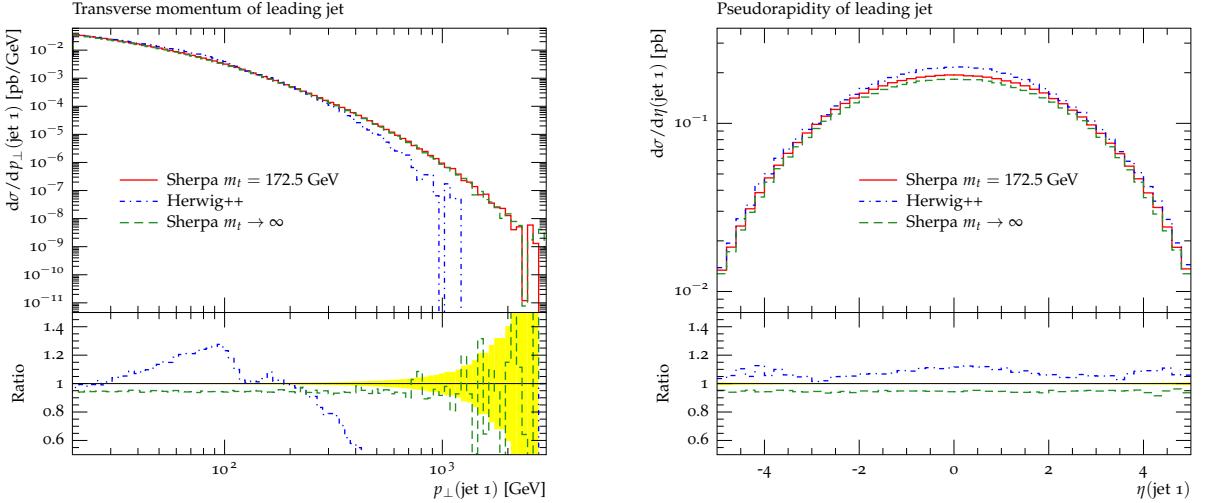
Figure 7.27: Transverse momentum (left) and pseudorapidity of the leading jet in $gg \to h$ fusion at nominal LHC energies compared to HERWIG++.
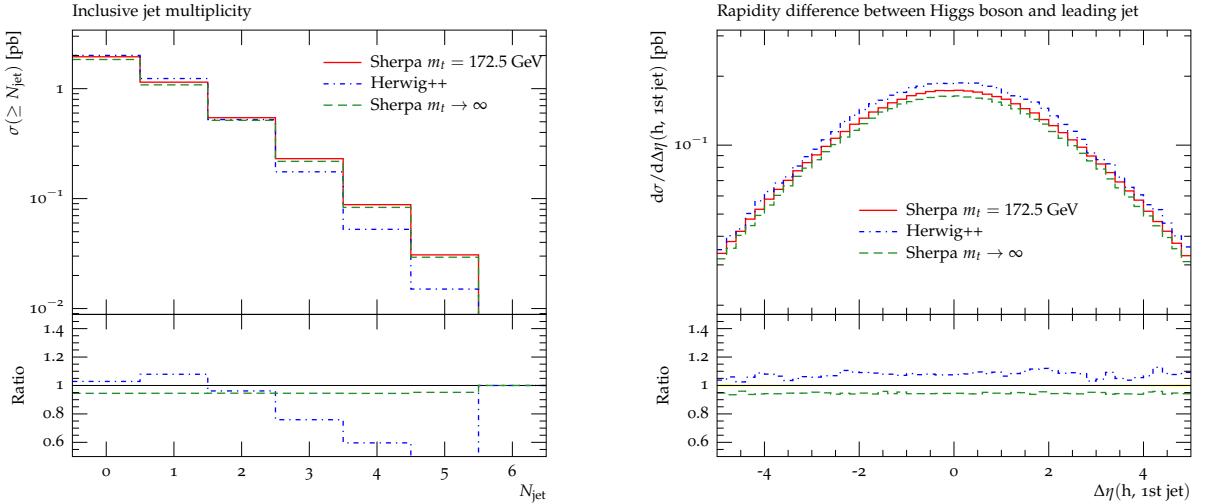
Figure 7.28: Inclusive jet multiplicity (left) and pseudorapidity separation of the leading jet to the reconstructed Higgs boson in $gg \to h$ fusion at nominal LHC energies compared to HERWIG++.

7.9 Results for processes with trivial colour structures   147

good agreement in the central region, while SHERPA produces more jets in the forward direction, $|\eta| > 3$. Regarding the leading jet, excellent agreement is also found for the exclusive jet multiplicity. For higher jet multiplicities one can see differences, with SHERPA producing more jets. At this point, it is important to stress that the production of multiple hard jets is described by the parton shower only, and the respective prediction is not systematically improved by the POWHEG method. A perfect agreement of the two results would therefore be rather unexpected, given the different assumptions underlying the parton shower algorithms in SHERPA and HERWIG++. Angular correlations between the lepton pair and the leading jet show some deviations especially in the region of low separation in ΔR and $\Delta\phi$ where multiple hard emissions become relevant. Here the DØ [245] data also favour the predictions from SHERPA.

For $gg \to h$ fusion at nominal LHC energies HERWIG++ is compared to two different settings of SHERPA: One with the correct dependence on the mass of the top quark in the effective $gg \to h$ vertex and one with the approximation $m_t \to \infty$ which has also been used for the plots in Section 7.9.3. In Figures 7.26-7.28 one finds agreement of the inclusive cross section on the level of a few percent between the generators using a finite top quark mass, while the $m_t \to \infty$ approximation leads to a change of $\approx 5\%$ in the total rates. The shape of the rapidity distribution of the reconstructed Higgs boson shows good agreement while its transverse momentum is considerably harder in the SHERPA predictions. A very similar feature can be found for the transverse momentum of the leading jet. The results for Drell-Yan lepton pair production at the Tevatron showed the same behaviour, albeit not as drastic as observed here. Good agreement is found for the shape of the pseudorapidity of the first jet. The jet multiplicity distribution shows a significant difference for the production of multiple hard jets where the difference between the parton showers in both generators becomes important. For the distribution of the rapidity difference between the reconstructed boson and the leading jet good agreement in the shape is found.

7.10 Results for processes with non-trivial colour structures

Contrary to the last section, this section presents results obtained for processes with non-trivial colour structures, containing at least three colour-correlated particles at the Born level. As discussed in Section 7.5, the equality of both projectors $\rho_{ij,k}$ and $\rho_{ij,k}^{(\mathrm{PS})}$, is mandatory in order to achieve full next-to-leading order accuracy for any observable. For the results presented in this section, however, the parton maps and projectors native to both the Catani-Seymour subtraction formalism and the CSS shower algorithm were left unchanged, i.e. no common projector $\bar{\rho}_{ij,k}$ was introduced. Nonetheless, since the CSS' splitting kernels are the (spin averaged) $N_c \to \infty$ approximations to the Catani-Seymour dipole terms, both parton maps coincide for emitter-spectator pairs which are colour correlated in this limit. The difference of both projectors, cf. eq. (7.5.6), is thus still of $\mathcal{O}(\alpha_s)$ but subleading in a $1/N_c$ expansion. The results presented in this section thus exhibit next-to-leading order accuracy in the limits $t \to 0$ and $t \to \infty$ and interpolate smoothly in between with the formal accuracy lowered to the leading colour approximation.

Similarly, the factor $H(\{\vec{a}\})$ present in the functional definitions of the projectors, as given in eq. (7.5.10), is chosen to coincide with the phase space constraint $\Theta(\{\vec{a}\})$. $\{\vec{a}\}$ again denotes a configuration in the Born phase space. As discussed in Section 7.5 this choice may lead incomplete subtractions of large contributions from either the real emission or the subtraction terms near the phase space boundaries, however, choosing coarsely grained observables reduces this effect to a minimum.
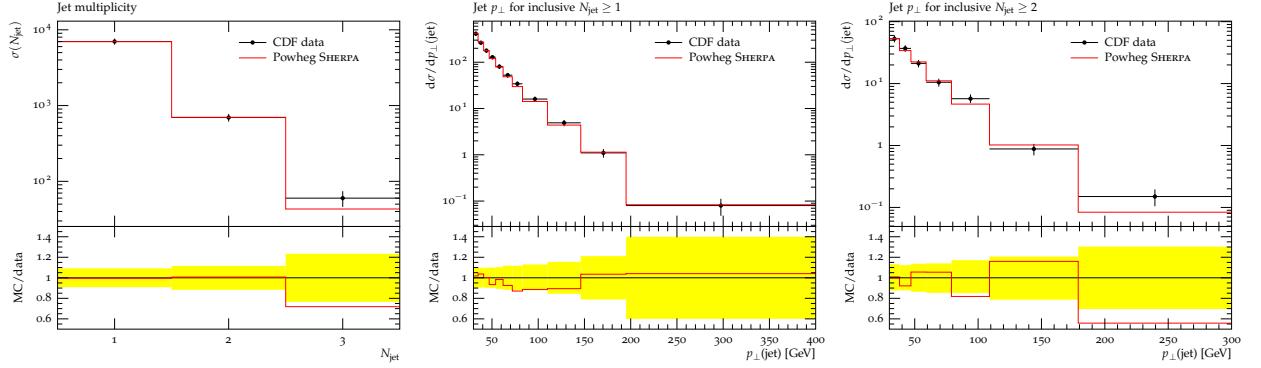
Figure 7.29: Inclusive jet cross sections and inclusive transverse momentum distributions of all and all-but-the-hardest jets compared to CDF data [247].

7.10.1 Comparison with experimental data

This section compares the predictions for Z+jet and W+jet production using the POWHEG method to experimental data. The one-loop matrix elements are supplied by BLACKHAT [54, 225, 226, 227, 228, 229]. The CTEQ6.6 [222] parton distribution functions (and, correspondingly, the $\overline{\text{MS}}$ renormalisation scheme) have been employed and the strong coupling has been defined accordingly as $\alpha_s(m_Z) = 0.118$ with NLO running for both the matrix elements and the parton shower. During the event generation every event was required to contain at least one jet with a transverse momentum of more than 10 GeV in the $\bar{B}$-function, defined using the anti-kt jet algorithm [246] with $D = 0.5$. The renormalisation and factorisation scales were chosen to be the transverse momentum of the hardest jet therein. The independence of the analyses' results on the precise value and definition of the required jet at generation time has been checked.

Further perturbative QCD corrections were effected through the parton shower [62, 64], and the leptonic decay of both the Z and the W bosons were corrected for next-to-leading order and soft resummation effects in the Yennie-Frautschi-Suura approach [74], cf. Part I of this thesis. Non-perturbative corrections, i.e. multiple parton interaction effects [66] according to [67], hadronisation [72] of all quarks and gluons into colour-neutral hadrons and their subsequent decay into stable or long-lived mesons and baryons, are also taken into account to allow for a direct comparison to the experimental data. All analyses have been performed using RIVET and are documented in the corresponding manual [80].

$Z + j$-production at the Tevatron

Turning first to Z production in association with at least one jet at the Tevatron at a centre-of-mass energy of 1.96 TeV, a measurement from the CDF collaboration [247] in the electron channel is considered. The reconstructed electrons are required to have transverse momenta $p_\perp > 25$ GeV and an invariant mass of $66 < m_{ee} < 116$ GeV. Jets are defined using the midpoint cone algorithm [250] with $R = 0.7$ and a split/merge fraction of 0.75. At least one jet with $p_\perp > 30$ GeV and $|y| < 2.1$ needs to be present and separated from both electrons by $\Delta R_{ej} > 0.7$. Figure 7.29 displays a comparison of the algorithm described in this thesis with experimental data. Cross sections and differential distributions both agree. It is remarkable that, despite only computing Z+jet production to next-to-leading order accuracy, the inclusive 2-jet rate and the transverse momentum spectrum of the second jet match the experimental data. These quantities are predicted at leading order only.
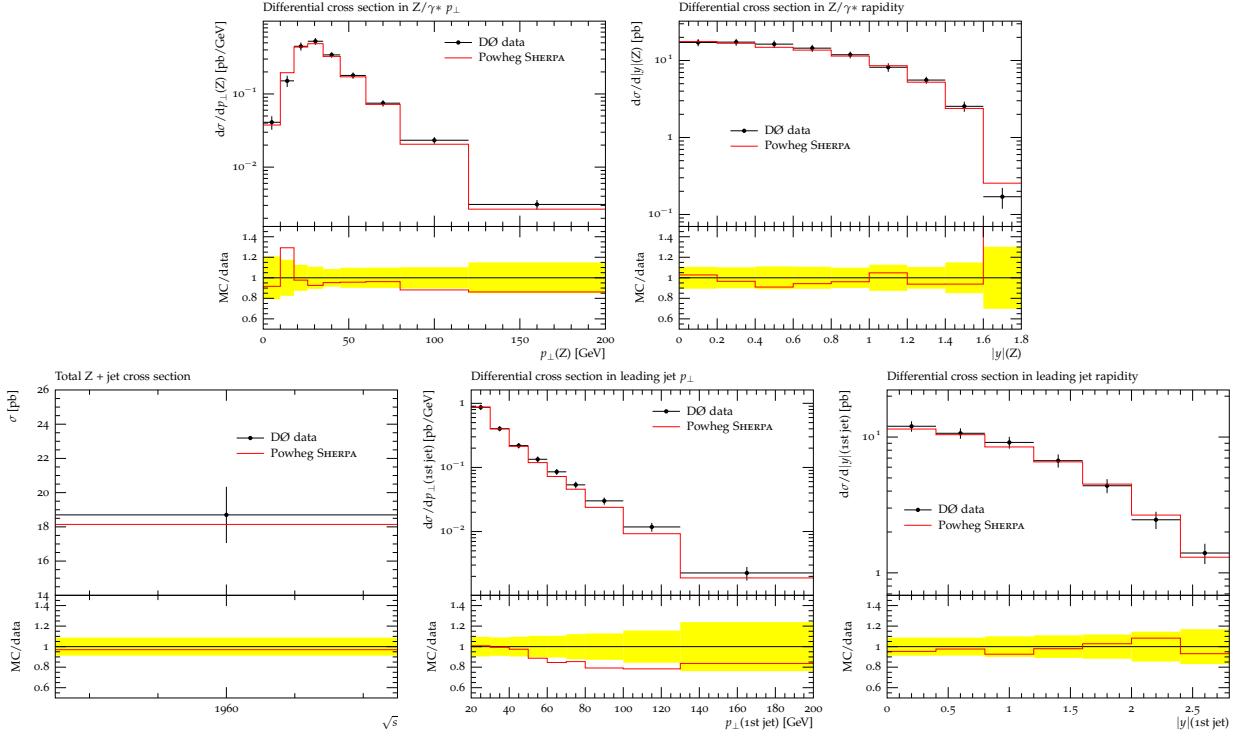
Figure 7.30: Transverse momentum and rapidity distributions of the reconstructed Z boson (top row), and the total cross section, the transverse momentum and rapidity distributions of the hardest jet (bottom row) in Drell-Yan production in association with at least one jet compared to DØ data [248].
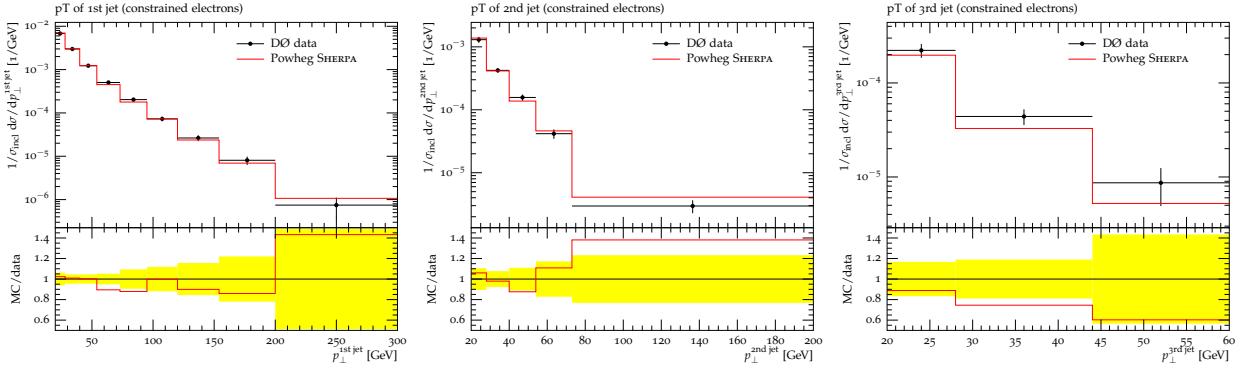
Figure 7.31: Transverse momentum distributions of the three hardest jets in Drell-Yan production in association with at least one jet compared to DØ data [249]. All SHERPA predictions are scaled to the normalised $Z + 1$ jet cross section as measured in data.

More characteristics of Z-boson plus jet production were investigated in a recent DØ analysis [248]. Events with two muons of invariant mass $65 < m_{\mu\mu} < 115$ GeV and with at least one jet of $p_\perp > 20$ GeV and $|y| < 2.8$ were collected. Jets were defined using the DØ midpoint cone algorithm [251] with $R = 0.5$ and a split/merge fraction of 0.5. Each jet had to be separated from both leptons by $\Delta R_{\mu j} > 0.5$. A comparison of Monte-Carlo predictions
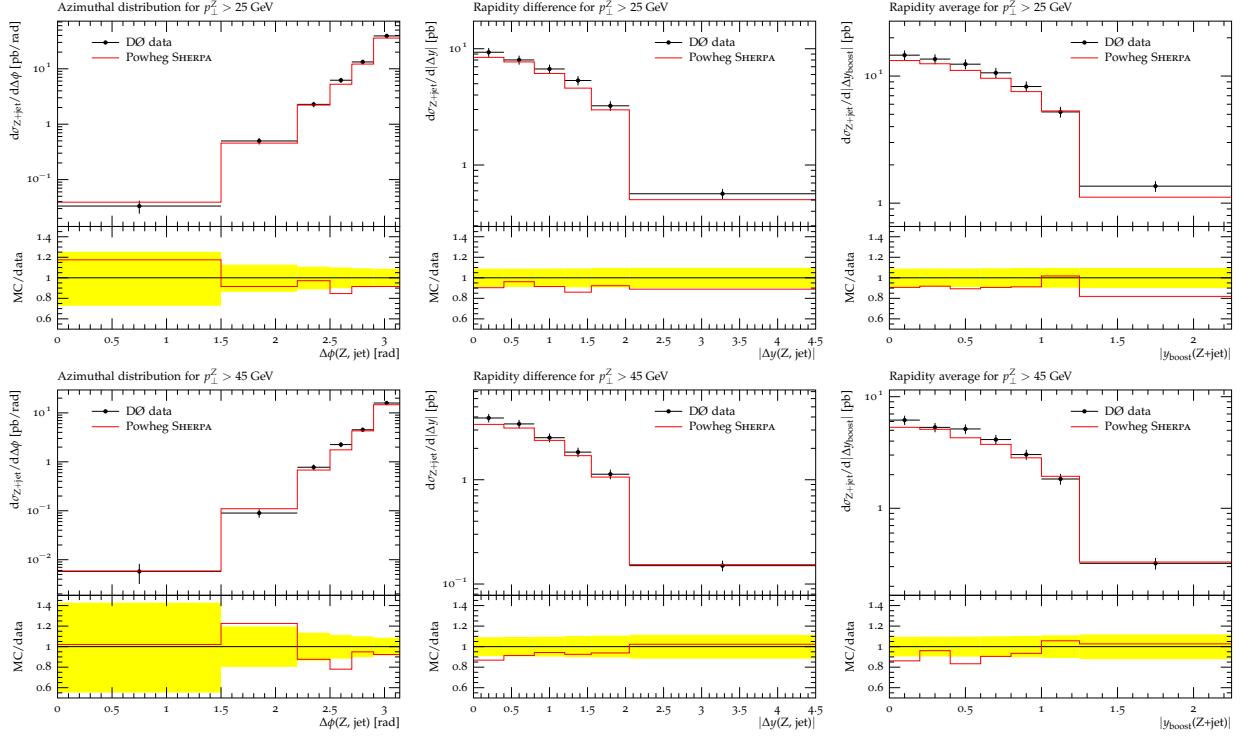
Figure 7.32: Azimuthal and rapidity difference distributions of the reconstructed Z boson and the hardest jet and their rapidity average in Drell-Yan production in association with at least one jet compared to DØ data [245].

with this measurement is shown in Figure 7.30. The agreement is excellent, except for the p_T-spectrum of the first jet, where a deficiency of the Monte-Carlo result in the range $p_T > 60$ GeV is observed.

A further measurement of Z+jet production in the electron channel was presented by the DØ collaboration in [249]. Each electron is required to have $p_\perp > 25$ GeV and the mass window $65 < m_{ee} < 115$ GeV is enforced. Jets are defined using the midpoint cone algorithm [251] with $R = 0.5$ and a split/merge fraction of 0.5. At least one jet with $p_\perp > 20$ GeV and $|\eta| < 2.5$ must be present in the event. Experimental data were normalized to the inclusive Drell-Yan cross section. This value is not predicted by the POWHEG simulation of Z+jet, and therefore all results presented here are scaled by the ratio between the 1-jet inclusive cross section measured in data and the one predicted by the simulation. Figure 7.31 displays the comparison of these scaled POWHEG predictions with the results from DØ . It is interesting to note that even the transverse momentum spectrum of the third jet is described well by the simulation. This observable is given in the parton-shower approximation only.

To quantify the success of the next-to-leading order calculation it is important not only to investigate single-particle spectra, but also correlations between the Z-boson and the hardest jet. Such observables give insights into the genuine one-loop effects in Z+jet production. We follow the analysis strategy of a measurement presented by the DØ collaboration in [245]. Opposite-sign muons with $p_\perp > 15$ GeV and an invariant mass of $65 < m_{\mu\mu} < 115$ GeV are required in association with at least one jet of $p_\perp > 20$ GeV and $|y| < 2.8$. Jets are defined using the midpoint cone algorithm [251] with $R = 0.5$ and a split/merge fraction of 0.5. Two event samples are defined, one requiring the transverse momentum of the reconstructed Z boson to be above 25 GeV, the other requiring it to be above 45 GeV. Figure 7.32 compares the predictions of the presented algorithm with the experimental measurement. The shape of distributions is matched very well, but a slight discrepancy of cross sections is observed. It does, however, not exceed the experimental uncertainties.
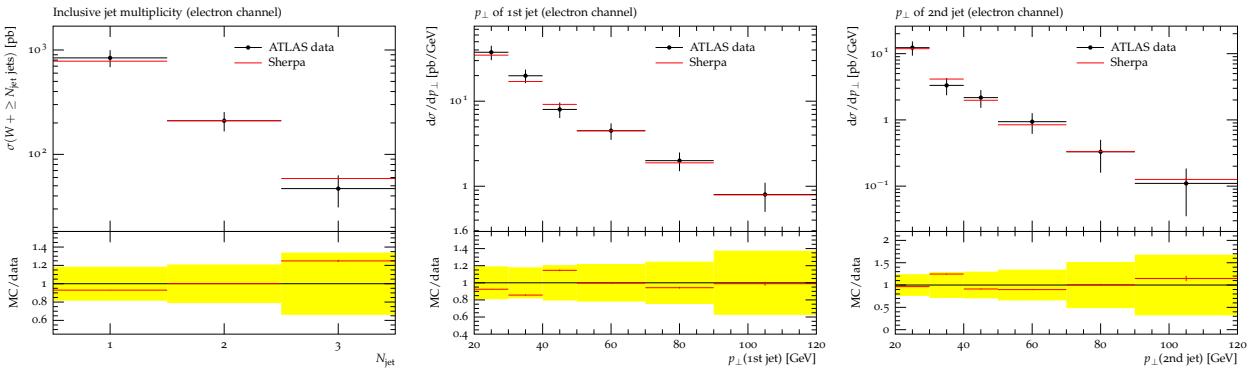
Figure 7.33: Inclusive jet cross sections and transverse momentum spectra of the hardest and second hardest jet in W production in association with at least one jet at the LHC compared to ATLAS data [**?**].

$W + j$ at the LHC

The production of a W boson in association with at least one hard jet in proton-proton collisions at $\sqrt{s} = 7$ TeV has been studied by the ATLAS collaboration at the CERN LHC [**?**]. In the electron channel events are selected by requiring an electron with $p_\perp > 20$ GeV defined at the particle level to include all photon radiation within a $\Delta R = 0.1$ cone. Only electrons in the fiducial volume $|\eta| < 1.37$ or $1.52 < |\eta| < 2.47$ are taken into account. $E_\perp^{\mathrm{miss}}$ at the particle level has been defined through the leading neutrino in the event which is required to have $p_\perp^\nu > 25$ GeV. The transverse mass cut is placed at $m_T = \sqrt{2p_\perp^\ell\, p_\perp^\nu\, (1 - \cos(\phi_\ell - \phi_\nu))} > 40$ GeV. Jets are reconstructed using the anti-k_t algorithm [246] with $R = 0.4$ and have been taken into account if $p_\perp^{\mathrm{jet}} > 20$ GeV, $|\eta_{\mathrm{jet}}| < 2.8$ and $\Delta R(\ell, \mathrm{jet}) > 0.5$. Muons, neutrinos and the leading electron were excluded from the input of jet reconstruction. The comparison in Figure 7.33 shows very good agreement of the SHERPA hadron level prediction with ATLAS data.

7.11   Summary and conclusions

In this thesis the successful implementation of the POWHEG algorithm for processes with trivial colour structures into the SHERPA framework was detailed. The program is fully automated, relying on SHERPA's efficient matrix-element generation modules, which allow to construct real-correction terms for given processes and their respective Catani-Seymour dipole terms in both differential and integrated form. It is worth stressing that this is the first time that the POWHEG method has been applied simultaneously to various higher-order calculations using Catani-Seymour dipole terms for partitioning the real-emission phase space. This implementation makes a number of processes, computed at NLO and available in public program libraries accessible for matching with a parton shower. Additional processes are easily added in SHERPA, by merely linking the corresponding code for the virtual correction terms[9].

The implementation was validated by a number of systematic checks, including

---

[9] A wealth of processes not discussed yet is, for instance, available in the extremely well-developed MCFM library.

- the stability of cross sections, as exhibited in Tables 7.3, 7.4 and 7.5;

- the radiation patterns, through comparison with a fake POWHEG algorithm, based on shower kernels, cf. Figure 7.2;

- the automated detection of Born zeroes and their stable cure, as shown in Figures 7.3 and 7.4;

- merged LO samples, see Figures 7.5 and 7.6;

- an independent POWHEG implementation, HERWIG++ 2.4.2, cf. Figures 7.21–7.28;

- and comparison with a variety of data, cf. Figures 7.15–7.20 and Figures 7.29–7.33.

The process of W-pair production has been investigated for the first time using the POWHEG technique. Results for this, along with some distributions in Z-pair production are displayed in Figures 7.11–7.14.

More processes with one coloured line only, such as WH and ZH as well as $W\gamma$ and $Z\gamma$ associated production or Higgs production in gluon fusion decaying in variety of final states, including $H \to \gamma\gamma$, $H \to 4\ell$ $H \to 2\ell 2\nu$, were added to the SHERPA framework since the time of publication of [65].

The formal relation of the POWHEG method and the MC@NLO method was established by exploiting their respective ambiguities regarding their exponentation behaviour.

Further, the principle methods presented in [65] was shown to hold for processes with non-trivial colour structures as well. Furthermore, the arising subtleties were discussed in great detail. Section 7.10 then presented the results of an approximate implementation giving predictions in the leading colour limit to the accuracy of the POWHEG method. There, a large variety of both Tevatron and LHC data is described very well.

Finally, the methods developed in this part of this thesis serve as the starting point for a combination with the ME+PS method of [29] to result in a simultaneous description of inclusive observables with next-to-leading order accuracy, as in the POWHEG method, and observables defined on the multi-jet final state with leading order accuracy, as in the ME+PS method. This combination, dubbed MENLOPS [172, 173], is detailed in Chapter 8.

Chapter 8

MEnloPS

To improve the description of multiple hard QCD radiation, "merging algorithms" (ME+PS), have been proposed [27, 28, 30, 32, 33, 252, 136] and compared in [36, 37]. A reformulation which generically maintains the logarithmic accuracy of the parton shower for any scattering process was achieved in [29][1], providing also the means to classify the various methods and implementations according to their formal accuracy. It necessitates use of *truncated* parton showers, a concept initially introduced in [12] in the context of the POWHEG method.

While the ME+PS methods succeed at improving the simulation of multijet events, they do not address the apparent problem that the total cross sections of the simulated inclusive samples are still of leading-order accuracy. However, this accuracy often is insufficient for tests of physics within and searches beyond the Standard Model. Examples for such situations range from luminosity measurements at the LHC through the production of W bosons to the determination of Yukawa couplings of the Higgs boson, once it is found. NLO cross-sections can included in a parton shower Monte-Carlo via either the POWHEG method [12, 13] or MC@NLO [11]. Both methods, however, lack the appropriate description of multiple hard emission.

Having at hand two, somewhat orthogonal, methods (ME+PS [29] and POWHEG [65], cf. Chapter 7) in one coherent Monte-Carlo event generator, SHERPA, enables the construction of an algorithm to improve both the hard QCD radiation activity *and* the total event rate in a given process. This is the topic addressed by this part of this thesis, cf. also [173]. In a parallel to the development of [173], Hamilton and Nason [172] suggested an identical method; however, their actual implementation only approximates the formal result. Due to the formal equivalence of both proposals, the new technique will generally be referred to as the MEnloPS approach.

This chapter therefore proceeds as follows: Section 8.1 recollects the prime features of both the POWHEG and the ME+PS methods, drawing heavily on the notation introduced in Chapter 7. Section 8.2 combines both methods into the MEnloPS method and assess its formal accuracy. In Section 8.3, presents consistency tests of the new method and some first predictions of the SHERPA implementation are exhibited, exemplifying the improvements that can be achieved. Section 8.4 then summarises the results. These results and their interpretation solidify the findings of [172].

8.1   Improving parton showers with higher-order matrix elements

This section is devoted to the introduction of a formalism that allows to describe, on the same footing, the two basic methods for correcting parton-shower algorithms with real-emission matrix elements, the reformulated POWHEG method of Chapter 7 and the ME+PS

---

[1] The algorithm has been further extended to include QED effects [64] and multi-scale problems [221].

method of [29]. As a common notation, the notation of Chapter 7, formally introduced in Section 7.1, will be used. To compare, and, ultimately, to combine both algorithms, only the expressions for the differential cross section describing the first emission off a given core interaction must therefore be worked out. This is where the combination takes place. The focus in the following sections rests on processes with a trivial colour structure, in particular the expressions for $N_c = 3$ and $N_c \to \infty$ coincide.

8.1.1 The POWHEG approach

As detailed in Chapter 7 the POWHEG method is reinterpreted as a matrix element reweighted parton shower supplemented with a NLO weight. Thus, using the simple corrective weight of eq. (7.3.1), it is possible to modify the parton-shower such that it produces the $\mathcal{O}(\alpha_s)$ radiation pattern of the matrix element as described. The corresponding dipole-dependent no-branching probability reads

$$
\Delta^{(\mathrm{ME})}_{\widetilde{ij},\tilde{k}}(t', t''; \{\vec{a}\}) = \exp\left\{ -\sum_{f_i=q,g} \frac{1}{16\pi^2} \int_{t'}^{t''} \mathrm{d}t \int_{z_{\min}}^{z_{\max}} \mathrm{d}z \int_0^{2\pi} \frac{\mathrm{d}\phi}{2\pi} J_{ij,k}(t,z,\phi) \right.
$$
$$
\left. \times \frac{1}{S_{ij}} \frac{S(r_{\widetilde{ij},\tilde{k}}(f_i; \{\vec{f}\}))}{S(\{\vec{f}\})} \frac{R_{ij,k}(r_{\widetilde{ij},\tilde{k}}(f_i,t,z,\phi; \{\vec{a}\}))}{B(\{\vec{a}\})} \right\},
$$
(8.1.1)

where the actual real emission matrix element projected on the singular region associated with the splitting $\{\widetilde{ij}, \tilde{k}\} \to \{ij, k\}$, $R_{ij,k}$, and the born matrix element B, which both also include the respective parton luminosity factors, replace the parton shower kernel $\mathcal{K}$ and the parton luminosities of the equation above.

The key point of the POWHEG method is to supplement Monte-Carlo event samples from such matrix-element corrected parton showers with an approximate next-to-leading order weight to arrive at NLO accuracy, cf. Section 7.4. This is achieved by multiplying eq. (8.1.1) with the local K-factor $\bar{B}(\{\vec{a}\})/B(\{\vec{a}\})$, where

$$
\bar{B}(\{\vec{a}\}) = B(\{\vec{a}\}) + \tilde{V}(\{\vec{a}\}) + I(\{\vec{a}\})
$$
$$
+ \sum_{\{\widetilde{ij},\tilde{k}\}} \sum_{f_i=q,g} \int \mathrm{d}\Phi^{ij,k}_{R|B} \left[R_{ij,k}(r_{\widetilde{ij},\tilde{k}}(\{\vec{a}\})) - S_{ij,k}(r_{\widetilde{ij},\tilde{k}}(\{\vec{a}\})) \right].
$$
(8.1.2)

In this expression, $\tilde{V}(\{\vec{a}\})$ is the NLO virtual contribution, including the collinear mass factorisation counterterms, while $S_{ij,k}(r_{\widetilde{ij},\tilde{k}}(a))$ and $I(\{\vec{a}\})$ denote real and integrated subtraction terms, respectively.

This yields the following master formula for the value of an infrared and collinear safe observable, O

$$
\langle O \rangle^{(\mathrm{POWHEG})} = \sum_{\{\vec{f}\}} \int \mathrm{d}\Phi_B(\{\vec{p}\}) \bar{B}(\{\vec{a}\}) \left[\Delta^{(\mathrm{ME})}(t_0, \mu^2; \{\vec{a}\}) O(\{\vec{p}\}) \right.
$$
$$
+ \sum_{\{\widetilde{ij},\tilde{k}\}} \sum_{f_i=q,g} \frac{1}{16\pi^2} \int_{t_0}^{\mu^2} \mathrm{d}t \int_{z_{\min}}^{z_{\max}} \mathrm{d}z \int_0^{2\pi} \frac{\mathrm{d}\phi}{2\pi} J_{ij,k}(t,z,\phi)
$$
$$
\times \frac{1}{S_{ij}} \frac{S(r_{\widetilde{ij},\tilde{k}}(\{\vec{f}\}))}{S(\{\vec{f}\})} \frac{R_{ij,k}(r_{\widetilde{ij},\tilde{k}}(\{\vec{a}\}))}{B(\{\vec{a}\})}
$$
$$
\left. \times \Delta^{(\mathrm{ME})}(t, \mu^2; \{\vec{a}\}) O(r_{\widetilde{ij},\tilde{k}}(\{\vec{p}\})) \right].
$$
(8.1.3)

Note that the second term in the square bracket describes resolved emissions, simulated by the matrix-element corrected parton shower, while the first term incorporates unresolved emissions and virtual corrections.

To reveal the fixed order properties of eq. (8.1.3) it is useful to inspect its expansion keeping terms up to $\mathcal{O}(\alpha_s)$. Thus, restating eq. (7.5.7),

$$
\begin{aligned}
\langle O \rangle^{(\text{POWHEG})} = {}& \sum_{\{\vec{f}\}} \int \mathrm{d}\Phi_B(\{\vec{p}\}) \left(\mathrm{B} + \tilde{\mathrm{V}} + \mathrm{I} \right)(\{\vec{a}\})\, O(\{\vec{a}\}) \\
& + \sum_{\{\vec{f}\}} \sum_{\{\widetilde{\imath\jmath},\tilde{k}\}} \sum_{f_i = q,g} \int \mathrm{d}\Phi_B(\{\vec{p}\})\, \mathrm{d}\Phi_{R|B}^{ij,k} \left(\bar{\rho}_{ij,k}(\bar{r}_{\widetilde{\imath\jmath},\tilde{k}}(\{\vec{a}\}))\, \mathrm{R}(\bar{r}_{\widetilde{\imath\jmath},\tilde{k}}(\{\vec{a}\}))\, \Theta(t_0 - t_{ij,k}) \right. \\
& \hspace{6cm} \left. - \mathrm{S}_{ij,k}(\bar{r}_{\widetilde{\imath\jmath},\tilde{k}}(\{\vec{a}\})) \right) O(\{\vec{a}\}) \\
& + \sum_{\{\vec{f}\}} \sum_{\{\widetilde{\imath\jmath},\tilde{k}\}} \sum_{f_i = q,g} \int_{t_0}^{\mu^2} \mathrm{d}\Phi_B(\{\vec{p}\})\, \mathrm{d}\Phi_{R|B}^{ij,k}\, \bar{\rho}_{ij,k}(\bar{r}_{\widetilde{\imath\jmath},\tilde{k}}(\{\vec{a}\}))\, \mathrm{R}(\bar{r}_{\widetilde{\imath\jmath},\tilde{k}}(\{\vec{a}\}))\, O(\bar{r}_{\widetilde{\imath\jmath},\tilde{k}}(\{\vec{a}\})) \\
& + \mathcal{O}(\alpha_s^2)\,.
\end{aligned}
\tag{8.1.4}
$$

It is imperative to note that neither the presence nor the precise form of $\Delta^{(\text{ME})}$ in the resolved emission term influence the fixed-order accuracy of the method at $\mathcal{O}(\alpha_s)$, as long as it expands as $\Delta^{(\text{ME})} = 1 + \mathcal{O}(\alpha_s)$. Similarly, different choices of scales at which α_s is evaluated in R, the $\bar{\mathrm{B}}$-function, and the matrix-element corrected parton shower emission terms contribute at $\mathcal{O}(\alpha_s^2)$ because $\alpha_s(\mu_1) = \alpha_s(\mu_2)\left(1 + \mathcal{O}(\alpha_s)\right)$ [12, 13].

In order to obtain the correct leading logarithmic behaviour of the real-emission term, α_s and the parton luminosities in $\Delta^{(\text{ME})}$ and the resolved emission term of eq. (8.1.3) must be evaluated at scale k_T^2. NLL accuracy can be restored for processes with no more than three coloured partons by means of the replacement [253, 254]

$$
\alpha_s \to \alpha_s \left\{ 1 + \frac{\alpha_s}{2\pi} \left[\left(\frac{67}{18} - \frac{\pi^2}{6} \right) C_A - \frac{5}{9} n_f \right] \right\}\,,
\tag{8.1.5}
$$

where the $\overline{\text{MS}}$ expression of α_s should be used. This Monte-Carlo implementation of the POWHEG method follows this approach.

8.1.2 The ME+PS approach

The ME+PS approach for the inclusion of matrix-element corrections into the parton-shower relies on a twofold generation of radiative corrections: Through an ordinary parton shower on the one hand and through real-radiation tree-level matrix elements on the other hand. In contrast to the POWHEG method, which only corrects the first emission off the core interaction, the ME+PS technique can be employed for arbitrary higher-order tree-level configurations.

A first algorithm to achieve this was presented in [27, 28]. The solution there is based on separating the radiative phase space into a region of soft/collinear emissions, the parton-shower (PS) region, and a region of hard emissions, the matrix-element (ME) region. By demanding each region to be filled by the respective way of generating radiation and some reweighting double counting and other problems can be avoided. The original formulation

has been tremendously improved in [29], by realising that, formally, separate splitting kernels in the ME and PS regions can be defined, which add up to the full splitting kernel:

$$\mathcal{K}_{ij,k}^{\mathrm{ME}}(t,z,\phi) = \mathcal{K}_{ij,k}(t,z,\phi)\,\Theta\left(Q_{ij,k}(t,z,\phi) - Q_{\mathrm{cut}}\right) \tag{8.1.6}$$

$$\mathcal{K}_{ij,k}^{\mathrm{PS}}(t,z,\phi) = \mathcal{K}_{ij,k}(t,z,\phi)\,\Theta\left(Q_{\mathrm{cut}} - Q_{ij,k}(t,z,\phi)\right)\;. \tag{8.1.7}$$

The functional form of the separation criterion $Q_{ij,k}$ is in principle arbitrary as long as it identifies soft and collinear divergences in the real-radiation matrix elements. The approach, fully outlined in [29], then replaces the splitting kernels in the ME region by the ratio of the real-emission and Born matrix elements, just like this is done in a matrix-element corrected parton shower. However, in contrast to a reweighting technique, only emission terms are modified and no correction is applied to the no-emission probabilities.

The ME+PS technique can be implemented in a master formula for the first emission, describing the expectation value of an arbitrary infrared safe observable O, similar to the POWHEG case:

$$
\begin{aligned}
\langle O \rangle^{(\mathrm{MEPS})} &= \sum_{\{\vec{f}\}} \int \mathrm{d}\Phi_B(\{\vec{p}\})\,\mathrm{B}(\{\vec{a}\})\left[\Delta^{(\mathrm{PS})}(t_0,\mu^2;\{\vec{a}\})\,O(\{\vec{a}\})\right.\\
&\quad + \sum_{\{\widetilde{ij},\tilde{k}\}}\sum_{f_i=q,g}\frac{1}{16\pi^2}\int_{t_0}^{\mu^2}\mathrm{d}t\int_{z_{\mathrm{min}}}^{z_{\mathrm{max}}}\mathrm{d}z\int_0^{2\pi}\frac{\mathrm{d}\phi}{2\pi}\,J_{ij,k}(t,z,\phi)\\
&\quad \times \frac{1}{S_{ij}}\left(\frac{8\pi\,\alpha_s}{t}\,\mathcal{K}_{ij,k}(t,z,\phi)\,\frac{\mathcal{L}(r_{\widetilde{ij},\tilde{k}}(f_i,t,z,\phi;\{\vec{a}\});t)}{\mathcal{L}(\{\vec{a}\};t)}\,\Theta\left(Q_{\mathrm{cut}} - Q_{ij,k}\right)\right.\\
&\quad \left.+ \frac{S(r_{\widetilde{ij},\tilde{k}}(\{\vec{f}\}))}{S(\{\vec{f}\})}\,\frac{\mathrm{R}_{ij,k}(r_{\widetilde{ij},\tilde{k}}(\{\vec{a}\}))}{\mathrm{B}(\{\vec{a}\})}\,\Theta\left(Q_{ij,k} - Q_{\mathrm{cut}}\right)\right)\\
&\quad \left.\times \Delta^{(\mathrm{PS})}(t,\mu^2;\{\vec{a}\})\,O(r_{\widetilde{ij},\tilde{k}}(\{\vec{a}\}))\right]\;.
\end{aligned}
\tag{8.1.8}
$$

There are three components to the differential cross section: The first term describing unresolved emissions, which is generated in the standard parton-shower approach, and the second term describing the resolved part, which is now split between the PS and the ME domain. Within the ME domain, the matrix-element generator is directly invoked to define the real-emission configuration. This is possible due to the restricted phase space, removing all infrared divergent regions by applying the cut in $Q_{ij,k} = Q_{ij,k}(t,z,\phi)$ and rendering the matrix element finite. In this case, the Sudakov form factor $\Delta^{(\mathrm{PS})}$, which makes the matrix element exclusive, must be added explicitly. It can either be calculated analytically, like in the original formulation of [27, 28], or by utilising the shower itself to generate the correct probabilities. This latter option is commonly referred to as the pseudoshower approach [30, 29].

A complication arises if the phase-space separation criterion $Q_{ij,k}$ is different from the parton-shower evolution variable t. This can imply the possibility of a shower emission $Q < Q_{\mathrm{cut}}$ being allowed "between" two branchings at $Q > Q_{\mathrm{cut}}$ in the parton-shower history of the matrix element. In such cases, in order not to spoil the logarithmic accuracy of the parton shower, the existing branchings need to be embedded into the subsequent parton-shower evolution. This leads to a truncated shower algorithm [12, 29].

If the expectation value $\langle O \rangle$ in eq. (8.1.8) is the total cross section, i.e. if $O = 1$, then

$$
\begin{aligned}
\sigma^{(\mathrm{MEPS})} = \sum_{\{\vec{f}\}} \int & \mathrm{d}\Phi_B(\{\vec{p}\})\, \mathrm{B}(\{\vec{a}\}) \left[\Delta^{(\mathrm{PS})}(t_0, \mu^2; \{\vec{a}\}) \right. \\
& + \sum_{\{\widetilde{ij},\tilde{k}\}} \sum_{f_i = q,g} \frac{1}{16\pi^2} \int_{t_0}^{\mu^2} \mathrm{d}t \int_{z_{\min}}^{z_{\max}} \mathrm{d}z \int_0^{2\pi} \frac{\mathrm{d}\phi}{2\pi}\, J_{ij,k}(t,z,\phi)\, O(r_{\widetilde{ij},\tilde{k}}(\{\vec{a}\})) \\
& \times \frac{1}{S_{ij}} \frac{8\pi\,\alpha_s}{t}\, \mathcal{K}_{ij,k}(t,z,\phi)\, \frac{\mathcal{L}(r_{\widetilde{ij},\tilde{k}}(f_i,t,z,\phi;\{\vec{a}\});t)}{\mathcal{L}(\{\vec{a}\};t)}\, \Delta^{(\mathrm{PS})}(t,\mu^2;\{\vec{a}\}) \\
& \left. \times \left(\Theta\left(Q_{\mathrm{cut}} - Q_{ij,k}\right) + w(r_{\widetilde{ij},\tilde{k}}(f_i,t,z,\phi;\{\vec{a}\}))\,\Theta\left(Q_{ij,k} - Q_{\mathrm{cut}}\right) \right) \right] .
\end{aligned}
$$

(8.1.9)

where (cf. eq. (7.3.3))

$$
w(\{\vec{a}\}) = \left[\sum_{\{m,n\}} \sum_{l \neq m,n} \frac{S(b_{mn,l}(\{\vec{f}\}))}{S(\{\vec{f}\})} \frac{\mathcal{B}(b_{mn,l}(\{\vec{a}\}))}{\mathcal{R}(\{\vec{a}\})} \frac{8\pi\,\alpha_s}{2\,p_m p_n} \mathcal{K}_{mn,l}(\{\vec{a}\}) \right]^{-1} .
$$

(8.1.10)

If $w(\{\vec{a}\})$ equals one, i.e. if the parton shower approximation is equal to the real-radiation matrix element, the t-integral can be performed easily and the square bracket in eq. (8.1.9) equals one. The total cross section is therefore identical to the leading order result, as a direct consequence of the unitarity constraint for the parton shower. The more common configuration will however be that $w(\{\vec{a}\}) \neq 1$. In this case, the square bracket in eq. (8.1.9) is different from one and the total cross section is not equal to the leading order result. The origin of the mismatch is a difference in the emission rate of the parton shower compared to the ratio R/B of matrix elements. While the former is exponentiated into the Sudakov form factor, the latter appears in the differential real-radiation probability only. Thus, for $w(\{\vec{a}\}) \neq 1$, the unitarity of the parton shower is violated. Hence, this effect is referred to as "unitarity violation" in the following. Its physical interpretation is the same as in, for example, the violation of the unitarity of the $\mathcal{S}$-matrix: the probability to scatter/radiate and the probability not to scatter/not to radiate do not add up to one. However, in the present case the unitarity violation merely leads to a correction to the total cross section which is formally of higher order, as is shown below, and, therefore, does not to unphysical results.

To investigate the consequences of this unitarity violation on arbitrary observables, eq. (8.1.8) can be expanded in powers of α_s, resulting in

$$
\begin{aligned}
\langle O \rangle^{(\mathrm{MEPS})} = \sum_{\{\vec{f}\}} \int & \mathrm{d}\Phi_B(\{\vec{p}\})\, \mathrm{B}(\{\vec{a}\})\, O(\{\vec{a}\}) \\
& + \sum_{\{\vec{f}\}} \sum_{\{\widetilde{ij},\tilde{k}\}} \sum_{f_i = q,g} \frac{1}{16\pi^2} \int \mathrm{d}\Phi_B(\{\vec{p}\}) \int_{t_0}^{\mu^2} \mathrm{d}t \int_{z_{\min}}^{z_{\max}} \mathrm{d}z \int_0^{2\pi} \frac{\mathrm{d}\phi}{2\pi}\, J_{ij,k}(t,z,\phi) \\
& \times \frac{8\pi\,\alpha_s}{t} \frac{1}{S_{ij}}\, \mathrm{B}(\{\vec{a}\})\, \mathcal{K}_{ij,k}(t,z,\phi)\, \frac{\mathcal{L}(r_{\widetilde{ij},\tilde{k}}(f_i,t,z,\phi;\{\vec{a}\});t)}{\mathcal{L}(\{\vec{a}\};t)} \\
& \times \left[O(r_{\widetilde{ij},\tilde{k}}(\{\vec{a}\})) - O(\{\vec{a}\}) \right]
\end{aligned}
$$

$$+ \sum_{\{\vec{f}\}} \sum_{\{\widetilde{ij},\tilde{k}\}} \sum_{f_i=q,g} \frac{1}{16\pi^2} \int d\Phi_B(\{\vec{p}\}) \int_{t_0}^{\mu^2} dt \int_{z_{\min}}^{z_{\max}} dz \int_0^{2\pi} \frac{d\phi}{2\pi} \ J_{ij,k}(t,z,\phi)$$

$$\times \ \frac{8\pi \, \alpha_s}{t} \frac{1}{S_{ij}} \ \mathrm{B}(\{\vec{a}\}) \, \mathcal{K}_{ij,k}(t,z,\phi) \frac{\mathcal{L}(r_{\widetilde{ij},\tilde{k}}(f_i,t,z,\phi;\{\vec{a}\});t)}{\mathcal{L}(\{\vec{a}\};t)}$$

$$\times \ \Theta \left(Q_{ij,k} - Q_{\mathrm{cut}} \right) \left[w(r_{\widetilde{ij},\tilde{k}}(f_i,t,z,\phi;\{\vec{a}\})) - 1 \right] O(r_{\widetilde{ij},\tilde{k}}(\{\vec{a}\}))$$

$$+ \ \mathcal{O}(\alpha_s^2) \ . \tag{8.1.11}$$

While the first and second terms represent the usual parton-shower prediction, the third term encodes the unitarity violation effected by the matrix element corrections in the region of well separated partons. In the ME+PS approach they enter at $\mathcal{O}(\alpha_s)$.

Such unitarity violations seem to be an undesirable side-effect of the ME+PS method at first. However, given eq. (8.1.11), they can serve as an indicator for the relevance of (or more precise the magnitude of non-logarithmic) higher-order real-emission corrections. This fact will be elaborated upon in some more detail in Section 8.3.

8.2   Merging POWHEG and ME+PS - The MENLOPS approach

In this section, the two master equations for the POWHEG, eq. (8.1.3), and ME+PS, eq. (8.1.8), approaches are combined into one single expression, defining the MENLOPS approach. The aim of this combination algorithm is to simultaneously have NLO accuracy in the cross section, leading logarithmic accuracy as implemented in the parton shower and hard higher-order emissions corrected using tree-level matrix elements.

Our method of choice is to simply replace the unresolved and the PS resolved part in eq. (8.1.8) with the respective POWHEG expression. This essentially amounts to the replacement of the parton-shower no-emission probability with the corresponding POWHEG result, $\Delta^{(\mathrm{PS})} \to \Delta^{(\mathrm{ME})}$ and a substitution of the leading-order weight B by $\bar{\mathrm{B}}$, like in the POWHEG method itself.

The ME part of the cross section is then generated separately, starting from real-emission matrix elements, as described in Section 8.1.2. This immediately implies that it will not automatically benefit from a POWHEG implementation regarding the local K-factor $\bar{\mathrm{B}}/\mathrm{B}$, and it is therefore necessary to supply this K-factor explicitly. There is no a-priori definition of a Born-level parton configuration in this context, because the ME event is defined in terms of a real-emission configuration. One rather has to identify a branching history $\{\vec{a}\} \to b_{ij,k}(\{\vec{a}\})$ such that $\bar{\mathrm{B}}/\mathrm{B}$ can be computed depending on $b_{ij,k}(\{\vec{a}\})$. The definition is achieved by clustering the real-emission configuration using an algorithm which is similar to a sequential recombination jet scheme and which determines the node to be clustered according to the related branching probability in the parton shower. For more details on this technique see [29].

Implementing these ideas, the master formula for the first emission in MENLOPS is obtained

as

$$\langle O \rangle^{(\text{MENLOPS})} = \sum_{\{\vec{f}\}} \int d\Phi_B(\{\vec{p}\}) \, \bar{B}(\{\vec{a}\}) \left[\Delta^{(\text{ME})}(t_0, \mu^2; \{\vec{a}\}) \, O(\{\vec{a}\}) \right.$$

$$+ \sum_{\{\widetilde{ij},\tilde{k}\}} \sum_{f_i=q,g} \frac{1}{16\pi^2} \int_{t_0}^{\mu^2} dt \int_{z_{\min}}^{z_{\max}} dz \int_0^{2\pi} \frac{d\phi}{2\pi} \, J_{ij,k}(t,z,\phi)$$

$$\times \frac{1}{S_{ij}} \frac{S(r_{\widetilde{ij},\tilde{k}}(\{\vec{f}\}))}{S(\{\vec{f}\})} \frac{R_{ij,k}(r_{\widetilde{ij},\tilde{k}}(\{\vec{a}\}))}{B(\{\vec{a}\})} \tag{8.2.1}$$

$$\times \left(\Delta^{(\text{ME})}(t,\mu^2; \{\vec{a}\}) \, \Theta\left(Q_{\text{cut}} - Q_{ij,k} \right) \right.$$

$$\left. \left. + \Delta^{(\text{PS})}(t,\mu^2; \{\vec{a}\}) \, \Theta\left(Q_{ij,k} - Q_{\text{cut}} \right) \right) O(r_{\widetilde{ij},\tilde{k}}(\{\vec{a}\})) \right] .$$

Again $Q_{ij,k} = Q_{ij,k}(t,z,\phi)$. The resolved-ME part of the expression in square brackets $(Q_{ij,k} > Q_{\text{cut}})$ exhibits an additional factor

$$\frac{\Delta^{(\text{PS})}(t,\mu^2; \{\vec{a}\})}{\Delta^{(\text{ME})}(t,\mu^2; \{\vec{a}\})}$$

$$= 1 + \sum_{\{\widetilde{ij},\tilde{k}\}} \sum_{f_i=q,g} \frac{1}{16\pi^2} \int_t^{\mu^2} d\bar{t} \int_{z_{\min}}^{z_{\max}} dz \int_0^{2\pi} \frac{d\phi}{2\pi} \, J_{ij,k}(\bar{t},z,\phi) \tag{8.2.2}$$

$$\times \frac{1}{S_{ij}} \left[\frac{S(r_{\widetilde{ij},\tilde{k}}(\{\vec{f}\}))}{S(\{\vec{f}\})} \frac{R_{ij,k}(r_{\widetilde{ij},\tilde{k}}(\{\vec{a}\}))}{B(\{\vec{a}\})} - \frac{8\pi\alpha_s}{\bar{t}} \mathcal{K}_{ij,k}(\bar{t},z,\phi) \frac{\mathcal{L}(r_{\widetilde{ij},\tilde{k}}(\{\vec{a}\}); \bar{t})}{\mathcal{L}(\{\vec{a}\}; \bar{t})} \right]$$

$$+ \mathcal{O}(\alpha_s^2)$$

compared to the POWHEG master formula. This makes the unitarity violation in the MENLOPS method explicit. However, the expectation value of O is still determined correct to $\mathcal{O}(\alpha_s)$, as can be seen by explicitly expanding eq. (8.2.1) in powers of α_s:

$$\langle O \rangle^{(\text{MENLOPS})} = \sum_{\{\vec{f}\}} \int d\Phi_B(\{\vec{p}\}) \left(B + \tilde{V} + I \right)(\{\vec{a}\}) \, O(\{\vec{a}\})$$

$$+ \sum_{\{\vec{f}\}} \sum_{\{\widetilde{ij},\tilde{k}\}} \sum_{f_i=q,g} \int d\Phi_B(\{\vec{p}\}) \, d\Phi_{R|B}^{ij,k} \left[R_{ij,k}(r_{\widetilde{ij},\tilde{k}}(\{\vec{a}\})) \, \Theta(t_0 - t) - S_{ij,k}(r_{\widetilde{ij},\tilde{k}}(\{\vec{a}\})) \right]$$

$$\times O(\{\vec{a}\})$$

$$+ \sum_{\{\vec{f}\}} \sum_{\{\widetilde{ij},\tilde{k}\}} \sum_{f_i=q,g} \int d\Phi_B(\{\vec{p}\}) \, d\Phi_{R|B}^{ij,k} \, R_{ij,k}(r_{\widetilde{ij},\tilde{k}}(\{\vec{a}\})) \, \Theta(t - t_0) \, \Theta\left(Q_{\text{cut}} - Q_{ij,k} \right)$$

$$\times O(r_{\widetilde{ij},\tilde{k}}(\{\vec{a}\}))$$

$$+ \sum_{\{\vec{f}\}} \sum_{\{\widetilde{ij},\tilde{k}\}} \sum_{f_i=q,g} \int \mathrm{d}\Phi_B(\{\vec{p}\})\, \mathrm{d}\Phi_{R|B}^{ij,k}\, \mathrm{R}_{ij,k}(r_{\widetilde{ij},\tilde{k}}(\{\vec{a}\}))\, \Theta(t-t_0)\, \Theta\left(Q_{ij,k}-Q_{\mathrm{cut}}\right)$$

$$\times\, O(r_{\widetilde{ij},\tilde{k}}(\{\vec{a}\}))$$

$$+ \mathcal{O}(\alpha_s^2) \, . \tag{8.2.3}$$

Comparing this with eq. (8.1.4), it is evident that the $\mathcal{O}(\alpha_s)$ accuracy of the MENLOPS method is identical to what is obtained from POWHEG. The potential mismatch between exact higher-order tree-level matrix elements and their respective parton-shower approximation, leading to a difference between $\Delta^{(\mathrm{ME})}$ and $\Delta^{(\mathrm{PS})}$, contributes terms of $\mathcal{O}(\alpha_s^2)$ or higher as long as $\Theta\left(Q_{ij,k}-Q_{\mathrm{cut}}\right)$ enforces $t > t_0$. The precise value of Q_{cut} must therefore be chosen such that this constraint is satisfied.

Apart from being of order α_s, the term in the square brackets of eq. (8.2.2) should be rather small in practice, as potential differences between matrix-element and parton-shower expressions merely lie in subleading logarithmic and power corrections. This corresponds to the mismatch between POWHEG and MENLOPS results being at most of order $\alpha_s^2 \log\left(\mu^2/Q_{\mathrm{cut}}^2\right)$ if the parton shower has LL accuracy, and of order α_s^2 if it has NLL accuracy.

Generating a second emission using the ME+PS method supplemented with the above mentioned local K-factor of course introduces additional unitarity violations, as described by eq. (8.1.11). However, because such terms are of $\mathcal{O}(\alpha_s^2)$, they do not spoil the next-to-leading order accuracy of the method.

At this point it is important to stress that in their publication Hamilton and Nason arrived at the same ideas [172].

8.3 Results

This section collects results obtained with an implementation of the algorithm described in the previous sections in the SHERPA framework. It aims at detailing the improved description of data collected in various collider experiments and at quantifying some of the systematic uncertainties inherent to the MENLOPS method, in particular those related to the merging of the multijet tree-level contributions. Note again, that the MENLOPS approach is designed to merge the next-to-leading order accurate description of a given core interaction (like for example $e^+e^- \to q\bar{q}$) through the POWHEG method with higher-order tree-level contributions (like $e^+e^- \to q\bar{q}gg$) described in the ME+PS approach. Since the total cross section is essentially defined by the POWHEG expression of the core process in question, uncertainties like those related to the choice of scales are encoded mostly there. They have been discussed in Chapter 7, while uncertainties related to the ME+PS method were discussed for example in [29, 221].

However, a comparison with results of the ME+PS and POWHEG techniques alone is extremely useful to assess the quality of the approach and the improvements related to it. The precise setup of SHERPA for this comparison, including in particular a parton shower based on Catani-Seymour subtraction terms [62] and an automated implementation of the Catani-Seymour subtraction method [50] in the matrix-element generator AMEGIC++ [25] was described in Section 7.8. Throughout this part of this thesis, the CTEQ6.6 parton distribution functions [222], (and, correspondingly, the $\overline{\mathrm{MS}}$ renormalisation scheme) with $\alpha_S(m_Z) = 0.118$ and NLO running, are used. If not stated otherwise, hadronisation is not accounted for. Multiple parton interactions are not included in the simulation. The RIVET program package [79, 80] and the HZTOOL library [81] are employed for analyses and comparison with data.

8.3.1 Merging Systematics

As pointed out in the previous section, the ME+PS approach violates the unitarity of the parton-shower simulation. This discrepancy is directly inherited by the MEnloPS method. The extent of this effect depends entirely on the quality of the parton-shower algorithm, as can be seen in eq. (8.2.2): If the parton-shower approximation to the real-emission matrix element is good, the correction factor, eq. (8.2.2), is close to one.
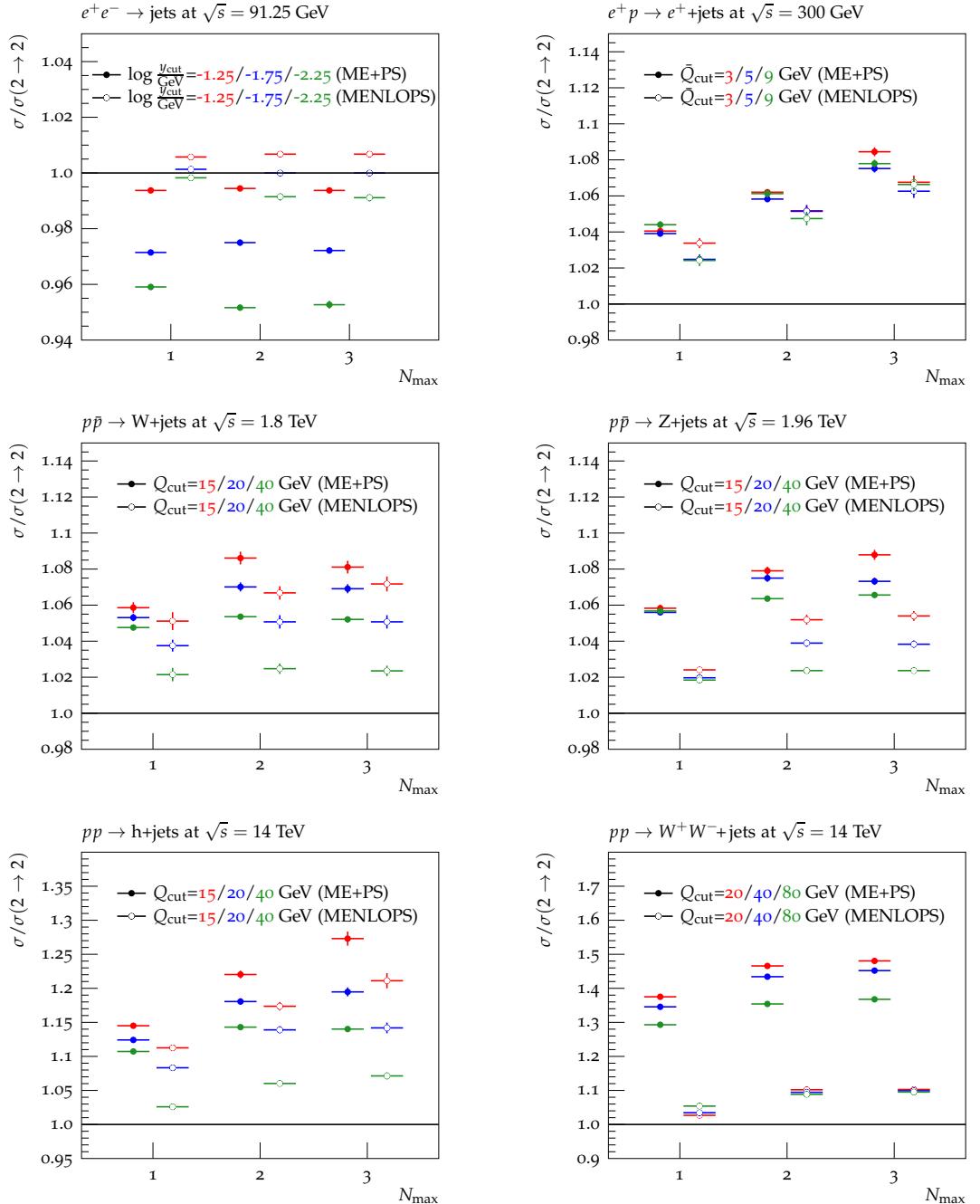

Figure 8.1: Visualisation of the unitarity violation, detailed in Tables 8.1–8.6, induced by the ME+PS and MEnloPS master formulas, eqs. (8.2.1) and (8.1.8), respectively.

$\log_{10} y_{\mathrm{cut}}$	$N_{\max}$							
	0		1		2		3	
	LO+PS	POWHEG	ME+PS	MEnloPS	ME+PS	MEnloPS	ME+PS	MEnloPS
-1.25	28.37(1)	29.43(1)	28.09(2)	29.60(2)	28.11(2)	29.63(2)	28.09(2)	29.63(2)
-1.75			27.46(2)	29.47(3)	27.56(3)	29.43(3)	27.48(3)	29.43(3)
-2.25			27.11(3)	29.38(3)	26.90(3)	29.18(4)	26.93(4)	29.17(4)

Table 8.1: Dependence of the inclusive $e^+e^- \to jets$ cross section in nb on the number of extra jets generated in both the ME+PS and the MEnloPS method. For $N_{\max} = 0$ these reduce to the LO+PS and POWHEG methods, respectively.

$\bar{Q}_{\mathrm{cut}}$	$N_{\max}$							
	0		1		2		3	
	LO+PS	POWHEG	ME+PS	MEnloPS	ME+PS	MEnloPS	ME+PS	MEnloPS
3 GeV	365.7(4)	322.4(6)	380.5(6)	333.5(9)	388.4(6)	339.3(1.0)	396.6(9)	344.4(1.2)
5 GeV			380.0(6)	330.6(9)	387.0(6)	339.2(1.1)	393.2(8)	342.8(1.2)
9 GeV			381.8(7)	330.4(1.0)	388.1(8)	337.9(1.2)	394.2(8)	344.0(1.2)

Table 8.2: Dependence of the DIS production cross section in nb on the number of extra jets generated in both the ME+PS and the MEnloPS method. For $N_{\max} = 0$ these reduce to the LO+PS and POWHEG methods, respectively. The precise definition of $\bar{Q}_{\mathrm{cut}}$ is given in [221].

Q_{cut}	$N_{\max}$							
	0		1		2		3	
	LO+PS	POWHEG	ME+PS	MEnloPS	ME+PS	MEnloPS	ME+PS	MEnloPS
15 GeV	1993(1)	2423(1)	2114(6)	2549(9)	2169(6)	2587(9)	2159(7)	2599(10)
20 GeV			2103(4)	2516(6)	2137(5)	2548(9)	2135(5)	2548(9)
40 GeV			2092(3)	2477(9)	2104(3)	2485(7)	2101(3)	2482(7)

Table 8.3: Dependence of the W production cross section in pb on the number of extra jets generated in both the ME+PS and the MEnloPS method. For $N_{\max} = 0$ these reduce to the LO+PS and POWHEG methods, respectively.

Q_{cut}	N_{max}							
	0		1		2		3	
	LO+PS	Powheg	ME+PS	Menlops	ME+PS	Menlops	ME+PS	Menlops
15 GeV			417.7(8)	489.3(8)	425.9(9)	502.6(1.3)	429.4(1.1)	503.6(1.3)
20 GeV	394.7(1)	477.8(1)	416.8(7)	487.2(9)	424.3(8)	496.4(1.0)	423.6(8)	496.1(1.0)
40 GeV			417.1(4)	486.6(6)	419.8(5)	489.1(6)	420.6(5)	489.1(6)

Table 8.4: Dependence of the Z production cross section in pb on the number of extra jets generated in both the ME+PS and the Menlops method. For $N_{\text{max}} = 0$ these reduce to the LO+PS and Powheg methods, respectively.

Q_{cut}	N_{max}							
	0		1		2		3	
	LO+PS	Powheg	ME+PS	Menlops	ME+PS	Menlops	ME+PS	Menlops
15 GeV			1.217(4)	2.698(11)	1.297(6)	2.846(15)	1.353(11)	2.937(27)
20 GeV	1.063(1)	2.425(1)	1.195(3)	2.627(9)	1.255(5)	2.762(13)	1.270(7)	2.769(19)
40 GeV			1.177(2)	2.488(6)	1.215(3)	2.571(10)	1.212(4)	2.598(13)

Table 8.5: Dependence of the Higgs production cross section in pb in gluon fusion on the number of extra jets generated in both the ME+PS and the Menlops method. For $N_{\text{max}} = 0$ these reduce to the LO+PS and Powheg methods, respectively.

Q_{cut}	N_{max}							
	0		1		2		3	
	LO+PS	Powheg	ME+PS	Menlops	ME+PS	Menlops	ME+PS	Menlops
20 GeV			1.305(4)	1.369(5)	1.391(6)	1.469(7)	1.405(7)	1.470(9)
40 GeV	0.949(1)	1.333(1)	1.277(3)	1.379(5)	1.361(4)	1.459(6)	1.378(6)	1.465(6)
80 GeV			1.227(2)	1.405(5)	1.285(3)	1.451(5)	1.298(5)	1.460(5)

Table 8.6: Dependence of the W^+W^--production cross section in pb on the number of extra jets generated in both the ME+PS and the Menlops method. For $N_{\text{max}} = 0$ these reduce to the LO+PS and Powheg methods, respectively.

The quality of the algorithms is tested in the reactions $e^+e^- \to$ hadrons, deep-inelastic lepton-nucleon scattering, Drell-Yan lepton-pair production, W- and Higgs-boson production and W^+W^--production by varying the phase-space separation cut, Q_{cut}, and the maximum number of partons, N_{max}, which is simulated with matrix elements in the MENLOPS approach. This is in close correspondence to the sanity checks of the ME+PS method which have been presented in [29]. The respective results are summarised in Tabs. 8.1-8.6 and depicted in Figure 8.1. It is interesting to note that differences in the total cross-section are smallest for the MENLOPS samples with $N_{\mathrm{max}} = 1$, and that they increase steadily for larger N_{max}. This indicates that the parton shower tends to underestimate the cross section of higher-order tree-level contributions.

Two important effects, which allow judgment of the quality of the MENLOPS approach with respect to NLO accuracy, are observed: Firstly, for $N_{\mathrm{max}} = 1$ the unitarity violations never exceed the size of the NLO corrections. Secondly, for any given value of Q_{cut} and N_{jet}, the relative difference between the cross sections from MENLOPS and POWHEG is always smaller than the one between the cross sections from ME+PS and LO+PS. This is best seen in Figure 8.1, and it gives some confidence that the MENLOPS technique can help to improve perturbative QCD predictions from parton-shower Monte Carlo.

The above analysis can be seen from a different perspective as follows: Usually, the biggest intrinsic uncertainty of the ME+PS approach stems from the freedom to choose the phase-space separation cut, Q_{cut}, as explained and exemplified in a number of processes in [29].
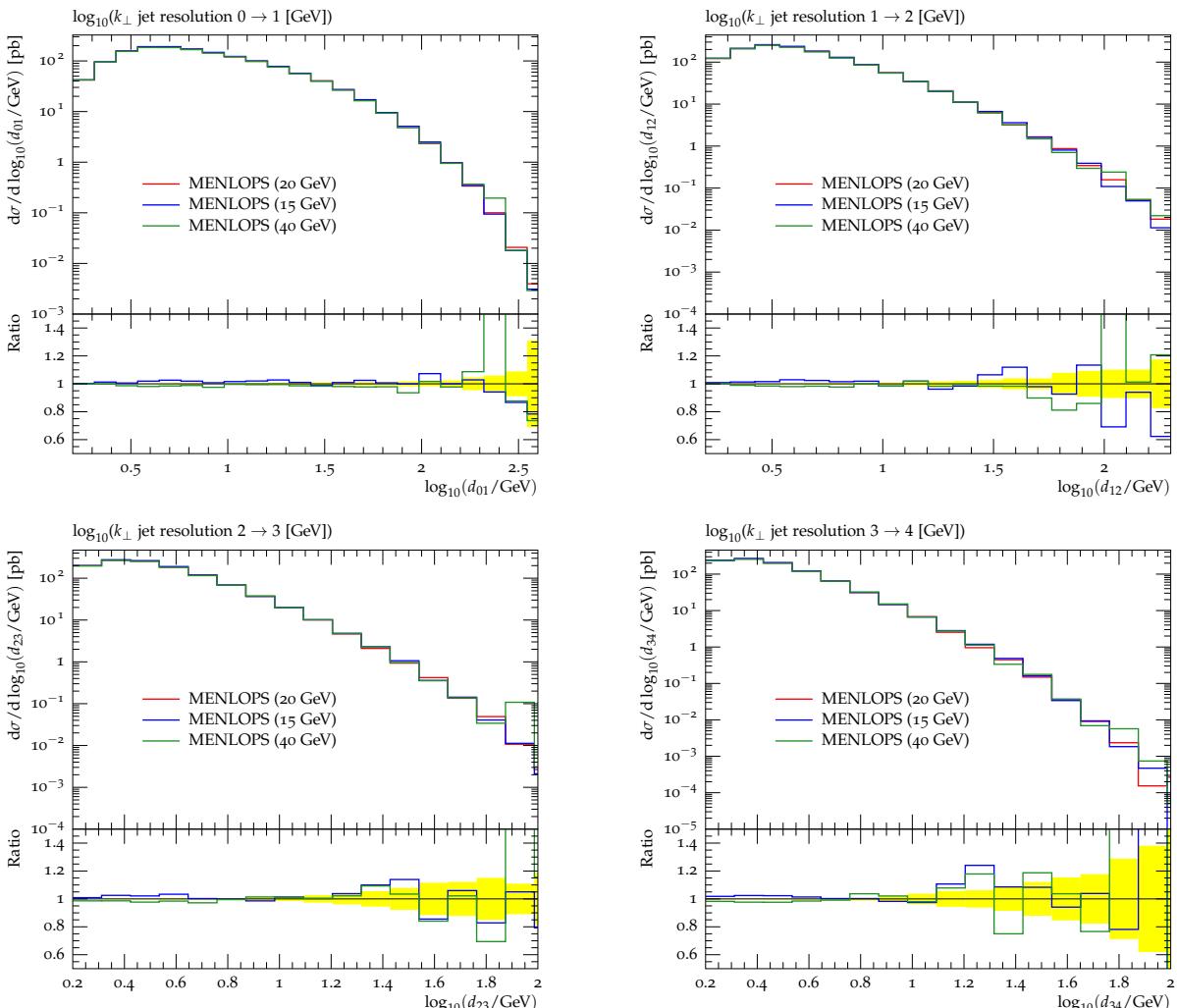

Figure 8.2: Differential jet rates $d_{n\,n+1}$ for three different merging cuts, Q_{cut}, in Drell-Yan lepton-pair production at the Tevatron at $\sqrt{s} = 1.96$ TeV.

Since the MENLOPS method relies on identical ideas to separate the real-emission phase space, it naturally inherits this source of uncertainty. Deviations of MENLOPS results from results with different values of Q_{cut} are to be expected. However, their small size in a reasonable range of Q_{cut} is a sign of the algorithm working well. The following rule of thumb can be applied: If the value of Q_{cut} is chosen too large, too much extra emission phase space is left to the POWHEG simulation, typically leading to an underestimation of jet rates, since POWHEG only simulates the first emission through matrix elements. If, on the other hand, this value is too small, too much phase space is filled by matrix elements with large final-state multiplicity, which may lead to noticeable unitarity violations. The value of Q_{cut} should therefore lie well between the parton-shower cutoff and the factorisation scale of the core process, with some margin on either side of this interval.

The stability of the MENLOPS implementation with respect to variations of Q_{cut} is exemplified in Figure 8.2. Due to their similarity to $Q_{ij,k}$, the differential jet rates shown there are extremely sensitive to the details of the radiation pattern and thus to the accuracy of the ME+PS implementation. They tend to expose even the slightest mismatch between PS and ME subsamples, which then shows up as a kink in the distribution. However, when varying Q_{cut} in a rather wide range, no sizable discrepancies between the respective MENLOPS predictions are observed, which is a very encouraging result regarding the quality of the algorithm and its implementation in SHERPA.
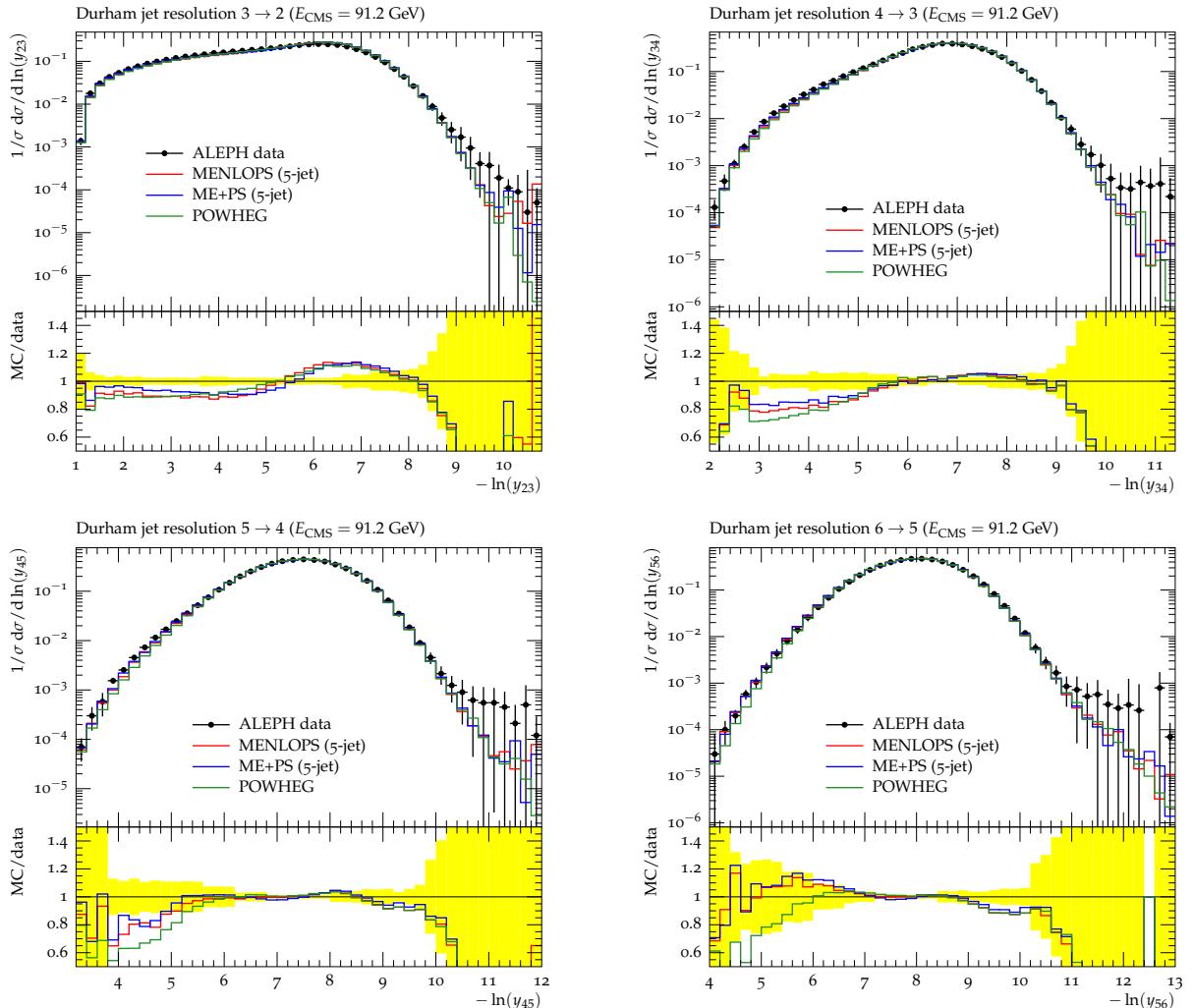

Figure 8.3: Durham $d_{n\,n+1}$ jet resolutions at LEP compared to data taken by the ALEPH experiment [239].
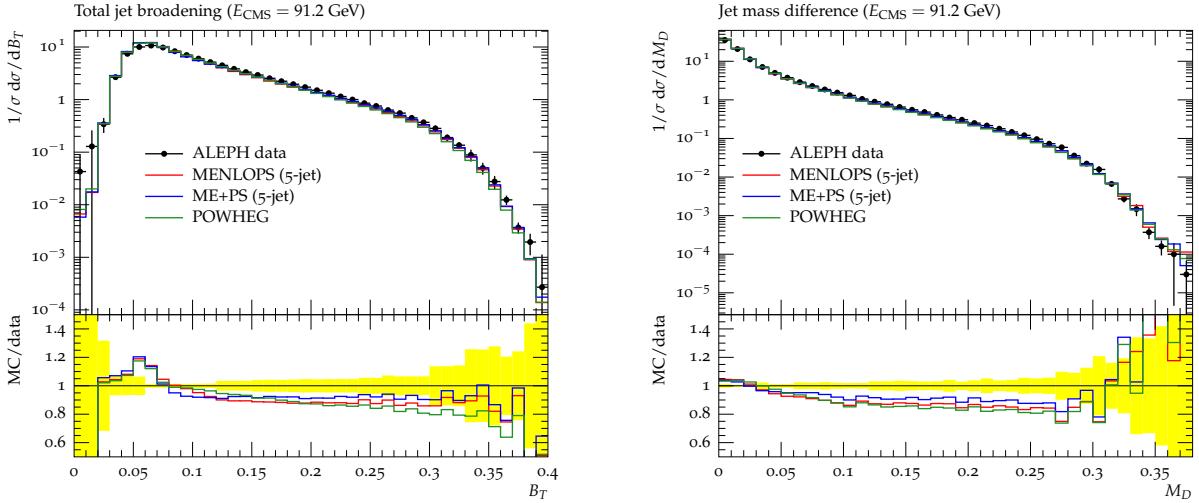
Figure 8.4: Total jet broadening and jet mass difference at LEP compared to data taken by the ALEPH experiment [239].
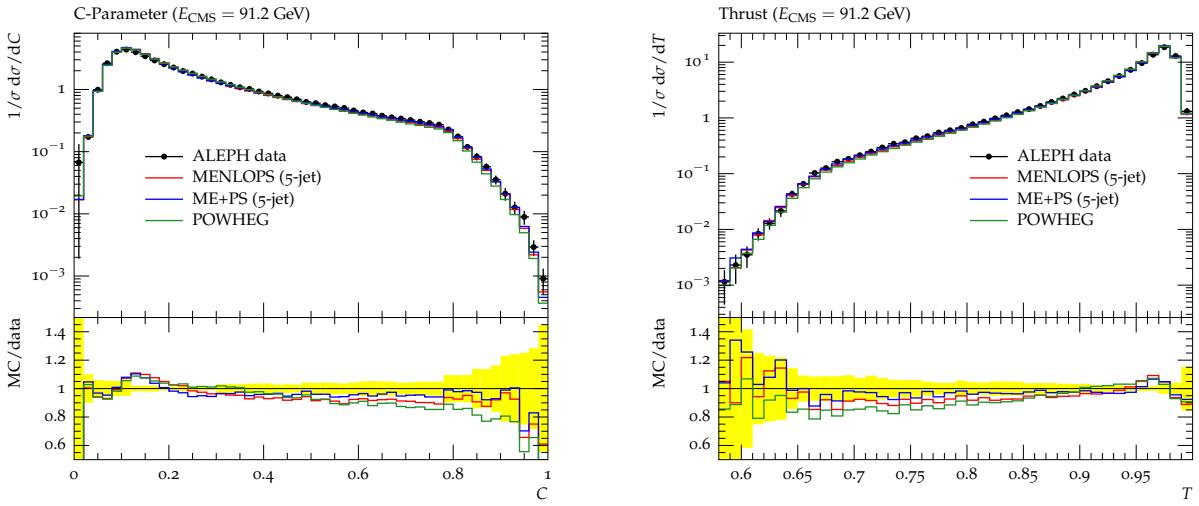

Figure 8.5: C-parameter and thrust distribution at LEP compared to data taken by the ALEPH experiment [239].

8.3.2 $e^+e^- \to$ jets

In this section the focus rests on electron-positron annihilation into hadrons at LEP energies ($\sqrt{s} = 91.25$ GeV). The core process of the simulation is therefore the reaction $e^+e^- \to q\bar{q}$. A full wealth of experimental data has been provided by the LEP experiments, which allows to assess the quality of the MENLOPS approach in this simplest realistic scenario. Although the improvements discussed in this thesis concern only the perturbative QCD part of the Monte-Carlo simulation, the presented results account for hadronisation effects using the Lund model [223, 224, 256, 2] to make them comparable to experimental data. Virtual matrix elements needed for the simulation were supplied by code provided by the BLACKHAT collaboration [54, 225, 226, 227, 228, 229].

Figure 8.3 highlights the improvement in the description of jet data. In the hard-emission region the MENLOPS results for the $2 \to 3$-, the $3 \to 4$- and the $4 \to 5$-jet rate are generally closer to the data than the POWHEG ones, which hints at the success of the simulation.
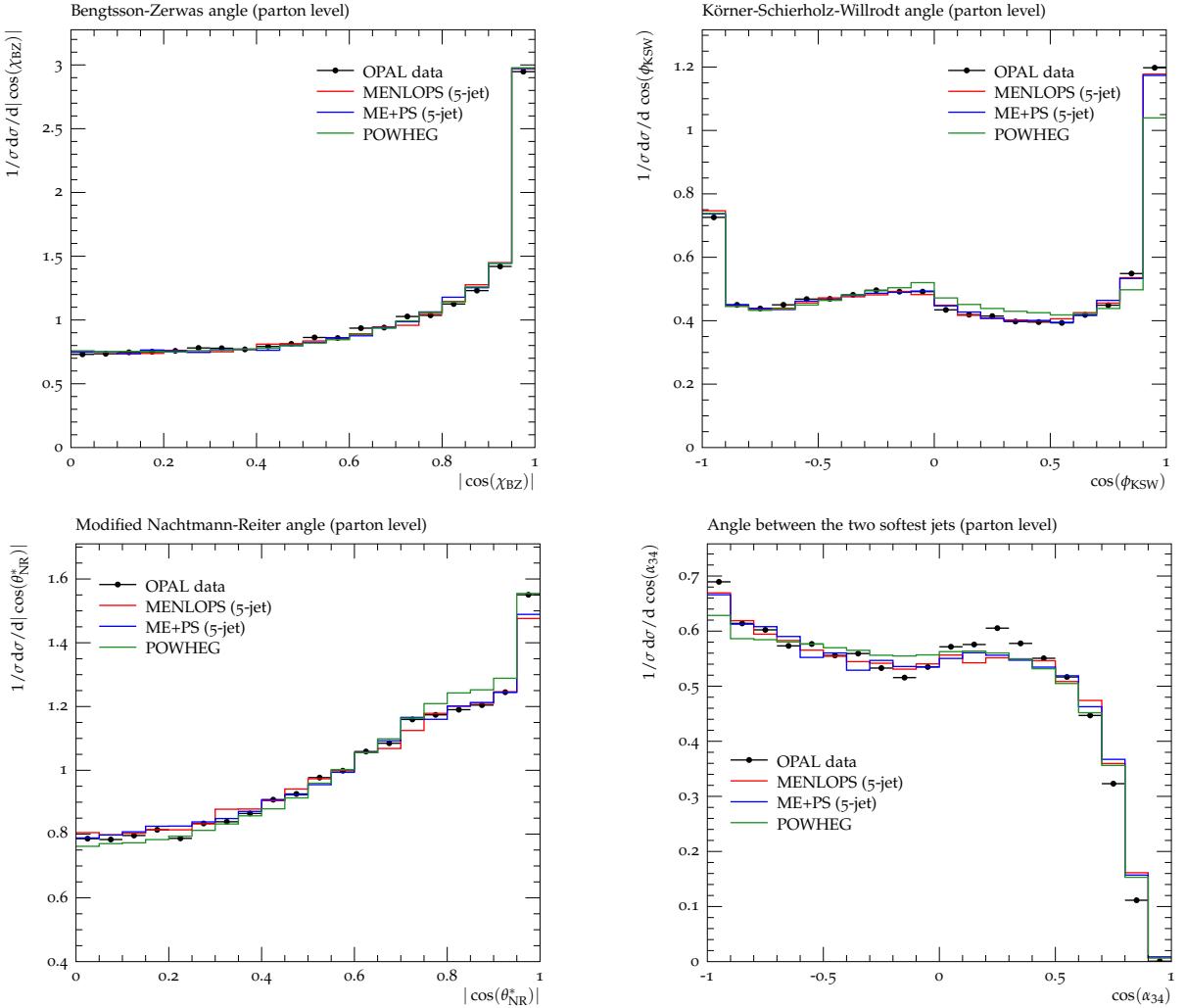
Figure 8.6: Angles between the leading (in energy) four jets defined using the Durham algorithm with $y_{\text{cut}} = 0.008$. Results at the parton level are compared to data from the OPAL experiment [255].

Deviations in the $5 \rightarrow 6$-jet rate are most likely due to the fact that matrix elements for six-jet production are not included. Note that these distributions are normalised to the total cross section, such that no rate difference between the ME+PS and the MENLOPS samples can be observed.

Figures 8.4 and 8.5 show examples of event-shape variables, which are all very well described in the hard-emission region by the MENLOPS simulation. Several distributions for jet angular correlations in 4-jet production, that have been important for the analysis of QCD and searches for physics beyond the Standard Model are investigated in Figure 8.6. The good fit to those data proves that correlations amongst the final-state partons are correctly implemented by the higher-order matrix elements.

8.3.3 Deep-inelastic lepton-nucleon scattering

Deep-inelastic scattering (DIS) is one of the best understood processes in perturbative QCD. However, it has been an obstacle for a very long time to properly simulate hadronic final
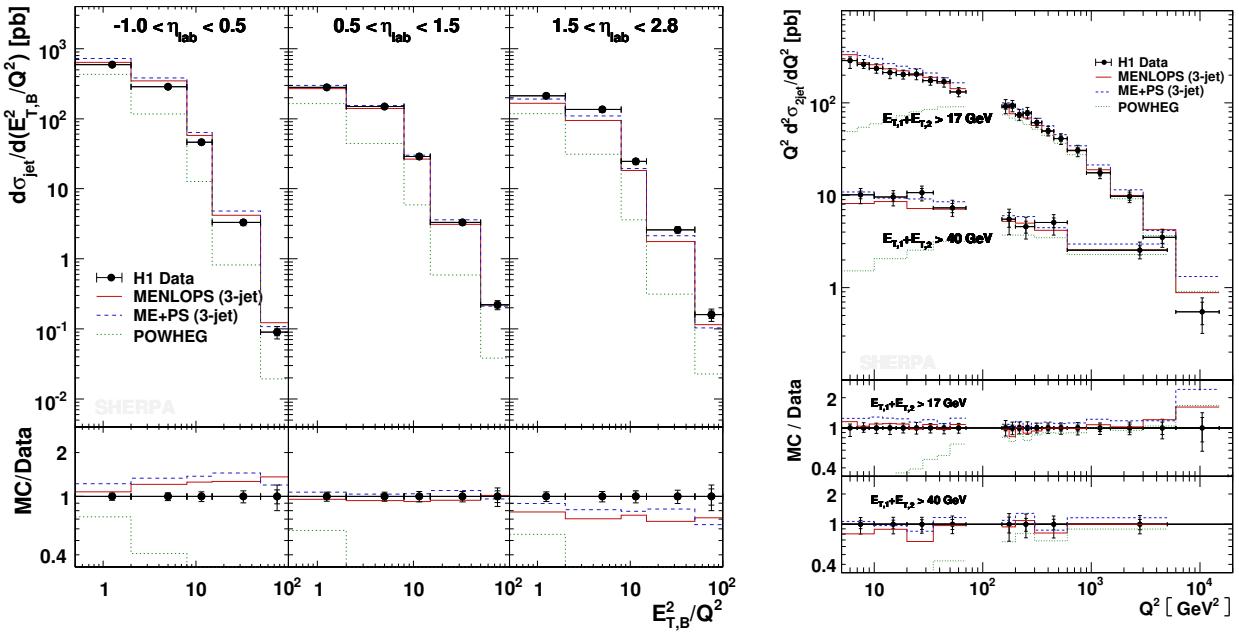
Figure 8.7: Left: The inclusive jet cross section as a function of $E_{T,B}^2/Q^2$ in bins of η_{lab}, compared to data from the H1 collaboration [257]. $E_{T,B}^2$ is the jet transverse energy in the Breit frame, while η_{lab} denotes the jet rapidity in the laboratory frame. Right: The dijet cross section as a function of Q^2 in bins of $E_{T,1}+E_{T,2}$, compared to data from the H1 collaboration [240].
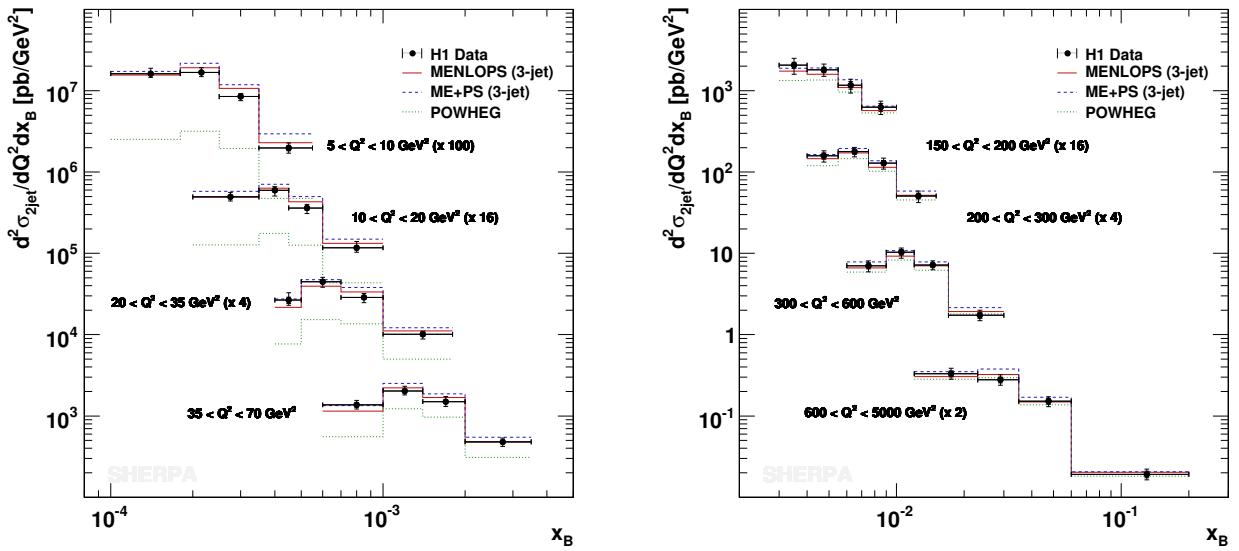

Figure 8.8: The dijet cross section as a function of the Bjørken variable x_B, compared to data from the H1 collaboration [240].
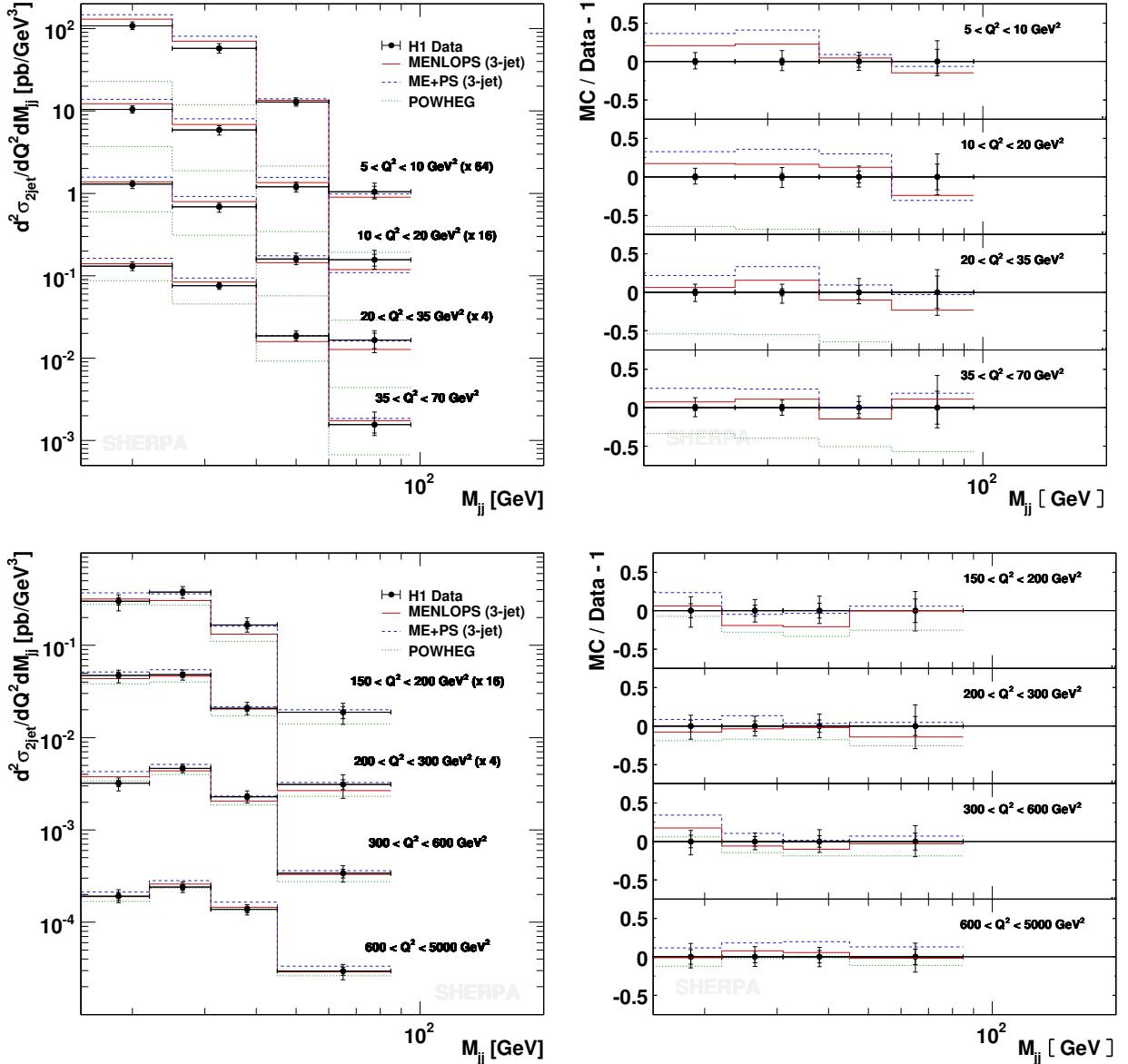
Figure 8.9: The dijet cross section as a function of the dijet mass m_{jj}, compared to data from the H1 collaboration [240].

states in DIS using general-purpose Monte Carlo based on collinear factorisation. Only recently, a consistent approach was presented [221], that allows to describe jet data throughout the experimentally accessible range of Q^2, the negative virtuality of the exchanged virtual γ^*/Z-boson. It is absolutely mandatory for this method that a large number of final-state partons can be described by hard matrix elements in order to lift the severe restrictions on the real-emission phase space of the parton shower, which are imposed by the factorisation theorem.

In all simulations the core process $e^+q \to e^+q$ is used. The first is the measurement of inclusive jet production in [257], which covers different ranges of jet-pseudorapidity in the laboratory frame, η_{lab}, in the low-Q^2 domain $5 < Q^2 < 100\,\mathrm{GeV}^2$. Jets are defined using the inclusive k_T-algorithm [258, 259] and are constrained to $E_{T,B} > 5\,\mathrm{GeV}$ and the pseudorapidity range $-1 < \eta_{lab} < 2.8$, where $E_{T,B}$ is the jet transverse energy in the Breit frame. The second analysis corresponds to the measurement of dijet production in [240], which covered a
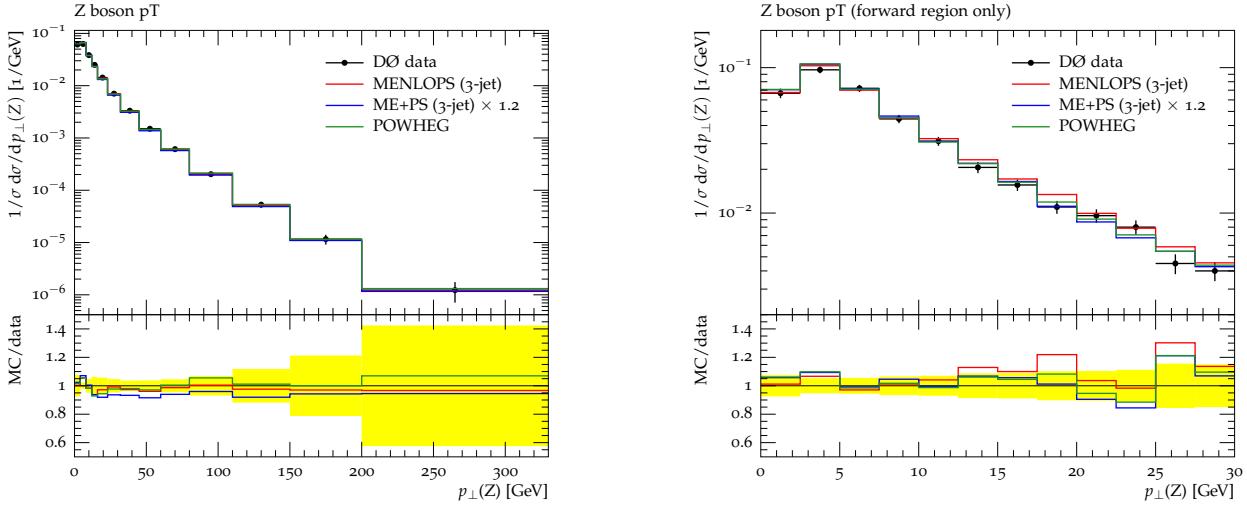
Figure 8.10: The transverse momentum of the reconstructed Z boson in Drell-Yan lepton-pair production at the Tevatron at $\sqrt{s} = 1.96$ TeV. Experimental data stem from the DØ experiment [242, 261] and are described in the text.

wider range of Q^2 and produced many doubly differential jet spectra. The acceptance region is $5 < Q^2 < 15000 \, \text{GeV}^2$ and $-1 < \eta_{lab} < 2.5$. Jet transverse energies are subject to the cuts $E_{T,B\,1,2} > 5 \, \text{GeV}$ and $E_{T,B\,1} + E_{T,B\,2} > 17 \, \text{GeV}$. The latter requirement is introduced to avoid $E_{T,B\,1} \approx E_{T,B\,2}$, which is the region of the phase space where next-to-leading order corrections are unstable due to implicit restrictions on soft emissions [260].

As outlined in [221], a crucial observable is given by the inclusive jet cross section, differential with respect to $E_{T,B}^2/Q^2$. For $E_{T,B}^2/Q^2 > 1$ it probes a part of the phase space where leading order Monte-Carlo models without the inclusion of low-x effects are bound to fail in their description of jet spectra. Another very good observable to validate the proper Monte-Carlo simulation is the dijet cross section as a function of Q^2. While still a relatively inclusive quantity, it is an important indicator for the correct simultaneous implementation of inclusive DIS and the additional production of hard QCD radiation. The high quality of the MENLOPS prediction for the two above observables is confirmed in Figure 8.7. Discrepancies in the description of the $E_{T,B}^2/Q^2$-spectrum in the forward region can be attributed to the fact that the simulation is limited to three additional partons in the hard matrix elements. This restriction is imposed by the usage of the matrix-element generator AMEGIC++ [25]. Figures 8.8 and 8.9 exemplify again that the MENLOPS simulation correctly predicts multijet differential distributions in all regions of the phase space, while the POWHEG approach fails in the low-Q^2 domain.

8.3.4   Drell-Yan lepton-pair production

Results for lepton-pair production through the Drell-Yan process are compared to data from the Tevatron at $\sqrt{s} = 1.96$ TeV in Figures 8.10-8.13, using the core process $q\bar{q} \to \ell\ell$, where $\ell = e, \mu$. The invariant mass of the lepton pair was restricted to be within $66 < m_{\ell\ell}/\text{GeV} < 116$ in the simulation. The MENLOPS and ME+PS samples use tree-level matrix elements up to $Z + 3$ jets with a merging cut of $Q_{\text{cut}} = 20$ GeV. Virtual matrix elements are provided by BLACKHAT [54, 225, 226, 227, 228, 229]. The $Z \to \ell^+\ell^-$ decay is corrected for QED next-to-leading order and soft-resummation effects using the Yennie-Frautschi-Suura (YFS) approach [74].
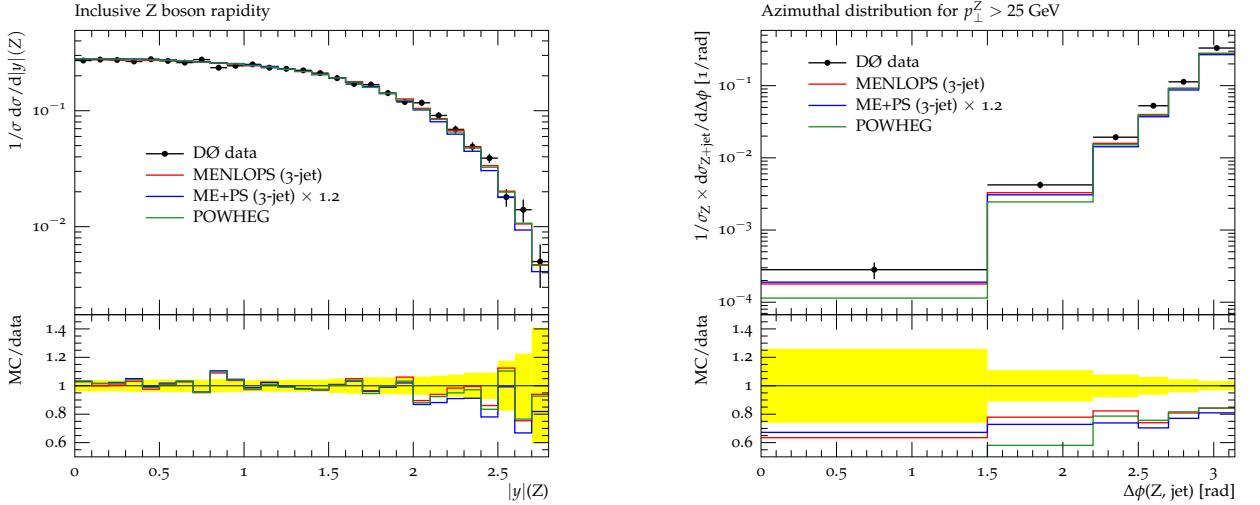
Figure 8.11: Rapidity of the reconstructed Z boson [243] (left) and azimuthal separation of the boson and the leading jet [245] (right) in Drell-Yan lepton-pair production at the Tevatron at $\sqrt{s} = 1.96$ TeV.

The Tevatron experiments provide a wealth of measurements sensitive to QCD corrections in Drell-Yan production. Figure 8.10 shows the transverse momentum distribution of the lepton pair in two different analyses from the DØ experiment. The left hand plot displays a very recent analysis using the $Z \to \mu\mu$ channel [242] to measure the Z-$p_\perp$ distribution normalised to the inclusive cross section. It requires muons with $p_\perp > 15$ GeV in a mass window of $65 < m_{\mu\mu}/\text{GeV} < 115$ and with $|\eta| < 1.7$. The muon signal is corrected to the particle level including photons clustered in a cone of radius $R = 0.2$ around each lepton. The plot on the right hand side stems from an analysis in the electron channel [261] which uses Monte-Carlo models to correct the leptons for all acceptances including the pseudorapidity range and minimal transverse momentum. Here the peak region of the transverse momentum of forward Z bosons with $|y_Z| > 2$ is displayed. The agreement between all three approaches and the measurement is outstanding. In the bins at $p_\perp < 10$ GeV non-perturbative effects like the intrinsic transverse momentum of partons in a proton might play a role. Related Monte-Carlo models in SHERPA could be tuned to reach an even better agreement. Still, the Monte-Carlo prediction lies within the experimental error band over the full range.

Two more measurements from the DØ experiment are displayed in Figure 8.11. The pseudorapidity of the Z boson [243] was measured in the electron channel requiring electrons with $p_\perp > 15$ GeV in the mass window $71 < m_{ee}/\text{GeV} < 111$. Again, all three Monte-Carlo approaches agree very well with the experimental data. The right hand plot shows the azimuthal correlation between the Z boson and the leading jet [245]. This is a measurement in the muon channel with the same selection cuts as described above. The distribution has been normalised using the inclusive Z cross section and the comparison shows that the three approaches underestimate the total rate for Z+jet production with respect to inclusive Z production by approximately 10%. This might hint at the need for NLO accuracy also in the Z+jet process. It is remarkable though that the inclusion of higher-order tree-level matrix elements significantly improves the shape of the distribution with respect to the POWHEG simulation.

The observables presented so far are mainly sensitive to the correct description of the leading jet. For that reason even the POWHEG approach is well capable of providing sufficient accuracy in their prediction.

Proceeding to observables sensitive to higher-order corrections, Figure 8.12 (left) shows the inclusive jet multiplicity [262] for jets constructed using the DØ improved legacy cone algorithm [251] with a cone radius of $R = 0.5$ and $p_\perp > 20$ GeV. Jets were required to lie in
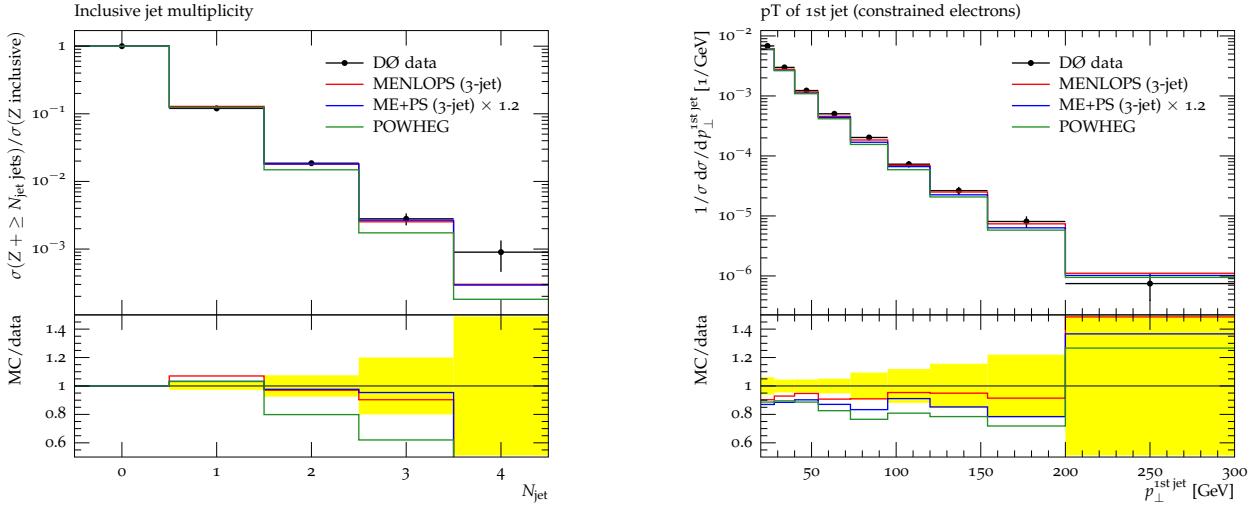
Figure 8.12: Inclusive jet multiplicity [262] (left) and transverse momentum of the leading jet [249] (right) in Z+jets events at the Tevatron at $\sqrt{s} = 1.96$ TeV.
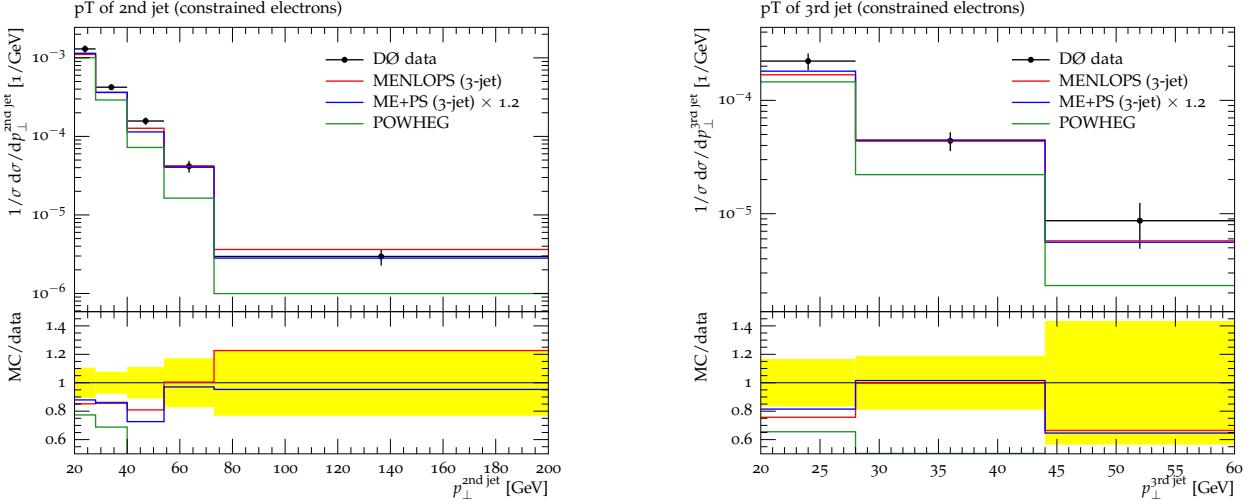
**Figure 8.13:** Transverse momentum of the second and third jet [249] in Z+jets events at the Tevatron at $\sqrt{s} = 1.96$ TeV.

$|\eta| < 2.5$ and to be separated from the leptons by $\Delta R(\ell, \text{jet}) > 0.4$. While POWHEG agrees with the data for the $N_{\text{jet}} = 1$ bin it fails to predict the rate of events with more than one jet. The MENLOPS and ME+PS predictions impressively demonstrate the effect of higher-order corrections provided by tree-level matrix elements up to the third jet. They agree with the measurement within the error bands for $N_{\text{jet}} = 2, 3$ and as expected fail to predict the correct four-jet rate because no matrix-element corrections have been applied at that multiplicity.

Transverse momentum spectra of the three leading jets accompanying the Z boson were measured by DØ in [249]. The distributions in Figure 8.12 (right) and 8.13 are normalised to the inclusive cross section for Z production and the jets have been constructed using the same settings as in the multiplicity measurement. Both MENLOPS and ME+PS deliver a very good description of these spectra while POWHEG fails to describe the rate and shape for the second and third jet.
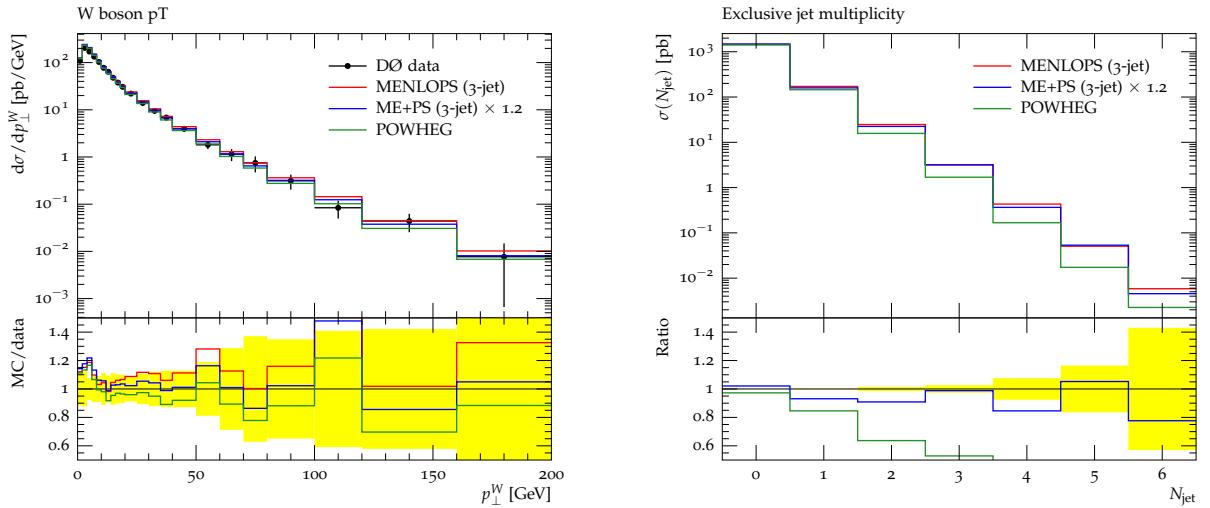
Figure 8.14: Transverse momentum of the W, compared to data taken by the DØ collaboration [244], and the exclusive jet multiplicity in inclusive W production at the Tevatron at $\sqrt{S} = 1.8$ TeV.
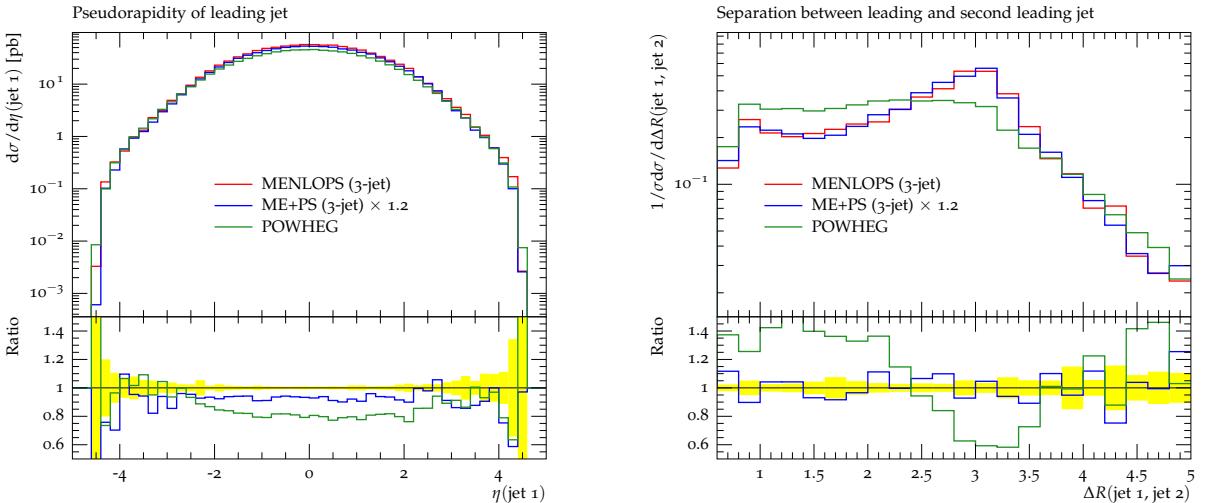

Figure 8.15: Pseudorapidity of the hardest jet and angular separation of the first two hardest jets in inclusive W production at the Tevatron at $\sqrt{S} = 1.8$ TeV.

8.3.5 W+jets Production

In this section the focus rests on the production of W-bosons and their subsequent decay into an electron-neutrino pair at the Tevatron at $\sqrt{s} = 1.8$ TeV. The core process of the Monte-Carlo simulation is therefore $q\bar{q}' \to \ell\bar{\nu}$. The separation criterion is set to $Q_{\text{cut}} = 20$ GeV and up to three extra jets are taken into account. The electron-neutrino pair is required to have an invariant mass of $m_{e\nu} > 10$ GeV. The $W \to e\nu$ decay is corrected for QED next-to-leading order and soft-resummation effects using the YFS approach [74]. Virtual matrix elements are supplied by BLACKHAT [54, 225, 226, 227, 228, 229].

The left panel of Figure 8.14 displays the transverse momentum of the W-boson as compared to data taken by the DØ collaboration [244], while the right panel shows the exclusive jet multiplicity of $k_\perp$-clustered jets ($D = 0.7$) with at least 20 GeV. Although the event sample generated using the POWHEG technique only provides the best match to the central value of the data, all three event samples are well within the experimental uncertainties. On the
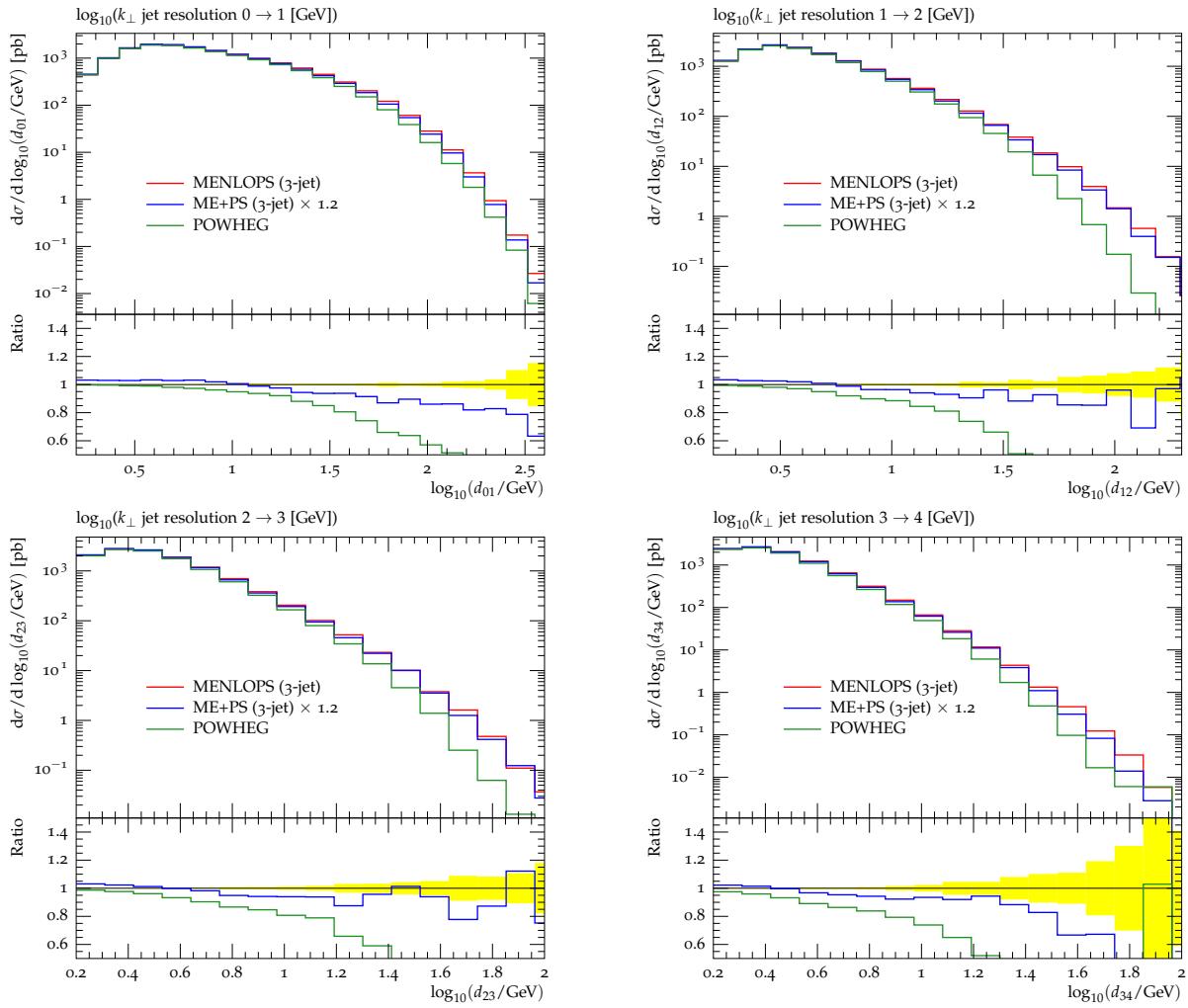
Figure 8.16: Differential jet rates $d_{n\,n+1}$ in W production at the Tevatron at $\sqrt{s} = 1.8$ TeV.

other hand, already in the rate of single-jet events deviations between the POWHEG sample and both the MENLOPS and ME+PS samples are visible, with the latter two agreeing very well. Similarly, the POWHEG sample underestimates the amount of radiation into the central detector region, as exemplified in Figure 8.15. The right panel of this figure shows that, since the POWHEG approach is capable of modeling the second hardest emission using the soft-collinear approximation of the parton shower only, its description of the angular separation of the the first two hardest jets is missing prominent features originating in the wide angle region. These features are of course present in the approaches having fixed-order matrix elements at their disposal.

Figure 8.16 shows the differential jet rates d_{01}, d_{12}, d_{23} and d_{34} using the above $k_\perp$-algorithm. While the first three of them, for the matrix-element merged samples, are described by matrix element to matrix element transitions, only the softer part of d_{01} is described by such a transition for the POWHEG sample. The harder part of the d_{01} receives corrections by matrix elements of higher jet multiplicity which are clustered into a single hard jet first. Of course, these corrections are missing in the POWHEG sample. Furthermore, d_{12} is described by a matrix element to parton shower transition only in the POWHEG sample. Hence, it strongly underestimates the amount of hard wide-angle radiation. Similarly, both d_{23} and d_{34} are described by the parton shower only in the POWHEG sample, showing the same behaviour. It is worth noting that both the MENLOPS sample, implementing local K-factors, and the ME+PS, scaled by a global K-factor, agree within their respective statistical uncertainties over the whole range, indicating the well known fact of the approximate momentum independence of the virtual corrections to the leading order process.
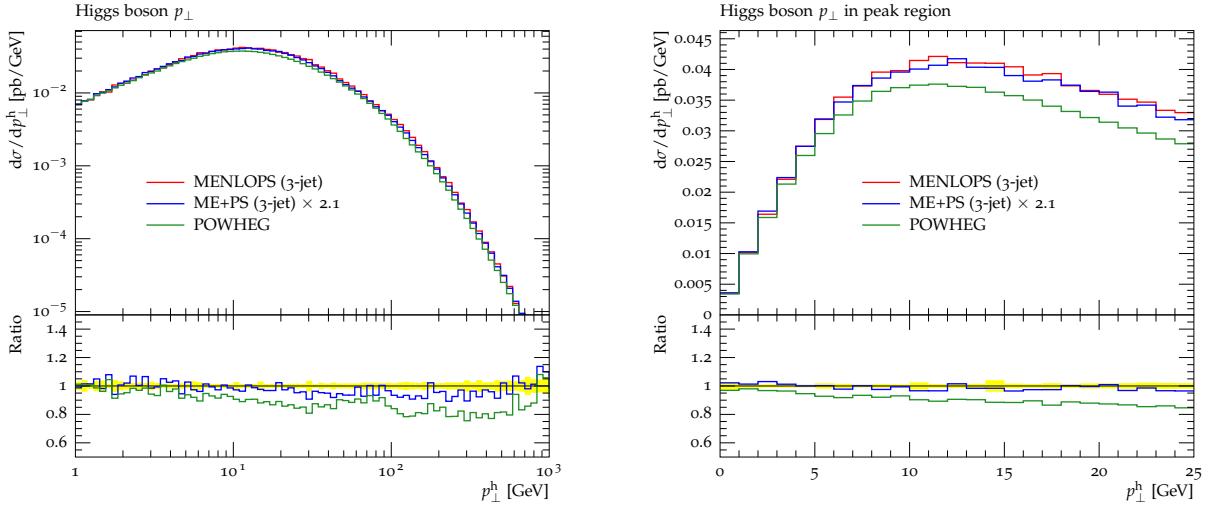
Figure 8.17: Transverse momentum of the reconstructed Higgs boson in the gluon-fusion process at nominal LHC energies (14 TeV).
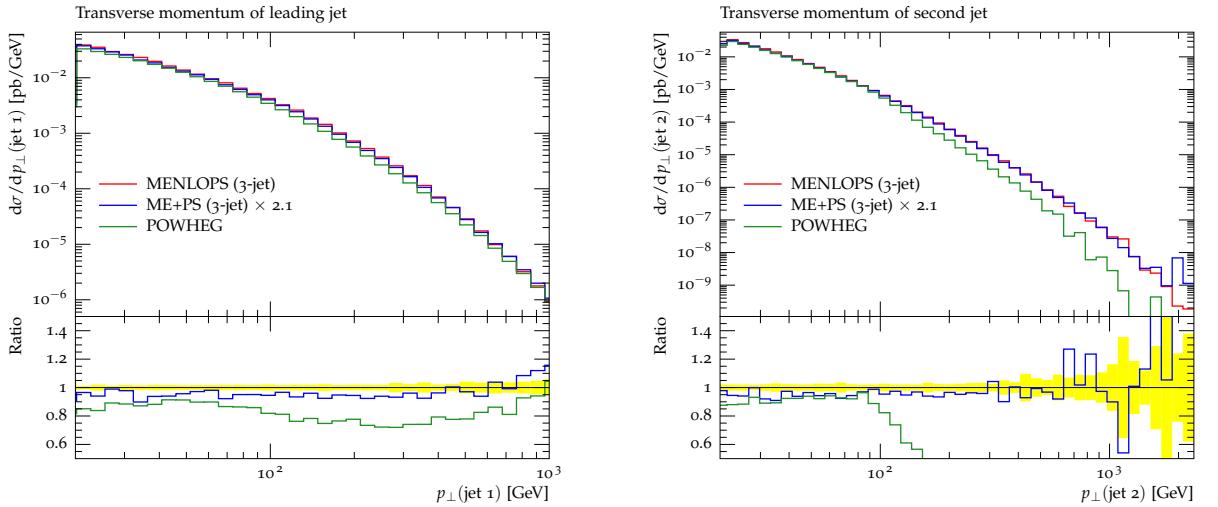

Figure 8.18: Transverse momentum of the first and second hardest jet in Higgs-boson production via gluon fusion at nominal LHC energies (14 TeV).

8.3.6 Higgs boson production

This section presents predictions for Higgs boson production via gluon fusion at nominal LHC energies of $\sqrt{s} = 14$ TeV. As NLO corrections to the core process $gg \to h \to \tau^+\tau^-$ are rather large, tremendous efforts have been made to perform fully differential calculations at NNLO [232, 233, 234] and several predictions have been presented which merged such fixed-order results with resummation at next-to-next-to-leading logarithmic accuracy [235, 236]. Within the confines of the MEnloPS approach there are no means for an improvement of the resummed calculation. Instead it is restricted by the limitations of the parton-shower model. However, the systematic inclusion of higher-order tree-level matrix elements through the MEnloPS method can yield a significant improvement of existing NLO predictions, thus partially closing the gap between full NNLO predictions and Monte-Carlo results. It was shown, for example, in [263] that the predictions from ME+PS algorithms are often competitive to NNLO results if only the shape, not the normalisation, of observable distributions is concerned.
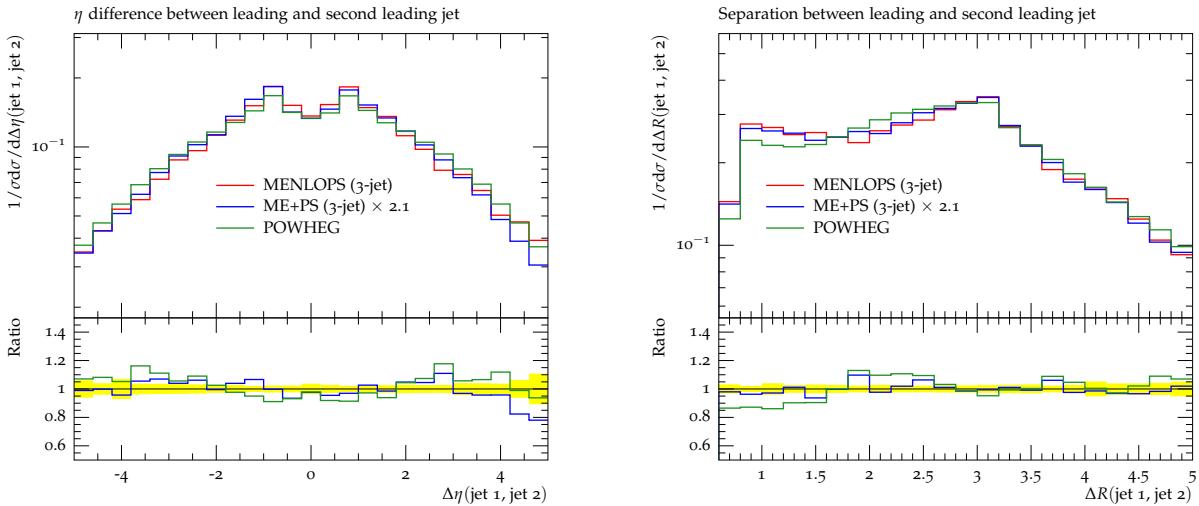
Figure 8.19: Pseudorapidity difference and angular separation of the first and second hardest jet in Higgs-boson production via gluon fusion at nominal LHC energies (14 TeV).

In the simulations $m_H = 120$ GeV is set, and the decay $h \to \tau^+\tau^-$ and Γ_h are included. However, the analysis focuses on the properties of QCD radiation associated with production of the Higgs boson. The invariant τ-pair mass is restricted to $115 < m_{\tau\tau}/\text{GeV} < 125$ at the matrix-element level. Virtual matrix elements are implemented according to [230, 231]. The decay $h \to \tau^+\tau^-$ is corrected for QED soft-resummation and approximate next-to-leading order effects using the YFS approach [74].

Figure 8.17 shows the transverse momentum spectrum of the reconstructed Higgs boson. Therein, it is to note that both the POWHEG and MENLOPS samples are very consistent in the prediction of this rather inclusive observable. On the other hand, differences are observed in the results for individual jet transverse momentum spectra, cf. Figure 8.18. They increase with jet multiplicity and with increasing transverse momentum, as can be expected, since the higher multiplicity jets are described by the uncorrected parton shower in the POWHEG method. Deviations are also found in the prediction of the dijet separation in $\eta - \phi$ space, which is shown in Figure 8.19. However, it was previously found that the ME+PS result yields a prediction which is very similar to the NNLO result [263]. This feature is naturally retained in the MENLOPS simulation.

8.3.7 W^+W^-+jets Production

In this section predictions for the production of the $W^+[\to e^+\nu_e]\,W^-[\to \mu^-\bar{\nu}_\mu]$ final state at nominal LHC energies of $\sqrt{s} = 14$ TeV are presented. The lepton-neutrino pairs are required to have an invariant mass of $m_{\ell\nu} > 10$ GeV each. The $W \to \ell\nu$ decays are corrected for QED next-to-leading order and soft-resummation effects using the YFS approach [74]. Virtual matrix elements are supplied by MCFM [9, 237, 238]. Again, this study focuses mainly on the properties of QCD radiation accompanying the diboson production process. Up to three additional jets at $Q_{\text{cut}} = 20$ GeV are simulated in both, the MENLOPS and the ME+PS sample. It is known that high-multiplicity matrix elements in the ME+PS approach yield sizable effects on total event rates and shapes in this reaction [264], a feature which is inherited by the MENLOPS method. Setting the phase-space separation criterion to a rather low value compared to the average partonic centre-of-mass energy will thus always lead to sizable emission-rate differences, which might be an indication of potentially large higher-order corrections. A similar effect was observed in a recent analysis of Z-boson pair production in association with a hard jet [265]. While the NLO corrections to
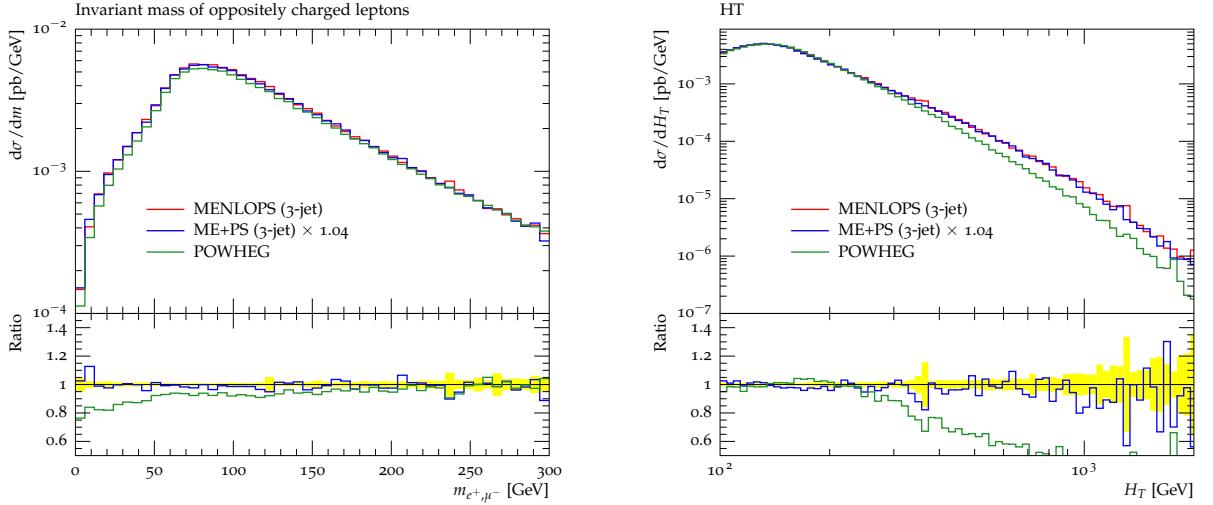
Figure 8.20: Invariant mass of the electron-muon pair (left) and H_T (right) in W^+W^- production at nominal LHC energies (14 TeV).
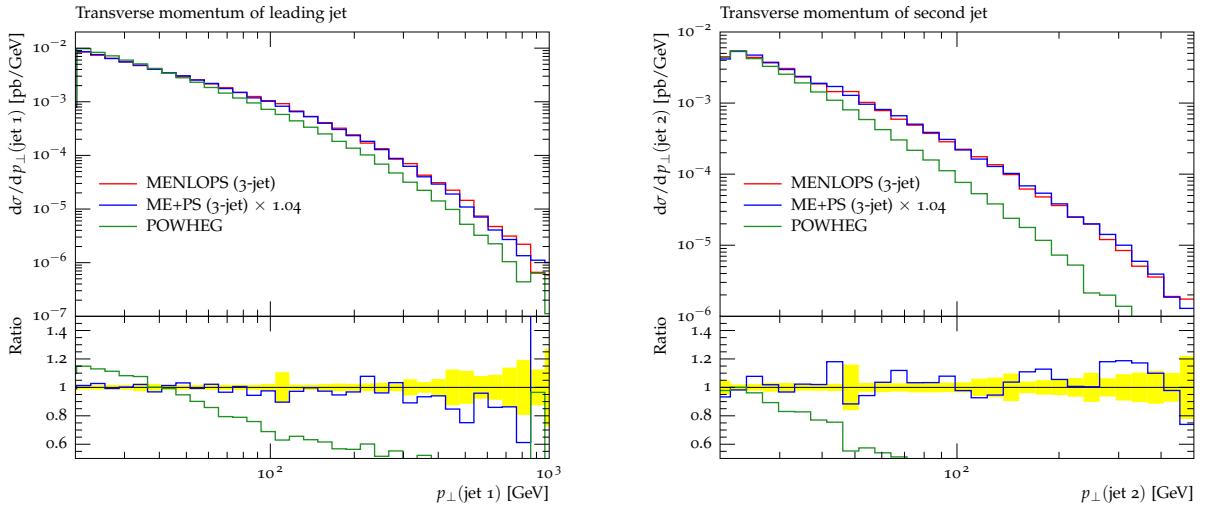
Figure 8.21: Transverse momentum of the first and second hardest jet in W^+W^- production at nominal LHC energies (14 TeV).
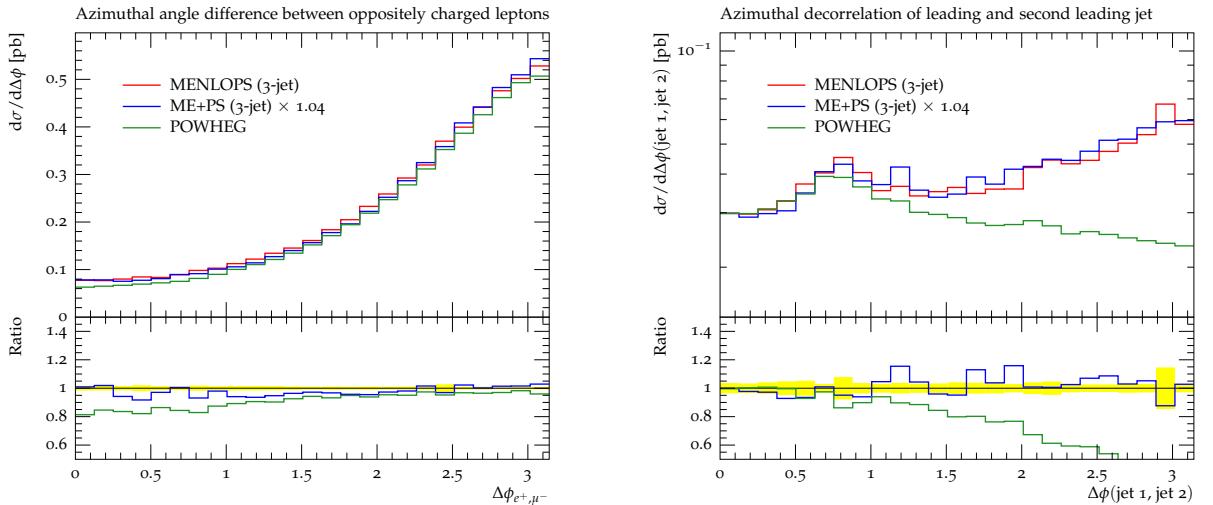
Figure 8.22: Azimuthal separation of the electron and the muon (left) and of the two hardest jets (right) in W^+W^- production at nominal LHC energies (14 TeV).
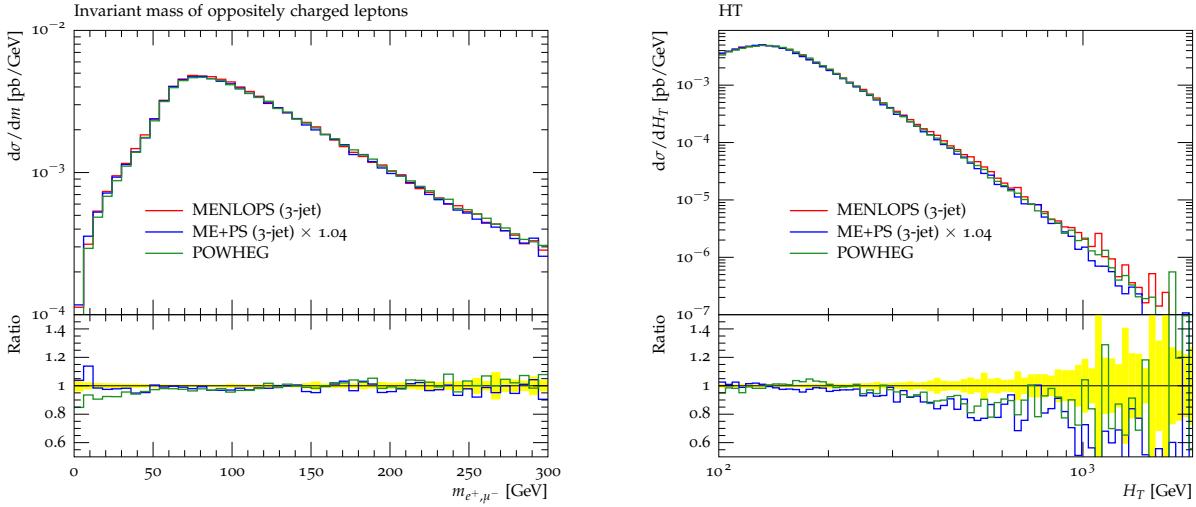
Figure 8.23: Invariant mass of the electron-muon pair (left) and H_T (right) in W^+W^- production at nominal LHC energies (14 TeV) after vetoing events with more than one jet with $p_T > 20$ GeV.
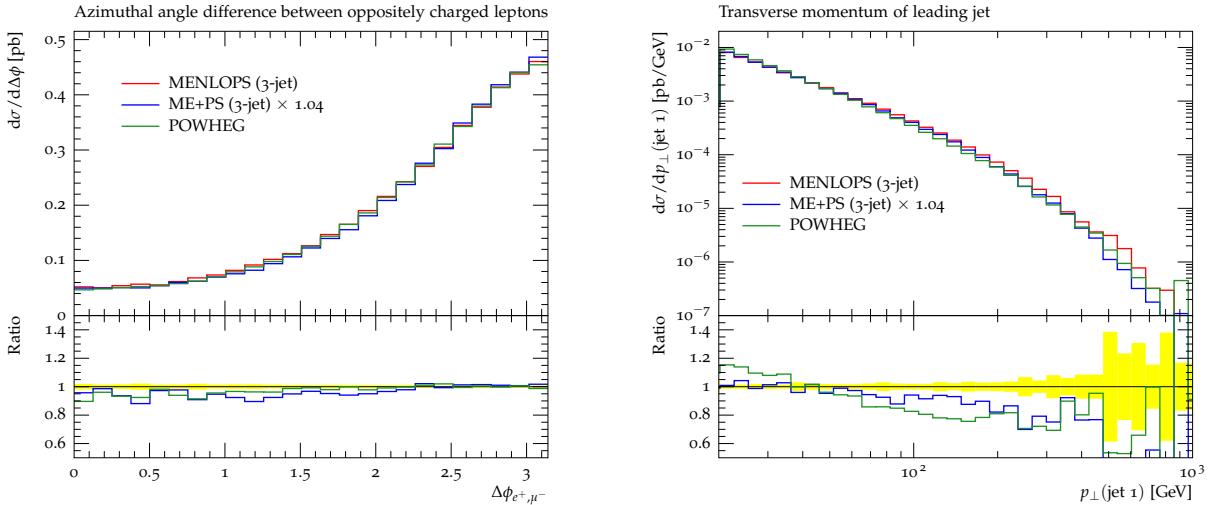
Figure 8.24: Azimuthal separation of the electron and the muon (left) and transverse momentum of the hardest jet in W^+W^- production at nominal LHC energies (14 TeV) after vetoing events with more than one jet with $p_T > 20$ GeV.

this process are comparably small at Tevatron, they can be rather large at nominal LHC energies. Restricting the available final-state phase space by a jet veto, the corrections were again limited to smaller values, which makes the importance of the $ZZ+2$ jets final state explicit. As up to three additional jets in the simulation of W^+W^- production are included, similar effects are observed.

Figure 8.20 displays the invariant mass of the lepton pair and the scalar sum of transverse momenta of the jets, leptons and the missing transverse energy, H_T. While the former is described very well by the next-to-leading order calculation used in the POWHEG sample and receives only mild corrections from higher-order matrix elements, H_T receives sizable corrections at rather low values already. The reason for this is easily found in the sensitivity of H_T to *any* jet activity and thus to higher-order matrix element corrections of the parton shower. This can be seen in comparison to Figure 8.23, where a veto on additional jet activity was applied. Figure 8.21 exemplifies that the ME+PS part of the MENLOPS simulation

predicts significantly harder radiation than the POWHEG subsample. The corresponding corrections naturally amplify the deviations between the respective predictions of H_T. The impact of a jet veto on this distribution is shown in the right panel of Figure 8.24.

Figure 8.22 presents predictions for the azimuthal separation of the leptons and the two hardest jets. Again, the former receives only comparably small corrections, while higher-order matrix-element corrections have large impact on the latter. This hints at the importance to include higher-order matrix elements in Monte-Carlo simulations of hadron-collider events if the hadronic centre-of-mass energy is large. The effect of a jet veto on the azimuthal separation of the leptons is shown in the left panel of Figure 8.24.

8.4   Summary and conclusions

In this part of this thesis, a parallel development and independent implementation [173] of the MENLOPS algorithm, first discussed in [172], has been presented. This new algorithm combines the so far most advanced methods to include higher-order corrections to a given core process: The POWHEG technique, which allows to produce inclusive samples for that process with next-to-leading order accuracy, and the ME+PS technique, which allows to generate inclusive samples with a leading-order cross section, but with the production of additional hard radiation corrected by higher-order tree-level matrix elements.

Until the work of Hamilton and Nason [172] and the work presented here, these two approaches were considered orthogonal and thus used independent from each other, in the regime of their respective strengths and validity. With the recent efforts on combining them, the shortcomings of each method, i.e. the description of higher jet multiplicities in POWHEG and lack of the correct NLO cross section in ME+PS, have been expunged.

The findings of Hamilton and Nason are fully confirmed concerning both the formalism and the relative improvement in the simulation obtained through it. This is even more emphasised here, since the implementation of the MENLOPS method as presented in [172] seems to suffer from the choice of tools. As already indicated in the introduction, the omission of truncated showering in the program used to simulate the ME region may have caused a few of the uncertainties. The superior quality of the ME+PS part of the simulation in SHERPA, including the truncated showering, is the only reason behind the improved simulation here – the formalism is identical in both publications. The drastically reduced uncertainties stress the great improvement by the MENLOPS method.

The results presented here and the ones presented by Hamilton and Nason in fact show a significant improvement of many aspects of previous simulations in a variety of processes, including here e^+e^- annihilation to hadrons, hadronic final states in DIS, jets in association with single vector bosons and with vector boson pairs, and the production of Higgs bosons through gluon fusion.

In the future, the description of many more processes with this combined NLO matching and multijet merging will become feasible. This is possible, because *both* the POWHEG and the ME+PS part of the implementation are fully automated in SHERPA.

It is also worth pointing out that the methods developed so far will naturally serve as a starting point to promote the ME+PS idea to full NLO, in the sense that merging sequences of multijet matrix elements at NLO into one inclusive sample becomes feasible. A first attempt to achieve this from a somewhat different angle has been presented in [171].

Summary

Summary

In this thesis the consistent combination of two types of resummations, the Yennie-Frautschi-Suura (YFS) resummation resumming large soft photon logarithms and the Dokshitzer-Gribov-Lipatov-Altarelli-Parisi (DGLAP) resummation resumming large collinear parton radiation logarithms, and fixed-order next-to-leading order matrix element has been achieved. The description of photon and parton radiation, respectively, therefore exhibits the best descriptions available over the whole radiation phase space, both hard and soft, and both collinear and wide angle, respectively.

Part I discussed the YFS resummation and how fixed order hard photon emission matrix elements can be incorporated. An algorithm implementing this resummation, allowing for the incorporation of higher order matrix elements to any decay process up to any order in the QED coupling constant α, has been implemented as an independent physics module, PHOTONS++, in the SHERPA event generator framework. An automated construction for the collinear approximation to any decay matrix element, for processes which do not have dedicated exact matrix elements implemented, was presented. Thus, the bulk of the hard photon radiation can always be described correctly to $\mathcal{O}(\alpha)$. For processes that have dedicated higher order matrix elements implemented, these are not restricted to next-to-leading order real emission matrix elements. On the contrary, the implementation is constructed such that real as well as virtual emission matrix elements, in the form of the squared infrared subtracted matrix elements $\tilde{\beta}_m^n$, can be added to any order in α without modifying PHOTONS++' core. This implementation has then been compared to traditional parton shower implementations by calculating the expectation values of selected observables in Drell-Yan production. Very good agreement was found. As well as a reduced sensitivity to unphysical cutoff parameters. Similarly, the predictions of the algorithm for the radiative decay widths of μ and τ decays has been compared to data published by the Particle Data Group and excellent agreement was found.

Chapter 5 used the versatility of the implementation to calculate observables in semileptonic B meson decays, key processes at past and present B-factories. Therefore, the electroweak corrections to such processes were calculated in the respective effective decay model augmented with QED gauge invariance. These corrections were implemented to facilitate their use with the automated resummation implementation. The results show good agreement with the parallely implemented fixed-order next-to-leading order result in large regions of the phase space. However, regions of the various observables which are dominated by resummation effects have been identified and a considerable improvement has been found.

Part II was dedicated to discuss the DGLAP resummation and how its results can be consistently combined with fixed order results. Therefore, the established POWHEG method has been reformulated on the basis of the evolution of single legs, as present in the DGLAP formalism. This enabled its reinterpretation as an advanced matrix element reweighting of conventional parton showers, supplied with a next-to-leading order weight. For the prove of full next-to-leading order correctness for inclusive observables as well as (next-to-)leading logarithmic correctness of the parton evolution, intimate relations between the subtraction algorithm, enabling a numeric implementation of next-to-leading order corrections, and the parton shower have been established. Together with the automated tree-level matrix element generators and the automated implementation of the Catani-Seymour dipole subtraction present within the SHERPA framework this reformulation of the POWHEG method led to

its automated implementation, given the virtual matrix element is linked from an external source. This automated implementation has thoroughly tested both for internal consistency and its ability to describe experimental data. Very good agreement was found. Further, the formal relation of the POWHEG method and the MC@NLO method has been established exploiting their respective ambiguities regarding their exponentiation behaviour.

The new formulation of the POWHEG method and its automated implementation in SHERPA led to a straightforward combination with the ME+PS algorithm, merging samples of successively increasing final state parton multiplicity into one inclusive event sample. The resulting MENLOPS algorithm is thus able to describe inclusive observables with the same accuracy as the POWHEG algorithm and observables depending on higher order real parton emissions with the same accuracy as the ME+PS method. Of course, also the intrajet parton evolution, described at the same level of accuracy in both POWHEG and ME+PS, is not spoiled either. These facts have been verified by extensive cross-algorithm comparisons. Finally the predictions for a wealth of observables have been compared to a wide range of data and very good agreement was found.

Altogether, in can be concluded that the SHERPA event generator is thus able to simultaneously calculate a very wide range of observables with the highest accuracy. The comparison to data has shown the improved quality of its description over a wide range of experiments, from the data taken by the e^+e^- collider BABAR at the $\Upsilon(4S)$ resonance to the e^+e^- collider LEP taking data at the Z pole, including the deep inelastic scattering data from the ep-collider HERA and data from the two hadron colliders Tevatron, colliding $p\bar{p}$ at 1.8 TeV and 1.96 TeV, and LHC, colliding pp at 7 TeV.

Appendix

Appendix A

Details on the YFS resummation implementation

A.1 The YFS-Form-Factor

In this appendix, the cancellation of virtual and real soft singularities will explicitly be performed and the YFS-Form-Factor will be calculated. As already defined in Chapters 2 and 3 the YFS-Form-Factor $Y(\Omega)$ reads

$$Y(\Omega) = 2\alpha \sum_{i<j} \left(\mathcal{R}e\, B(p_i, p_j) + \tilde{B}(p_i, p_j, \Omega) \right) , \tag{A.1.1}$$

where the virtual infrared factor is given by

$$B(p_i, p_j) = -\frac{i}{8\pi^3} Z_i Z_j \theta_i \theta_j \int \frac{\mathrm{d}^4 k}{k^2} \left(\frac{2p_i\theta_i - k}{k^2 - 2(k \cdot p_i)\theta_i} + \frac{2p_j\theta_j + k}{k^2 + 2(k \cdot p_j)\theta_j} \right)^2 \tag{A.1.2}$$

and the real infrared factor reads

$$\tilde{B}(p_i, p_j, \Omega) = \frac{1}{4\pi^2} Z_i Z_j \theta_i \theta_j \int \mathrm{d}^4 k\, \delta(k^2)\,(1 - \Theta(k, \Omega)) \left(\frac{p_i}{(p_i \cdot k)} - \frac{p_j}{(p_j \cdot k)} \right)^2 . \tag{A.1.3}$$

As before, Z_i and Z_j are the charges of particles i and j in units of the positron charge, respectively, and the sign factors $\theta_{i,j} = \pm 1$ for final (initial) state particles. Again, Ω is the "unresolved" region of the phase space for the soft photons. In this form the divergences need to be regularised, which can be achieved by either introducing a fictitious small photon mass λ, as in the original YFS paper [75], or through dimensional regularisation. In both cases, however, the limited real emission phase space Ω will lead to potentially large logarithms.

After performing the momentum integration, the virtual infrared factor can be written as

$$B(p_i, p_j) = -\frac{Z_i Z_j \theta_i \theta_j}{2\pi} \left(\ln \frac{m_i m_j}{\lambda^2} + \tfrac{1}{2}(p_i \cdot p_j)\theta_i \theta_j \int\limits_{-1}^{1} \mathrm{d}x \frac{\ln \frac{p_x'^2}{\lambda^2}}{p_x'^2} + \tfrac{1}{4} \int\limits_{-1}^{1} \mathrm{d}x \ln \frac{p_x'^2}{m_i m_j} \right) , \tag{A.1.4}$$

where

$$p_x' = \frac{(p_i\theta_i - p_j\theta_j) + x(p_i\theta_i + p_j\theta_j)}{2} \tag{A.1.5}$$

and

$$-\ln \lambda^2 = \frac{1}{\epsilon} - \ln \tilde{\mu}^2 \qquad (A.1.6)$$

contains the infrared divergence. Similarly, the real infrared factor reads

$$\tilde{B}(p_i, p_j, \omega) = \frac{Z_i Z_j \theta_i \theta_j}{2\pi} \left[\ln \frac{\omega^2}{\lambda^2} + \ln \frac{m_i m_j}{E_i E_j} - \tfrac{1}{2}(p_i \cdot p_j) \int_{-1}^{1} dx \frac{\ln \frac{p_x^2}{\lambda^2}}{p_x^2} + \tfrac{1}{2}(p_i \cdot p_j) \int_{-1}^{1} dx \frac{\ln \frac{E_x^2}{\omega^2}}{p_x^2} \right.$$
$$\left. - \tilde{G}(1) - \tilde{G}(-1) + (p_1 \cdot p_2) \int_{-1}^{1} dx \frac{\tilde{G}(x)}{p_x^2} \right] , \qquad (A.1.7)$$

with

$$p_x = \frac{(p_i + p_j) + x(p_i - p_j)}{2} \qquad (A.1.8)$$

and ω is the momentum cut-off specifying Ω in the frame $\tilde{B}$ is to be evaluated in. Furthermore,

$$\tilde{G}(x) = \frac{1 - \beta_x}{2\beta_x} \ln \frac{1 + \beta_x}{1 - \beta_x} + \ln \frac{1 + \beta_x}{2} . \qquad (A.1.9)$$

with

$$\beta_x = \frac{|\vec{p}_x|}{p_x^0} = \frac{\sqrt{(\vec{p}_i + \vec{p}_j)^2 + 2x(\vec{p}_i^2 - \vec{p}_j^2) + x^2(\vec{p}_i - \vec{p}_j)^2}}{(E_i + E_j) + x(E_i - E_j)} . \qquad (A.1.10)$$

Combining both terms to the YFS-Form-Factor the divergences cancel and a finite result is obtained. The remaining parameter integrals do not give rise to further divergences as long as $p_i^2, p_j^2 > 0$, i.e. as long as the emitting particles are massive. Thus, taken together, the YFS form factor reads

$$Y(p_i, p_j, \omega) = -\frac{\alpha}{\pi} Z_i Z_j \theta_i \theta_j \left[\ln \frac{E_i E_j}{\omega^2} - \tfrac{1}{2}(p_i \cdot p_j) \int_{-1}^{1} dx \frac{\ln \frac{E_x^2}{\omega^2}}{p_x^2} + \tfrac{1}{4} \int_{-1}^{1} dx \ln \frac{p_x'^2}{m_i m_j} \right.$$
$$+ \tfrac{1}{2}(p_i \cdot p_j) \Theta(\theta_i \theta_j) \left(\frac{8\pi^2 \Theta(x_1' x_2')}{(x_2' - x_1')(p_i + p_j)^2} + \int_{-1}^{1} dx \frac{\ln x^2}{p_x^2} \right)$$
$$\left. + \tilde{G}(1) + \tilde{G}(-1) - (p_i \cdot p_j) \int_{-1}^{1} dx \frac{\tilde{G}(x)}{p_x^2} \right] , \qquad (A.1.11)$$

where $x_{1,2}'$ are the roots of $p_x'^2$ with $x_1' < x_2'$. The general case cannot be evaluated in closed form. This is due to the fact that the term

$$\int_{-1}^{1} dx \frac{\tilde{G}(x)}{p_x^2} , \qquad (A.1.12)$$

although completely finite, can only be evaluated analytically for the dipole in its rest frame or in the rest frame of one of either of its constituent particles. This can only be achieved if there is one dipole only. All other cases need to be evaluated numerically.

A.1.1 Special cases

Decay into two particles with $(p_i\theta_i + p_j\theta_j)^2 < 0$

If the multipole consists of only two particles in the final state, e.g. for decays of the type $Z \to \ell\bar{\ell}$, then there is an analytical solution in the rest frame of the dipole formed by the two charged particles. In the high-energy limit, given by $E_i \gg m_i$ for both QED corrected charged particles, the critical term above can be written as

$$(p_i \cdot p_j) \int\limits_{-1}^{1} \mathrm{d}x \frac{\tilde{G}(x)}{p_x^2} \cong \tfrac{1}{6}\pi^2 .$$
(A.1.13)

Therefore, in this case, the full YFS form factor reads

$$Y(p_i, p_j, \omega) \cong -\frac{\alpha}{\pi} Z_i Z_j \theta_i \theta_j \left[\left(1 - \ln\frac{2(p_i \cdot p_j)}{m_i m_j}\right) \ln\frac{E_i E_j}{\omega^2} + \ln\frac{E_i}{E_j}\ln\frac{m_i}{m_j} - \tfrac{1}{2}\ln^2\frac{E_i}{E_j} \right.$$
$$\left. + \tfrac{1}{2}\ln\frac{(p_i\theta_i + p_j\theta_j)^2}{m_i m_j} - 1 - \tfrac{\pi^2}{6} \right] .$$
(A.1.14)

This result in the high-energy limit agrees with the result stated in [75].

Decay of a charged particle with one charged final state with $(p_i\theta_i + p_j\theta_j)^2 = 0$

A similar, but nonetheless different case occurs for the decay of a charged particle into a final state involving only one charged particle, e.g. the case of W-decays, $W \to \ell\nu_\ell$. Then, in the corresponding dipole's rest frame neither $m_W \ll E_W$ nor $(p_i\theta_i + p_j\theta_j)^2 < 0$ and therefore this case is different from the one above. In this case, for $(p_W - p_l)^2 = 0$,

$$Y_W(\omega) = \frac{\alpha}{\pi}\left[2\left(1 - \ln\frac{m_W}{m_l}\right)\ln\frac{m_W}{\omega\sqrt{8}} + \ln\frac{m_W}{m_l} - \tfrac{1}{2} + \tfrac{3}{2}\ln 2 - \tfrac{3}{12}\pi^2\right] .$$
(A.1.15)

This result of course differs from the result in [98] since both results are given in different Lorentz-frames. Also, if in this process a photon is radiated, then $(p_W - p_l)^2 = 2(p_\nu \cdot p_\gamma) > 0$ and the YFS-Form-Factor takes a different a form.

A.1.2 The full YFS form factor

Here the complete solutions to analytically integrable parameter integrals in the YFS form factor are given. In the following, using the invariance of $Y(\Omega)$ under the interchange of $p_i \leftrightarrow p_j$, the labels p_i and p_j are chosen such that $E_j \geq E_i$. It is useful to define

$$x_{1,2} = -\frac{p_i^2 - p_j^2 \pm 2\sqrt{(p_i \cdot p_j)^2 - p_i^2 p_j^2}}{(p_i - p_j)^2}$$
(A.1.16)

as the roots of p_x^2 and

$$x'_{1,2} = -\frac{p_i^2 - p_j^2 \pm 2\sqrt{(p_i \cdot p_j)^2 - p_i^2 p_j^2}}{(p_i + p_j)^2}$$
(A.1.17)

as those of $p_x'^2$ in case of $\theta_i\theta_j = +1$, satisfying $x_{1,2} \notin [-1,1]$ and $x_{1,2}' \in (-1,1)$, respectively. It holds that $x_1, x_2' > 0$ and $x_2, x_1' < 0$ if $(p_i - p_j)^2 < 0$ and $0 < x_1 < x_2$ and $0 < x_1' < x_2'$ if $(p_i - p_j)^2 > 0$. These difference in the relations between x_1 and x_2 necessitate the differentiation of distinct cases in the calculations.

If $(p_i - p_j)^2 = 0$ then $x_{1,2}$ are not defined. If $\theta_i\theta_j = -1$ then $p_x'^2 = p_x^2$ and $x_{1,2}'$ are meaningless, leading to another set of distinct cases.

When evaluating the first set of the parameter integrals that fact simplifies matters a lot resulting in

$$\mathcal{R}e\left(\theta_i\theta_j \int_{-1}^{1} dx \frac{\ln \frac{p_x'^2}{\lambda^2}}{p_x'^2} + \int_{-1}^{1} dx \frac{\ln \frac{p_x^2}{\lambda^2}}{p_x^2}\right) \overset{\theta_i\theta_j = -1}{=} 0. \tag{A.1.18}$$

Otherwise, the evaluation is more complicated and involves shifting the poles at $x_{1,2}'$ off the real axis. The solution then is

$$\mathcal{R}e\left(\theta_i\theta_j \int_{-1}^{1} dx \frac{\ln \frac{p_x'^2}{\lambda^2}}{p_x'^2} + \int_{-1}^{1} dx \frac{\ln \frac{p_x^2}{\lambda^2}}{p_x^2}\right)$$

$$= \frac{8\pi^2\Theta\left(x_1' x_2'\right)}{(x_2' - x_1')(p_i + p_j)^2} + \frac{8}{(x_1 - x_2)(p_i - p_j)^2}\left[\ln|x_1|\left(\text{Li}_2\left(\frac{x_1-1}{x_1}\right) - \text{Li}_2\left(\frac{x_1+1}{x_1}\right)\right)\right.$$

$$\left. - \ln|x_2|\left(\text{Li}_2\left(\frac{x_2-1}{x_2}\right) - \text{Li}_2\left(\frac{x_2+1}{x_2}\right)\right)\right]. \tag{A.1.19}$$

In any case, the last piece of the divergence has cancelled, leaving finite terms negligible in the high energy limit.

The other integral containing $p_x'^2$ is to be evaluated next. In total there are three cases to consider.

- $\theta_i\theta_j = +1$

$$\mathcal{R}e\left(\int_{-1}^{1} dx \ln \frac{p_x'^2}{m_i m_j}\right)$$

$$= 2\ln\frac{(p_i + p_j)^2}{4m_i m_j} + \ln\left[(1 - x_1'^2)(1 - x_2'^2)\right] - x_1'\ln\left|\frac{1 - x_1'}{1 + x_1'}\right| - x_2'\ln\left|\frac{1 - x_2'}{1 + x_2'}\right| \tag{A.1.20}$$

  Although, there again are poles within the range of integration the integral over them is finite.

- $\theta_i\theta_j = -1$. The range of integration does not comprise any poles and, thus, is real, giving

$$\int_{-1}^{1} dx \ln \frac{p_x^2}{m_i m_j}$$

$$= 2\ln\frac{|(p_i - p_j)^2|}{4m_i m_j} + \ln\left[(1 - x_1^2)(1 - x_2^2)\right] + x_1\ln\left|\frac{1 + x_1}{1 - x_1}\right| + x_2\ln\left|\frac{1 + x_2}{1 - x_2}\right| \tag{A.1.21}$$

Evidently, the case $(p_i - p_j)^2 = 0$ has to be treated separately. It yields

$$\int\limits_{-1}^{1} dx \ln \frac{p_x^2}{m_i m_j} \;=\; 2\ln \frac{|p_i^2 - p_j^2|}{2 m_i m_j} + \ln|1 - x_p^2| + x_p \ln \left| \frac{1 + x_p}{1 - x_p} \right| - 2 \,. \qquad \text{(A.1.22)}$$

where $x_p = -\frac{p_i^2 + p_j^2}{p_i^2 - p_j^2}$. In decay matrix elements it is not kinematically possible to also have $m_i = m_j$.

The last integral that is generally solvable analytically differentiates even more cases. The easiest to solve is the case of $E_i = E_j$, as it is occurring in leptonic Z-decays. Here, E_x is independent of x, thus giving

$$\int\limits_{-1}^{1} dx \frac{\ln \frac{E_x^2}{\omega^2}}{p_x^2} \;=\; \frac{8}{(x_1 - x_2)(p_i - p_j)^2} \ln \frac{E_i + E_j}{2\omega} \ln \left| \frac{(1 - x_1)(1 + x_2)}{(1 + x_1)(1 - x_2)} \right| \,. \qquad \text{(A.1.23)}$$

For all other dipoles three distinct cases appear:

- $(p_i - p_j)^2 < 0$

$$\int\limits_{-1}^{1} dx \frac{\ln \frac{E_x^2}{\omega^2}}{p_x^2}$$

$$= \frac{8}{(x_1 - x_2)(p_i - p_j)^2} \left[\ln \frac{E_i}{\omega} \ln \left| \frac{1 - x_1}{1 + x_1} \right| + \ln|y_1| \ln \left| \frac{1 - x_1}{1 + x_1} \right| \right.$$

$$- \ln \frac{(1 + x_2)E_i + (1 - x_2)E_j}{2\omega} \ln \left| \frac{1 - x_2}{1 + x_2} \right|$$

$$\left. + \text{Li}_2\left(-\frac{\zeta(1 + x_1)}{y_1} \right) - \text{Li}_2\left(\frac{\zeta(1 - x_1)}{y_1} \right) - \text{Li}_2\left(-\frac{1 + x_2}{x_E - x_2} \right) + \text{Li}_2\left(\frac{1 - x_2}{x_E - x_2} \right) \right]$$

$$\qquad \text{(A.1.24)}$$

with $y_1 = 1 + \zeta(1 - x_1)$, $\zeta = -\frac{E_i - E_j}{2 E_i}$ and $x_E = -\frac{E_i + E_j}{E_i - E_j}$.

- $(p_i - p_j)^2 > 0$

$$\int\limits_{-1}^{1} dx \frac{\ln \frac{E_x^2}{\omega^2}}{p_x^2}$$

$$= \frac{8}{(x_1 - x_2)(p_i - p_j)^2} \left[\ln \frac{E_i}{\omega} \ln \left| \frac{1 - x_1}{1 + x_1} \right| + \ln|y_1| \ln \left| \frac{1 - x_1}{1 + x_1} \right| \right.$$

$$+ \frac{1}{2}\ln^2 \left| \frac{y_2}{\xi(1 + x_2)} \right| - \frac{1}{2}\ln^2 \left| \frac{y_2}{\xi(1 - x_2)} \right|$$

$$- \ln \frac{E_j}{\omega} \ln \left| \frac{1 - x_2}{1 + x_2} \right| + \ln|y_2| \ln \left| \frac{1 - x_2}{1 + x_2} \right|$$

$$\left. + \text{Li}_2\left(-\frac{\zeta(1 + x_1)}{y_1} \right) - \text{Li}_2\left(\frac{\zeta(1 - x_1)}{y_1} \right) - \text{Li}_2\left(-\frac{y_2}{\xi(1 - x_2)} \right) + \text{Li}_2\left(\frac{y_2}{\xi(1 + x_2)} \right) \right]$$

with $y_2 = 1 + \xi(1 + x_2)$ and $\xi = \frac{E_i - E_j}{2E_j}$.

- $(p_i - p_j)^2 = 0$
  With the definitions for x_E and x_p from above it allways holds that $x_E > x_p > 1$, thus

$$
\int_{-1}^{1} \mathrm{d}x \frac{\ln \frac{E_x^2}{\omega^2}}{p_x^2}
$$

$$
= \frac{4}{p_j^2 - p_i^2} \left[\ln \frac{E_j - E_i}{2\omega} \ln \left| \frac{1 + x_p}{1 - x_p} \right| + \ln(x_E - x_p) \ln \left| \frac{1 + x_p}{1 - x_p} \right| \right.
$$

$$
\left. + \mathrm{Li}_2 \left(\frac{x_p - 1}{x_p - x_E} \right) - \mathrm{Li}_2 \left(\frac{x_p + 1}{x_p - x_E} \right) \right]
$$

(A.1.26)

The last integral can generally only be solved numerically. This is due to the complexity of β_x. If, however, the dipole is in its rest frame or in the rest frame of one of its constituents, there are analytical solutions. Because PHOTONS++ always treats multipoles in their rest frames solutions for the integral will only be given in that frame. Two important cases are:

- $m_i = m_j$

$$
\int_{-1}^{1} \mathrm{d}x \frac{\tilde{G}(x)}{p_x^2}
$$

$$
= \frac{1}{\beta E^2} \left[\frac{1}{2} \ln^2 \frac{1 + \beta}{2} + \ln 2 \ln(1 + \beta) - \frac{1}{2} \ln^2 2 - \frac{1}{2} \ln^2(1 + \beta) \right.
$$

$$
\left. + \mathrm{Li}_2 \left(\frac{1 - \beta}{2} \right) - \mathrm{Li}_2 \left(\frac{1 + \beta}{2} \right) + \mathrm{Li}_2 \left(\beta \right) - \mathrm{Li}_2 \left(-\beta \right) \right]
$$

(A.1.27)

with $\beta = \frac{|\vec{p}_i|}{E_i} = \frac{|\vec{p}_j|}{E_j}$ and $E = E_i = E_j$.

- Leptonic W-decay $(m_i \ll m_j = m_W)$

$$
\int_{-1}^{1} \mathrm{d}x \frac{\tilde{G}(x)}{p_x^2} \cong \frac{2}{m_j^2} \left[\frac{3}{12} \pi^2 + \mathrm{Li}_2 \left(-2 \right) \right] .
$$

(A.1.28)

A.2 Details on the photon generation

In this section the generation of the photon distribution is detailed.
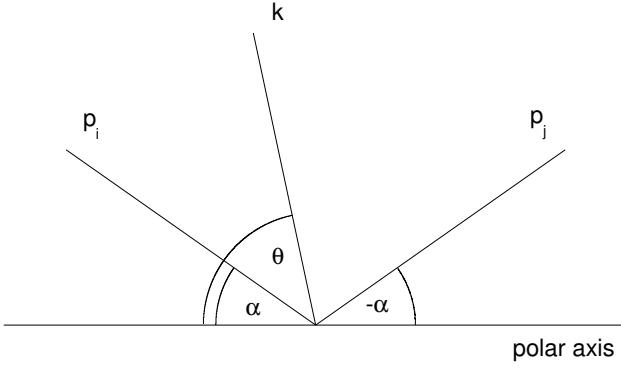
Figure A.1: Sketch of how the axes are chosen in the angular integration in multipoles.

A.2.1 Avarage photon multiplicity

The average photon multiplicity $\bar{n}$ is the average of the Poisson distribution before it is corrected by the various weights. It is therefore not immediately connected to the true average photon multiplicity of the final event. Nonetheless, it is an integral part of the generation procedure. An analytical result in closed form is available for both dipoles and multipoles. However, the calculations for multipoles are more involved as the integrations do not nicely separate as they do in the dipole case in the chosen frame. Thus, as a starting point the analytical result for the dipole in its rest frame will be given. It reads

$$\bar{n} = \int_{\omega_{\min}}^{\omega_{\max}} \frac{\mathrm{d}^3 k}{k^0} \tilde{S}_q(k) = -\frac{\alpha}{\pi} Z_1 Z_2 \theta_1 \theta_2 \, \ln \frac{\omega_{\max}}{\omega_{\min}} \, \left(\frac{1 + \beta_1 \beta_2}{\beta_1 + \beta_2} \ln \frac{(1 + \beta_1)(1 + \beta_2)}{(1 - \beta_1)(1 - \beta_2)} \, - 2 \right) ,$$

where $\omega_{\min}$ is the infrared cut-off and $\omega_{\max}$ is the maximal kinematically allowed photon energy. The latter can be determined by setting the rescaling parameter u to zero in eqs. (3.1.17) and (3.1.22), respectively, and by assuming single photon emission. Additionally, $\beta_i = \frac{|\vec{p}_i|}{E_i}$.

In the case of a multipole, the integral over the photon energy can still be separated, as long as the soft photon region is sufficiently well-behaved. This is the case, if $\Theta(k, \Omega)$ forms an isotropic hypersurface in the frame of the integration. However, the angular integration still remains to be done:

$$\begin{aligned}
\bar{n} &= \int \frac{\mathrm{d}^3 k}{k^0} \Theta(k, \Omega) \tilde{S}_q(k) \\
&= \frac{\alpha}{4\pi^2} \sum_{i<j} Z_i Z_j \theta_i \theta_j \int \frac{\mathrm{d}^3 k}{k^0} \Theta(k, \Omega) \left(\frac{q_i}{(q_i \cdot k)} - \frac{q_j}{(q_j \cdot k)} \right)^2 \\
&= \frac{\alpha}{4\pi^2} \ln \frac{\omega_{\max}}{\omega_{\min}} \sum_{i<j} Z_i Z_j \theta_i \theta_j \left(8\pi - \int \mathrm{d}\Omega \frac{2(q_i \cdot q_j)}{(q_i \cdot e_k)(q_j \cdot e_k)} \right) .
\end{aligned} \qquad (A.2.1)$$

Choosing different orientations of the polar axes for each interference term of every constituent dipole, all angular integrations can be done analytically. This choice simplifies the

integration immensely. The orientation for each of the interference terms is thus chosen to be such that both momenta lie symmetrically in the unit sphere, both forming an angle α_{ij} with the polar axis, see Fig. A.1. Therefore, by this choice,

$$
\begin{aligned}
(q_i \cdot q_j) &= E_i E_j \left(1 - a_i a_j + b_i b_j\right) \\
(q_i \cdot e_k) &= E_i \left(1 - a_i \sin \varphi \sin \theta - b_i \cos \theta\right) \\
(q_j \cdot e_k) &= E_j \left(1 - a_j \sin \varphi \sin \theta + b_j \cos \theta\right) ,
\end{aligned}
\tag{A.2.2}
$$

where e_k^μ again is $\frac{1}{k^0} k^\mu$ with $e_k^2 = 0$, cf. Eq. (3.1.33), and the further parameters are given by

$$
a_{i,j} = \beta_{i,j} \sin \alpha_{ij} \quad \text{and} \quad b_{i,j} = \beta_{i,j} \cos \alpha_{ij} .
\tag{A.2.3}
$$

With these choices the last integral reads

$$
\begin{aligned}
&\int d\Omega \frac{E_i E_j}{(q_i \cdot e_k)(q_j \cdot e_k)} \\
&= \int_0^{2\pi} d\varphi \int_0^\pi d\theta \, \sin \theta \, \frac{1}{\left(1 - a_i \sin \varphi \sin \theta - b_i \cos \theta\right) \left(1 - a_j \sin \varphi \sin \theta + b_j \cos \theta\right)} .
\end{aligned}
\tag{A.2.4}
$$

Using the decomposition

$$
\frac{1}{b_j \left(1 - a_i \sin \varphi \sin \theta - b_i \cos \theta\right)} - \frac{1}{b_i \left(1 - a_j \sin \varphi \sin \theta + b_j \cos \theta\right)}
\tag{A.2.5}
$$

$$
= \frac{(b_i - b_j) + 2 b_i b_j \cos \theta}{b_i b_j \left(1 - a_i \sin \varphi \sin \theta - b_i \cos \theta\right) \left(1 - a_j \sin \varphi \sin \theta + b_j \cos \theta\right)}
\tag{A.2.6}
$$

and $a_i b_j = a_j b_i$, this can be easily integrated giving

$$
\begin{aligned}
&\int d\Omega \frac{E_i E_j}{(q_i \cdot e_k)(q_j \cdot e_k)} \\
&= 2\pi \left[\frac{b_i}{\sqrt{B^2 C_i - ABD_i + A^2 E_i}} \ln \frac{A + B}{A - B} \frac{\sqrt{C_i - D_i + E_i} + \frac{B(2C_i - D_i) - A(D_i - 2E_i)}{2\sqrt{B^2 C_i - ABD_i + A^2 E_i}}}{\sqrt{C_i + D_i + E_i} + \frac{B(2C_i + D_i) - A(D_i + 2E_i)}{2\sqrt{B^2 C_i - ABD_i + A^2 E_i}}} \right. \\
&= \quad \left. - \frac{b_j}{\sqrt{B^2 C_j - ABD_j + A^2 E_j}} \ln \frac{A + B}{A - B} \frac{\sqrt{C_j - D_j + E_j} + \frac{B(2C_j - D_j) - A(D_j - 2E_j)}{2\sqrt{B^2 C_j - ABD_j + A^2 E_j}}}{\sqrt{C_j + D_j + E_j} + \frac{B(2C_j + D_j) - A(D_j + 2E_j)}{2\sqrt{B^2 C_j - ABD_j + A^2 E_j}}} \right] ,
\end{aligned}
\tag{A.2.7}
$$

with

$$
\begin{aligned}
A &= b_i - b_j \\
B &= 2 b_i b_j \\
C_{i,j} &= 1 - a_{i,j} \\
D_{i,j} &= \mp b_{i,j} \\
E_{i,j} &= a_{i,j}^2 + b_{i,j}^2 .
\end{aligned}
\tag{A.2.8}
$$

Upon closer examination it can be seen that for $\alpha_{ij} \to 0$ the result of the dipole case is recovered.

A.2.2 Photon energy

Due to the decomposition of the integration over the photon energy and the integration over the unit sphere, the photon energy distribution and the photon angular distribution can be generated separately. Of course, this independence of distributions is no longer true after the reweighting procedure, but it alleviates the generation of the crude distribution.

In the implementation presented here, the photon energy is distributed according to $\frac{1}{k^0}$, generated through

$$k^0 = \omega_{\text{min}} \left(\frac{\omega_{\text{max}}}{\omega_{\text{min}}} \right)^{\mathcal{R}} \tag{A.2.9}$$

where $\mathcal{R}$ is a uniformly distributed random number on the interval $[0, 1]$.

A.2.3 Photon angles

Similar to all other parts of the photon distribution, the photon angles are also generated according to $\tilde{S}_q(k)$. For this, the relevant function is recast into the form

$$-\left(\frac{q_i}{(q_i \cdot e_k)} - \frac{q_j}{(q_j \cdot e_k)} \right)^2$$
$$= -\frac{1 - \beta_i^2}{(1 - \beta_i \cos\theta)^2} + \frac{2(1 + \beta_i \beta_j)}{(1 - \beta_i \cos\theta)(1 + \beta_j \cos\theta)} - \frac{1 - \beta_j^2}{(1 + \beta_j \cos\theta)^2}, \tag{A.2.10}$$

where θ is some polar angle w.r.t. the dipole axis in the dipole rest frame. In this frame, the generation of the azimuthal is trivial - it just follows a flat distribution in $[0, 2\pi]$. The polar distribution above can be bound from above through the interference term. This allows to generate the true distribution by generating the angle according to the interference term and applying a hit-or-miss rejection. The interference term can be decomposed analogously to the general case above into two independent terms according to

$$\frac{1}{(1 - \beta_i \cos\theta)(1 + \beta_j \cos\theta)} = \frac{\beta_i \beta_j}{\beta_i + \beta_j} \left(\frac{1}{\beta_j (1 - \beta_i \cos\theta)} - \frac{1}{\beta_i (1 + \beta_j \cos\theta)} \right). \tag{A.2.11}$$

The cosine of the polar angle, $\cos\theta$, is then generated to either of the two terms, i.e. it is generated according to $(1 - \beta_i \cos\theta)^{-1}$ with probability

$$P_i = \frac{\ln \frac{1 + \beta_i}{1 - \beta_i}}{\ln \frac{1 + \beta_i}{1 - \beta_i} + \ln \frac{1 + \beta_j}{1 - \beta_j}} \tag{A.2.12}$$

and according to $(1 + \beta_j \cos\theta)^{-1}$ with probability $P_j = 1 - P_i$, selected through a random number. These angles can be generated by

$$\cos\theta = \frac{1}{\beta_i} \left[1 - (1 + \beta_i) \left(\frac{1 - \beta_i}{1 + \beta_i} \right)^{\mathcal{R}} \right] \tag{A.2.13}$$

in the former case and

$$\cos\theta = -\frac{1}{\beta_j} \left[1 - (1 - \beta_j) \left(\frac{1 + \beta_j}{1 - \beta_j} \right)^{\mathcal{R}} \right] \tag{A.2.14}$$

in the latter. $\mathcal{R}$ again is a uniformly distributed random number on $[0, 1]$. The correction weight for obtaining the full distribution reads

$$W = \frac{-\frac{1-\beta_i^2}{(1-\beta_i \cos\theta)^2} + \frac{2(1+\beta_i\beta_j)}{(1-\beta_i \cos\theta)(1+\beta_j \cos\theta)} - \frac{1-\beta_j^2}{(1+\beta_j \cos\theta)^2}}{\frac{2(1+\beta_i\beta_j)}{(1-\beta_i \cos\theta)(1+\beta_j \cos\theta)}} \le 1 \,. \tag{A.2.15}$$

The azimuthal angle φ is distributed uniformly.

A.2.4 Photons from multipoles

In a multipole configuration again the photons are generated according to $\tilde{S}_q(k)$. The integral over photon energies can still be separated from the angular integrations, decoupling the generation of the energy of a single photon as above. However, its angular distribution is very complex. But due to

$$\tilde{S}_q(k) = \sum_{i<j} \tilde{S}(q_i, q_j, k) \tag{A.2.16}$$

the photon angles are distributed according to

$$-\sum_{i<j} |Z_i Z_j \theta_i \theta_j| \left(\frac{q_i}{(q_i \cdot e_k)} - \frac{q_j}{(q_j \cdot e_k)} \right)^2 \,. \tag{A.2.17}$$

This is nothing but a sum of angular distributions of different dipoles which are not in their respective rest frame.

Subsequently, one of those constituent dipoles is chosen with the probability

$$P_{ij} = \frac{|\bar{n}_{ij}|}{\sum\limits_{i<j} |\bar{n}_{ij}|} = \frac{\left| \int \frac{\mathrm{d}^3 k}{k^0} \tilde{S}(q_i, q_j, k) \right|}{\sum\limits_{i<j} \left| \int \frac{\mathrm{d}^3 k}{k^0} \tilde{S}(q_i, q_j, k) \right|} \,. \tag{A.2.18}$$

Then, photon angle generation can proceed as above in the rest frame of the dipole. To obtain the right distribution in the rest frame of the overall multipole, a null-vector of unit length is created in the rest frame of the dipole using the newly generated angles φ ant θ. Then this null vector is boosted into the rest frame of the multipole. It now has the angular distribution according to its constituent dipole in this frame. Since it is a null vector it has the properties of a photon and only needs to be rescaled to the energy generated earlier.

A.3 Massive dipole splitting functions

The massive dipole splitting functions are needed for the calculation of the approximation to the infrared subtracted single hard photon emission matrix element $\tilde{\beta}_1^1$. They are taken directly from [94] for spin-$\frac{1}{2}$ emitters and are generalised from [52] for all other cases. Problems arising during this generalisation are related to the fact that these splitting functions for spin-1 particles are only given for massless gluons and that all initial states are considered massless as well. The extension to radiation off massive spin-1 particles is rather straight forward by augmentation with a simple mass term. The extension to massive initial states

is less clear since decay matrix element are far off the massless initial state limit. However, the decaying particle is always much more massive than its decay products when those are supposed to emit hard bremsstrahlung. Thus, photons are predominantly emitted at large angles to the initial state resulting in negligible contributions from these splitting functions. Hence, they can safely be omitted.

Also, velocity factors from [52] have been omitted. They were introduced to facilitate the analytic integration and change neither the infrared nor the quasi-collinear limit. They only result in a different interpolation inbetween. The same is true for the factor R_{ij} in the massive fermion splitting function of [94]. Nonetheless, here this factor is kept because of the direct applicability of these splitting functions to the completely massive splitting.

Three cases need to be differentiated regarding the state, initial or final, the emitter and spectator are in. The fourth case where both emitter and spectator are in the initial state lies outside the present applicability of this program, it will therefore be omitted.

To repeat the notation, p_i is the 4-momentum of the emitter, p_j that of the spectator and k is the emitted photon. All massive dipole splitting functions will be given, in that order, for spin-0, spin-$\frac{1}{2}$ and spin-1 emitters. Since there are no massive dipole splitting functions available for emitters of spin-$\frac{3}{2}$ or spin-2, their emissions have to be described by the soft limit only. Of course, it is always possible to implement exact process specific matrix elements.

A.3.1   Final State Emitter, Final State Spectator

In case of a final state emitter and a final state spectator the dipole splitting functions read

$$
\begin{aligned}
g_{ij}(p_i, p_j, k) &= g_{ij}^{(\text{soft})}(p_i, p_j, k) \\
&= \frac{1}{(p_i \cdot k) R_{ij}(y_{ij})} \left[\frac{2}{1 - z_{ij}(1 - y_{ij})} - 1 - z_{ij} - \frac{m_i^2}{(p_i \cdot k)} \right] \\
&= \frac{1}{(p_i \cdot k)} \left[\frac{2}{1 - z_{ij}(1 - y_{ij})} + \frac{2}{1 - z_{kj}(1 - y_{ij})} + 2 z_{ij} z_{kj} - 4 - \frac{m_i^2}{(p_i \cdot k)} \right]
\end{aligned}
\tag{A.3.1}
$$

with

$$
\begin{aligned}
y_{ij} &= \frac{p_i k}{p_i p_j + p_i k + p_j k} \\
z_{ij} &= \frac{p_i p_j}{p_i p_j + p_j k} \\
z_{kj} &= 1 - z_{ij} \\
v_{ik,j} &= \tfrac{1}{2} R_{ij}(y_{ij}) \frac{\sqrt{\lambda(P_{ij}^2, m_i^2, m_j^2)}}{(p_i + k) \cdot p_j}
\end{aligned}
\tag{A.3.2}
$$

and

$$
R_{ij}(x) = \frac{\sqrt{\left(2 m_j^2 + \bar{P}_{ij}^2 (1 - x)\right)^2 - 4 P_{ij}^2 m_j^2}}{\sqrt{\lambda(P_{ij}^2, m_i^2, m_j^2)}}
\tag{A.3.3}
$$

with

$$
\begin{aligned}
P_{ij} &= p_i + p_j + k \\
\bar{P}_{ij}^2 &= P_{ij}^2 - m_i^2 - m_j^2 = 2 \left(p_i p_j + p_i k + p_j k \right)
\end{aligned}
\tag{A.3.4}
$$

wherein the photon is massless, $\lambda(x, y, z) = x^2 + y^2 + z^2 - 2xy - 2xz - 2yz$ is the Kallen-function.

A.3.2 Final State Emitter, Initial State Spectator

In case of a final state emitter and an initial state spectator the dipole splitting functions read

$$
\begin{aligned}
g_{ij}(p_i, p_j, k) &= g_{ij}^{(\text{soft})}(p_i, p_j, k) \\
&= \frac{1}{(p_i \cdot k) x_{ij}} \left[\frac{2}{2 - x_{ij} - z_{ij}} - 1 - z_{ij} - \frac{m_i^2}{(p_i \cdot k)} \right] \\
&= \frac{1}{(p_i \cdot k) x_{ij}} \left[\frac{2}{2 - x_{ij} - z_{ij}} + \frac{2}{2 - x_{ij} - z_{kj}} + 2 z_{ij} z_{kj} - 4 - \frac{m_i^2}{(p_i \cdot k)} \right]
\end{aligned}
\tag{A.3.5}
$$

with

$$
\begin{aligned}
x_{ij} &= \frac{p_i p_j + p_j k - p_i k}{p_i p_j + p_j k} \\
z_{ij} &= \frac{p_i p_j}{p_i p_j + p_j k} \\
z_{kj} &= 1 - z_{ij}
\end{aligned}
\tag{A.3.6}
$$

A.3.3 Initial State Emitter, Final State Spectator

In the case of radiation off an initial state emitter some simplifications occur. Here, the emitting particle is always assumed to be much heavier than its decay products resulting in its contributions to the real emission corrections to be negligible. Thus,

$$
g_{ij}(p_i, p_j, k) = g_{ij}^{(\text{soft})}(p_i, p_j, k) \tag{A.3.7}
$$

is set irrespective of the emitter's spin.

Appendix B

Formfactors and higher order matrix elements for semileptonic B meson decays

B.1 Form factor models of exclusive semileptonic B meson decays

B.1.1 Form factors for $B \to D\,\ell\,\nu$

Parameter	Value
$\mathcal{G}(1)$	0.98
ρ_D^2	1.19

Table B.1: Parameter values used for the transition current $\langle D|V^\mu|B\rangle$ taken from Heavy Quark Effective Theory.

The vector current describing the semileptonic $B \to D\,\ell\,\nu$ decay is given by

$$\langle D|V^\mu|B\rangle = \sqrt{m_B m_D}\left(h_+(w)(v_B+v_D)^\mu + h_-(w)(v_B-v_D)^\mu\right)\,, \tag{B.1.1}$$

with the heavy quark form factors $h_\pm$ parametrised [266]

$$\begin{aligned}
h_+(w) &= \mathcal{G}(1) \times \left[1 - 8\rho_D^2\,z + (51\rho_D^2 - 10)\,z^2 - (252\rho_D^2 - 84)\,z^3)\right]\,, \\
h_-(w) &= 0\,.
\end{aligned} \tag{B.1.2}$$

It is $z = \frac{\sqrt{w+1}-\sqrt{2}}{\sqrt{w+1}+\sqrt{2}}$ with $w = \frac{m_B^2 + m_D^2 - t}{2m_B m_D}$, ρ_D^2 the form factor slope, and $\mathcal{G}(1)$ the normalisation at $w = 1$. The values used are given in Tab. B.1.

B.1.2 Form factors for $B \to \pi\,\ell\,\nu$

The vector current describing the semileptonic $B \to \pi\,\ell\,\nu$ decay is given by

$$\langle \pi|V^\mu|B\rangle = \left((p_B+p_\pi)^\mu - \frac{m_B^2 - m_\pi^2}{t}(p_B - p_\pi)^\mu\right)f_+(t) + \left(\frac{m_B^2 - m_\pi^2}{t}(p_B - p_\pi)^\mu\right)f_0(t)\,,$$

Parameter	Value		Parameter	Value
m^2_{f+1}	28.40 GeV^2		r_{f+1}	0.744
m^2_{f+2}	40.73 GeV^2		r_{f+2}	-0.486
$m^2_{f_0}$	33.81 GeV^2		r_{f_0}	0.258

Table B.2: Parameter values used for the transition current $\langle \pi | V^\mu | B \rangle$ taken from the pole parametrisation in [267].

$$\tag{B.1.3}$$

with form factors parametrised as [267]

$$f_+(t) = \frac{r_{f+1}}{1 - \frac{t}{m^2_{f+1}}} + \frac{r_{f+2}}{1 - \frac{t}{m^2_{f+2}}} \,,$$

$$f_0(t) = \frac{r_{f_0}}{1 - \frac{t}{m^2_{f_0}}} \,.$$

$$\tag{B.1.4}$$

r_{f+1}, r_{f+2}, and r_{f_0} are normalisations and m_{f+1}, m_{f+2}, and m_{f_0} pole masses. Their values are listed in Tab. B.2.

B.1.3   Form factors for $B \to D_0^* \ell \nu$

Parameter	Value		Parameter	Value
ϵ_c	0.3571 GeV^{-1}		$\bar{\Lambda}$	0.4 GeV
ϵ_b	0.1042 GeV^{-1}		$\bar{\Lambda}^*$	0.75 GeV
ζ'	-1.0		$\zeta(1)$	1.0

Table B.3: Parameter values used for the transition current $\langle D_0^* | A^\mu | B \rangle$ taken from the pole parametrisation in [268, 269].

The axial-vector current describing the semileptonic $B \to D_0^* \ell \nu$ decay is given by

$$\langle D_0^* | A^\mu | B \rangle = \sqrt{m_B m_{D_0^*}} \left(g_+(w)(v_B + v_{D_0^*})^\mu + g_-(w)(v_B - v_{D_0^*})^\mu \right) . \tag{B.1.5}$$

with the form factors $g_\pm$ parametrised as [268, 269]

$$g_+(w) = \epsilon_c \left[2(w-1)\zeta_1(w) - 3\zeta(w) \frac{w\bar{\Lambda}^* - \bar{\Lambda}}{w+1} \right]$$

$$- \epsilon_b \left[\frac{\bar{\Lambda}^*(2w+1) - \bar{\Lambda}(w+2)}{w+1} \zeta(w) - 2(w-1)\zeta_1(w) \right] ,$$

$$g_-(w) = \zeta(w) . \tag{B.1.6}$$

with

$$\zeta(w) = \zeta(1) \times [1 + \zeta'(w-1)] \,,$$

$$\zeta_1(w) = \bar{\Lambda} \zeta(w) . \tag{B.1.7}$$

where ζ' denotes the form factor slope. The parameters are defined as $\epsilon_c \equiv \frac{1}{2m_c}$, $\epsilon_b \equiv \frac{1}{2m_b}$, $\bar{\Lambda} \equiv m_D - m_c$, and $\bar{\Lambda}^* \equiv m_{D_0^*} - m_c$. Their values are listed in Tab. B.3. As can be seen from the hadronic current of eq. (B.1.5) the role of vector and axial-vector terms are reversed in decays to scalars as opposed to decays to pseudo-scalars. Thus, in the discussion of IB and SD terms the role of $V_{\mu\nu}$ and $A_{\mu\nu}$ are reversed. In particular, $V_{\mu\nu}^{\text{IB}} = 0$ and $A_{\mu\nu}^{\text{IB}} \neq 0$.

B.2   NLO matrix elements

In the following, the real emission and virtual one-loop correction matrix elements which serve as primary ingredient to the calculation of the electroweak next-to-leading order corrections to semileptonic B meson corrections.

B.2.1   Real emission matrix elements

This appendix presents details on the real emission matrix elements with special focus on the inner bremsstrahlungs (IB) vertex emission terms. The summed real emission matrix element of the Feynman graphs a to c in Figure 5.3 for $B^+ \to \bar{X}^0 \, \ell^+ \, \nu_\ell \, \gamma$ is

$$
\begin{aligned}
\mathcal{M}_1^{\frac{1}{2}} =& \, i \, e \, \frac{G_{\text{F}}}{\sqrt{2}} V_{\text{xb}} \, H_\mu(p_B, p_X; t) \ \bar{u}_\nu \, P_{\text{R}} \gamma^\mu \, \frac{p_\ell \cdot \epsilon^* + \frac{1}{2} \slashed{k} \slashed{\epsilon}^*}{p_\ell \cdot k} \, v_\ell \\
&- i \, e \, \frac{G_{\text{F}}}{\sqrt{2}} V_{\text{xb}} \, \frac{p_B \cdot \epsilon^*}{p_B \cdot k} \, H_\mu(p_B - k, p_X; t') \ \bar{u}_\nu \, P_{\text{R}} \gamma^\mu \, v_\ell \\
&+ \mathcal{M}_{1,\text{vertex emission}}^{\frac{1}{2}} \, .
\end{aligned}
\tag{B.2.1}
$$

Similarly, the summed matrix element of the Feynman graphs a to c in Fig. 5.4 for $B^0 \to \bar{X}^- \, \ell^+ \, \nu_\ell \, \gamma$ is

$$
\begin{aligned}
\mathcal{M}_1^{\frac{1}{2}} =& \, i \, e \, \frac{G_{\text{F}}}{\sqrt{2}} V_{\text{xb}} \, H_\mu(p_B, p_X; t) \ \bar{u}_\nu \, P_{\text{R}} \gamma^\mu \, \frac{p_\ell \cdot \epsilon^* + \frac{1}{2} \slashed{k} \slashed{\epsilon}^*}{p_\ell \cdot k} \, v_\ell \\
&- i \, e \, \frac{G_{\text{F}}}{\sqrt{2}} V_{\text{xb}} \, \frac{p_X \cdot \epsilon^*}{p_X \cdot k} \, H_\mu(p_B, p_X + k; t') \ \bar{u}_\nu \, P_{\text{R}} \gamma^\mu \, v_\ell \\
&+ \mathcal{M}_{1,\text{vertex emission}}^{\frac{1}{2}} \, .
\end{aligned}
\tag{B.2.2}
$$

The real emission changes the definition of the four momentum transfer squared, depending on the emission leg:

$$
t \, = \, \left(p_B - p_X\right)^2 \, = \, \left(p_\ell + p_\nu + k\right)^2 , \qquad t' \, = \, \left(p_B - p_X - k\right)^2 \, = \, \left(p_\ell + p_\nu\right)^2 , \tag{B.2.3}
$$

and it is

$$
H_\mu(p_1, p_2; t) \, = \, \left(p_1 + p_2\right)_\mu \text{f}_+(t) + \left(p_1 - p_2\right)_\mu \text{f}_-(t) , \tag{B.2.4}
$$

as defined in eq. (5.1.3). The emission terms off the external mesons and leptons in eqs. (B.2.1) and (B.2.2) are, however, not gauge invariant by themselves. The vertex emission terms are thus needed to restore gauge invariance. Assuming $t = t'$, $\text{f}_\pm(t) = \text{f}_\pm(t')$, the

vertex emission terms of the constant-form-factor QED invariant Lagrangian of eq. (5.2.8) are recovered:

$$\mathcal{M}^{\frac{1}{2}}_{1,\text{vertex emission}} = -i e \frac{G_F}{\sqrt{2}} V_{xb} \left(f_+(t) + f_-(t) \right) \ \bar{u}_\nu P_R \not{\epsilon}^* v_\ell \qquad (B^+ \to \bar{X}^0 \ell^+ \nu_\ell)$$

$$\mathcal{M}^{\frac{1}{2}}_{1,\text{vertex emission}} = +i e \frac{G_F}{\sqrt{2}} V_{xb} \left(f_+(t) - f_-(t) \right) \ \bar{u}_\nu P_R \not{\epsilon}^* v_\ell \qquad (B^0 \to \bar{X}^- \ell^+ \nu_\ell) .$$

(B.2.5)

This is a reasonable approximation for heavy meson processes. Here, hard photons are emitted predominantly collinear to the charged lepton. Light meson processes, however, also radiate a considerable fraction of their hard radiation in the direction of the light meson and, hence, give rise to non-negligible corrections for $t \neq t'$. There are two ways to obtain these corrections.

A: Supposing the form factors $f_\pm$ can be expanded around t, the hadronic current reads

$$H_\mu(t') = H_\mu(t) + k' \frac{dH_\mu}{dt} \Big|_{k=0} + k'^2 \frac{1}{2} \frac{d^2 H_\mu}{dt'^2} \Big|_{k=0} + \mathcal{O}(k^3) ,$$

(B.2.6)

with $t' = t + k'$ and $k' = -2k \cdot (p_B - p_X)$. Introducing eq. (B.2.6) into eqs. (B.2.1) and (B.2.2) and employing Ward's identity [270] to obtain the gauge restoring terms, results in

$$\mathcal{M}^{\frac{1}{2}, \, B^+ \to \bar{X}^0 \ell^+ \nu_\ell}_{1,\text{vertex emission}}$$
$$= i e \frac{G_F}{\sqrt{2}} V_{xb} \ \bar{u}_\nu P_R \gamma^\mu v_\ell \left(\frac{p_B \cdot \epsilon^*}{p_B \cdot k} k_\alpha - \epsilon^*_\alpha \right) \left(\delta^\alpha_{\ \mu} \left(f_+(t) + f_-(t) \right) - 2 (p_B - p_X)^\alpha \frac{dH_\mu}{dt'} \Big|_{k=0} \right)$$
$$+ \mathcal{O}(k^2) ,$$

(B.2.7)

and

$$\mathcal{M}^{\frac{1}{2}, \, B^0 \to \bar{X}^- \ell^+ \nu_\ell}_{1,\text{vertex emission}}$$
$$= -i e \frac{G_F}{\sqrt{2}} V_{xb} \bar{u}_\nu P_R \gamma^\mu v_\ell \left(\frac{p_X \cdot \epsilon^*}{p_X \cdot k} k_\alpha - \epsilon^*_\alpha \right) \left(\delta^\alpha_{\ \mu} \left(f_+(t) - f_-(t) \right) - 2 (p_B - p_X)^\alpha \frac{dH_\mu}{dt'} \Big|_{k=0} \right)$$
$$+ \mathcal{O}(k^2) ,$$

(B.2.8)

respectively. Neglecting higher order terms in the expansion of eq. (B.2.6) results in Low's matrix element [106] for these processes. This approach, by implying the existence of a Taylor-series representation of the form factors $f_\pm(t)$, yields a consistent result both for the interaction terms of the phenomenological Lagrangian and the Feynman rules. However, the exact functional form of the form factors has to be known. Further, by including higher order corrections in k structure dependent contributions to the matrix element are introduced: the isolated terms that restore gauge invariance are not unique, and undesired ambiguities are apparent. The impact of such terms were studied for K_{l3} decays in [271, 125], finding negligible impact on the next-to-leading order decay rate. This result however can't be extrapolated to B meson decays, due to the wide range of possible excited intermediate states.

B: A result independent of the functional form of the form factors, and thus not relying on their differentiability, can be derived similarly. Instead of their argument, the form factors themselves are decomposed

$$f_\pm(t') = f_\pm(t) + Z_\pm(t, t') .$$

(B.2.9)

Now, the missing terms for achieving gauge invariance of the real emission amplitude are determined as

$$
\mathcal{M}^{\frac{1}{2},\, B^+ \to \bar{X}^0 \ell^+ \nu_\ell}_{1,\text{vertex emission}}
$$
$$
= \; i\, e\, \frac{G_\text{F}}{\sqrt{2}} V_\text{xb}\; \bar{u}_\nu\, P_\text{R} \gamma^\mu v_\ell \; \Big(- \left(\text{f}_+(t') + \text{f}_-(t') \right) \epsilon^*_\mu
$$
$$
+ (p_B + p_X)_\mu\, \epsilon^{*\cdot} Z_+(t,t') + (p_B - p_X)_\mu\, \epsilon^{*\cdot} Z_-(t,t') \Big) \tag{B.2.10}
$$

and

$$
\mathcal{M}^{\frac{1}{2},\, B^0 \to \bar{X}^+ \ell^- \nu_\ell}_{1,\text{vertex emission}}
$$
$$
= \; i\, e\, \frac{G_\text{F}}{\sqrt{2}} V_\text{xb}\; \bar{u}_\nu\, P_\text{R} \gamma^\mu v_\ell \; \Big(\left(\text{f}_+(t') - \text{f}_-(t') \right) \epsilon^*_\mu
$$
$$
+ (p_B + p_X)_\mu\, \epsilon^{*\cdot} Z_+(t,t') + (p_B - p_X)_\mu\, \epsilon^{*\cdot} Z_-(t,t') \Big) \tag{B.2.11}
$$

respectively. $Z_\pm(t,t') = \frac{k \cdot n}{k \cdot n} Z_\pm(t,t') = k_\alpha \frac{n^\alpha}{k \cdot n} \left(\text{f}_\pm(t') - \text{f}_\pm(t) \right) \equiv k_\alpha Z^\alpha_\pm(t,t')$, $k \cdot n \neq 0$. Through the definition of n, however, again ambiguities are introduced into this generic result which, again, are assumed to be negligible in this paper. Further, because these ambiguities satisfy $k_\alpha \delta Z^\alpha_\pm(t,t') = 0$, they can be considered part of $V^\text{SD}_{\mu\nu}$. Thus, the (minimal) emission terms constructed this way constitute the inner-bremsstrahlungs part of the non-local emission term $V^\text{IB}_{\mu\nu}$ of Section 5.2.4.

B.2.2 Virtual emission matrix elements

The section lists the corresponding virtual emission matrix elements. They are calculated in $D = 4 - 2\epsilon$ dimensions and are UV regularised using the Pauli-Villars prescription [117] of introducing an unphysical heavy photon of mass Λ, the matching scale to the short distance result. Thus, the infrared subtracted squared matrix elements (using the definitions of eqs. (2.1.1), (2.3.3), (5.2.9) and (5.2.21)) and ultraviolety regulated are defined via

$$
\tilde{\beta}^1_0(\Lambda) = 2\mathcal{R}e \left(M^0_0 \cdot M^{1*}_0(\Lambda) \right) . \tag{B.2.12}
$$

They are evaluated under the additional assumption

$$
\int \text{d}^D k\, \frac{\text{f}_\pm(t(k))\; k^{\mu_1} \cdots k^{\mu_1}}{k^2\, d_1 \ldots d_N} \; \approx \; \text{f}_\pm(t) \int \text{d}^D k\, \frac{k^{\mu_1} \cdots k^{\mu_1}}{k^2\, d_1 \ldots d_N} , \tag{B.2.13}
$$

introduced to render the calculation feasible.

Decays $B^0 \to X^- \ell^+ \nu_\ell$

The infrared subtracted one-loop matrix elements $M_0^1(\Lambda)$ for this process can be decomposed as

$$
\begin{aligned}
M_0^1(\Lambda) &= \mathcal{M}_0^1(\Lambda) - \alpha B \\
&= \frac{G_\mathrm{F}}{\sqrt{2}} V_\mathrm{xb} \frac{\alpha}{2\pi} \bigg\{ \bar{u}_\nu \, P_\mathrm{R} \left(\mathrm{f}_+(t)(\not{p}_B + \not{p}_X) + \mathrm{f}_-(t)(\not{p}_B - \not{p}_X) \right) v_\ell \\
&\qquad \times \left[\mathcal{M}_{0,X\ell}^{1,1}(\Lambda) + \mathcal{M}_{0,VX}^1(\Lambda) + \mathcal{M}_{0,V\ell}^1(\Lambda) + L(\Lambda) \right. \\
&\qquad\qquad \left. + \tfrac{1}{2}\delta_{Z,X}(\Lambda) + \tfrac{1}{2}\delta_{Z,\ell}(\Lambda) - 2\pi B \right] \\
&\qquad + \bar{u}_\nu \, P_\mathrm{R} \, \not{p}_X v_\ell \; \left[\mathrm{f}_+ \mathcal{M}_{0,X\ell}^{1,2+}(\Lambda) + \mathrm{f}_- \mathcal{M}_{0,X\ell}^{1,2-}(\Lambda) \right] \\
&\qquad + \bar{u}_\nu \, P_\mathrm{R} \, v_\ell \; m_\ell \left[\mathrm{f}_+ \mathcal{M}_{0,X\ell}^{1,3+}(\Lambda) + \mathrm{f}_- \mathcal{M}_{0,X\ell}^{1,3-}(\Lambda) \right] \bigg\} .
\end{aligned}
\tag{B.2.14}
$$

Therein, the $\mathcal{M}_{0,X\ell}^1$ correspond to the terms, decomposed into their Dirac structure, containing a virtual photon linking the final state meson and the charged lepton. Similarly, the $\mathcal{M}_{0,VX}^1$ and $\mathcal{M}_{0,V\ell}^1$ correspond to the terms containing a photon loop from the vertex to the final state meson and the charged lepton, respectively. $\delta_{Z,X}$ and $\delta_{Z,X}$ are the wave-function corrections. These terms exhibit ultraviolet divergences and, thus, include the regulating terms from Pauli-Villars heavy photon diagrams. Finally, αB is the YFS approximation in the infrared limit. It needs to be subtracted here in order to be exponentiated, cf. Section 5.2.5. L is the Sirlin logarithm of the short-distance picture, containing the renormalisation, cf. Section 5.2.2.

The precise forms of these terms are listed in the following.

$$
\begin{aligned}
\delta_{Z,X}(\Lambda) &= 2 \left(B_1(m_X^2; 0, m_X^2) - B_1(m_X^2; \Lambda^2, m_X^2) \right) \\
&\quad + 4 \left(B_0(m_X^2; 0, m_X^2) - B_0(m_X^2; \Lambda^2, m_X^2) \right) \\
&\quad - 4m_X^2 \left(C_0(m_X^2, 0, m_X^2; 0, m_X^2, m_X^2) - C_0(m_X^2, 0, m_X^2; \Lambda^2, m_X^2, m_X^2) \right) \\
&\quad - 8m_X^2 \left(C_{10}(m_X^2, 0, m_X^2; 0, m_X^2, m_X^2) - C_{10}(m_X^2, 0, m_X^2; \Lambda^2, m_X^2, m_X^2) \right) \\
&\quad - 4m_X^2 \left(C_{20}(m_X^2, 0, m_X^2; 0, m_X^2, m_X^2) - C_{20}(m_X^2, 0, m_X^2; \Lambda^2, m_X^2, m_X^2) \right) \\
&\quad - 4 \left(C_{24}(m_X^2, 0, m_X^2; 0, m_X^2, m_X^2) - C_{24}(m_X^2, 0, m_X^2; \Lambda^2, m_X^2, m_X^2) \right) \\
&\quad + \Lambda^2 \left(C_0(m_X^2, 0, m_X^2; \Lambda^2, m_X^2, m_X^2) + C_{10}(m_X^2, 0, m_X^2; 0, m_X^2, m_X^2) \right)
\end{aligned}
\tag{B.2.15}
$$

$$
\begin{aligned}
\delta_{Z,\ell}(\Lambda) &= (D-2) \left(B_0(m_\ell^2; 0, m_\ell^2) - B_0(m_\ell^2; \Lambda^2, m_\ell^2) \right) \\
&\quad + 4m_\ell^2 \left(C_0(m_\ell^2, 0, m_\ell^2; 0, m_\ell^2, m_\ell^2) - C_0(m_\ell^2, 0, m_\ell^2; \Lambda^2, m_\ell^2, m_\ell^2) \right) \\
&\quad - 2(D-4)m_\ell^2 \left(C_{10}(m_\ell^2, 0, m_\ell^2; 0, m_\ell^2, m_\ell^2) - C_{10}(m_\ell^2, 0, m_\ell^2; \Lambda^2, m_\ell^2, m_\ell^2) \right) \\
&\quad - 2(D-2)m_\ell^2 \left(C_{20}(m_\ell^2, 0, m_\ell^2; 0, m_\ell^2, m_\ell^2) - C_{20}(m_\ell^2, 0, m_\ell^2; \Lambda^2, m_\ell^2, m_\ell^2) \right) \\
&\quad - 2(D-2) \left(C_{24}(m_\ell^2, 0, m_\ell^2; 0, m_\ell^2, m_\ell^2) - C_{24}(m_\ell^2, 0, m_\ell^2; \Lambda^2, m_\ell^2, m_\ell^2) \right)
\end{aligned}
\tag{B.2.16}
$$

$$
\begin{aligned}
\mathcal{M}_{0,VX}^1(\Lambda) &= 2 \left(B_0(m_X^2; 0, m_X^2) - B_0(m_X^2; \Lambda^2, m_X^2) \right) \\
&\quad + \left(B_1(m_X^2; 0, m_X^2) - B_1(m_X^2; \Lambda^2, m_X^2) \right)
\end{aligned}
\tag{B.2.17}
$$

$$\mathcal{M}_{0,V\ell}^{1}(\Lambda) = 2\left(B_0(m_\ell^2;0,m_\ell^2) - B_0(m_\ell^2;\Lambda^2,m_\ell^2)\right)$$
$$- (D-2)\left(B_1(m_\ell^2;0,m_\ell^2) - B_1(m_\ell^2;\Lambda^2,m_\ell^2)\right) \tag{B.2.18}$$

$$2\pi\, B = -4(p_X \cdot p_\ell)\, C_0(m_X^2, s_{X\ell}, m_\ell^2; 0, m_X^2, m_\ell^2)$$
$$- 2m_X^2\, C_0(m_X^2, 0, m_X^2; 0, m_X^2, m_X^2)$$
$$- 2m_\ell^2\, C_0(m_\ell^2, 0, m_\ell^2; 0, m_\ell^2, m_\ell^2)$$
$$- B_0(s_{X\ell}; m_X^2, m_\ell^2) \tag{B.2.19}$$
$$+ \tfrac{1}{2} B_0(0; m_X^2, m_X^2)$$
$$+ \tfrac{1}{2} B_0(0; m_\ell^2, m_\ell^2)$$

$$L(\Lambda) = \ln\frac{m_W^2}{\Lambda^2} \tag{B.2.20}$$

$$\mathcal{M}_{0,X\ell,1}^{1}(\Lambda) = 2(m_X^2 - p_X \cdot p_\ell)\left(C_{11}(m_X^2, s_{X\ell}, m_\ell^2; 0, m_X^2, m_\ell^2)\right.$$
$$\left. - C_{11}(m_X^2, s_{X\ell}, m_\ell^2; \Lambda^2, m_X^2, m_\ell^2)\right)$$
$$+ 2(m_\ell^2 - 2p_X \cdot p_\ell)\left(C_{12}(m_X^2, s_{X\ell}, m_\ell^2; 0, m_X^2, m_\ell^2)\right.$$
$$\left. - C_{12}(m_X^2, s_{X\ell}, m_\ell^2; \Lambda^2, m_X^2, m_\ell^2)\right)$$
$$- 4(p_X \cdot p_\ell)\left(C_0(m_X^2, s_{X\ell}, m_\ell^2; 0, m_X^2, m_\ell^2) - C_0(m_X^2, s_{X\ell}, m_\ell^2; \Lambda^2, m_X^2, m_\ell^2)\right)$$
$$- \Lambda^2\, C_0(m_X^2, s_{X\ell}, m_\ell^2; \Lambda^2, m_X^2, m_\ell^2) \tag{B.2.21}$$

$$\mathcal{M}_{0,X\ell}^{1;2+}(\Lambda) = -4(p_X \cdot p_\ell)\left(C_{11}(m_X^2, s_{X\ell}, m_\ell^2; 0, m_X^2, m_\ell^2) - C_{11}(m_X^2, s_{X\ell}, m_\ell^2; \Lambda^2, m_X^2, m_\ell^2)\right)$$
$$- 2m_\ell^2\left(C_{12}(m_X^2, s_{X\ell}, m_\ell^2; 0, m_X^2, m_\ell^2) - C_{12}(m_X^2, s_{X\ell}, m_\ell^2; \Lambda^2, m_X^2, m_\ell^2)\right)$$
$$- 2(p_X \cdot p_\ell)\left(C_{21}(m_X^2, s_{X\ell}, m_\ell^2; 0, m_X^2, m_\ell^2) - C_{21}(m_X^2, s_{X\ell}, m_\ell^2; \Lambda^2, m_X^2, m_\ell^2)\right)$$
$$+ 2m_\ell^2\left(C_{23}(m_X^2, s_{X\ell}, m_\ell^2; 0, m_X^2, m_\ell^2) - C_{23}(m_X^2, s_{X\ell}, m_\ell^2; \Lambda^2, m_X^2, m_\ell^2)\right)$$
$$- \Lambda^2\, C_{11}(m_X^2, s_{X\ell}, m_\ell^2; \Lambda^2, m_X^2, m_\ell^2)$$
$$- 2\Lambda^2\, C_0(m_X^2, s_{X\ell}, m_\ell^2; \Lambda^2, m_X^2, m_\ell^2) \tag{B.2.22}$$

$$\mathcal{M}_{0,X\ell}^{1;2-}(\Lambda) = 4(p_X \cdot p_\ell)\left(C_{11}(m_X^2, s_{X\ell}, m_\ell^2; 0, m_X^2, m_\ell^2) - C_{11}(m_X^2, s_{X\ell}, m_\ell^2; \Lambda^2, m_X^2, m_\ell^2)\right)$$
$$- 2m_\ell^2\left(C_{12}(m_X^2, s_{X\ell}, m_\ell^2; 0, m_X^2, m_\ell^2) - C_{12}(m_X^2, s_{X\ell}, m_\ell^2; \Lambda^2, m_X^2, m_\ell^2)\right)$$
$$+ 2(p_X \cdot p_\ell)\left(C_{21}(m_X^2, s_{X\ell}, m_\ell^2; 0, m_X^2, m_\ell^2) - C_{21}(m_X^2, s_{X\ell}, m_\ell^2; \Lambda^2, m_X^2, m_\ell^2)\right)$$
$$- 2m_\ell^2\left(C_{23}(m_X^2, s_{X\ell}, m_\ell^2; 0, m_X^2, m_\ell^2) - C_{23}(m_X^2, s_{X\ell}, m_\ell^2; \Lambda^2, m_X^2, m_\ell^2)\right)$$
$$+ \Lambda^2\, C_{11}(m_X^2, s_{X\ell}, m_\ell^2; \Lambda^2, m_X^2, m_\ell^2)$$
$$+ 2\Lambda^2\, C_0(m_X^2, s_{X\ell}, m_\ell^2; \Lambda^2, m_X^2, m_\ell^2)$$

$$\text{(B.2.23)}$$

$$
\begin{aligned}
\mathcal{M}^{1,3+}_{0,X\ell}(\Lambda) = & -4(m_X^2 + 2p_X \cdot p_\ell)\left(C_{12}(m_X^2, s_{X\ell}, m_\ell^2; 0, m_X^2, m_\ell^2)\right. \\
& \left. \qquad\qquad\qquad - C_{12}(m_X^2, s_{X\ell}, m_\ell^2; \Lambda^2, m_X^2, m_\ell^2)\right) \\
& + 2m_\ell^2\left(C_{22}(m_X^2, s_{X\ell}, m_\ell^2; 0, m_X^2, m_\ell^2) - C_{22}(m_X^2, s_{X\ell}, m_\ell^2; \Lambda^2, m_X^2, m_\ell^2)\right) \\
& - 2(p_X \cdot p_\ell)\left(C_{23}(m_X^2, s_{X\ell}, m_\ell^2; 0, m_X^2, m_\ell^2) - C_{23}(m_X^2, s_{X\ell}, m_\ell^2; \Lambda^2, m_X^2, m_\ell^2)\right) \\
& + 2\left(C_{24}(m_X^2, s_{X\ell}, m_\ell^2; 0, m_X^2, m_\ell^2) - C_{24}(m_X^2, s_{X\ell}, m_\ell^2; \Lambda^2, m_X^2, m_\ell^2)\right) \\
& - \Lambda^2\, C_{12}(m_X^2\, s_{X\ell}, m_\ell^2; 0, m_X^2, m_\ell^2)
\end{aligned}
$$

$$\text{(B.2.24)}$$

$$
\begin{aligned}
\mathcal{M}^{1,3-}_{0,X\ell}(\Lambda) = & -2m_\ell^2\left(C_{22}(m_X^2, s_{X\ell}, m_\ell^2; 0, m_X^2, m_\ell^2) - C_{22}(m_X^2, s_{X\ell}, m_\ell^2; \Lambda^2, m_X^2, m_\ell^2)\right) \\
& + 2(p_X \cdot p_\ell)\left(C_{23}(m_X^2, s_{X\ell}, m_\ell^2; 0, m_X^2, m_\ell^2) - C_{23}(m_X^2, s_{X\ell}, m_\ell^2; \Lambda^2, m_X^2, m_\ell^2)\right) \\
& - 2\left(C_{24}(m_X^2, s_{X\ell}, m_\ell^2; 0, m_X^2, m_\ell^2) - C_{24}(m_X^2, s_{X\ell}, m_\ell^2; \Lambda^2, m_X^2, m_\ell^2)\right) \\
& + \Lambda^2\, C_{12}(m_X^2\, s_{X\ell}, m_\ell^2; 0, m_X^2, m_\ell^2)
\end{aligned}
$$

$$\text{(B.2.25)}$$

Decays $B^+ \to X^0\,\ell^+\,\nu_\ell$

In these types of decays, the infrared subtracted one-loop matrix element can be decomposed similarly to eq. (B.2.14). It reads

$$
\begin{aligned}
M_0^1(\Lambda) = & \ \mathcal{M}_0^1(\Lambda) - \alpha B \\
= & \ \frac{G_F}{\sqrt{2}} V_{xb} \frac{\alpha}{2\pi}\left\{ \bar{u}_\nu\, P_R\left(\mathrm{f}_+(t)(\not{p}_B + \not{p}_X) + \mathrm{f}_-(t)(\not{p}_B - \not{p}_X)\right)v_\ell \right. \\
& \qquad\qquad \times \left[\mathcal{M}^{1,1}_{0,B\ell}(\Lambda) + \mathcal{M}^1_{0,VB}(\Lambda) + \mathcal{M}^1_{0,V\ell}(\Lambda) + L(\Lambda)\right. \\
& \qquad\qquad\qquad \left. + \tfrac{1}{2}\delta_{Z,B}(\Lambda) + \tfrac{1}{2}\delta_{Z,\ell}(\Lambda) - 2\pi\, B\right] \\
& \qquad + \bar{u}_\nu\, P_R\, \not{p}_B v_\ell\ \left[\mathrm{f}_+\, \mathcal{M}^{1,2+}_{0,B\ell}(\Lambda) + \mathrm{f}_-\, \mathcal{M}^{1,2-}_{0,B\ell}(\Lambda)\right] \\
& \qquad \left. + \bar{u}_\nu\, P_R\, v_\ell\ m_\ell\left[\mathrm{f}_+\, \mathcal{M}^{1,3+}_{0,B\ell}(\Lambda) + \mathrm{f}_-\, \mathcal{M}^{1,3-}_{0,B\ell}(\Lambda)\right]\right\}.
\end{aligned}
$$

$$\text{(B.2.26)}$$

The decomposition terms take the same meaning as before. Of course, the wave-function corrections are identical to the ones in the case of $\bar{B}^0 \to X^-\,\ell^+\,\nu_\ell$ decays with the replacement $m_X \to m_B$ in $\delta_{Z,B}$. Similarly, also the short distance term $L(\Lambda)$ remains unchanged. Also, $\mathcal{M}^1_{0,VB}$ and $\mathcal{M}^1_{0,V\ell}$ take the same form as in the previous Subsection, with the replacement $m_X \to m_B$. The remaining terms now read

$$
\begin{aligned}
2\pi\, B = & \ +4(p_B \cdot p_\ell)\, C_0(m_B^2, s_{B\ell}, m_\ell^2; 0, m_B^2, m_\ell^2) \\
& - 2m_B^2\, C_0(m_B^2, 0, m_B^2; 0, m_B^2, m_B^2) \\
& - 2m_\ell^2\, C_0(m_\ell^2, 0, m_\ell^2; 0, m_\ell^2, m_\ell^2) \\
& - B_0(s_{B\ell}; m_B^2, m_\ell^2) \\
& + \tfrac{1}{2}\, B_0(0; m_B^2, m_B^2) \\
& + \tfrac{1}{2}\, B_0(0; m_\ell^2, m_\ell^2)
\end{aligned}
$$

$$\text{(B.2.27)}$$

$$
\begin{aligned}
\mathcal{M}^1_{0,B\ell,1}(\Lambda) = {} & 2(m_B^2 + p_B \cdot p_\ell) \left(C_{11}(m_B^2, s_{B\ell}, m_\ell^2; 0, m_B^2, m_\ell^2) \right. \\
& \left. - C_{11}(m_B^2, s_{B\ell}, m_\ell^2; \Lambda^2, m_B^2, m_\ell^2) \right) \\
& + 2(m_\ell^2 + 2p_B \cdot p_\ell) \left(C_{12}(m_B^2, s_{B\ell}, m_\ell^2; 0, m_B^2, m_\ell^2) \right. \\
& \left. - C_{12}(m_B^2, s_{B\ell}, m_\ell^2; \Lambda^2, m_B^2, m_\ell^2) \right) \\
& + 4(p_B \cdot p_\ell) \left(C_0(m_B^2, s_{B\ell}, m_\ell^2; 0, m_B^2, m_\ell^2) - C_0(m_B^2, s_{B\ell}, m_\ell^2; \Lambda^2, m_B^2, m_\ell^2) \right) \\
& - \Lambda^2 \, C_0(m_B^2, s_{B\ell}, m_\ell^2; \Lambda^2, m_B^2, m_\ell^2)
\end{aligned}
$$

$$(\text{B.2.28})$$

$$
\begin{aligned}
\mathcal{M}^{1,2+}_{0,B\ell}(\Lambda) = {} & 4(p_B \cdot p_\ell) \left(C_{11}(m_B^2, s_{B\ell}, m_\ell^2; 0, m_B^2, m_\ell^2) - C_{11}(m_B^2, s_{B\ell}, m_\ell^2; \Lambda^2, m_B^2, m_\ell^2) \right) \\
& - 2m_\ell^2 \left(C_{12}(m_B^2, s_{B\ell}, m_\ell^2; 0, m_B^2, m_\ell^2) - C_{12}(m_B^2, s_{B\ell}, m_\ell^2; \Lambda^2, m_B^2, m_\ell^2) \right) \\
& + 2(p_B \cdot p_\ell) \left(C_{21}(m_B^2, s_{B\ell}, m_\ell^2; 0, m_B^2, m_\ell^2) - C_{21}(m_B^2, s_{B\ell}, m_\ell^2; \Lambda^2, m_B^2, m_\ell^2) \right) \\
& + 2m_\ell^2 \left(C_{23}(m_B^2, s_{B\ell}, m_\ell^2; 0, m_B^2, m_\ell^2) - C_{23}(m_B^2, s_{B\ell}, m_\ell^2; \Lambda^2, m_B^2, m_\ell^2) \right) \\
& - \Lambda^2 \, C_{11}(m_B^2, s_{B\ell}, m_\ell^2; \Lambda^2, m_B^2, m_\ell^2) \\
& - 2\Lambda^2 \, C_0(m_B^2, s_{B\ell}, m_\ell^2; \Lambda^2, m_B^2, m_\ell^2)
\end{aligned}
$$

$$(\text{B.2.29})$$

$$
\begin{aligned}
\mathcal{M}^{1,2-}_{0,B\ell}(\Lambda) = {} & 4(p_B \cdot p_\ell) \left(C_{11}(m_B^2, s_{B\ell}, m_\ell^2; 0, m_B^2, m_\ell^2) - C_{11}(m_B^2, s_{B\ell}, m_\ell^2; \Lambda^2, m_B^2, m_\ell^2) \right) \\
& + 2m_\ell^2 \left(C_{12}(m_B^2, s_{B\ell}, m_\ell^2; 0, m_B^2, m_\ell^2) - C_{12}(m_B^2, s_{B\ell}, m_\ell^2; \Lambda^2, m_B^2, m_\ell^2) \right) \\
& + 2(p_B \cdot p_\ell) \left(C_{21}(m_B^2, s_{B\ell}, m_\ell^2; 0, m_B^2, m_\ell^2) - C_{21}(m_B^2, s_{B\ell}, m_\ell^2; \Lambda^2, m_B^2, m_\ell^2) \right) \\
& + 2m_\ell^2 \left(C_{23}(m_B^2, s_{B\ell}, m_\ell^2; 0, m_B^2, m_\ell^2) - C_{23}(m_B^2, s_{B\ell}, m_\ell^2; \Lambda^2, m_B^2, m_\ell^2) \right) \\
& - \Lambda^2 \, C_{11}(m_B^2, s_{B\ell}, m_\ell^2; \Lambda^2, m_B^2, m_\ell^2) \\
& - 2\Lambda^2 \, C_0(m_B^2, s_{B\ell}, m_\ell^2; \Lambda^2, m_B^2, m_\ell^2)
\end{aligned}
$$

$$(\text{B.2.30})$$

$$
\begin{aligned}
\mathcal{M}^{1,3+}_{0,B\ell}(\Lambda) = {} & 4(m_B^2 + 2p_B \cdot p_\ell) \left(C_{12}(m_B^2, s_{B\ell}, m_\ell^2; 0, m_B^2, m_\ell^2) \right. \\
& \left. - C_{12}(m_B^2, s_{B\ell}, m_\ell^2; \Lambda^2, m_B^2, m_\ell^2) \right) \\
& - 2m_\ell^2 \left(C_{22}(m_B^2, s_{B\ell}, m_\ell^2; 0, m_B^2, m_\ell^2) - C_{22}(m_B^2, s_{B\ell}, m_\ell^2; \Lambda^2, m_B^2, m_\ell^2) \right) \\
& - 2(p_B \cdot p_\ell) \left(C_{23}(m_B^2, s_{B\ell}, m_\ell^2; 0, m_B^2, m_\ell^2) - C_{23}(m_B^2, s_{B\ell}, m_\ell^2; \Lambda^2, m_B^2, m_\ell^2) \right) \\
& - 2 \left(C_{24}(m_B^2, s_{B\ell}, m_\ell^2; 0, m_B^2, m_\ell^2) - C_{24}(m_B^2, s_{B\ell}, m_\ell^2; \Lambda^2, m_B^2, m_\ell^2) \right) \\
& + \Lambda^2 \, C_{12}(m_B^2 \, s_{B\ell}, m_\ell^2; 0, m_B^2, m_\ell^2)
\end{aligned}
$$

$$(\text{B.2.31})$$

$$
\begin{aligned}
\mathcal{M}^{1,3-}_{0,B\ell}(\Lambda) = {} & - 2m_\ell^2 \left(C_{22}(m_B^2, s_{B\ell}, m_\ell^2; 0, m_B^2, m_\ell^2) - C_{22}(m_B^2, s_{B\ell}, m_\ell^2; \Lambda^2, m_B^2, m_\ell^2) \right) \\
& - 2(p_B \cdot p_\ell) \left(C_{23}(m_B^2, s_{B\ell}, m_\ell^2; 0, m_B^2, m_\ell^2) - C_{23}(m_B^2, s_{B\ell}, m_\ell^2; \Lambda^2, m_B^2, m_\ell^2) \right) \\
& - 2 \left(C_{24}(m_B^2, s_{B\ell}, m_\ell^2; 0, m_B^2, m_\ell^2) - C_{24}(m_B^2, s_{B\ell}, m_\ell^2; \Lambda^2, m_B^2, m_\ell^2) \right) \\
& + \Lambda^2 \, C_{12}(m_B^2 \, s_{B\ell}, m_\ell^2; 0, m_B^2, m_\ell^2)
\end{aligned}
$$

$$(\text{B.2.32})$$

B.3 Scalar Integrals

B.3.1 General definitions

The scalar integrals used in Appendix B.2.2 are derived through Passarino-Veltman tensor reduction [272, 273, 274]. Thus, the relevant tensor integrals are defined by, in the notation of [275],

$$A_0(m^2) = f_\Gamma \int d^D\ell \, \frac{1}{[\ell^2 - m^2]} \tag{B.3.1}$$

$$B_0(p^2; m_1^2, m_2^2) = f_\Gamma \int d^D\ell \, \frac{1}{[\ell^2 - m_1^2][(\ell + p)^2 - m_2^2]} \tag{B.3.2}$$

$$B_0(0; m^2, m^2) = f_\Gamma \int d^D\ell \, \frac{1}{[\ell^2 - m^2]^2} \tag{B.3.3}$$

$$B^\mu(p^2; m_1^2, m_2^2) = p^\mu B_1(p^2; m_1^2, m_2^2)$$
$$= f_\Gamma \int d^D\ell \, \frac{\ell^\mu}{[\ell^2 - m_1^2][(\ell + p)^2 - m_2^2]} \tag{B.3.4}$$

$$C_0(p_1^2, s, p_2^2; m_0^2, m_1^2, m_2^2) = f_\Gamma \int d^D\ell \, \frac{1}{[\ell^2 - m_0^2][(\ell + p_1)^2 - m_1^2][(\ell + p_2)^2 - m_2^2]} \tag{B.3.5}$$

$$C^\mu(p_1^2, s, p_2^2; m_0^2, m_1^2, m_2^2) = p_1^\mu C_{11} + p_2^\mu C_{12}$$
$$= f_\Gamma \int d^D\ell \, \frac{\ell^\mu}{[\ell^2 - m_0^2][(\ell + p_1)^2 - m_1^2][(\ell + p_2)^2 - m_2^2]} \tag{B.3.6}$$

$$C^{\mu\nu}(p_1^2, s, p_2^2; m_0^2, m_1^2, m_2^2) = p_1^\mu p_1^\nu C_{21} + p_2^\mu p_2^\nu C_{22} + (p_1^\mu p_2^\nu + p_2^\mu p_1^\nu)C_{23} + g^{\mu\nu}C_{24}$$
$$= f_\Gamma \int d^D\ell \, \frac{\ell^\mu \ell^\nu}{[\ell^2 - m_0^2][(\ell + p_1)^2 - m_1^2][(\ell + p_2)^2 - m_2^2]} \tag{B.3.7}$$

$$C_0(p^2, 0, p^2; m_0^2, m^2, m^2) = f_\Gamma \int d^D\ell \, \frac{1}{[\ell^2 - m_0^2][(\ell + p)^2 - m^2]^2} \tag{B.3.8}$$

$$C^\mu(p^2, 0, p^2; m_0^2, m^2, m^2) = p^\mu C_{10}$$
$$= f_\Gamma \int d^D\ell \, \frac{\ell^\mu}{[\ell^2 - m_0^2][(\ell + p)^2 - m^2]^2} \tag{B.3.9}$$

$$C^{\mu\nu}(p^2, 0, p^2; m_0^2, m^2, m^2) = p^\mu p^\nu C_{20} + g^{\mu\nu}C_{24}$$
$$= f_\Gamma \int d^D\ell \, \frac{\ell^\mu \ell^\nu}{[\ell^2 - m_0^2][(\ell + p)^2 - m^2]^2} \tag{B.3.10}$$

with the common prefactors

$$f_\Gamma = \frac{\mu^{4-D}}{i\pi^{\frac{D}{2}} r_\Gamma} \quad \text{and} \quad r_\Gamma = \frac{\Gamma^2(1 - \epsilon)\,\Gamma(1 + \epsilon)}{\Gamma(1 - 2\epsilon)}. \tag{B.3.11}$$

The obvious arguments on the C_{1i} and C_{2i} have been suppressed for brevity. The triangle integrals with a squared propagator, i.e. $p = p_1 = p_2$ and, consequently, $s = (p_1 - p_2)^2 = 0$, occur in the evaluation of massive wave function renormalisations and the YFS virtual subtraction term. They can equally well be calculated as the derivative of a bubble integral with respect to p. In this form, however, their infrared divergence structure arises straight forwardly and not as a transformed ultraviolet divergence.

The scalar components of above integrals relevant for the results of Appendix B.2.2 are listed in the following sections.

B.3.2 Tadpole integrals

Within the confines of this thesis, only the scalar tadpole integral is of interest. It solves to

$$A_0(0) = 0 \tag{B.3.12}$$

$$A_0(m^2) = m^2 \left[\frac{1}{\epsilon_{\mathrm{UV}}} + \ln \frac{\mu^2}{m^2} + 1 \right] . \tag{B.3.13}$$

B.3.3 Bubble integrals

In case of the two point integrals, both the scalar integral as well as the scalar components of rank one tensor integral, both in the ordinary form and in the form with a squared propagator are needed. They read

$$B_0(m^2; 0, m^2) = \frac{1}{\epsilon_{\mathrm{UV}}} + \ln \frac{\mu^2}{m^2} + 2 \tag{B.3.14}$$

$$B_0(m^2; \Lambda^2, m^2) = \frac{1}{\epsilon_{\mathrm{UV}}} + \ln \frac{\mu^2}{m^2} + \sum_{i=1,2} \left[l_i^\Lambda \ln \frac{l_i^\Lambda - 1}{l_i^\Lambda} - \ln(l_i^\Lambda - 1) \right] + 2 \tag{B.3.15}$$

$$B_0(s; m_1^2, m_2^2) = \frac{1}{\epsilon_{\mathrm{UV}}} + \ln \frac{\mu^2}{s - i\epsilon} + \sum_{i=1,2} \left[l_i^s \ln \frac{l_i^s - 1}{l_i^s} - \ln(l_i^s - 1) \right] + 2 \tag{B.3.16}$$

$$B_0(0; m^2, m^2) = \frac{1}{\epsilon_{\mathrm{UV}}} + \ln \frac{\mu^2}{m^2} \tag{B.3.17}$$

$$B_1(m^2; 0, m^2) = -\frac{1}{2} \frac{A_0(m^2)}{m^2} \tag{B.3.18}$$

$$B_1(m^2; \Lambda^2, m^2) = \frac{1}{2m^2} \left[A_0(\Lambda^2) - A_0(m^2) - \Lambda^2 B_0(m^2; \Lambda^2, m^2) \right] \tag{B.3.19}$$

with

$$l_{1,2}^\Lambda = \frac{\Lambda^2}{2m^2} \left[1 + \sqrt{1 - 4\frac{m^2}{\Lambda^2}} \right] \tag{B.3.20}$$

$$l_{1,2}^s = \frac{s - m_2^2 + m_1^2 + \sqrt{(s - m_2^2 + m_1^2)^2 - 4m_1^2(s - i\epsilon)}}{2s} . \tag{B.3.21}$$

The term $i\epsilon$ signifies a tiny imaginary part to define the correct Riemann sheet.

B.3.4 Triangle integrals

$$C_0(m^2, 0, m^2; 0, m^2, m^2) = \frac{1}{2m^2} \left[\frac{1}{\epsilon_{\mathrm{IR}}} + \ln \frac{\mu^2}{m^2} - 2 + 2\ln 2 \right] \tag{B.3.22}$$

$$C_0(m^2, 0, m^2; \Lambda^2, m^2, m^2) = \frac{1}{m^2\, l^\Lambda} \ln \left[\frac{l^\Lambda + \frac{\Lambda^2}{m^2} - 2}{l^\Lambda - \frac{\Lambda^2}{m^2} + 2} \cdot \frac{l^\Lambda - \frac{\Lambda^2}{m^2}}{l^\Lambda + \frac{\Lambda^2}{m^2}} \right] \tag{B.3.23}$$

$$C_0(m_1^2, s, m_2^2; 0, m_1^2, m_2^2) = \frac{1}{2sb} \left[\frac{1}{\epsilon_{\text{IR}}} \ln(x_+ x_-) - \ln \frac{\mu^2}{sb} \ln(x_+ x_-) \right.$$
$$+ \tfrac{1}{2} \ln^2(-g_+) - \tfrac{1}{2} \ln^2(1 - g_+)$$
$$- \tfrac{1}{2} \ln^2(g_-) + \tfrac{1}{2} \ln^2(g_- - 1)$$
$$- \text{Li}_2 \left(\frac{1 - g_-}{b} \right) - \text{Li}_2 \left(\frac{g_+}{b} \right)$$
$$\left. + \text{Li}_2 \left(\frac{g_+ - 1}{b} \right) + \text{Li}_2 \left(\frac{-g_-}{b} \right) \right] \tag{B.3.24}$$

$$C_0(m_1^2, s, m_2^2; \Lambda^2, m_1^2, m_2^2) = \frac{1}{N} \sum_{i=0,1,2} \left[R(y_i, y_i^+) + R(y_i, y_i^-) + S_i \right] \tag{B.3.25}$$

$$C_{10}(m^2, 0, m^2; 0, m^2, m^2) = \frac{1}{2m^2} \left[B_0(m^2; 0, m^2) - B_0(0; m^2, m^2) \right] \tag{B.3.26}$$

$$C_{10}(m^2, 0, m^2; \Lambda^2, m^2, m^2) = \frac{1}{2m^2} \left[B_0(m^2; \Lambda^2, m^2) - B_0(0; m^2, m^2) - \Lambda^2 C_0 \right] \tag{B.3.27}$$

$$C_{11}(m_1^2, s, m_2^2; 0, m_1^2, m_2^2) = -\frac{2}{\lambda(s, m_1^2, m_2^2)}$$
$$\times \left[m_2^2 \left(B_0(m_2^2; 0, m_2^2) - B_0(m_2^2; m_1^2, m_2^2) \right) \right.$$
$$\left. - \tfrac{1}{2}(s - m_1^2 - m_2^2) \left(B_0(m_1^2; 0, m_1^2) - B_0(m_2^2; m_1^2, m_2^2) \right) \right] \tag{B.3.28}$$

$$C_{11}(m_1^2, s, m_2^2; \Lambda^2, m_1^2, m_2^2) = -\frac{2}{\lambda(s, m_1^2, m_2^2)}$$
$$\times \left[m_2^2 \left(B_0(m_2^2; \Lambda^2, m_2^2) - B_0(m_2^2; m_1^2, m_2^2) - \Lambda^2 C_0 \right) \right.$$
$$- \tfrac{1}{2}(s - m_1^2 - m_2^2) \left(B_0(m_1^2; \Lambda^2, m_1^2) - B_0(m_2^2; m_1^2, m_2^2) \right.$$
$$\left. \left. - \Lambda^2 C_0 \right) \right] \tag{B.3.29}$$

$$C_{12}(m_1^2, s, m_2^2; 0, m_1^2, m_2^2) = -\frac{2}{\lambda(s, m_1^2, m_2^2)}$$
$$\times \left[m_1^2 \left(B_0(m_1^2; 0, m_1^2) - B_0(m_1^2; m_2^2, m_1^2) \right) \right.$$
$$\left. - \tfrac{1}{2}(s - m_1^2 - m_2^2) \left(B_0(m_2^2; 0, m_2^2) - B_0(m_1^2; m_2^2, m_1^2) \right) \right] \tag{B.3.30}$$

$$C_{12}(m_1^2, s, m_2^2; \Lambda^2, m_1^2, m_2^2) = -\frac{2}{\lambda(s, m_1^2, m_2^2)}$$
$$\times \left[m_1^2 \left(B_0(m_1^2; \Lambda^2, m_1^2) - B_0(m_1^2; m_2^2, m_1^2) - \Lambda^2 C_0 \right) \right.$$
$$- \tfrac{1}{2}(s - m_1^2 - m_2^2) \left(B_0(m_2^2; \Lambda^2, m_2^2) - B_0(m_1^2; m_2^2, m_1^2) \right.$$
$$\left. \left. - \Lambda^2 C_0 \right) \right] \tag{B.3.31}$$

$$C_{20}(m^2, 0, m^2; 0, m^2, m^2) = \frac{1}{m^2 (D-1)}$$
$$\times \left[\frac{D}{2} \big(B_1(m^2; 0, m^2) + B_0(0; m^2, m^2) \big) - B_0(0; m^2, m^2) \right]$$
$$(B.3.32)$$

$$C_{20}(m^2, 0, m^2; \Lambda^2, m^2, m^2) = \frac{1}{m^2 (D-1)}$$
$$\times \left[\frac{D}{2} \big(B_1(m^2; \Lambda^2, m^2) + B_0(0; m^2, m^2) - \Lambda^2 C_{10} \big) \right.$$
$$\left. - \big(B_0(0; m^2, m^2) + \Lambda^2 C_0 \big) \right]$$
$$(B.3.33)$$

$$C_{21}(m_1^2, s, m_2^2; 0, m_1^2, m_2^2) = - \frac{2}{\lambda(s, m_1^2, m_2^2)}$$
$$\times \left[m_2^2 \big(B_1(s; m_1^2, m_2^2) - B_0(s; m_1^2, m_2^2) - 2C_{24} \big) \right.$$
$$\left. - \tfrac{1}{2}(s - m_1^2 - m_2^2) \big(B_1(m_1^2; 0, m_1^2) - B_1(s; m_2^2, m_1^2) \big) \right]$$
$$(B.3.34)$$

$$C_{21}(m_1^2, s, m_2^2; \Lambda^2, m_1^2, m_1^2) = - \frac{2}{\lambda(s, m_1^2, m_2^2)}$$
$$\times \left[m_2^2 \big(B_1(s; m_1^2, m_2^2) - B_0(s; m_1^2, m_2^2) - \Lambda^2 C_{11} - 2C_{24} \big) \right.$$
$$- \tfrac{1}{2}(s - m_1^2 - m_2^2) \big(B_1(m_1^2; \Lambda^2, m_1^2) - B_1(s; m_2^2, m_1^2)$$
$$\left. - \Lambda^2 C_{12} \big) \right]$$
$$(B.3.35)$$

$$C_{22}(m_1^2, s, m_2^2; 0, m_1^2, m_2^2) = - \frac{2}{\lambda(s, m_1^2, m_2^2)}$$
$$\times \left[m_1^2 \big(B_1(s; m_2^2, m_1^2) - B_0(s; m_2^2, m_1^2) - 2C_{24} \big) \right.$$
$$\left. - \tfrac{1}{2}(s - m_1^2 - m_2^2) \big(B_1(m_2^2; 0, m_2^2) - B_1(s; m_1^2, m_2^2) \big) \right]$$
$$(B.3.36)$$

$$C_{22}(m_1^2, s, m_2^2; \Lambda^2, m_1^2, m_1^2) = - \frac{2}{\lambda(s, m_1^2, m_2^2)}$$
$$\times \left[m_1^2 \big(B_1(s; m_2^2, m_1^2) - B_0(s; m_2^2, m_1^2) - \Lambda^2 C_{12} - 2C_{24} \big) \right.$$
$$- \tfrac{1}{2}(s - m_1^2 - m_2^2) \big(B_1(m_2^2; \Lambda^2, m_2^2) - B_1(s; m_1^2, m_2^2)$$
$$\left. - \Lambda^2 C_{11} \big) \right]$$
$$(B.3.37)$$

$$C_{23}(m_1^2, s, m_2^2; 0, m_1^2, m_2^2) = - \frac{2}{\lambda(s, m_1^2, m_2^2)}$$
$$\times \left[m_1^2 \big(B_1(m_1^2; 0, m_1^2) - B_1(s; m_2^2, m_1^2) \big) \right.$$
$$- \tfrac{1}{2}(s - m_1^2 - m_2^2) \big(B_1(s; m_1^2, m_2^2) + B_0(s; m_1^2, m_2^2)$$
$$\left. - 2C_{24} \big) \right]$$
$$(B.3.38)$$

$$C_{23}(m_1^2, s, m_2^2; \Lambda^2, m_1^2, m_1^2) = -\frac{2}{\lambda(s, m_1^2, m_2^2)}$$
$$\times \Big[m_1^2 \big(B_1(m_1^2; \Lambda^2, m_1^2) - B_1(s; m_2^2, m_1^2) - \Lambda^2 C_{12} \big)$$
$$- \tfrac{1}{2}(s - m_1^2 - m_2^2) \big(B_1(s; m_1^2, m_2^2) + B_0(s; m_1^2, m_2^2)$$
$$- \Lambda^2 C_{11} - 2C_{24} \big) \Big] \qquad \text{(B.3.39)}$$

$$C_{24}(m_1^2, s, m_2^2; 0, m_1^2, m_2^2) = \frac{1}{2(D-2)} B_0(s; m_1^2, m_2^2) \qquad \text{(B.3.40)}$$

$$C_{24}(m_1^2, s, m_2^2; \Lambda^2, m_1^2, m_1^2) = \frac{1}{D-2} \Big[\Lambda^2 C_0 + \tfrac{1}{2} B_0(s; m_1^2, m_2^2) + \Lambda^2 C_{11} + \Lambda^2 C_{12} \Big] \qquad \text{(B.3.41)}$$

$$C_{24}(m^2, 0, m^2; 0, m^2, m^2) = \frac{1}{D-1} \Big[-\tfrac{1}{2} \big(B_1(m^2; 0, m^2) + B_0(0; m^2, m^2) \big)$$
$$- B_0(0; m^2, m^2) \Big] \qquad \text{(B.3.42)}$$

$$C_{24}(m^2, 0, m^2; \Lambda^2, m^2, m^2) = \frac{1}{D-1} \Big[-\tfrac{1}{2} \big(B_1(m^2; \Lambda^2, m^2) + B_0(0; m^2, m^2) - \Lambda^2 C_{10} \big)$$
$$- \big(B_0(0; m^2, m^2) + \Lambda^2 C_0 \big) \Big] \qquad \text{(B.3.43)}$$

with

$$l^\Lambda = \frac{\Lambda^2}{m^2} \sqrt{1 - 4\frac{m^2}{\Lambda^2}} \qquad \text{(B.3.44)}$$

$$b = \frac{\sqrt{(-s + m_1^2 + m_2^2)^2 - 4m_1^2 m_2^2}}{s} \qquad \text{(B.3.45)}$$

$$g_\pm = \tfrac{1}{2} \left[\frac{s - m_1^2 + m_2^2}{s} \pm b \right] \qquad \text{(B.3.46)}$$

$$x_+ = \frac{g_+ - 1}{g_+} \qquad x_- = \frac{g_-}{g_- - 1} \qquad \text{(B.3.47)}$$

and $\lambda(x, y, z) = x^2 + y^2 + z^2 - 2xy - 2xz - 2yz$ is the Kallen function. Again, obvious arguments have been suppressed. The definitions for N, $R(a, b)$, S_i, y_i and $y_i^\pm$ for the general UV and IR finite triangle $C_0(m_1^2, s, m_2^2; \Lambda^2, m_1^2, m_2^2)$ can be found in [273].

Appendix C

# Explicit form of the leading order Altarelli-Parisi splitting functions
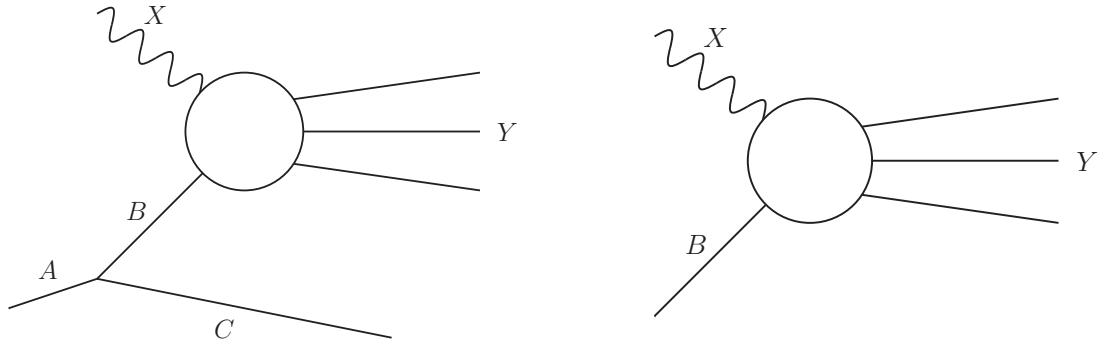
Figure C.1: The scattering process with (left) and without (right) next-to-leading order corrections to the parton model.

In this section, reviewing the results of [93], the explicit form of the leading order splitting kernel $P_{BA}^{(0)}(z)$ is computed directly from the QCD vertices. The value of the splitting kernels is first computed for $z < 0$, leaving out the divergence at $z = 1$. There, the splitting kernels have a direct physical interpretation as the probability to find parton B inside parton A at momentum fraction z in the infinite momentum frame, i.e.

$$ \mathrm{d}\mathcal{P}_{BA}(z)\,\mathrm{d}z \;=\; \frac{\alpha_s}{2\pi}\,\hat{P}_{BA}(z)\,\mathrm{d}z\,\mathrm{d}\log p_\perp^2 \;. \tag{C.0.1} $$

Considering now the differential scattering cross section of a hadron and a second initial state X with $(\mathrm{d}\sigma_a)$ and without $(\mathrm{d}\sigma_b)$ NLO QCD corrections to the parton model, as depicted in Figure C.1, they read

$$ \mathrm{d}\sigma_a \;=\; \frac{1}{8E_A E_X}\;\frac{|V_{A\to B+C}|^2\,|V_{B+X\to Y}|^2}{(2E_B)^2\,(E_B + E_C - E_A)^2}\,(2\pi)^2\,\delta(p_A + p_X - p_C - p_Y)\,\frac{\mathrm{d}^3 p_C}{(2\pi)^3(2E_C)}\,\mathrm{d}\Phi_Y $$

$$ \mathrm{d}\sigma_b \;=\; \frac{1}{8E_B E_X}\qquad\quad |V_{B+X\to Y}|^2 \qquad (2\pi)^2\,\delta(p_B + p_X - p_Y)\,\mathrm{d}\Phi_Y \;. $$

$$ \tag{C.0.2} $$

Therein, the E_i and p_i are the energy and the momenta of the respective states, and the $V_{A\to B+C}$, $V_{B+X\to Y}$ and $V_{B+X\to Y}$ are the relevant transition matrix elements. Their absolute

square can be identified with the vertex functions F_{BA} etc. of Section 6.2 eq. (6.2.6). Φ_Y is the phase space of the arbitrary final state Y. $\mathrm{d}\sigma_a$ has been decomposed in the limit of a collinear splitting $A \to B + C$, such that the intermediate state B is on-shell. The on-shell propagator is encoded in the $1/(E_B + E_C - E_A)^2$ term, whereas the factor $1/(2E_B)^2$ is removed from the vertex function $V_{A\to B+C}$. According to eq. (6.1.2) both expressions are related by

$$\mathrm{d}\sigma_a \; = \; \mathrm{d}\mathcal{P}_{BA}(z)\,\mathrm{d}z\,\mathrm{d}\sigma_b \,. \tag{C.0.3}$$

Thus, using eq. (C.0.2)

$$\mathrm{d}\mathcal{P}_{BA}(z)\,\mathrm{d}z \; = \; \frac{E_B}{E_A}\,\frac{|V_{A\to B+C}|^2}{(2E_B)^2(E_B + E_C - E_A)^2}\,\frac{\mathrm{d}^3 p_C}{(2\pi)^3(2E_C)} \,. \tag{C.0.4}$$

Introducing now the relative transverse momentum $p_\perp$ of the states B and C, the momenta of the states A, B and C read in the collinear limit

$$p_A \; = \; \left(p, 0, p\right)$$

$$p_B \; = \; \left(zp + \frac{p_\perp^2}{2zp}, p_\perp, zp\right) \tag{C.0.5}$$

$$p_C \; = \; \left((1-z)p + \frac{p_\perp^2}{2(1-z)p}, -p_\perp, (1-z)p\right) \,.$$

Again, the assumption $z < 1$ is implied. Eq. (C.0.5) can then be used to rewrite the final state phase space element of parton C in terms of z and the absolute of $p_\perp$, $p_\perp^2$. Integrating out the azimuthal degree of freedom, ϕ, equivalent to an averaging over spins and/or polarisations of the involved partons, it reads

$$\frac{\mathrm{d}^3 p_C}{(2\pi)^3(2E_C)} \; = \; \frac{\mathrm{d}z\,\mathrm{d}p_\perp^2}{16\pi^2(1-z)} \,. \tag{C.0.6}$$

Hence, the differential probability to find parton B in parton A at momentum fraction z now reads

$$\mathrm{d}\mathcal{P}_{BA}(z)\,\mathrm{d}z \; = \; \frac{z(1-z)}{2}\,\overline{\sum_{\text{spins}}}\,\frac{|V_{A\to B+C}|^2}{p_\perp^2}\,\mathrm{d}z\,\mathrm{d}\log p_\perp^2 \,, \tag{C.0.7}$$

making the dependence on $p_\perp^2$ explicit. The unregularised Altarelli-Parisi splitting function then reads, with eq. (C.0.1),

$$\frac{\alpha_s}{2\pi}\,\hat{P}_{BA}(z) \; = \; \frac{z(1-z)}{2}\,\overline{\sum_{\text{spins}}}\,\frac{|V_{A\to B+C}|^2}{p_\perp^2} \qquad\qquad (z < 1) \,. \tag{C.0.8}$$

Thus, recovering the result of eq. (6.2.7), the unregularised Altarelli-Parisi splitting functions are given in terms of the vertex functions. A similar analysis holds for final state splittings, leading to the same splitting functions, as was shown in Section 6.2.

C.1 Collinear limit of real emission matrix elements

In the following the unregularised splitting functions for all four possible parton splittings are derived. The regularised Altarelli-Parisi splitting functions are then determined via the reinterpretation of the $1/(1-z)$ terms as $(\dots)_+$ distributions and adding the appropriate terms proportional to $\delta(1-z)$ to fulfil the constraints of eq. (6.1.17).

## C.1.1 $q \rightarrow gq$ splittings
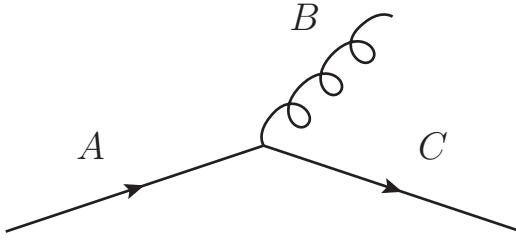
Figure C.2: The quark-gluon vertex determining $\hat{P}_{gq}$.

The probability to find a gluon of momentum fraction z in a quark is determined by the vertex function depicted in Figure C.2, and thus by the QCD quark-gluon vertex. It reads in the collinear approximation

$$\frac{\alpha_s}{2\pi} \, \hat{P}_{gq}(z) \;=\; \frac{z(1-z)}{2} \, \overline{\sum_{\substack{\text{spins} \\ \text{pols}}}} \frac{|V_{q \rightarrow gq}|^2}{p_\perp^2} \qquad\qquad (z < 1) \,, \tag{C.1.1}$$

with

$$\overline{\sum_{\substack{\text{spins} \\ \text{pols}}}} |V_{q \rightarrow gq}|^2 \;=\; \tfrac{1}{2} \frac{\alpha_s}{2\pi} \, C_F \, \mathrm{Tr}(\slashed{p}_C \gamma^\mu \slashed{p}_A \gamma^\nu) \, \overline{\sum_{\text{pols}}} \epsilon_\mu^* \epsilon_\nu \,. \tag{C.1.2}$$

Herein, the momenta are labeled with A, B and C as before, ϵ signifies the gluon polarisation. The factor $\frac{1}{2}$ arises from averaging over the initial state quark's spin. As the intermediate gluon is taken to be on its mass shell, only its physical polarisations contribute. Thus,

$$\overline{\sum_{\text{pols}}} \epsilon_\mu^* \epsilon_\nu \;=\; \begin{cases} \delta^{\mu\nu} - \dfrac{p_B^\mu p_B^\nu}{p_B^2} & \mu, \nu \in \{1, 2, 3\} \\ 0 & \text{else.} \end{cases} \tag{C.1.3}$$

With the parametrisation of eq. (C.0.5) the spin average now reads

$$\overline{\sum_{\substack{\text{spins} \\ \text{pols}}}} |V_{q \rightarrow gq}|^2 \;=\; \frac{\alpha_s}{2\pi} \, C_F \, \frac{2p_\perp^2}{z(1-z)} \, \frac{1 + (1-z)^2}{z} \,. \tag{C.1.4}$$

Thus,

$$\hat{P}_{gq}(z) \;=\; C_F \, \frac{1 + (1-z)^2}{z} \,. \tag{C.1.5}$$

Because $\hat{P}_{gq}(z)$ is finite as $z \rightarrow 1$ the regularised Altarelli-Parisi splitting function equals the unregularised one, i.e.

$$P_{gq}^{(0)}(z) \;=\; \hat{P}_{gq}(z) \,. \tag{C.1.6}$$
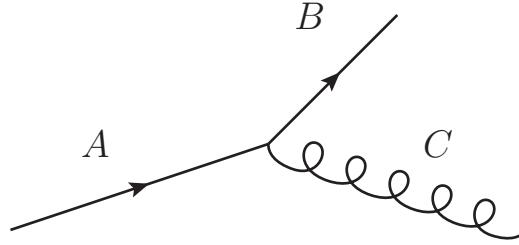
Figure C.3: The quark-gluon vertex determining $\hat{P}_{qq}$.

C.1.2 $q \rightarrow qg$ splittings

The probability to find a quark of momentum fraction z in a quark, depicted in Figure C.3, is directly related to the result of the last Section by momentum conservation, i.e.

$$\hat{P}_{qq}(z) = \hat{P}_{gq}(1-z) .$$

<div align="right">(C.1.7)</div>

Thus,

$$\hat{P}_{qq}(z) = C_F \frac{1+z^2}{1-z} .$$

<div align="right">(C.1.8)</div>

Unlike eq. (C.1.5) eq. (C.1.8) exhibits a divergence at $z = 1$. Hence, following the procedure outlined above, interpreting the $1/(1-z)$ as $1/(1-z)_+$ and adding a term proportional to $\delta(1-z)$ to fulfil eq. (6.1.17), gives the regularised Altarelli-Parisi splitting function

$$P_{qq}^{(0)}(z) = C_F \left[\frac{1+z^2}{(1-z)_+} + \tfrac{3}{2}\delta(1-z) \right] .$$

<div align="right">(C.1.9)</div>

C.1.3 $g \rightarrow qq$ splittings
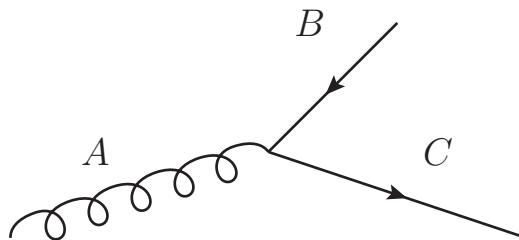
Figure C.4: The quark-gluon vertex determining $\hat{P}_{qg}$.

The vertex function to determine the probability to find a quark of momentum fraction z in a gluon is depicted in Figure C.4. The Altarelli-Parisi splitting function again arises out of

the quark-gluon vertex. The spin and polarisation summed and averaged vertex function in this rotation reads

$$\overline{\sum_{\substack{\text{spins}\\\text{pols}}}|V_{g\to qq}|^2} = \tfrac{1}{2}\frac{\alpha_s}{2\pi}\text{Tr}(\not{p}_C\gamma^\mu\not{p}_B\gamma^\nu)\overline{\sum_{\text{pols}}\epsilon^*_\mu\epsilon_\nu}\ . \tag{C.1.10}$$

Again, care has to be taken to account for physical polarisation states only. This leads to

$$\overline{\sum_{\substack{\text{spins}\\\text{pols}}}|V_{g\to qq}|^2} = \frac{\alpha_s}{2\pi}T_R\,2p_\perp^2\left(\frac{1-z}{z}+\frac{z}{1-z}\right)$$

$$= \frac{\alpha_s}{2\pi}T_R\,\frac{2p_\perp^2}{z(1-z)}\left(z^2-(1-z)^2\right)\ . \tag{C.1.11}$$

Thus,

$$\hat{P}_{qg}(z) = T_R\left(z^2-(1-z)^2\right)\ . \tag{C.1.12}$$

Herein, the symmetry of $z\leftrightarrow 1-z$ is evident. Again, $\hat{P}_{qg}(z)$ is finite for $z\to 1$, hence the regularised Altarelli-Parisi splitting function is equal to the unregularised one,

$$P_{qg}^{(0)}(z) = \hat{P}_{qg}(z) \tag{C.1.13}$$

C.1.4 $\quad g\to gg$ splittings
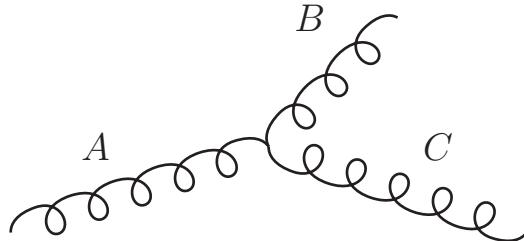
Figure C.5: The triple gluon vertex determining $\hat{P}_{gg}$.

Contrary to the other three cases the Altarelli-Parisi splitting function for the probability to find a gluon of momentum fraction z inside another gluon is determined by the triple gluon vertex of QCD. Here, the vertex function of Figure C.5 needs to be summed and averaged over the external gluon polarisations ϵ_A, ϵ_B and ϵ_C, leading to

$$\overline{\sum_{\text{pols}}|V_{g\to gg}|^2} = 2\frac{\alpha_s}{2\pi}C_A\,\frac{2p_\perp^2}{z(1-z)}\left[\frac{z}{1-z}+\frac{1-z}{z}+z(1-z)\right]\ . \tag{C.1.14}$$

Thus, the unregularised Altarelli-Parisi splitting function reads

$$\hat{P}_{gg}(z) = 2C_A\left[\frac{z}{1-z}+\frac{1-z}{z}+z(1-z)\right]\ . \tag{C.1.15}$$

Again, the symmetry under $z \leftrightarrow 1 - z$ is evident as is the pole at $z = 1$. The regularised splitting function consequently reads

$$P_{gg}^{(0)}(z) = 2C_A \left[\frac{z}{(1-z)_+} + \frac{1-z}{z} + z(1-z) \right] + \frac{11C_A - 4N_f T_R}{6} \delta(1-z) . \qquad \text{(C.1.16)}$$

For completeness sake, the next-to-leading order expressions for the Altarelli-Parisi splitting functions in the $\overline{\text{MS}}$ factorisation and renormalisation schemes can be found in [192, 193].

Bibliography

[1] A. Buckley et al., *General-purpose event generators for LHC physics*, Phys. Rept. **504** (2011), 145–233, [`arXiv:1101.2599` [hep-ph]].

[2] T. Sjöstrand, S. Mrenna and P. Skands, *PYTHIA 6.4 physics and manual*, JHEP **05** (2006), 026, [`hep-ph/0603175`].

[3] G. Corcella et al., *HERWIG 6: an event generator for hadron emission reactions with interfering gluons (including supersymmetric processes)*, JHEP **01** (2001), 010, [`hep-ph/0011363`].

[4] G. Corcella, I. G. Knowles, G. Marchesini, M. Moretti, K. Odagiri, P. Richardson, M. H. Seymour and B. R. Webber, *HERWIG 6.5 Release Note*, `hep-ph/0210213`.

[5] T. Sjöstrand, S. Mrenna and P. Skands, *A brief introduction to PYTHIA 8.1*, Comput. Phys. Commun. **178** (2008), 852–867, [`arXiv:0710.3820` [hep-ph]].

[6] S. Gieseke, D. Grellscheid, K. Hamilton, A. Papaefstathiou, S. Platzer et al., *Herwig++ 2.5 Release Note*, `arXiv:1102.1672` [hep-ph].

[7] T. Gleisberg, S. Höche, F. Krauss, A. Schälicke, S. Schumann and J. Winter, Sherpa *1.α, a proof-of-concept version*, JHEP **02** (2004), 056, [`hep-ph/0311263`].

[8] T. Gleisberg, S. Höche, F. Krauss, M. Schönherr, S. Schumann, F. Siegert and J. Winter, *Event generation with* Sherpa *1.1*, JHEP **02** (2009), 007, [`arXiv:0811.4622` [hep-ph]].

[9] J. Campbell, R. K. Ellis and C. Williams, *MCFM – Monte Carlo for FeMtobarn processes*.

[10] Z. Nagy, *Next-to-leading order calculation of three-jet observables in hadron-hadron collisions*, Phys. Rev. **D68** (2003), 094002, [`hep-ph/0307268`].

[11] S. Frixione and B. R. Webber, *Matching NLO QCD computations and parton shower simulations*, JHEP **06** (2002), 029, [`hep-ph/0204244`].

[12] P. Nason, *A new method for combining NLO QCD with shower Monte Carlo algorithms*, JHEP **11** (2004), 040, [`hep-ph/0409146`].

[13] S. Frixione, P. Nason and C. Oleari, *Matching NLO QCD computations with parton shower simulations: the POWHEG method*, JHEP **11** (2007), 070, [`arXiv:0709.2092` [hep-ph]].

[14] S. Frixione, F. Stoeckli, P. Torrielli, B. R. Webber and C. D. White, *The MCaNLO 4.0 Event Generator*, `arXiv:1010.0819` [hep-ph].

[15] S. Alioli, P. Nason, C. Oleari and E. Re, *A general framework for implementing NLO calculations in shower Monte Carlo programs: the POWHEG BOX*, JHEP **06** (2010), 043, [`arXiv:1002.2581` [hep-ph]].

[16] M. L. Mangano, M. Moretti, F. Piccinini, R. Pittau and A. D. Polosa, *ALPGEN, a generator for hard multiparton processes in hadronic collisions*, JHEP **07** (2003), 001, [`hep-ph/0206293`].

[17] E. Boos et al., The CompHEP collaboration, *CompHEP 4.4 - automatic computations from Lagrangians to events*, Nucl. Instrum. Meth. **A534** (2004), 250–259, [`hep-ph/0403113`].

[18] A. Pukhov, *CalcHEP 3.2: MSSM, structure functions, event generation, batchs, and generation of matrix elements for other packages*, `hep-ph/0412191`.

[19] A. Kanaki and C. G. Papadopoulos, *HELAC: A package to compute electroweak helicity amplitudes*, Comput. Phys. Commun. **132** (2000), 306–315, [`hep-ph/0002082`].

[20] C. G. Papadopoulos, *PHEGAS: A phase-space generator for automatic cross-section computation*, Comput. Phys. Commun. **137** (2001), 247–254, [`hep-ph/0007335`].

[21] A. Cafarella, C. G. Papadopoulos and M. Worek, *HELAC-PHEGAS: A generator for all parton level processes*, Comput. Phys. Commun. **180** (2009), 1941–1955, [`arXiv:0710.2427 [hep-ph]`].

[22] T. Stelzer and W. F. Long, *Automatic generation of tree level helicity amplitudes*, Comput. Phys. Commun. **81** (1994), 357–371, [`hep-ph/9401258`].

[23] J. Alwall, M. Herquet, F. Maltoni, O. Mattelaer and T. Stelzer, *MadGraph 5 : Going Beyond*, JHEP **1106** (2011), 128, [`arXiv:1106.0522 [hep-ph]`].

[24] W. Kilian, T. Ohl and J. Reuter, *WHIZARD: Simulating Multi-Particle Processes at LHC and ILC*, Eur. Phys. J. **C71** (2007), 1742, [`arXiv:0708.4233 [hep-ph]`].

[25] F. Krauss, R. Kuhn and G. Soff, *AMEGIC++ 1.0: A Matrix Element Generator In C++*, JHEP **02** (2002), 044, [`hep-ph/0109036`].

[26] T. Gleisberg and S. Höche, *Comix, a new matrix element generator*, JHEP **12** (2008), 039, [`arXiv:0808.3674 [hep-ph]`].

[27] S. Catani, F. Krauss, R. Kuhn and B. R. Webber, *QCD matrix elements + parton showers*, JHEP **11** (2001), 063, [`hep-ph/0109231`].

[28] F. Krauss, *Matrix elements and parton showers in hadronic interactions*, JHEP **0208** (2002), 015, [`hep-ph/0205283`].

[29] S. Höche, F. Krauss, S. Schumann and F. Siegert, *QCD matrix elements and truncated showers*, JHEP **05** (2009), 053, [`arXiv:0903.1219 [hep-ph]`].

[30] L. Lönnblad, *Correcting the colour-dipole cascade model with fixed order matrix elements*, JHEP **05** (2002), 046, [`hep-ph/0112284`].

[31] N. Lavesson and L. Lönnblad, *W +jets matrix elements and the dipole cascade*, JHEP **07** (2005), 054, [`hep-ph/0503293`].

[32] M. L. Mangano, M. Moretti and R. Pittau, *Multijet matrix elements and shower evolution in hadronic collisions: $Wb\bar{b} + n$-jets as a case study*, Nucl. Phys. **B632** (2002), 343–362, [`hep-ph/0108069`].

[33] M. L. Mangano, M. Moretti, F. Piccinini and M. Treccani, *Matching matrix elements and shower evolution for top-pair production in hadronic collisions*, JHEP **01** (2007), 013, [`hep-ph/0611129`].

[34] S. Mrenna and P. Richardson, *Matching matrix elements and parton showers with HERWIG and PYTHIA*, JHEP **05** (2004), 040, [`hep-ph/0312274`].

[35] J. Alwall, S. de Visscher and F. Maltoni, *QCD radiation in the production of heavy colored particles at the LHC*, JHEP **02** (2009), 017, [`arXiv:0810.5350 [hep-ph]`].

[36] S. Höche et al., *Matching Parton Showers and Matrix Elements*, `hep-ph/0602031`.

[37] J. Alwall et al., *Comparative study of various algorithms for the merging of parton showers and matrix elements in hadronic collisions*, Eur. Phys. J. **C53** (2008), 473–500, [`arXiv:0706.2569 [hep-ph]`].

[38] R. Kleiss and W. J. Stirling, *Spinor techniques for calculating $p\bar{p} \rightarrow W^{\pm}/Z^0 + jets$*, Nucl. Phys. **B262** (1985), 235–262.

[39] A. Ballestrero, E. Maina and S. Moretti, *Heavy quarks and leptons at e^+e^- colliders*, Nucl. Phys. **B415** (1994), 265–292, [`hep-ph/9212246`].

[40] T. Gleisberg, F. Krauss, C. G. Papadopoulos, A. Schälicke and S. Schumann, *Cross sections for multi-particle final states at a linear collider*, Eur. Phys. J. **C34** (2004), 173–180, [`hep-ph/0311273`].

[41] K. Hagiwara et al., *Supersymmetry simulations with off-shell effects for the CERN LHC and an ILC*, Phys. Rev. **D73** (2006), 055005, [`hep-ph/0512260`].

[42] T. Gleisberg, F. Krauss, K. T. Matchev, A. Schälicke, S. Schumann and G. Soff, *Helicity formalism for spin-2 particles*, JHEP **09** (2003), 001, [`hep-ph/0306182`].

[43] N. D. Christensen and C. Duhr, *FeynRules - Feynman rules made easy*, Comput. Phys. Commun. **180** (2009), 1614–1641, [`arXiv:0806.4194 [hep-ph]`].

[44] N. D. Christensen, P. de Aquino, C. Degrande, C. Duhr, B. Fuks, M. Herquet, F. Maltoni and S. Schumann, *A comprehensive approach to new physics simulations*, Eur. Phys. J. **C71** (2011), 1541, [`arXiv:0906.2474 [hep-ph]`].

[45] R. Kleiss and R. Pittau, *Weight optimization in multichannel Monte Carlo*, Comput. Phys. Commun. **83** (1994), 141–146, [`hep-ph/9405257`].

[46] F. A. Berends, R. Pittau and R. Kleiss, *All electroweak four-fermion processes in electron-positron collisions*, Nucl. Phys. **B424** (1994), 308, [`hep-ph/9404313`].

[47] G. P. Lepage, *VEGAS - An Adaptive Multi-dimensional Integration Program*, CLNS-80/447.

[48] R. Kleiss, W. J. Stirling and S. D. Ellis, *A new Monte Carlo treatment of multiparticle phase space at high energies*, Comput. Phys. Commun. **40** (1986), 359.

[49] A. van Hameren and C. G. Papadopoulos, *A hierarchical phase space generator for QCD antenna structures*, Eur. Phys. J. **C25** (2002), 563–574, [`hep-ph/0204055`].

[50] T. Gleisberg and F. Krauss, *Automating dipole subtraction for QCD NLO calculations*, Eur. Phys. J. **C53** (2008), 501–523, [`arXiv:0709.2881 [hep-ph]`].

[51] S. Catani and M. H. Seymour, *A general algorithm for calculating jet cross sections in NLO QCD*, Nucl. Phys. **B485** (1997), 291–419, [`hep-ph/9605323`].

[52] S. Catani, S. Dittmaier, M. H. Seymour and Z. Trocsanyi, *The dipole formalism for next-to-leading order QCD calculations with massive partons*, Nucl. Phys. **B627** (2002), 189–265, [`hep-ph/0201036`].

[53] T. Binoth et al., *A proposal for a standard interface between Monte Carlo tools and one-loop programs*, Comput. Phys. Commun. **181** (2010), 1612–1622, [`arXiv:1001.1307` [hep-ph]].

[54] D. Maître, private communication.

[55] C. Duhr, S. Höche and F. Maltoni, *Color-dressed recursive relations for multi-parton amplitudes*, JHEP **08** (2006), 062, [`hep-ph/0607057`].

[56] F. A. Berends and W. T. Giele, *Recursive calculations for processes with n gluons*, Nucl. Phys. **B306** (1988), 759.

[57] F. A. Berends and W. Giele, *The six-gluon process as an example of Weyl-van der Waerden spinor calculus*, Nucl. Phys. **B294** (1987), 700.

[58] F. A. Berends, W. T. Giele and H. Kuijf, *Exact expressions for processes involving a vector boson and up to five partons*, Nucl. Phys. **B321** (1989), 39.

[59] R. Kleiss and H. Kuijf, *Multi-gluon cross-sections and five jet production at hadron colliders*, Nucl. Phys. **B312** (1989), 616.

[60] F. A. Berends, W. T. Giele and H. Kuijf, *On six-jet production at hadron colliders*, Phys. Lett. **B232** (1989), 266.

[61] T. Gleisberg, S. Höche, F. Krauss and R. Matyskiewicz, *How to calculate colourful cross sections efficiently*, `arXiv:0808.3672` [hep-ph].

[62] S. Schumann and F. Krauss, *A parton shower algorithm based on Catani-Seymour dipole factorisation*, JHEP **03** (2008), 038, [`arXiv:0709.1027` [hep-ph]].

[63] Z. Nagy and D. E. Soper, *Final state dipole showers and the DGLAP equation*, JHEP **05** (2009), 088, [`arXiv:0901.3587` [hep-ph]].

[64] S. Höche, S. Schumann and F. Siegert, *Hard photon production and matrix-element parton-shower merging*, Phys. Rev. **D81** (2010), 034026, [`arXiv:0912.3501` [hep-ph]].

[65] S. Höche, F. Krauss, M. Schönherr and F. Siegert, *Automating the POWHEG method in SHERPA*, JHEP **04** (2011), 024, [`arXiv:1008.5399` [hep-ph]].

[66] S. Alekhin et al., *HERA and the LHC - A workshop on the implications of HERA for LHC physics: Proceedings Part A*, `hep-ph/0601012`.

[67] T. Sjöstrand and M. van Zijl, *A multiple-interaction model for the event structure in hadron collisions*, Phys. Rev. **D36** (1987), 2019.

[68] T. D. Gottschalk, *A realistic model for e^+e^- annihilation including parton bremsstrahlung effects*, Nucl. Phys. **B214** (1983), 201.

[69] T. D. Gottschalk, *An improved description of hadronization in the QCD cluster model for e^+e^- annihilation*, Nucl. Phys. **B239** (1984), 349.

[70] B. R. Webber, *A QCD model for jet fragmentation including soft gluon interference*, Nucl. Phys. **B238** (1984), 492.

[71] T. D. Gottschalk and D. A. Morris, *A new model for hadronization and e^+e^- annihilation*, Nucl. Phys. **B288** (1987), 729.

[72] J.-C. Winter, F. Krauss and G. Soff, *A modified cluster-hadronisation model*, Eur. Phys. J. **C36** (2004), 381–395, [`hep-ph/0311085`].

[73] F. Krauss, T. Laubrich and F. Siegert, *Simulation of hadron decays in Sherpa*, in preparation.

[74] M. Schönherr and F. Krauss, *Soft photon radiation in particle decays in Sherpa*, JHEP **12** (2008), 018, [`arXiv:0810.5071` [hep-ph]].

[75] D. R. Yennie, S. C. Frautschi and H. Suura, *The Infrared Divergence Phenomena and High-Energy Processes*, Ann. Phys. **13** (1961), 379–452.

[76] E. Barberio and Z. Wąs, *PHOTOS - a universal monte carlo for QED radiative corrections: version 2.0*, Comput. Phys. Commun. **79** (1994), 291–308.

[77] M. R. Whalley, D. Bourilkov and R. C. Group, *The Les Houches Accord PDFs (LHAPDF) and LHAGLUE*, `hep-ph/0508110`.

[78] P. Skands et al., *SUSY Les Houches accord: interfacing SUSY spectrum calculators, decay packages, and event generators*, JHEP **07** (2004), 036, [`hep-ph/0311123`].

[79] A. Buckley, *Tools for event generator tuning and validation*, `arXiv:0809.4638` [hep-ph].

[80] A. Buckley et al., *Rivet user manual*, `arXiv:1003.0694` [hep-ph].

[81] B. M. Waugh et al., *HZTool and Rivet: Toolkit and framework for the comparison of simulated final states and data at colliders*, `hep-ph/0605034`.

[82] S. Jadach, B. F. L. Ward and Z. Wąs, *The precision Monte Carlo event generator KK for two- fermion final states in e^+e^- collisions*, Comput. Phys. Commun. **130** (2000), 260–325, [`hep-ph/9912214`].

[83] S. Jadach, B. F. L. Ward and Z. Was, *Coherent exclusive exponentiation for precision Monte Carlo calculations*, Nucl. Phys. Proc. Suppl. **89** (2000), 106–111, [`hep-ph/0012124`].

[84] S. Jadach, W. Płaczek, M. Skrzypek, B. F. L. Ward and Z. Wąs, *Precision predictions for (un)stable W^+W^- pair production at and beyond LEP2 energies*, Phys. Rev. **D65** (2002), 093010, [`hep-ph/0007012`].

[85] S. Jadach, W. Płaczek, M. Skrzypek, B. F. L. Ward and Z. Wąs, *The Monte Carlo program KoralW version 1.51 and the concurrent Monte Carlo KoralW&YFSWW3 with all background graphs and first order corrections to W pair production*, Comput. Phys. Commun. **140** (2001), 475–512, [`hep-ph/0104049`].

[86] M. Schönherr, *Modeling of QED Effects in Particle Decays on the Basis of the Yennie-Frautschi-Suura-Formalism*, Diploma thesis.

[87] E. Barberio, B. van Eijk and Z. Was, *PHOTOS: A Universal Monte Carlo for QED radiative corrections in decays*, Comput.Phys.Commun. **66** (1991), 115–128.

[88] G. Nanava and Z. Wąs, *Scalar QED, NLO and PHOTOS Monte Carlo*, Eur. Phys. J. **C51** (2007), 569–583, [`hep-ph/0607019`].

[89] K. Hamilton and P. Richardson, *Simulation of QED radiation in particle decays using the YFS formalism*, JHEP **07** (2006), 010, [`hep-ph/0603034`].

[90] Z. Was, P. Golonka and G. Nanava, *PHOTOS Monte Carlo and its theoretical accuracy*, `arXiv:0807.2762` [hep-ph].

[91] T. Kinoshita, *Mass Singularities of Feynman Amplitudes*, J.Math.Phys. **3** (1962), 650–677.

[92] T. Lee and M. Nauenberg, *Degenerate Systems and Mass Singularities*, Phys. Rev. **133** (1964), B1549–B1562.

[93] G. Altarelli and G. Parisi, *Asymptotic freedom in parton language*, Nucl. Phys. **B126** (1977), 298–318.

[94] S. Dittmaier, *A general approach to photon radiation off fermions*, Nucl. Phys. **B565** (2000), 69–122, [`hep-ph/9904440`].

[95] S. Catani, S. Dittmaier and Z. Trocsanyi, *One-loop singular behaviour of QCD and SUSY QCD amplitudes with massive partons*, Phys. Lett. **B500** (2001), 149–160, [`hep-ph/0011222`].

[96] S. Jadach and B. Ward, *YFS2: The Second Order Monte Carlo for Fermion Pair Production at LEP / SLC with the Initial State Radiation of Two Hard and Multiple Soft Photons*, Comput.Phys.Commun. **56** (1990), 351–384.

[97] F. A. Berends, W. van Neerven and G. Burgers, *Higher Order Radiative Corrections at LEP Energies*, Nucl.Phys. **B297** (1988), 429.

[98] W. Placzek and S. Jadach, *Multiphoton radiation in leptonic W boson decays*, Eur.Phys.J. **C29** (2003), 325–339, [`arXiv:hep-ph/0302065 [hep-ph]`].

[99] M. H. Seymour, *Photon radiation in final state parton showering*, Z. Phys. **C56** (1992), 161–170.

[100] Y. L. Dokshitzer and D. Kharzeev, *Heavy quark colorimetry of QCD matter*, Phys.Lett. **B519** (2001), 199–206, [`arXiv:hep-ph/0106202 [hep-ph]`].

[101] C. Amsler et al., The Particle Data Group collaboration, *Review of particle physics*, Phys. Lett. **B667** (2008), 1.

[102] N. Cabibbo, *Unitary Symmetry and Leptonic Decays*, Phys. Rev. Lett. **10** (1963), 531–533.

[103] M. Kobayashi and T. Maskawa, *CP Violation in the Renormalizable Theory of Weak Interaction*, Prog. Theor. Phys. **49** (1973), 652–657.

[104] J. Charles et al., The CKMfitter Group collaboration, *CP violation and the CKM matrix: Assessing the impact of the asymmetric B factories*, Eur. Phys. J. **C41** (2005), 1–131, [`hep-ph/0406184`].

[105] M. Bona et al., The UTfit collaboration, *The UTfit collaboration report on the status of the unitarity triangle beyond the standard model. I: Model- independent analysis and minimal flavour violation*, JHEP **03** (2006), 080, [`hep-ph/0509219`].

[106] F. E. Low, *Bremsstrahlung of very low-energy quanta in elementary particle collisions*, Phys. Rev. **110** (1958), 974–977.

[107] A. Sirlin, *Current Algebra Formulation of Radiative Corrections in Gauge Theories and the Universality of the Weak Interactions*, Rev.Mod.Phys. **50** (1978), 573.

[108] A. Sirlin, *Large m(W), m(Z) Behavior of the O(alpha) Corrections to Semileptonic Processes Mediated by W*, Nucl.Phys. **B196** (1982), 83.

[109] S. Eidelman et al., The Particle Data Group collaboration, *Review of particle physics*, Phys. Lett. **B592** (2004), 1.

[110] A. Sher et al., *New, high statistics measurement of the $K^+ \to \pi^0 e^+ \nu$ (Ke3) branching ratio*, Phys. Rev. Lett. **91** (2003), 261802, [`hep-ex/0305042`].

[111] T. Alexopoulos et al., The KTeV collaboration, *A Determination of the CKM Parameter $|V_{us}|$*, Phys. Rev. Lett. **93** (2004), 181802, [`hep-ex/0406001`].

[112] T. Alexopoulos et al., The KTeV collaboration, *Measurements of KL Branching Fractions and the CP Violation Parameter $|\eta^{\pm}|$*, Phys. Rev. **D70** (2004), 092006, [`hep-ex/0406002`].

[113] T. Alexopoulos et al., The KTeV collaboration, *Measurements of Semileptonic KL Decay Form Factors*, Phys. Rev. **D70** (2004), 092007, [`hep-ex/0406003`].

[114] T. C. Andre, *Radiative corrections in K0l3 decays*, Nucl. Phys. Proc. Suppl. **142** (2005), 58–61, UMI-31-49380.

[115] F. U. Bernlochner and H. Lacker, *A phenomenological model for radiative corrections in exclusive semileptonic B-meson decays to (pseudo)scalar final state mesons*, `arXiv:1003.1620` [hep-ph].

[116] S. Descotes-Genon and B. Moussallam, *Radiative corrections in weak semi-leptonic processes at low energy: A two-step matching determination*, Eur. Phys. J. **C42** (2005), 403–417, [`hep-ph/0505077`].

[117] W. Pauli and F. Villars, *On the Invariant regularization in relativistic quantum theory*, Rev. Mod. Phys. **21** (1949), 434–444.

[118] T. Burnett and N. M. Kroll, *Extension of the low soft photon theorem*, Phys.Rev.Lett. **20** (1968), 86.

[119] D. Becirevic and B. Haas, *$D^* \to D$ pi and $D^* \to D$ gamma decays: Axial coupling and Magnetic moment of D^* meson*, `arXiv:0903.2407` [hep-lat].

[120] J. Gasser, B. Kubis, N. Paver and M. Verbeni, *Radiative K(e3) decays revisited*, Eur. Phys. J. **C40** (2005), 205–227, [`hep-ph/0412130`].

[121] D. Becirevic and N. Kosnik, *Soft photons in semileptonic $B \to D$ decays*, Acta Phys.Polon.Supp. **3** (2010), 207–214, [`arXiv:0910.5031` [hep-ph]].

[122] J. Bijnens, G. Ecker and J. Gasser, *Radiative semileptonic kaon decays*, Nucl.Phys. **B396** (1993), 81–118, [`arXiv:hep-ph/9209261` [hep-ph]].

[123] A. A. Poblaguev, *What can be learned from an experimental study of radiative K(l3) decay?*, Phys. Atom. Nucl. **62** (1999), 975–979.

[124] V. Cirigliano and D. Pirjol, *Factorization in exclusive semileptonic radiative B decays*, Phys. Rev. **D72** (2005), 094021, [`hep-ph/0508095`].

[125] H. W. Fearing, E. Fischbach and J. Smith, *Current algebra, anti-k0-l-3 form-factors, and radiative anti-k0-l-3 decay*, Phys. Rev. **D2** (1970), 542–560.

[126] P. Golonka and Z. Wąs, *PHOTOS Monte Carlo: A Precision tool for QED corrections in Z and W decays*, Eur. Phys. J. **C45** (2006), 97–107, [`hep-ph/0506026`].

[127] B. Aubert et al., The BABAR Collaboration collaboration, *Measurement of $|V(cb)|$ and the Form-Factor Slope in $\bar{B} \to Dl^- \bar{\nu}$ Decays in Events Tagged by a Fully Reconstructed B Meson*, Phys.Rev.Lett. **104** (2010), 011802, [`arXiv:0904.4063` [hep-ex]].

[128] B. Aubert et al., The BABAR Collaboration collaboration, *Measurements of the Semileptonic Decays* $\bar{B} \to Dl\bar{\nu}$ *and* $\bar{B} \to D * l\bar{\nu}$ *Using a Global Fit to D X l anti-nu Final States*, Phys.Rev. **D79** (2009), 012002, [arXiv:0809.0828 [hep-ex]].

[129] M. B. Wise, *Chiral perturbation theory for hadrons containing a heavy quark*, Phys. Rev. **D45** (1992), 2188–2191.

[130] G. Burdman and J. F. Donoghue, *Union of chiral and heavy quark symmetries*, Phys.Lett. **B280** (1992), 287–291.

[131] T.-M. Yan et al., *Heavy quark symmetry and chiral dynamics*, Phys. Rev. **D46** (1992), 1148–1164.

[132] M. B. Wise, *Combining chiral and heavy quark symmetry*, hep-ph/9306277.

[133] B. Aubert et al., The BABAR collaboration, *Measurement of the* $B^0 \to \pi^- l^+ \nu$ *Form-Factor Shape and Branching Fraction, and Determination of* $|V_{ub}|$ *with a Loose Neutrino Reconstruction Technique*, Phys. Rev. Lett. **98** (2007), 091801, [hep-ex/0612020].

[134] M. Bähr et al., *Herwig++ Physics and Manual*, Eur. Phys. J. **C58** (2008), 639–707, [arXiv:0803.0883 [hep-ph]].

[135] J. André and T. Sjöstrand, *Matching of matrix elements and parton showers*, Phys. Rev. **D57** (1998), 5767–5772, [hep-ph/9708390].

[136] K. Hamilton, P. Richardson and J. Tully, *A modified CKKW matrix element merging approach to angular-ordered parton showers*, JHEP **11** (2009), 038, [arXiv:0905.3072 [hep-ph]].

[137] S. Frixione, P. Nason and B. R. Webber, *Matching NLO QCD and parton showers in heavy flavour production*, JHEP **08** (2003), 007, [hep-ph/0305252].

[138] S. Frixione, E. Laenen, P. Motylinski and B. R. Webber, *Single-top production in MC@NLO*, JHEP **03** (2006), 092, [hep-ph/0512250].

[139] S. Frixione, E. Laenen, P. Motylinski, B. R. Webber and C. D. White, *Single-top hadroproduction in association with a W boson*, JHEP **07** (2008), 029, [arXiv:0805.3067 [hep-ph]].

[140] C. Weydert, S. Frixione, M. Herquet, M. Klasen, E. Laenen, T. Plehn, G. Stavenga and C. D. White, *Charged Higgs boson production in association with a top quark in MC@NLO*, Eur. Phys. J. **C67** (2010), 617–636, [arXiv:0912.3430 [hep-ph]].

[141] T. Toll and S. Frixione, *Charm and bottom photoproduction at HERA with MC@NLO*, arXiv:1106.1614 [hep-ph].

[142] P. Torrielli and S. Frixione, *Matching NLO QCD computations with PYTHIA using MC@NLO*, JHEP **04** (2010), 110, [arXiv:1002.4293 [hep-ph]].

[143] P. Nason and G. Ridolfi, *A positive-weight next-to-leading-order Monte Carlo for Z pair hadroproduction*, JHEP **08** (2006), 077, [hep-ph/0606275].

[144] S. Frixione, P. Nason and G. Ridolfi, *A positive-weight next-to-leading-order Monte Carlo for heavy flavour hadroproduction*, JHEP **09** (2007), 126, [arXiv:0707.3088 [hep-ph]].

[145] S. Alioli, P. Nason, C. Oleari and E. Re, *NLO Higgs boson production via gluon fusion matched with shower in POWHEG*, JHEP **04** (2009), 002, [`arXiv:0812.0578` [hep-ph]].

[146] S. Alioli, P. Nason, C. Oleari and E. Re, *NLO vector-boson production matched with shower in POWHEG*, JHEP **07** (2008), 060, [`arXiv:0805.4802` [hep-ph]].

[147] S. Alioli, P. Nason, C. Oleari and E. Re, *NLO single-top production matched with shower in POWHEG: s- and t-channel contributions*, JHEP **09** (2009), 111, [`arXiv:0907.4076` [hep-ph]].

[148] P. Nason and C. Oleari, *NLO Higgs boson production via vector-boson fusion matched with shower in POWHEG*, JHEP **02** (2010), 037, [`arXiv:0911.5299` [hep-ph]].

[149] C. Oleari and L. Reina, *W b bbar production in POWHEG*, JHEP **1108** (2011), 061, [`arXiv:1105.4488` [hep-ph]].

[150] T. Melia, P. Nason, R. Rontsch and G. Zanderighi, W^+W^+ *plus dijet production in the POWHEGBOX*, Eur.Phys.J. **C71** (2011), 1670, [`arXiv:1102.4846` [hep-ph]].

[151] T. Melia, P. Nason, R. Rontsch and G. Zanderighi, *W+W-, WZ and ZZ production in the POWHEG BOX*, `arXiv:1107.5051` [hep-ph].

[152] S. Alioli, P. Nason, C. Oleari and E. Re, *Vector boson plus one jet production in POWHEG*, JHEP **1101** (2011), 095, [`arXiv:1009.5594` [hep-ph]].

[153] S. Alioli, K. Hamilton, P. Nason, C. Oleari and E. Re, *Jet pair production in POWHEG*, JHEP **1104** (2011), 081, [`arXiv:1012.3380` [hep-ph]].

[154] A. Kardos, C. Papadopoulos and Z. Trocsanyi, *Top quark pair production in association with a jet with NLO parton showering*, `arXiv:1101.2672` [hep-ph].

[155] M. Garzelli, A. Kardos, C. Papadopoulos and Z. Trocsanyi, *Standard Model Higgs boson production in association with a top anti-top pair at NLO with parton showering*, `arXiv:1108.0387` [hep-ph].

[156] O. Latunde-Dada, S. Gieseke and B. Webber, *A positive-weight next-to-leading-order Monte Carlo for e^+e^- annihilation to hadrons*, JHEP **02** (2007), 051, [`hep-ph/0612281`].

[157] K. Hamilton, P. Richardson and J. Tully, *A positive-weight next-to-leading order Monte Carlo simulation of Drell-Yan vector boson production*, JHEP **10** (2008), 015, [`arXiv:0806.0290` [hep-ph]].

[158] O. Latunde-Dada, *Applying the `POWHEG` method to top-pair production and decays at the ILC*, Eur. Phys. J. **C58** (2008), 543–554, [`arXiv:0806.4560` [hep-ph]].

[159] A. Papaefstathiou and O. Latunde-Dada, *NLO production of W' bosons at hadron colliders using the MC@NLO and POWHEG methods*, JHEP **07** (2009), 044, [`arXiv:0901.3685` [hep-ph]].

[160] K. Hamilton, P. Richardson and J. Tully, *A positive-weight Next-to-Leading Order Monte Carlo Simulation for Higgs boson production*, JHEP **04** (2009), 116, [`arXiv:0903.4345` [hep-ph]].

[161] L. D'Errico and P. Richardson, *A Positive-Weight Next-to-Leading-Order Monte Carlo Simulation of Deep Inelastic Scattering and Higgs Boson Production via Vector Boson Fusion in Herwig++*, `arXiv:1106.2983` [hep-ph].

[162] L. D'Errico and P. Richardson, *Next-to-Leading-Order Monte Carlo Simulation of Diphoton Production in Hadronic Collisions*, `arXiv:1106.3939` [hep-ph].

[163] M. H. Seymour, *Matrix-element corrections to parton shower algorithms*, Comp. Phys. Commun. **90** (1995), 95–101, [`hep-ph/9410414`].

[164] M. H. Seymour, *A simple prescription for first-order corrections to quark scattering and annihilation processes*, Nucl. Phys. **B436** (1995), 443–460, [`hep-ph/9410244`].

[165] G. Corcella and M. H. Seymour, *Matrix element corrections to parton shower simulations of heavy quark decay*, Phys. Lett. **B442** (1998), 417–426, [`hep-ph/9809451`].

[166] G. Miu and T. Sjöstrand, *W production in an improved parton-shower approach*, Phys. Lett. **B449** (1999), 313–320, [`hep-ph/9812455`].

[167] G. Corcella and M. H. Seymour, *Initial state radiation in simulations of vector boson production at hadron colliders*, Nucl. Phys. **B565** (2000), 227–244, [`hep-ph/9908388`].

[168] E. Norrbin and T. Sjöstrand, *QCD radiation off heavy particles*, Nucl. Phys. **B603** (2001), 297–342, [`hep-ph/0010012`].

[169] R. Frederix, S. Frixione, V. Hirschi, F. Maltoni, R. Pittau et al., *Scalar and pseudoscalar Higgs production in association with a top-antitop pair*, Phys.Lett. **B701** (2011), 427–433, [`arXiv:1104.5613` [hep-ph]].

[170] R. Frederix, S. Frixione, V. Hirschi, F. Maltoni, R. Pittau and P. Torrielli, *W and $Z/\gamma*$ boson production in association with a bottom-antibottom pair*, JHEP **1109** (2011), 061, [`arXiv:1106.6019` [hep-ph]].

[171] N. Lavesson and L. Lönnblad, *Extending CKKW-merging to one-loop matrix elements*, JHEP **12** (2008), 070, [`arXiv:0811.2912` [hep-ph]].

[172] K. Hamilton and P. Nason, *Improving NLO-parton shower matched simulations with higher order matrix elements*, JHEP **06** (2010), 039, [`arXiv:1004.1764` [hep-ph]].

[173] S. Höche, F. Krauss, M. Schönherr and F. Siegert, *NLO matrix elements and truncated showers*, JHEP **08** (2011), 123, [`arXiv:1009.1127` [hep-ph]].

[174] V. N. Gribov and L. N. Lipatov, *Deep inelastic e-p scattering in perturbation theory*, Sov. J. Nucl. Phys. **15** (1972), 438–450.

[175] L. N. Lipatov, *The parton model and perturbation theory*, Sov. J. Nucl. Phys. **20** (1975), 94–102.

[176] Y. L. Dokshitzer, *Calculation of the structure functions for deep inelastic scattering and e^+e^- annihilation by perturbation theory in quantum chromodynamics*, Sov. Phys. JETP **46** (1977), 641–653.

[177] R. K. Ellis, W. J. Stirling and B. R. Webber, *QCD and collider physics*, ed. 1, vol. 8, Cambridge Monogr. Part. Phys. Nucl. Phys. Cosmol., 1996.

[178] M. E. Peskin and D. V. Schroeder, *An Introduction to quantum field theory*, Westview Press, 1995.

[179] V. V. Sudakov, *Vertex parts at very high-energies in quantum electrodynamics*, Sov. Phys. JETP **3** (1956), 65–71.

[180] R. P. Feynman, *Photon-hadron interactions*, Reading, MA, USA: Benjamin, 1972.

[181] J. C. Collins and D. E. Soper, *The theorems of perturbative QCD*, Ann. Rev. Nucl. Part. Sci. **37** (1987), 383–409.

[182] J. C. Collins, D. E. Soper and G. Sterman, *Soft gluons and factorization*, Nucl. Phys. **B308** (1988), 833–856.

[183] J. C. Collins, D. E. Soper and G. Sterman, *Factorization of hard processes in QCD*, Adv. Ser. Direct. High Energy Phys. **5** (1988), 1–91, [`hep-ph/0409313`].

[184] J. Bjorken, *Asymptotic Sum Rules at Infinite Momentum*, Phys.Rev. **179** (1969), 1547–1553.

[185] A. D. Martin, W. J. Stirling, R. S. Thorne and G. Watt, *Parton distributions for the LHC*, Eur. Phys. J. **C63** (2009), 189–295, [`arXiv:0901.0002` [hep-ph]].

[186] H.-L. Lai, M. Guzzi, J. Huston, Z. Li, P. M. Nadolsky et al., *New parton distributions for collider physics*, Phys.Rev. **D82** (2010), 074024, [`arXiv:1007.2241` [hep-ph]].

[187] S. Lionetti, R. D. Ball, V. Bertone, F. Cerutti, L. Del Debbio et al., *Precision determination of α_s using an unbiased global NLO parton set*, Phys.Lett. **B701** (2011), 346–352, [`arXiv:1103.2369` [hep-ph]].

[188] S. Alekhin, J. Blumlein, S. Klein and S. Moch, *The 3, 4, and 5-flavor NNLO Parton from Deep-Inelastic-Scattering Data and at Hadron Colliders*, Phys.Rev. **D81** (2010), 014032, [`arXiv:0908.2766` [hep-ph]].

[189] The H1 and ZEUS Collaborations, *Combined measurement and QCD analysis of the Inclusive $e^{\pm}p$ scattering cross sections at HERA*, JHEP **01** (2009), 109, [`arXiv:0911.0884` [hep-ex]].

[190] H. Georgi and H. Politzer, *Electroproduction scaling in an asymptotically free theory of strong interactions*, Phys.Rev. **D9** (1974), 416–420.

[191] D. J. Gross and F. Wilczek, *Asymptotically free gauge theories. II*, Phys. Rev. **D9** (1974), 980–993.

[192] G. Curci, W. Furmanski and R. Petronzio, *Evolution of parton densities beyond leading order: The non-singlet case*, Nucl. Phys. **B175** (1980), 27.

[193] W. Furmanski and R. Petronzio, *Singlet parton densities beyond leading order*, Phys. Lett. **B97** (1980), 437.

[194] E. Floratos, D. Ross and C. T. Sachrajda, *Higher Order Effects in Asymptotically Free Gauge Theories: The Anomalous Dimensions of Wilson Operators*, Nucl.Phys. **B129** (1977), 66–88.

[195] A. Gonzalez-Arroyo, C. Lopez and F. Yndurain, *Second Order Contributions to the Structure Functions in Deep Inelastic Scattering. 1. Theoretical Calculations*, Nucl.Phys. **B153** (1979), 161–186.

[196] E. Floratos, C. Kounnas and R. Lacaze, *Higher Order QCD Effects in Inclusive Annihilation and Deep Inelastic Scattering*, Nucl.Phys. **B192** (1981), 417.

[197] K. J. Golec-Biernat, S. Jadach, W. Placzek and M. Skrzypek, *Markovian Monte Carlo solutions of the NLO QCD evolution equations*, Acta Phys.Polon. **B37** (2006), 1785–1832, [`arXiv:hep-ph/0603031` [hep-ph]].

[198] A. Kusina, S. Jadach, M. Skrzypek and M. Slawinska, *NLO evolution kernels: Monte Carlo versus $M\bar{S}$*, Acta Phys.Polon. **B42** (2011), 1475, [`arXiv:1106.1787` [hep-ph]].

[199] D. Amati, A. Bassetto, M. Ciafaloni, G. Marchesini and G. Veneziano, *A treatment of hard processes sensitive to the infrared structure of QCD*, Nucl. Phys. **B173** (1980), 429.

[200] D. A. Kosower, *Antenna factorization of gauge-theory amplitudes*, Phys. Rev. **D57** (1998), 5410–5416, [`hep-ph/9710213`].

[201] D. A. Kosower, *Antenna factorization in strongly-ordered limits*, Phys. Rev. **D71** (2005), 045016, [`hep-ph/0311272`].

[202] A. Gehrmann-De Ridder, T. Gehrmann and E. W. N. Glover, *Antenna subtraction at NNLO*, JHEP **09** (2005), 056, [`hep-ph/0505111`].

[203] A. Daleo, T. Gehrmann and D. Maître, *Antenna subtraction with hadronic initial states*, JHEP **04** (2007), 016, [`hep-ph/0612257`].

[204] G. Marchesini and B. R. Webber, *Simulation of QCD Jets Including Soft Gluon Interference*, Nucl. Phys. **B238** (1984), 1.

[205] G. Marchesini and B. R. Webber, *Monte Carlo Simulation of General Hard Processes with Coherent QCD Radiation*, Nucl. Phys. **B310** (1988), 461.

[206] M. Bengtsson and T. Sjöstrand, *A comparative study of coherent and non-coherent parton shower evolution*, Nucl. Phys. **B289** (1987), 810.

[207] S. Frixione, Z. Kunszt and A. Signer, *Three-jet cross-sections to next-to-leading order*, Nucl. Phys. **B467** (1996), 399–442, [`hep-ph/9512328`].

[208] S. Frixione, *A general approach to jet cross sections in QCD*, Nucl. Phys. **B507** (1997), 295–314, [`hep-ph/9706545`].

[209] G. Gustafson, *Dual description of a confined colour field*, Phys. Lett. **B175** (1986), 453.

[210] G. Gustafson and U. Pettersson, *Dipole formulation of QCD cascades*, Nucl. Phys. **B306** (1988), 746.

[211] B. Andersson, G. Gustafson and L. Lönnblad, *Gluon splitting in the color dipole cascades*, Nucl. Phys. **B339** (1990), 393–406.

[212] S. Frixione, *Colourful FKS subtraction*, JHEP **1109** (2011), 091, [`arXiv:1106.0155 [hep-ph]`].

[213] M. Dinsdale, M. Ternick and S. Weinzierl, *Parton showers from the dipole formalism*, Phys. Rev. **D76** (2007), 094003, [`arXiv:0709.1026 [hep-ph]`].

[214] W. T. Giele, D. A. Kosower and P. Z. Skands, *A Simple shower and matching algorithm*, Phys. Rev. **D78** (2008), 014026, [`arXiv:0707.3652 [hep-ph]`].

[215] R. D. Field, *Applications of perturbative QCD*, Addison-Wesley, Redwood City, USA, 1989, Frontiers in physics, 77.

[216] S. Plätzer and S. Gieseke, *Coherent Parton Showers with Local Recoils*, JHEP **01** (2011), 024, [`arXiv:0909.5593 [hep-ph]`].

[217] A. Ballestrero and E. Maina, *A new method for helicity calculations*, Phys. Lett. **B350** (1995), 225–233, [`hep-ph/9403244`].

[218] G. P. Lepage, *A New Algorithm for Adaptive Multidimensional Integration*, J. Comput. Phys. **27** (1978), 192.

[219] Z. Nagy and D. E. Soper, *Matching parton showers to NLO computations*, JHEP **10** (2005), 024, [`hep-ph/0503053`].

[220] Z. Nagy and D. E. Soper, *A new parton shower algorithm: Shower evolution, matching at leading and next-to-leading order level*, `hep-ph/0601021`.

[221] T. Carli, T. Gehrmann and S. Höche, *Hadronic final states in deep-inelastic scattering with SHERPA*, Eur. Phys. J. **C67** (2010), 73, [`arXiv:0912.3715 [hep-ph]`].

[222] P. M. Nadolsky et al., *Implications of CTEQ global analysis for collider observables*, Phys. Rev. **D78** (2008), 013004, [`arXiv:0802.0007 [hep-ph]`].

[223] B. Andersson, G. Gustafson, G. Ingelman and T. Sjöstrand, *Parton Fragmentation and String Dynamics*, Phys. Rept. **97** (1983), 31–145.

[224] B. Andersson, *The Lund model*, vol. 7, Camb. Monogr. Part. Phys. Nucl. Phys. Cosmol., 1997.

[225] C. F. Berger, Z. Bern, L. J. Dixon, F. Febres-Cordero, D. Forde, T. Gleisberg, H. Ita, D. A. Kosower and D. Maître, *Precise Predictions for W + 3 Jet Production at Hadron Colliders*, Phys. Rev. Lett. **102** (2009), 222001, [`arXiv:0902.2760 [hep-ph]`].

[226] C. F. Berger et al., *Next-to-leading order QCD predictions for W+3-Jet distributions at hadron colliders*, Phys. Rev. **D80** (2009), 074036, [`arXiv:0907.1984 [hep-ph]`].

[227] C. F. Berger, Z. Bern, L. J. Dixon, F. Febres-Cordero, D. Forde, T. Gleisberg, H. Ita, D. A. Kosower and D. Maître, *Next-to-leading order QCD predictions for Z, γ^*+3-Jet distributions at the Tevatron*, Phys. Rev. **D82** (2010), 074002, [`arXiv:1004.1659 [hep-ph]`].

[228] Z. Bern, G. Diana, L. Dixon, F. Febres-Cordero, D. Forde et al., *Left-Handed W Bosons at the LHC*, Phys. Rev. **D84** (2011), 034008, [`arXiv:1103.5445 [hep-ph]`].

[229] Z. Bern, G. Diana, L. Dixon, F. Febres-Cordero, S. Höche et al., *Driving Missing Data at Next-to-Leading Order*, `arXiv:1106.1423 [hep-ph]`.

[230] S. Dawson, *Radiative corrections to Higgs boson production*, Nucl. Phys. **B359** (1991), 283–300.

[231] A. Djouadi, M. Spira and P. Zerwas, *Production of Higgs bosons in proton colliders: QCD corrections*, Phys. Lett. **B264** (1991), 440–446.

[232] C. Anastasiou, K. Melnikov and F. Petriello, *Fully differential Higgs boson production and the di-photon signal through next-to-next-to-leading order*, Nucl. Phys. **B724** (2005), 197–246, [`hep-ph/0501130`].

[233] C. Anastasiou, G. Dissertori and F. Stöckli, *NNLO QCD predictions for the $H \to WW \to l\nu l\nu$ signal at the LHC*, JHEP **09** (2007), 018, [`arXiv:0707.2373 [hep-ph]`].

[234] C. Anastasiou, R. Boughezal and F. Petriello, *Mixed QCD-electroweak corrections to Higgs boson production in gluon fusion*, JHEP **04** (2009), 003, [`arXiv:0811.3458 [hep-ph]`].

[235] S. Catani, D. de Florian, M. Grazzini and P. Nason, *Soft-gluon resummation for Higgs boson production at hadron colliders*, JHEP **07** (2003), 028, [`hep-ph/0306211`].

[236] G. Bozzi, S. Catani, D. de Florian and M. Grazzini, *Transverse-momentum resummation and the spectrum of the Higgs boson at the LHC*, Nucl. Phys. **B737** (2006), 73–120, [`hep-ph/0508068`].

[237] J. M. Campbell and R. K. Ellis, *Update on vector boson pair production at hadron colliders*, Phys. Rev. **D60** (1999), 113006, [`hep-ph/9905386`].

[238] L. J. Dixon, Z. Kunszt and A. Signer, *Helicity amplitudes for $\mathcal{O}(\alpha_s)$ production of W^+W^-, $W^\pm Z$, ZZ, $W^\pm\gamma$, or $Z\gamma$ pairs at hadron colliders*, Nucl. Phys. **B531** (1998), 3–23, [`hep-ph/9803250`].

[239] A. Heister et al., The ALEPH collaboration, *Studies of QCD at e^+e^- centre-of-mass energies between 91 and 209 GeV*, Eur. Phys. J. **C35** (2004), 457–486.

[240] C. Adloff et al., The H1 collaboration, *Measurement and QCD analysis of jet cross sections in deep-inelastic positron-proton collisions at $\sqrt{s}$ of 300 GeV*, Eur. Phys. J. **C19** (2001), 289–311, [`hep-ex/0010054`], DESY-00-145.

[241] C. Adloff et al., The H1 collaboration, *Three-jet production in deep-inelastic scattering at HERA*, Phys. Lett. **B515** (2001), 17–29, [`hep-ex/0106078`], DESY-01-073.

[242] V. M. Abazov et al., The DØ collaboration, *Measurement of the normalized $Z/\gamma^* \to \mu^+\mu^-$ transverse momentum distribution in $p\bar{p}$ collisions at $\sqrt{s} = 1.96$ TeV*, Phys. Lett. **B693** (2010), 522–530, [`arXiv:1006.0618 [hep-ex]`].

[243] V. M. Abazov et al., The DØ collaboration, *Measurement of the shape of the boson rapidity distribution for $p\bar{p} \to Z/\gamma^* \to e^+e^- + X$ events produced at $\sqrt{s}$ of 1.96 TeV*, Phys. Rev. **D76** (2007), 012003, [`hep-ex/0702025`].

[244] B. Abbott et al., The DØ collaboration, *Differential cross section for W boson production as a function of transverse momentum in $p\bar{p}$ collisions at $\sqrt{s} = 1.8$ TeV*, Phys. Lett. **B513** (2001), 292–300, [`hep-ex/0010026`].

[245] V. M. Abazov et al., The DØ collaboration, *Measurement of $Z/\gamma^*+jet+X$ angular distributions in $p\bar{p}$ collisions at $\sqrt{s} = 1.96$ TeV*, Phys. Lett. **B682** (2010), 370–380, [`arXiv:0907.4286 [hep-ex]`].

[246] M. Cacciari, G. P. Salam and G. Soyez, *The Anti-k(t) jet clustering algorithm*, JHEP **0804** (2008), 063, [`arXiv:0802.1189 [hep-ph]`].

[247] T. Aaltonen et al., The CDF collaboration, *Measurement of Inclusive Jet Cross Sections in $Z/\gamma^*(\to ee)+$ jets Production in $p\bar{p}$ Collisions at $\sqrt{s} = 1.96$ TeV*, Phys. Rev. Lett. **100** (2008), 102001, [`arXiv:0711.3717 [hep-ex]`].

[248] V. M. Abazov et al., The DØ collaboration, *Measurement of differential $Z/\gamma^* + jet + X$ cross sections in $p\bar{p}$ collisions at $\sqrt{s} = 1.96$ TeV*, Phys. Lett. **B669** (2008), 278–286, [`arXiv:0808.1296 [hep-ex]`].

[249] V. Abazov et al., The DØ collaboration, *Measurements of differential cross sections of $Z/\gamma^*+jets+X$ events in proton anti-proton collisions at $\sqrt{s} = 1.96$ TeV*, Phys. Lett. **B678** (2009), 45–54, [`arXiv:0903.1748 [hep-ex]`].

[250] A. Abulencia et al., The CDF collaboration, *Measurement of the inclusive jet cross section in $p\bar{p}$ interactions at $\sqrt{s} = 1.96$-TeV using a cone-based jet algorithm.*, Phys. Rev. **D74** (2006), 071103, [`hep-ex/0512020`].

[251] G. C. Blazey et al., *Run II jet physics*, `hep-ex/0005012`.

[252] N. Lavesson and L. Lönnblad, *Merging parton showers and matrix elements – back to basics*, JHEP **04** (2008), 085, [`arXiv:0712.2966 [hep-ph]`].

[253] S. Catani and L. Trentadue, *Resummation of the QCD perturbative series for hard processes*, Nucl. Phys. **B327** (1989), 323.

[254] S. Catani, B. R. Webber and G. Marchesini, *QCD coherent branching and semiinclusive processes at large x*, Nucl. Phys. **B349** (1991), 635–654.

[255] G. Abbiendi et al., The OPAL collaboration, *A simultaneous measurement of the QCD colour factors and the strong coupling*, Eur. Phys. J. **C20** (2001), 601–615, [hep-ex/0101044].

[256] T. Sjöstrand, PYTHIA 5.7 and JETSET 7.4 *Physics and Manual*, hep-ph/9508391.

[257] C. Adloff et al., The H1 collaboration, *Measurement of inclusive jet cross-sections in deep-inelastic ep scattering at HERA*, Phys. Lett. **B542** (2002), 193–206, [hep-ex/0206029], DESY-02-079.

[258] S. D. Ellis and D. E. Soper, *Successive combination jet algorithm for hadron collisions*, Phys. Rev. **D48** (1993), 3160–3166, [hep-ph/9305266].

[259] S. Catani, Y. L. Dokshitzer, M. H. Seymour and B. R. Webber, *Longitudinally-invariant $k_\perp$-clustering algorithms for hadron–hadron collisions*, Nucl. Phys. **B406** (1993), 187–224.

[260] S. Frixione and G. Ridolfi, *Jet photoproduction at HERA*, Nucl. Phys. **B507** (1997), 315–333, [hep-ph/9707345].

[261] V. M. Abazov et al., The DØ collaboration, *Measurement of the shape of the boson transverse momentum distribution in $p\bar{p} \to Z/\gamma^* \to ee + X$ events produced at $\sqrt{s} = 1.96$ TeV*, Phys. Rev. Lett. **100** (2008), 102002, [arXiv:0712.0803 [hep-ex]].

[262] V. M. Abazov et al., The DØ collaboration, *Measurement of the ratios of the $Z/\gamma^*+ \geq n$ jet production cross sections to the total inclusive Z/γ^* cross section in $p\bar{p}$ collisions at $\sqrt{s}$=1.96 TeV*, Phys. Lett. **B658** (2008), 112–119, [hep-ex/0608052].

[263] J. M. Butterworth et al., *The Tools and Monte Carlo working group: Summary report*, arXiv:1003.1643 [hep-ph], Proceedings of the Workshop "Physics at TeV Colliders", Les Houches, France, 8-26 June, 2009.

[264] T. Gleisberg, F. Krauss, A. Schälicke, S. Schumann and J.-C. Winter, *Studying W^+W^- production at the Fermilab Tevatron with* SHERPA, Phys. Rev. **D72** (2005), 034028, [hep-ph/0504032].

[265] T. Binoth, T. Gleisberg, S. Karg, N. Kauer and G. Sanguinetti, *NLO QCD corrections to ZZ+jet production at hadron colliders*, Phys. Lett. **B683** (2010), 154–159, [arXiv:0911.3181 [hep-ph]].

[266] I. Caprini, L. Lellouch and M. Neubert, *Dispersive bounds on the shape of $\bar{B} \to D^{(*)}l\bar{\nu}$ form factors*, Nucl. Phys. **B530** (1998), 153–181, [hep-ph/9712417].

[267] P. Ball and R. Zwicky, *New results on $B \to \pi, K, \eta$ decay form factors from light-cone sum rules*, Phys. Rev. **D71** (2005), 014015, [hep-ph/0406232].

[268] A. K. Leibovich, Z. Ligeti, I. W. Stewart and M. B. Wise, *Semileptonic B decays to excited charmed mesons*, Phys. Rev. **D57** (1998), 308–330, [hep-ph/9705467].

[269] A. K. Leibovich, Z. Ligeti, I. W. Stewart and M. B. Wise, *Model independent results for $B \to D1(2420)$ l anti-nu and $B \to D*2(2460)$ l anti-nu at order Lambda(QCD)/m(c,b)*, Phys. Rev. Lett. **78** (1997), 3995–3998, [hep-ph/9703213].

[270] J. C. Ward, *An Identity in Quantum Electrodynamics*, Phys. Rev. **78** (1950), 182.

[271] E. Fischbach and J. Smith, *Current algebra, k-l-3+ form-factors, and radiative k-l-3+ decay*, Phys. Rev. **184** (1969), 1645–1660.

[272] G. Passarino and M. Veltman, *One Loop Corrections for e^+e^- Annihilation Into $\mu^+\mu^-$ in the Weinberg Model*, Nucl.Phys. **B160** (1979), 151.

[273] D. Y. Bardin and G. Passarino, *The standard model in the making: Precision study of the electroweak interactions*, Oxford, UK: Clarendon, 1999.

[274] R. Ellis and G. Zanderighi, *Scalar one-loop integrals for QCD*, JHEP **0802** (2008), 002, [`arXiv:0712.1851` [hep-ph]].

[275] R. Ellis, *QCDloop: A repository for one-loop scalar integrals*, http://qcdloop.fnal.gov/.

Declaration

The work in this thesis is based on research carried out at the Institut für Kern- und Teilchenphysik, Technische Universität Dresden.

The research described in this thesis was carried out in collaboration with Jennifer Archibald, Dr. Florian Bernlochner, Dr. Tanju Gleisberg, Dr. Stefan Höche, Dr. Frank Krauss, Dr. Steffen Schumann, Dr. Frank Siegert, Dr. Jan Winter.

Refereed Publications

- Marek Schönherr, Frank Krauss,
  Soft Photon Radiation in Particle Decays in SHERPA,
  JHEP 12(2008)018 [arXiv:0810.5071]

- Tanju Gleisberg, Stefan Höche, Frank Krauss, Marek Schönherr, Steffen Schumann, Frank Siegert, Jan Winter,
  Event generation with SHERPA *1.1*,
  JHEP 02(2009)007 [arXiv:0811.4622]

- Stefan Höche, Frank Krauss, Marek Schönherr, Frank Siegert,
  Automating the POWHEG *method in Sherpa*,
  JHEP 04(2011)024 [arXiv:1008.5399]

- Stefan Höche, Frank Krauss, Marek Schönherr, Frank Siegert,
  NLO matrix elements and truncated showers,
  JHEP 08(2011)123 [arXiv:1009.1127]

Preprints

- Florian U. Bernlochner, Marek Schönherr,
  Comparing different ansatzes to describe electroweak radiative corrections to exclusive semileptonic B meson decays into (pseudo)scalar final state mesons using Monte-Carlo techniques,
  arXiv:1010.5997

Conference Proceedings

- Tanju Gleisberg, Stefan Höche, Frank Krauss, Radoslaw Matyszkiewicz, Marek Schönherr, Steffen Schumann, Frank Siegert, Jan Winter,
  New trends in modern event generators,
  arXiv:0705.4648

- Jennifer Archibald, Tanju Gleisberg, Stefan Höche, Frank Krauss, Marek Schönherr, Steffen Schumann, Frank Siegert, Jan Winter,
  Simulation of photon-photon interactions in hadron collisions with SHERPA,
  Nucl.Phys.Proc.Suppl.179-180 (2008) 218-225

- Jennifer Archibald, Tanju Gleisberg, Stefan Höche, Frank Krauss, Marek Schönherr, Steffen Schumann, Frank Siegert, Jan Winter,
  Recent developments in SHERPA,
  Nucl.Phys.Proc.Suppl.183 (2008) 60-66

- Jennifer Archibald, Tanju Gleisberg, Stefan Höche, Frank Krauss, Marek Schönherr, Steffen Schumann, Frank Siegert, Jan Winter,
  Recent developments in SHERPA,
  Prepared for 16th International Workshop on Deep Inelastic Scattering and Related Subjects (DIS 2008), London, England, 7-11 Apr 2008

- Stefan Höche, Frank Krauss, Marek Schönherr, Frank Siegert,
  Next-to-leading order matrix elements and truncated showers,
  To appear in the proceedings of Physics at the LHC 2010 (PLHC2010), Hamburg, Germany, 7-12 Jun 2010. Published in *Hamburg 2010, Physics at the LHC 2010* 199-203 [arXiv:1009.1477]

- Frank Siegert, Stefan Höche, Frank Krauss, Marek Schönherr,
  Multi-jet merging with NLO matrix elements,
  Prepared for 35th International Conference on High Energy Physics: ICHEP 2010, Paris, France, 21-28 Jul 2010. Published in PoS ICHEP2010:119, 2010 [arXiv:1011.6657]

Acknowledgements

Versicherung

Hiermit versichere ich, dass ich die vorliegende Arbeit ohne unzulässige Hilfe Dritter und ohne Benutzung anderer als der angegebenen Hilfsmittel angefertigt habe; die aus fremden Quellen direkt oder indirekt übernommenen Gedanken sind als solche kenntlich gemacht. Die Arbeit wurde bisher weder im Inland noch im Ausland in gleicher oder ähnlicher Form einer anderen Prüfungsbehörde vorgelegt.

Die vorliegende Arbeit wurde am Institut für Kern- und Teilchenphysik der Technischen Universität Dresden unter wissenschaftlicher Betreuung von Herrn Prof. Dr. Dominik Stöckinger angefertigt.

Es haben keine früheren erfolglosen Promotionsverfahren stattgefunden.

Hiermit erkenne ich die Promotionsordnung der Fakultät für Mathematik und Naturwissenschaften der Technischen Universität Dresden vom 23. Februar 2011 an.

Dresden, 15.09.2011   Marek Schönherr